Contribution to the analysis of turbulent wakes of bluff bodies : impact on the aerodynamic drag

Roshan Shanmughan

UNIVERSITÉ D'ORLÉANS

ÉCOLE DOCTORALE ÉNERGIE, MATÉRIAUX, SCIENCES DE LA TERRE ET DE L'UNIVERS

Laboratoire PRISME

THÈSE présentée par :

Roshan SHANMUGHAN

soutenue le : 13 Juin 2022

pour obtenir le grade de : **Docteur de l'Université d'Orléans**
Discipline/ Spécialité : **Sciences de l'ingénieur. Mécanique des fluides**

Contribution to the analysis of turbulent wakes of bluff bodies: Impact on the aerodynamic drag.

THÈSE dirigée par :

M.	KOURTA Azeddine	Professeur, Université d'Orléans.

RAPPORTEURS :

M.	DAVID Laurent	Professeur, Université de Poitiers.
M.	PASTUR Luc	Professeur, ENSTA Paris.

JURY :

M.	MAZELLIER Nicolas	Professeur, Université d'Orléans.
M.	MORRISON Jonathan	Professeur, Imperial College London.
M.	PASSAGGIA Pierre-Yves	Maître de Conférences, Université d'Orléans.
Mme.	PODVIN Bérengère	Directeur de recherche, CNRS. (Président du jury)

To my beloved Amma and Achan,
May they rest in peace.

Acknowledgements

This work was supported by the Agence Nationale de la Recherche (ANR) through the Investissements d'Avenir program under the Labex CAPRYSSES Project (ANR-11-LABX-0006-01).

Personal acknowledgements

The journey to get a doctorate has finally come to an end. It was not an easy one, but filled with intellectual adventures through the unfathomable sea of fluid mechanics. It is time to express gratitude to all the kind personalities who accompanied me on this unforgettable journey.

I would like to express my sincere gratitude to my thesis director, Prof.Azeddine Kourta and my co-supervisors Prof. Nicolas Mazellier and Dr Pierre-Yves Passaggia for giving me an opportunity to pursue my dream of a PhD, guiding and advising me on this path. I sincerely acknowledge their time, effort, and ideas, which were key elements of the work presented in this thesis. A special word of gratitude is reserved for Pierre-Yves, who always motivated and cheered me up during difficult times and helped me advance. Their commitment to research, scientific approach and life has always been a motivating example to me. I am also indebted to Mr. Stéphane Loyer, the ultimate boss when it comes to wind tunnel experiments, for his generous and continuous support in mounting the experimental setup and in the acquisition of high-quality data. I also thank the laboratory engineer Mr. Yahia Haidous for his time and support to set up the experiments. Furthermore, I also thank the informatics support engineers, Mr. Xavier Michau and Mr. Benoit Clavier, who were always ready to help in case my PC ran into problems.

I would like to extend my gratitude to all members of the ESA team, my colleagues, and all support staff. I sincerely thank my colleagues (other Ph.D. students or currently doctors) for the fun-filled, stressful days we shared and for the beers we had together. A special thanks to Marco Castagna & Stefano Macri, for their very friendly and kind nature. I have always enjoyed their company and conversations, and will never forget the day when I learned that associating ketchup with pizza is really offensive. A special word of thanks goes to Wassim, with whom I started this journey, and we had so much fun together during this period. I would also like to thank Sophie, though we shared the office together for only a few months, for her very kind and friendly nature. A special word of thanks goes to Noura Bettaib, the ATER at ESA, for her friendly nature, and I have always appreciated her company. I would also like to thank Leo, Ernesto, Mathieu, Gaétan, Brian, and Mylène, who joined as I was about to finish my PhD, for their nice company. From the seniors, I would like to thank Prof. Annie Leroy for her friendly and welcoming nature. She always had a smiling face whenever we met. I thank Dr Cedric, who joined the team as maître de conférences recently and is a very friendly person and ready to help anytime. A great word of thanks goes to Sylvie Plessard (PRISME) and Pauline Loury (Ecole Doctorale), for helping me with all the administrative formalities and procedures.

I would also like to extend my sincere gratitude to François Bounis and his family, and

Jocelyne Desprez. They always made us (me and my wife) feel at home. Memories of our dinners and trips together will always be in my heart. Of course, I thank François' cherry trees for their shade, fruits and for keeping me sane during the confinement period of Covid-19. A special word of gratitude to Marie Christine, Patricia, and Claire and her family for their friendly and welcoming nature during my stay in Orléans. I am happy and fortunate to have friends like them.

Most importantly, I thank my father, Mr Shanmughan M.V (Achan), and my mother, Ms Soudamini Shanmughan (Amma), who were my main driving force in pursuing higher studies. I am sure they would have been happy and I hope they watch over me from heaven. I also extend my sincere thanks to my dear wife, Jinitha (Unnimol), who had always supported me during my PhD. My sincere gratitude also goes to my father and mother-in-law, Mr. Unniraj and Ms Premalatha, who had always been supportive. They were always there to help and care for my father during his last days, during my final year of Ph.D., when I had difficulties travelling to India to see him due to Covid-19 restrictions.

I would also like to extend my sincere gratitude to my thesis reviewers and external jury members, Prof. David Laurent, Prof. Luc Pastur, Prof. Jonathan Morrison and Prof. Podvin Bérengère, for being part of the jury, authorising me to defend, sparing time and being there for my defence in spite of their very busy schedule, for their insightful comments and interesting questions, for constructive feed backs and for declaring me as a Doctor.

Last but not least, I thank all the support staff of Université d'Orléans and Polytech d'Orléans, whose support made my work and stay a pleasant experience. Please forgive me if I have unknowingly left out anyone, and please note that it is purely unintentional.

Thank you...

Roshan Shanmughan
March 29, 2023

Résumé du Manuscrit

Le sillage produit en aval des corps non profilés a été étudié à plusieurs reprises pendant les dernières décennies. Ses applications se retrouvent dans un grand nombre de domaines tel que le transport pour n'en citer qu'un. Pour des raisons pratiques, les véhicules du transport routier sont généralement dit à culot droit, ce qui entraîne le décollement de la couche limite produit autour du véhicule, ce qui est à l'origine de pertes de performances aérodynamiques. Dans le cas d'un véhicule, ce décollement entraîne non seulement un impact négatif sur la consommation de carburant, mais aussi dans sa stabilité et sa contrôlabilité. Le décollement peut être retardé dans le cas de géométries simples à courbure continue et finie. Un archétype se trouve être la géométrie cylindrique où le décollement à grands nombre de Reynolds peut être maîtrisé, ce qui permet d'obtenir des effets positifs sur la force de traînée. La situation est différente pour une géométrie avec un bord saillant, ou pour une courbure suffisamment importante, où le décollement est fixé sur le bord d'attaque et/ou sur la borde de fuite. Dans ce travail, on considère une géométrie simple en forme de "D" avec un bord de fuite à angle droit, fixant le point de décollement. La partie frontale à un bord d'attaque circulaire afin de minimiser les effets de décollement. Le corps a aussi une longueur suffisante pour maintenir une couche limite laminaire jusqu'au décollement.

Le sillage en aval des corps non profilés fait apparaître des structures instationnaires et cohérentes dans le sillage, plus connues sous le nom d'Allées de tourbillons de von Kármán". Ici, on parle de structures cohérentes, car ces dernières font apparaître une périodicité en espace et/ou en temps. Ce phénomène se manifeste une fois que le nombre Reynolds dépasse une valeur limite, peu importe la section ou la géométrie de l'objet. En augmentant le nombre de Reynolds, le sillage passe par de nombreuses déformations menant au développement d'instabilités. L'apparition de ces structures est associée à une réduction de la pression à l'arrière du corps et par conséquent, une augmentation de la traînée de pression, qui est la contribution principale à la traînée totale. Les méthodes de contrôle pour réduire la traînée peuvent être divisées en deux catégories, c'est-à-dire passive ou active. Le contrôle passif vise à modifier la géométrie par des appendices qui visent à affaiblir où à supprimer les structures cohérentes. La seconde correspond aux méthodes utilisant des actionneurs fonctionnant suivant une loi de contrôle basée sur un modèle ad hoc ou un modèle d'ordre réduit.

Bien que de nombreux travaux soient dédiés à la réduction de la traînée, avec une attention particulière apportée aux structures cohérentes, plusieurs zones d'ombres restent encore à lever afin de fournir des caractéristiques basées sur la physique pour concevoir les méthodes efficaces pour le contrôle de la traînée. C'est tout l'enjeu de cette thèse de doctorat dont l'objectif principal est de caractériser finement le sillage, permettant d'identifier les régions importantes et les plus sensibles pour comprendre les mécanismes physiques

qui contrôlent les structures cohérentes et, par conséquent, la traînée. Pour cela, ce travail s'appuie sur les démarches expérimentales où des approches hybrides numériques sont développées pour l'analyse des équations de la physique. Les combinaisons de ces outils originaux ont permis d'expliquer les phénomènes observés et à proposer des mécanismes pertinents associés à la traînée. Afin de faciliter la lecture, les détails de ces travaux sont organisée en sept chapitres, traduit en langue anglaise, ou chacun aborde un sujet spécifique. De plus, une annexe décrit la méthode suivie pour le développement des outils.

Chapitre 1: est une introduction générale du sujet. La première partie de ce chapitre explique le choix du corps épais bi-dimensionnel avec le bord de fuite à angle droit par rapport aux autres modèles plus complexes. Les caractéristiques clés du sillage, présentant les diffèrent régimes de l'écoulement selon le nombre de Reynolds est introduit en référence à plusieurs études déjà menées. Ensuite, les méthodes de contrôle de la traînée issues de la littérature sont présentées en expliquant les stratégies utilisées pour atténuer les effets des structures cohérentes sur la traînée, suivi par des références aux travaux menés sur l'étude des mécanismes d'interaction des structures cohérentes avec d'autres structures cohérentes ou son rôle dans la production de turbulence dans le sillage. Ce chapitre se termine par la description des objectifs de cette thèse.

Chapitre 2 fournit les détails sur les méthodes expérimentales utilisées pour obtenir les données dans le sillage. L'homogénéité de l'écoulement sans le corps est vérifiée en mesurant le profil de vitesse moyen par la technique d'anémométrie par fil chaud. Le modèle en forme de "D" est installé dans la soufflerie en maintenant un angle d'attaque proche de zéro afin de pouvoir obtenir un sillage symétrique. La pression autour du corps est mesurée par les capteurs installés autour de ce dernier. La technique utilisée pour mesurer le sillage est celle de la "Vélocimétrie par Images de Particules" (PIV) où l'écoulement est ensemencé de particules qui suivent le fluide de manière fidèle. L'écoulement est illuminé par une nappe laser et deux photos successives haute résolution sont analysées pour obtenir le champ de vitesse instantané. En plus, la technique d'anémomètre par fil chaud est aussi utilisée pour vérifier les données obtenues à partir de la PIV. Les paramètres de contrôle sont le nombre de Reynolds et la turbulence dans l'écoulement amont, la dernière utilisant une grille régulière placée dans la veine d'essai.

Chapitre 3 présente un nouvel outil pour l'estimation précise du champ de pression moyen dans le sillage. L'objet du développement de cet outil est la fermeture du bilan de quantité de mouvement moyen afin de pouvoir répondre aux questions concernant les mécanismes associés à la traînée. Le champ de pression moyen est estimée en utilisant les champs de vitesse moyenne et les contraintes de Reynolds obtenus à partir de la technique de PIV, par l'inversion de l'opérateur Laplacien et en utilisant les conditions aux limites de type Neumann. En exploitant une méthode de contrôle optimal, la pression moyenne obtenue à partir des capteurs de pression installés sur le corps sont utilisés afin de réduire la propagation des erreurs des conditions aux limites au champ de pression moyenne. La précision de ce champ de pression corrigé est estimée en comparant la traînée obtenue à partir des bilans autour des surfaces de contrôle et ceux obtenus utilisant des capteurs, où les deux sont en excellent accord.

Chapitre 4 présente en première partie les caractéristiques qualitatives des champs de vitesse moyen, contraintes de Reynolds et pression moyenne du sillage. En utilisant l'outil développé dans le chapitre 3 et en exploitant la linéarité de l'opérateur Laplacien, la pression est décomposée. Le bilan révèle le processus d'échange de quantité de mouvement dans le sillage proche. Les composantes normales du tenseur des contraintes Reynolds jouent un rôle de source et de puits pour la traînée, tandis que la composante de cisaillement redistribue la quantité de mouvement. La décomposition de la pression moyenne montre que la condition initiale du sillage est importante proche de la base du corps alors que la contrainte normale transversale du tenseur de Reynolds contrôle la pression. Cependant, l'analyse de l'équation de transport des contraintes de Reynolds moyennes ne peut pas être menée à son terme en raison des termes non résolus, issues des termes relatifs à la pression fluctuante et de la dissipation.

Chapitre 5 aborde la question des mécanismes de transport des contraintes de Reynolds en décomposant les fluctuations totale en structures cohérentes et en fluctuations incohérentes. Leurs contributions respectives sont comparables dans le bilan de traînée. Cependant, ce sont les structures cohérentes qui contribuent principalement à la pression moyenne, qui en retour est la contribution principale à la traînée. La décomposition des fluctuations est effectuée par l'intermédiaire de la technique de "Décomposition Orthogonale aux valeurs Propres" (POD) qui capture les structures les plus énergétiques à partir de la PIV. Une nouvelle méthode est développée pour reconstruire le champ de pression cohérent. La dérivée temporelle des champs de vitesse cohérente est estimée à partir de la dérivée temporelle de la fonction de courant, la dernière est estimée par l'inversion d'un problème de Poisson.

La pression des structures cohérentes permet d'estimer la portance et la traînée instationnaire cohérente qui sont en bon accord avec les mesures de pression obtenues par les capteurs. La dissipation induite par les structures cohérentes étant négligeables, la pression des structures cohérentes permet de clore le bilan du transport des contraintes de Reynolds cohérentes. Le bilan révèle que les termes de diffusion et d'étirement induits par la pression cohérente jouent un rôle important dans la redistribution de l'énergie spatiale et parmi les composants normales des contraintes de Reynolds cohérentes. En résume, les couches de cisaillement moyennes jouent un rôle de production et alimentent les structures cohérentes. De plus, la zone de recirculation forme une zone importante pour la redistribution d'énergie inter-composante à travers les termes de production normaux, et les termes de diffusion et redistribution par la pression cohérente. Son interaction avec la couche de cisaillement apparaît donc comme l'ingrédient principal pour la production d'énergie et donc de l'allée tourbillonnaire de von Kármán dans le sillage turbulent.

Chapitre 6 présente les effets de ces mécanismes identifiés dans les chapitres précédents. L'écoulement est perturbé par le biais de l'augmentation du nombre de Reynolds et par l'introduction de turbulence homogène et isotrope au moyen d'une grille régulière installée à l'entrée de la section d'essai. Dans le première cas, l'augmentation du nombre de Reynolds, le changement de condition à l'entrée du sillage entraîne une augmentation de l'énergie transférée vers les structures incohérentes. Cela mène une augmentation de la traînée par des contraintes de Reynolds incohérentes.

l'ajout de turbulence avec une échelle intégrale $\mathcal{L}_x/h < 1$, interagit avec les structures

cohérentes, entraînant une dislocation qui interrompt principalement le processus de redistribution par les termes associés à la pression cohérente. Ce phénomène de dislocation mène à une réduction des contraintes de Reynolds cohérentes, et par conséquent, à une réduction de la traînée. La longueur de la zone de recirculation augmente suite à l'affaiblissement des structures cohérentes, mais cette élongation n'est pas proportionnelle à la réduction de la traînée. Lorsque la perturbation induite par la turbulence agit à réduire la traînée, l'effet de blocage tend à l'augmenter, ce qui montre que les conditions initiales du sillage sont aussi importantes que les structures cohérentes pour contrôler la traînée.

Chapitre 7 conclut cette étude en résumant ces mécanismes. Des perspectives de recherche sont également proposées. L'un des point discutable de cette étude est la manière dont les structures cohérentes sont calculées, c'est-à-dire en utilisant la technique POD. Mais, on peut facilement surmonter cette difficulté en utilisant une méthode dite de PIV résolue en temps. L'analyse présentée dans cette étude peut facilement être étendue à des formes géométriques plus complexes. Par exemple, en changeant les conditions initiales du sillage, en introduisant plusieurs échelles, en variant la proximité au sol, ou en changement de l'angle de l'attaque. Les outils présentés dans cette étude peuvent être d'avantage utilisés pour le développement des lois-d'échelles ou pour améliorer les modelés d'ordres réduits, par exemple les modèles de Galerkin empiriques, qui forment les ingrédients principaux pour une méthode de contrôle de traînée efficace. Enfin, une extension des outils et des analyses actuels à un sillage complexe 3D tel que le corps d'Ahmed, représentatif des caractéristiques de sillage d'un véhicule réel, serait d'une valeur significative dans le développement des dispositifs de contrôle de la traînée.

Contents

List of Figures

List of Tables

Chapter 1

Introduction

1.1 Bluff body wake - An introduction

Bluff body wakes have been extensively studied for the past century. The term bluffness, according to [146], simply refers to the degree to which the body tends to diverge the incoming flow relative to another body with the same frontal area. Despite its simple geometry, a bluff body has significant engineering applications such as efficient design of bridges or structures [54, 203, 106, 49], combustion [115, 160, 116, 9, 126], offshore structures and pipe-lines [185, 170, 78, 204], energy harvesting from vortex induced vibration [63, 205, 168], road vehicles [72, 70] amongst others. The interested reader may also refer to the review in [46] and references therein for details on the applications.

The problem of flow separation from the surface of the bluff body is associated with the loss of aerodynamic performances of a bluff body, which for a vehicle has a negative impact not only for its fuel consumption, but also regarding its stability and controllability characteristics as described by [17]. Most road vehicles (ex: sports utility vehicle, trucks, buses) are three dimensional bluff bodies with a bluff trailing edge. Adding to the complexity of the three-dimensional body are the presence of detailed features such as side mirrors, wheels, wheel housing, rear diffuser etc.[100, 8, 87]. Although there exists several bluff-body models, the so called 'Ahmed Body' introduced by [2] with a rear slant angle has become one of the most studied laboratory scale model that can represent the flow features of a road vehicle. It is a three-dimensional model with an inherently complex three-dimensional wake, primarily because of the interactions between the top/bottom and lateral shear layers resulting in wake oscillations in the spanwise and transverse directions. Further, the ground proximity and the bi-stable pattern of the wake occurring for long time scales adds to the complex dynamics of the wake [65]. The complexity can be reduced significantly by isolating the interactions of the lateral shear layers, by extending the body in the spanwise direction making it two dimensional, and neglecting the ground proximity to yield a statistically two-dimensional symmetric flow. The work carried out on two-dimensional bluff bodies, representing road vehicles, are numerous. The current study is focused on a two-dimensional bluff body and the following sections describe the main features of the flow, extracted from a literature survey, in order to describe the topology of the mean flow and the mechanisms which couple the mean flow with perturbations' dynamics.

1.2 Flow over two dimensional bluff bodies

The flow over two-dimensional bluff bodies may be separated into two categories based on the shape of their cross section. It is an important factor when the point of flow separation is taken into account. As mentioned by [46], the cross-sectional shapes may be divided into shapes of (*i*) continuous and finite curvature (for example, circular or elliptical cylinders), (*ii*) sharp edged structures of an infinitely large curvature (for example, square or triangular cylinders) or (*iii*) a combination of the first two (for example, D-shaped cylinders). The differentiation is primarily based on the nature of the boundary layer separation and will become clear in the proceeding discussions.

Attempts for predicting the drag of a bluff body dates back to the nineteenth century. One of the oldest attempts by Kirchoff (1869) based on the aspects of flow separation, uses the potential theory and the technique of conformal mapping to predict the drag experienced by a flat plate normal to the flow. The model, constructed for a steady flow, gives a drag coefficient $C_d = 0.88$ with the pressure inside the cavity or the dead flow region (the region immediately behind the body) $C_{pb} = 0$ (see for example [202, 36]). The model assumes that the wake bubble does not close and extends to infinity, which however is not the case in actual flows. The consequence of the closure of the wake bubble in actual flows is negative pressure within the wake bubble resulting in a higher drag coefficient. This had been considered in the improved model by Riabouchinsky [143], where the wake closure is taken in to account by introducing the 'image body'. This introduces the wake length which is an important length-scale considering the bluff body flows and has been further used by [147] to develop a model for drag prediction for bluff body flows without the presence of unsteady vortex shedding.

The flow over bluff bodies has mostly been studied over a circular cylinder, because of its relative simplicity and engineering significance. The flow can be broadly classified into regimes based on the incoming flow Reynolds number which is the ratio of relative strength of inertial forces to viscous forces where it is defined as $Re_h = U_\infty h/\nu$ with h, U_∞, ν being the height of the body, the free-stream velocity of the incoming flow and the kinematic viscosity of the fluid respectively.

1.2.1 Boundary layer separation

Near-wall flows over the surface of the bluff body, must respect a zero velocity in order to satisfy the no-slip boundary condition. The fluid's viscosity causes the fluid parcels close to the boundary to slow down. Moving away from the surface, the resistance felt by the layer of fluid diminishes and at a certain distance the velocity of the fluid becomes equal to that of the fluid in the external flow. The distance at which this occurs is known as the thickness of the boundary layer, and the distance over which the gradient of the flow exists due to influence of the viscosity is known as the boundary layer. This is the simplest case with laminar boundary layers. When it comes to turbulent boundary layers, the viscous effects are felt only in a thin layer, much thinner than the entire boundary layer, known as the laminar sublayer. The turbulent boundary layer is much more complex than its laminar counterpart and is not treated here. In fact, in order to reduce the level of complexity introduced by the turbulent boundary layers, we opted to maintain laminar boundary layer along the surface of our bluff body. However, an interested reader

may refer to [152] or [161] and the references therein for a comprehensive analysis on turbulent boundary layers.

The thickness of the laminar boundary layer grows downstream as more and more fluid particles are influenced by the resistance due to the viscosity. The momentum is relatively low within the layer, due to the viscous resistance, and is sensitive to external pressure gradients. The presence of an adverse pressure gradient, said to exist when the pressure increases in the flow direction tending to decelerate the flow, initiates the separation of the previously attached flow at the body surface. This phenomenon is called as boundary layer separation. Once separated, the layer develops into the so called shear layer which may or may not reattach to the body surface depending on the incoming flow. This often sets the development of a low-pressure wake. The circular cylinder has an additional complexity due to its continuous and finite curvature that the flow separation point is not fixed, may oscillate and heavily depends on the flow conditions and other factors such as the surface roughness etc. This is one of the main reason why a D-shaped cylinder was adopted for this study, in order to simplify or reduce the number of parameters governing the problem. However, the salient features of the circular cylinder wake are briefly presented in the hope of providing a background on the nature of wake flows, mostly because of the substantial number of studies regarding the topic.

1.2.2 Flow over circular cylinder

The flow around the circular cylinder is divided into several regimes based on the Reynolds number. In order to describe it, we resort to the works of [147, 200] and referring to figures 1.1, 1.2, and 1.3a. For a Reynolds number $Re \to 0$, the flow is steady and smooth without separation. This type of flow is generally known as creeping flow and the drag experienced is mainly due to the viscous resistance in the boundary layer.

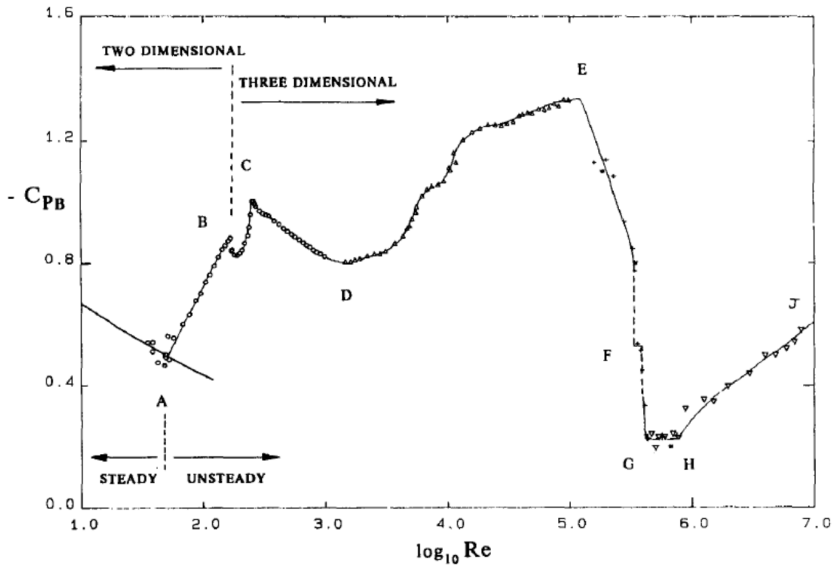

Figure 1.1: Variation of base suction coefficient with Reynolds number for the case of circular cylinders. Adopted from [147].

At a Reynolds number $4 < Re < 49$ (Regime upto A in figure 1.1), the wake comprises

of a recirculating flow region with two symmetric vortices on the upper and lower half of the wake. The length of the wake is observed to grow with an increase in Re in this regime, and the base suction decreases. In the regime A - B for the Reynolds number $Re \approx 49$ to 194, the wake instabilities starts to develop at $Re \approx 49$ initially from the end of the recirculating flow region. From now on, the flow becomes permanently unsteady. With an increase in Re, the vortices begin to separate regularly from the alternate sides of the cylinder, forming the "Von Karman vortex street" shown in figure 1.3a (c) . The strength of the instabilities increases with Re and as a result the Reynolds stresses increases as well, with a decrease in the length of the formation region, a characteristic length of the recirculation region, and a corresponding increase in the base suction. In this regime, the wake oscillations are purely periodic, subject to the end conditions of the cylinder, and can extend until $Re \approx 194$.

In the regime B - C in figure 1.1, from $Re \approx 190$ to 260, three dimensional effects are observed. Near $Re = 180$ to 194 where the first discontinuity is observed in base suction as well as in the shedding Strouhal number, figures 1.1 and 1.2, inception of mode A instabilities, which are streamwise vortex loops shown in figure 1.3b, and the formation of streamwise vortex pairs, due to the deformation of the primary Karman vortices, are observed. At the second second discontinuous range in the $St - Re$ relation in figure 1.2 near $Re \approx 230$ to 250, there is a gradual transfer of energy from mode A to mode B shedding, which are finer scale streamwise vortices. A large-scale intermittent low-frequency wake velocity fluctuations are also observed, due to the presence of large-scale vortex dislocations. The vortex dislocations are local phase dislocations of the shed-vortices. These small scale modes and the large scale dislocations are shown in figure 1.3b. The base suction and the Strouhal shedding frequency continues to increase in this regime.

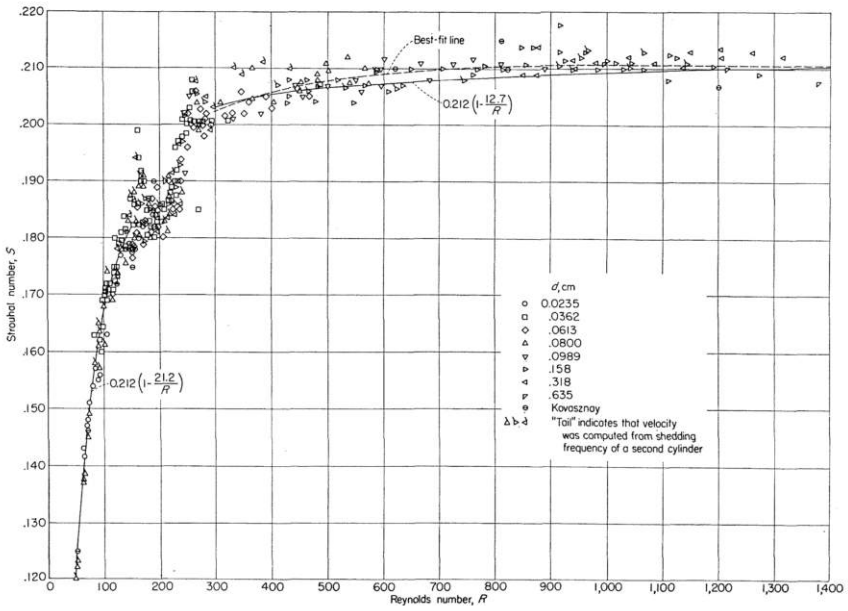

Figure 1.2: Variation of the non-dimensional vortex shedding frequency expressed in terms of Strouhal number as a function of Reynolds number for the case of circular cylinders. Adopted from [144]

In the regime that follows, C - D, the base suction is found to decrease with a cor-

responding increase in the formation length, due to the increasingly disordered fine-scale three dimensional structures appearing to cause a reduction in the Reynolds stresses.

In between D and E, the base suction is observed to increase with a corresponding reduction in the formation length. It is found to be due to the development of instabilities in the shear layer, shown in figure 1.3b, which increases the Reynolds stresses. With an increase in Re, the turbulent transition point in the shear layer moves upstream resulting in a turbulent wake shown in figure 1.3a(d), the Reynolds stresses increases with a corresponding increase in the base suction. The shear-layer vortices are basically two dimensional which eventually transition to turbulence with a rise in Re by the action of three-dimensional small-scale fluctuations [24, 197]. The transition mechanism of the shear layer is an important topic and many studies in the past were devoted to it. Most of this work was based on the circular cylinder starting with [24] who proposed a power-law scaling of the shear-layer vortex frequency, i.e. $f_{kh}/f_{vk} \propto Re^{0.5}$ where f_{kh} and f_{vk} are the frequency of the shear layer and Karman vortices respectively, based on dimensional considerations. Later, several studies considered the scaling and reported similar or slightly different exponents [197, 86, 134]. Nevertheless, these shear-layer vortices interacts with the primary von Karman vortices and aids in the entrainment of fluid into the formation region [197, 86]. With an increase in Re and with the transition taking place earlier, the entrainment process is even more enhanced with a corresponding increase in the Reynolds stresses and the base suction. Beyond E in figure 1.1, there is a steep decrease of base suction which occurs due to energized turbulent boundary layer reattaching onto the body forming a separation reattachment bubble and the final separation point is pushed further downstream to about 140^o which is known as the drag crisis phenomenon.

1.2.3 Flow over square cylinder

The brief presentation of the flow over a circular cylinder showed some of the salient features of wake flows such as boundary-layer separation, shear layer, vortex shedding, shear-layer vortices, transition etc. However, these features need not be the same when there is a change in the flow geometry such as the second category of bluff bodies, (i.e. sharp edged structures of an infinitely large curvature). The regimes in the flow over such a simple cross section (square cylinder) from the works of [10] is briefly presented. The various regimes are schematically presented in the figure 1.4a. At $Re \sim 1$, the flow around square cylinder is steady without any separation [157]. The separation starts at $Re \sim 2$ at the trailing edge of the square cylinder with the appearance of the recirculating flow bubble. The first regime according to [10] until $Re < 50$ is steady in nature with the two symmetric vortices appearing directly behind the base with the flow separating at the trailing edge. The length of the recirculating flow region grows in this regime while the drag coefficient is found to decline in figure 1.4b. The flow soon becomes unsteady within $50 < Re < 160$ with the appearance of laminar two dimensional vortex shedding. The trailing edge separation continues until $Re < 120$ after which the flow permanently separates from the leading edge of the body. There is a drop in the length of the recirculation region as well and the drag coefficient as well. Within the range $160 < Re < 220$, the prevalence of mode A and mode B instabilities causes the transition from two to three dimensional fluctuations in the wake with the drag coefficient reaching a minima while the length of the formation region remains unchanged. In between $220 < Re < 1000$, the transition to turbulence is found to occur in the shear layer beyond the trailing edge of

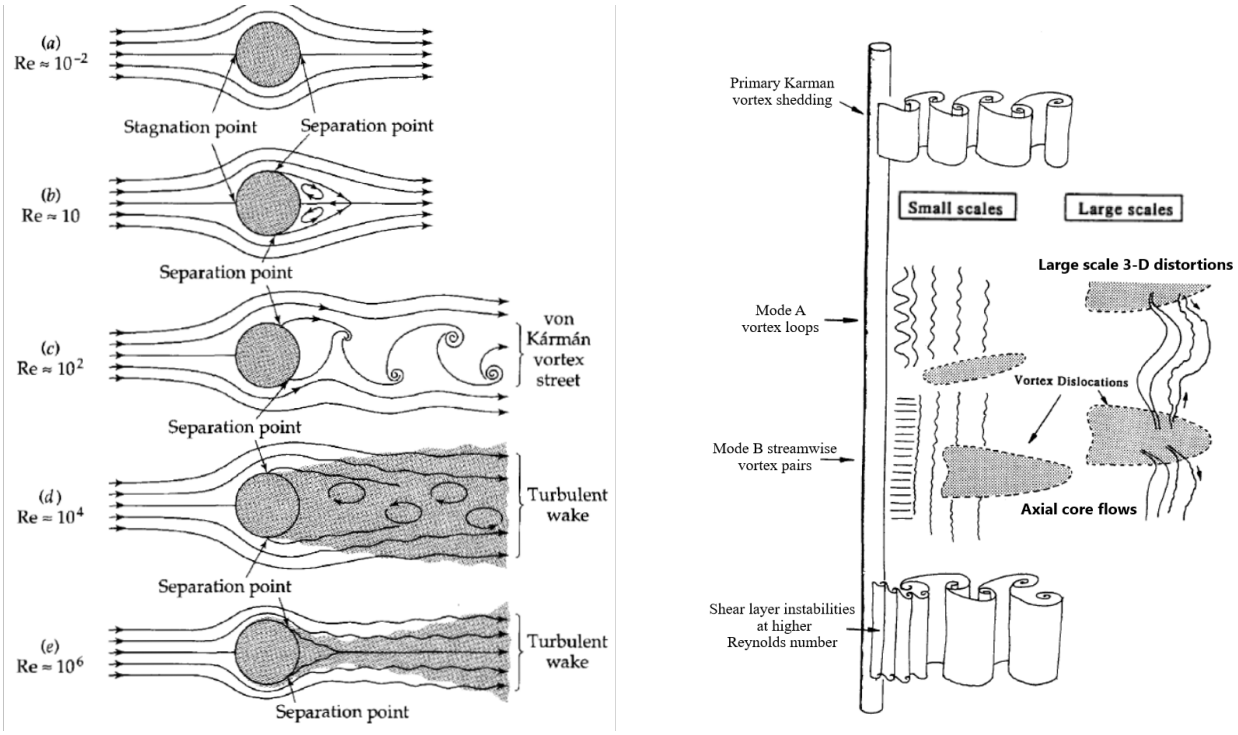

(a) (b)

Figure 1.3: Schematic of different flow regimes in the wake of a circular cylinder depending on the Reynolds number of the flow (a) - adopted from [23], and the schematic showing the primary vortex shedding, small-scale modes and the large-scale vortex dislocations (b) - adopted from [200].

the body with the formation length decreasing and the drag coefficient found to increase. Beyond $Re > 1000$, the transition within the shear layer takes place upstream of the trailing edge corner of the body, with the shear layer alternatively reattaching on the cylinder side-surface. The formation length and the drag coefficient asymptotically reaches a constant value of 1 and 2.21 respectively. An interesting comparison with the wake of the circular cylinder is that the sudden dip in the drag coefficient in case of circular cylinder, due to boundary layer transition and postponement of the flow separation, is not found in case of square cylinder because of the fixed separation point and insensitivity to Re.

Influence of Aspect ratio

An additional degree of complexity is added to the wake of the square cylinder with a varying aspect ratio. A recent study [101] highlights the effects of aspect ratio on rectangular cylinder, at low Reynolds number ranging from $30 \leq Re \leq 200$. The primary findings are summarised in the schematic from the same study shown in figure 1.2. The elongated bodies were found to have a stabilizing effects on the wake that the critical Re for the onset of vortex shedding increased with the aspect ratio. Increasing the aspect ratio increased the probability of the separated flow to reattach at the side surface of the body. The aspect ratio is found to have significant effects on the flow structure as well, for example at the smallest aspect ratio of 0.25 in the study at the smallest and intermediate Re, changing the aspect ratio to 4 made the flow steady with or without separation reattachment bubbles. At the largest Re considered in the study, starting from an aspect ratio of 0.25 to 4 made the three-dimensional flow change to a two-dimensional flow. The aerodynamic parameters, such as the drag or the shedding frequency, were found to be influenced strongly with a change in the aspect ratio as well. The strength of the shed vortices increased with Re, decreased with an increase in the aspect ratio. The influence of the leading-edge flow separation on the ensuing wake was studied by [107] at high $Re \sim \mathcal{O}(10^4)$. At high Re, the sharp leading edge corners induce the flow separation regardless of the pressure gradient. With a sufficiently long body, the separated flow, initially laminar in nature, soon undergoes transition to turbulence and reattach onto the side surface of the body. The influence of the leading edge separated and reattached shear layer on the wake formed after separation from the trailing edge diminished with an increasing aspect ratio.

This goes on to say that our bluff body was designed such that (i) the final flow separation is fixed at the trailing edge, as mentioned previously, (ii) a semicircular leading edge is chosen in order to minimize massive leading edge separation and (iii) an aspect ratio of 4 is chosen such that the boundary layer remains laminar at separation, even with the addition of free-stream turbulence, and to minimize the influence of the leading edge separation on the wake that develops after flow separation at the trailing edge.

1.2.4 Sources of drag and reduction strategies

The drag of the bluff body such as circular or a square cylinder, as briefly discussed above based on the vast amount of available literature, is seen to be dependent on many flow features starting with the nature of flow separation, appearance of unsteadiness, primary vortex shedding, development of spanwise instabilities, shear layer vortices, transition to turbulence etc. For example, the delay of separation on the circular cylinder caused the base suction to drop drastically whereas this was not witnessed in the case of

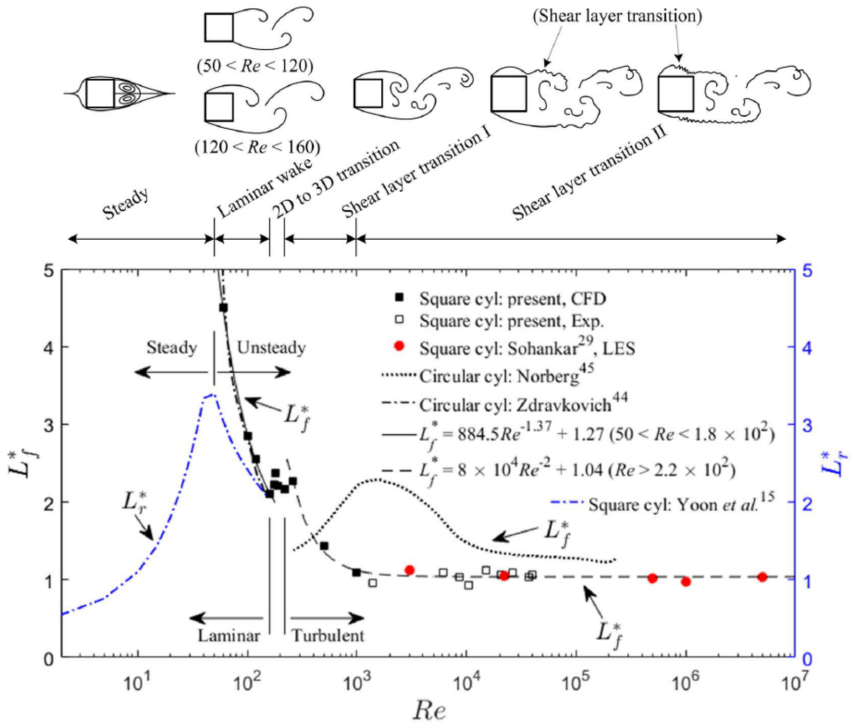

(a)

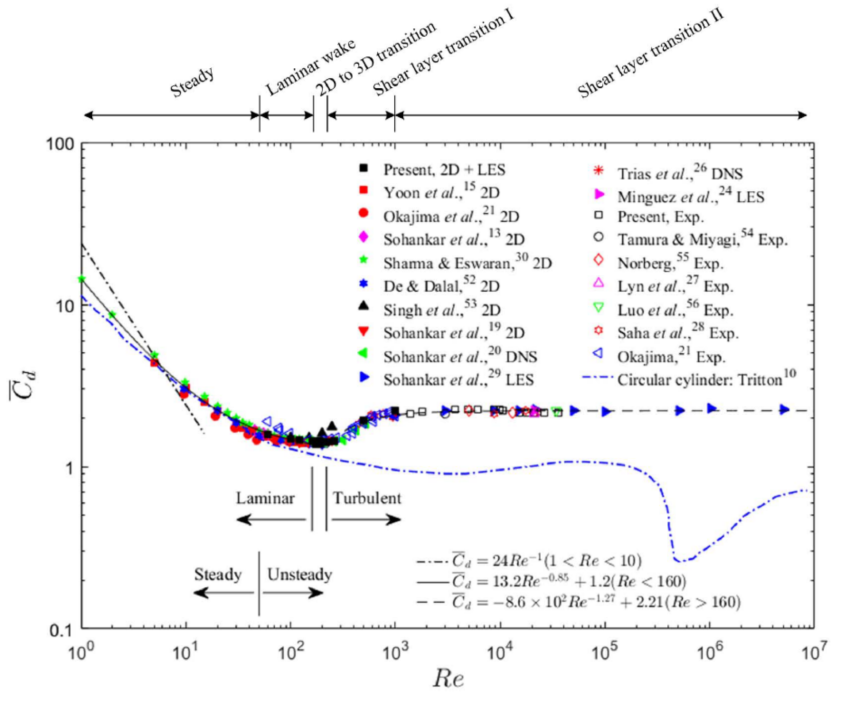

(b)

Figure 1.4: Variation of the recirculation length and the formation length (a) and the drag coefficient (b) as a function of Re. Figures adopted from [10]. For the works cited in the figure, one may refer to the references in [10].

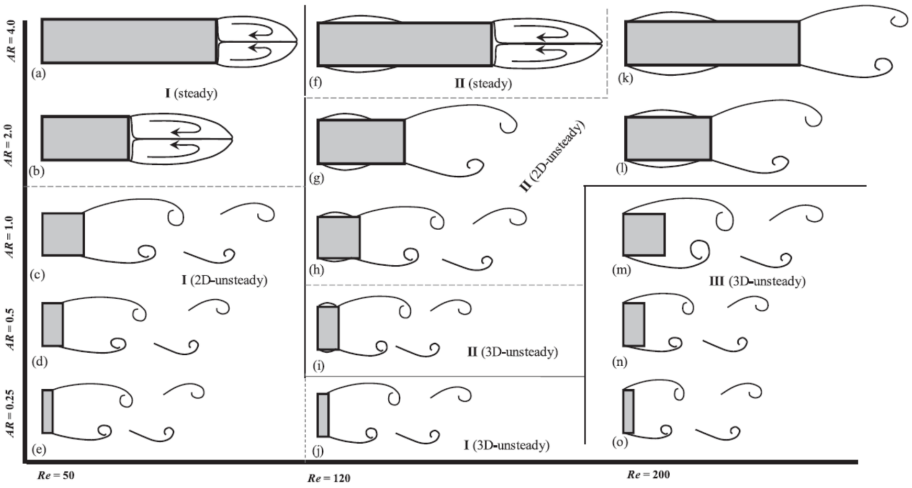

Figure 1.5: Influence of the aspect ratio of rectangular cylinder on the wake dynamics. Adopted from [101]

square cylinders which displays a fixed separation point, emphasizing the role of separation in drag. The onset of periodic motion caused a rise in the drag for both the circular and the square cylinder emphasizing the role of periodic vortex structures on the drag.

Further, these aerodynamic features are also found to change with the cross section of bluff bodies, for example: with a variation in the aspect ratio of the rectangular cross-sections, the bluff body with a combination of circular and rectangular cross section etc. In order to understand the mechanisms of drag and how to implement successful control strategies, it is important to identify the essential mechanisms that control drag and evaluate how successful previous control strategies performed.

Since the observation of vortex shedding lowering the base pressure by [144], several studies aimed at suppressing or manipulate the vortex shedding in order to reduce drag. The objective of the control strategies generally aims at delaying the onset of separation or the formation of vortices or reducing the strength of vortices. One of the earliest drag reduction strategies involved the use of splitter plates in the wake of the circular cylinder [146], shown in figure 1.6. It is placed along the center of the cylinder, parallel to the direction of the flow. This resulted in the interruption of interaction between the shear layers and subsequently influenced the vortex formation. The vortex formation took place at a larger distance which varied with the length of the splitter plate, for bluff bodies with fixed or moving separation, with the mean base pressure found to inversely vary with the length of the vortex formation region[16, 98]. The length of the splitter plate, be it short (for example : one sixteenth the height of the body) or long (for example: five times the height of the body) , modified significantly the near wake features [6, 5, 3].

The mechanics of the vortex formation, as explained by [61], involves the mutual interaction of the shear layers playing a key role. The end of the formation region, as defined by [24], is the streamwise position where the irrotational fluid first crosses the wake centerline by the action of the growing vortex. The growing vortex is continuously fed by circulation from the shear layer until it becomes strong enough to draw the opposite shear layer across the wake. The growing opposite shear layer with a sufficient amount of

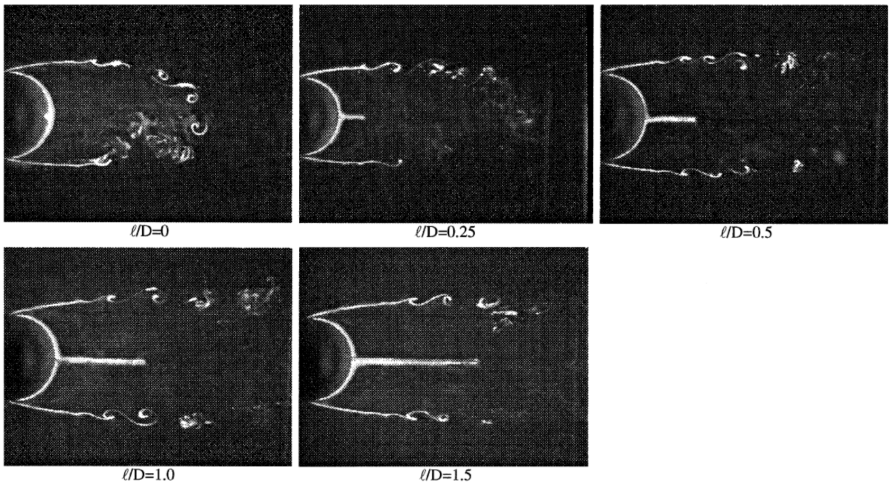

Figure 1.6: Influence of splitter plate on the vortex formation for experiments carried out at $Re = 5700$. Adopted from [3]

opposite circulation, relative to that of the first shear layer, further decreases the supply to the growing vortex which is then shed into the wake. A sketch adopted from [61], shown in figure 1.7 at the instant when the irrotational fluid first crosses the wake-centerline, shows the principal mechanism involved in the formation region. The irrotational fluid entering the wake, is partly entrained by the growing vortex itself, denoted by the arrow (a), in part by the shear layer upstream of the growing vortex, denoted by (b) and the remaining into the interior of the formation region (c). It is the balance between the entrainment into the shear layer and the reverse flow that determines the size of the formation region. By this argument [61] was able to explain the size of the shrinking formation region in the presence of free-stream turbulence and an elongated formation region in the presence of a splitter plate.

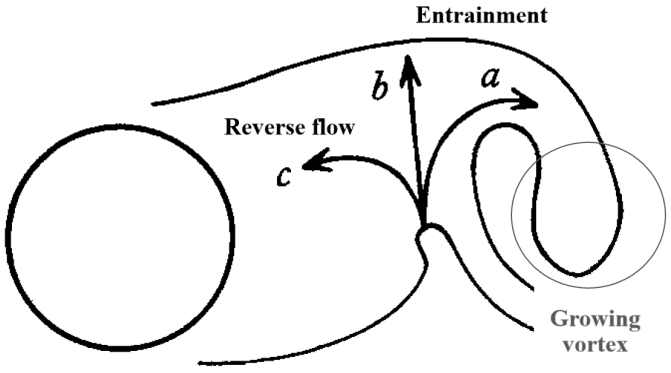

Figure 1.7: Sketch depicting the mechanics of the vortex formation region according to [61]. Adopted from [61]

The drag control strategies in the literature are numerous and can be classified into passive, active open or closed loop control strategies according to [37], which may further be divided as shown in the schematic adopted from [37] in figure 1.8. The passive control strategy generally does not require an external source of energy. It may be implemented in the form of surface/geometry modifications or by external attachments on the body. The splitter plate mentioned above is an example of passive control which requires no

additional input of energy. Active control methods involve some additional input in the form of steady or unsteady energy in order to influence/ manipulate a flow variable. Active control is further divided into open and closed loop controls of which the former does not involve sensors but actuators with power input. The later involves sensors and actuators and involves for example, comparing a measured flow variable with at some strategic location which is then used to trigger an actuator using some form of control law. An interested reader may refer to [7] for details on active flow control methods.

The control strategy is further divided into two-dimensional or three-dimensional forcing, and boundary-layer control or direct wake control. Two dimensional forcing for example normally refers to a modification of the surface of the body which is uniform in the spanwise direction whereas this is not the case for three dimensional forcing. The classification based on boundary layer control or direct wake control depends on the manner in which the control changes the boundary layer nature such as its state or modify directly the properties of the wake. The reader may refer to [37] for an excellent review on these strategies.The objective here is not to discuss the various control methods, but to understand the physical mechanism of the flow that is manipulated by the control strategy leading to reduction of drag. Therefore, a few out of the many cases of drag control shall be described with the hope of presenting the principal features of the wake flow which upon manipulation leads to reduction of drag. Further, the case of boundary layer control on continuous and finite curvature bodies such as the circular cylinder is avoided since it involves non-stationary separation points.

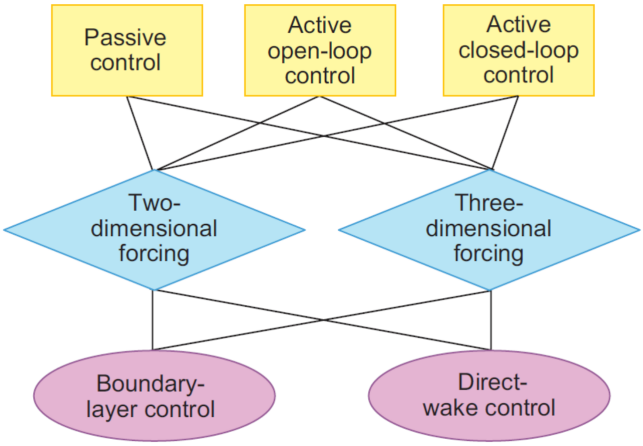

Figure 1.8: Classifications of flow control strategies with the objective of drag reduction. Adopted from [37].

The control strategies implemented in the literature mostly involve suppressing or manipulating the coherent von Karman vortices. The efficient control strategies, among the passive $2D$ and $3D$ forcing methods, recognised in the literature are those of three dimensional forcing type. The passive $3D$ forcing is normally implemented in the form of external attachments or leading/trailing edge modifications of the bluff body geometry. One of the earlier studies such as those of [173], installed segmented trailing edges to increase the base pressure and hence reduce the drag. The studies by [178] installed wavy trailing edge on a blunt edged model and found that the waviness increased the base pressure reducing the drag. The wavy trailing edge was found to induce vortex dislocations. The vortex dislocations come into existence when the shedding frequency is non uniform

in the spanwise direction. Neighboring 'vortex cells' at a specific frequency move either in phase or out of phase with each other due to its difference in shedding frequency with the adjacent cell. It appears as a consequence of the fact that a vortex line cannot end abruptly in a fluid. In order to accommodate this variations in the phase, the vortex from one cell links up with the vortices, with the same sign, of the adjacent cells which are in different phase, resulting in the appearance of twisted tangle of vortices [199, 178]. Numerical simulations conducted by [42] revealed interesting phenomena for square cylinder with wavy edges both at the leading as well as trailing edge. The wavy trailing edges were found to force vortex dislocations. Further, it induced three-dimensional fluctuations in the developing shear layer which made it less susceptible to roll up into von Karman vortices thereby reducing the drag. A recent study by [121] installed rectangular tabs along the spanwise direction, shown in figure 1.9, at $Re \sim \mathcal{O}(10^4)$. The role of the rectangular tabs was to induce spanwise dislocations of the vortices which lead to the disruption of the nominally two-dimensional nature of the von Karman vortices and increasing the base pressure.

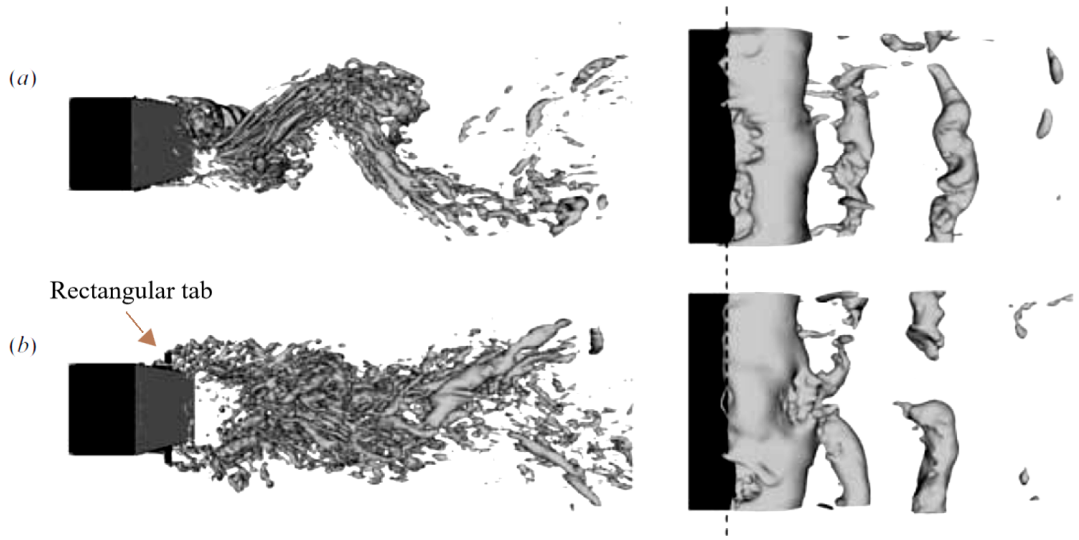

Figure 1.9: Instantaneous vorticity (iso-λ_2 surfaces) without control (a) and with control (b). Figures on the right shows the instantaneous iso-pressure surfaces. Adopted from [121].

The suppression of vortex shedding at low Re has been achieved in the studies of [166], where a relatively small cylinder is used to interrupt the vortex shedding. They explained that a properly placed control cylinder smears the vorticity contained in the shear layers (i.e. by spreading the velocity gradient over a larger distance). Similar studies were undertaken by [150] for a square cylinder at $Re \sim \mathcal{O}(10^4)$ and reported reductions in the mean as well as fluctuating forces when the control cylinder was located within a small region localised on the outer boundary of the separated shear layer. Numerical simulations performed by [105] showed similar results for the control cylinder, where they argued that the control cylinder locally stabilizes the shear layer by inducing a favorable pressure gradient, which led to the suppression of the von Karman vortex street at low Re. A similar kind of drag reduction strategy was studied by [120] in the wake of a D-shaped bluff body where reductions in mean drag was interpreted in terms of differences in shear layer diffusion and entrainment, with a corresponding changes in the length of

the recirculating flow region as well as dampening of the Reynolds stresses - especially the component related to the cross-stream mixing.

The modification of the boundary layer, prior to separation, also brings about changes in the vortex shedding frequency, strength and also the pressure drag [148, 181]. All the studies introduced in the above were passive drag control methods, and there exits numerous other studies based on passive control methods as well as active control methods. For example, [125] proposed open- and closed- loop control strategies based on a reduced-order vortex model which resolves the large scale energetic coherent flow structures. The control strategy synchronised the roll-up of upper and lower shear layers, decoupling the vortex formation from the shear layers, mitigating the appearance of asymmetries and therefore suppresses the effects of instability. A 40% increase in the base pressure corresponding to 15% reduction in drag was achieved in their study. A recent study used closed loop flow control strategy by using 'pulsed Coanda blowing' to reduce the drag [155]. During their open loop based test, to yield optimal non dimensional frequencies of forcing, vortex shedding was found to be suppressed/attenuated consequently an attenuation in the Reynolds stresses with a corresponding reduction in drag, however the extent of the recirculating flow region diminished due to the 'Coanda' effect deflecting flow into the near wake region. This attenuation is exploited as the feedback signal in the closed-loop control. For a review and detailed read of drag control strategies, one may refer to the review by [37] or the recent study by [155] and the references therein.

The literature shows the dominance of the primary mode of vortex shedding in determining the drag. Most of the studies, as seen above, are directed to attenuate or suppress the dominant vortex shedding process in order to yield favorable reductions in the drag. However, the dominance of vortex shedding is questioned in the studies of [113, 114], where multiple scales are introduced into an axisymmetric wake, by the use of fractal edges on polygonal plates normal to the flow, generated by non-axisymmetric bodies such as square plates. As the fractal dimensions and the iterations increased, the vortex intensity dropped, however with an increased in the drag. They explained that the function of the fractal edges were to re-distribute energy from the large scale coherent vortex structures to a broad range of scales in the flow.

1.2.5 Mathematical framework for the analysis of coherent structures

The role of coherent structures in the wake of the bluff body has been studied by several authors. Starting with the works of [142] who introduced the concept of triple decomposition, i.e. splitting the instantaneous velocity signal into its mean, a coherent periodic signal and a random component in order to better understand the role of organized waves in turbulent shear flows, there has been a steady interest to understand the mechanics of the coherent and the random flow structures, and their interactions, in a wide variety of flow settings through formal physical equations. The formalism followed by [142] allowed the splitting of total time averaged fluctuating stresses into the part that arises from organized wave like motions and random turbulence, and consequently to understand the interactions between them through transport equations for the energy arising from the coherent wave motions and the random turbulence.

One of the earliest notable works in this regard is of [32] where much of the effort was devoted to understanding the mechanics of large-scale vortex structure in the wake of a circular cylinder at $Re \sim \mathcal{O}(10^5)$. The large-scale vortex here is described as an organized structure with concentrated vorticity, energized primarily by entrainment. The terminology entrainment is used to refer to the transport of quantities such as mass or momentum across an interface. The instantaneous streamlines, for an observer moving the flow, forms a pattern of centers and streamline delineating the shed vortices between each other, and [32] explained that its formation and evolution is a dominant feature in the wake that controls the entrainment and the turbulence production process. Similar mechanisms can also be found in the studies of [75, 76], where they explained the importance of saddle (braids) and the smaller scale longitudinal vortices called as ribs, that resides on the braids, in the production of turbulence. According to [76], the large-scale spanwise vortices, three-dimensional in nature due to the distortions induced by the ribs, induces the motion of external irrotational fluid towards the wake, directed towards the saddles. This irrotational fluid attains some of the rotation due to the influence of the ribs and is subjected to the vortex stretching along the braided region, resulting in smaller scale turbulence production[75, 76]. The produced turbulence is advected into the rolls increasing the small-scale turbulence intensity near the center and back of the primary large scale structures. The most effective turbulence mixing, according to [76], is deduced to take place in regions A and B in figure 1.10 due to the interaction between the rib, of longitudinal vorticity, with the spanwise vorticity of the primary large scale structures. Similar findings, in the near wake region of a circular cylinder at high $Re \sim \mathcal{O}(10^5)$, on the role of large-scale coherent flow structures in the production of smaller scale turbulence has been reported in a recent study by [29], where the production terms, in a time averaged sense, was high in the strong shear regions (within the separated shear layer) whereas the smaller scale turbulence intensity peaked at the wake centre suggesting a transport of energy towards the wake center.

The works of [149] considers the energy exchange mechanisms between the mean, coherent and incoherent structures through the budget of coherent kinetic energy in the wake of a square cylinder at $Re \sim \mathcal{O}(10^2)$, where they notice that the work done due to pressure fluctuations, production term and the convection term play an important role in the energy exchange mechanism. A recent study [133], utilising DNS (Direct numerical simulation) data set in the wake of a square cylinder at $Re \sim \mathcal{O}(10^3)$, explains the role of coherent structures in the inter-scale and inter-space energy exchanges using the so called 'Karman-Howarth-Monin-Hill' equation. They find that the turbulent fluctuations are not directly fed by the mean flow, but through the coherent fluctuations which extract energy directly from the mean flow. Another interesting work by [12] studies the nature of multi-scale flows, where a number of primary coherent structures exists within the wake of multiple bodies. The kinetic energy budgets using the flow decomposition methodology of [142] performed at various strategic locations in the wake revealed that it is the coherent fluctuations that plays an important role in exciting the turbulent fluctuations because of the energy feeding mechanism by the coherent to the turbulent fluctuations. Further, secondary coherent structures were also recognized, and was found to be energized primarily by the nonlinear interactions between the primary shedding structures.

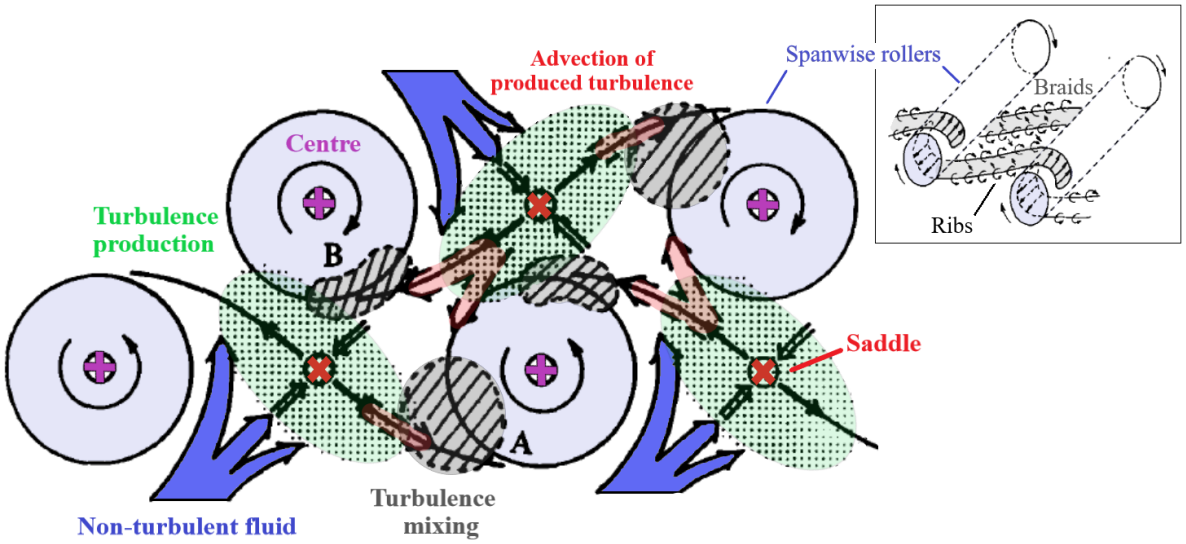

Figure 1.10: Schematic of the mechanisms of turbulence production within the wake consisting of alternatively shed vortices. Adopted from [76].

1.3 Thesis objective

The literature points to the role of the shear layer [166, 175, 120, 99] and the dominance of the coherent flow structures [146, 37, 125] in governing the base pressure, and hence the drag force, and its key role in driving the entrainment process or in the generation of turbulence [32, 75, 149]. The physical mechanism that drives the drag, or link the drag force to the coherent/ incoherent structures or to the entrainment process in the wake is a subject that still needs further research. It is hoped that identifying these mechanisms, at least those that involve the dominant coherent structures, would prove to be a valuable resource in the further design and development of efficient flow control strategies based on the physics of the flow. However, this remains a vast topic, as evident from the works briefed above, since the wake involves complex interactions between various flow features such as the boundary layer developing over the surface of the body, separated flow, the dominant primary large scale flow structures (for example: von Karman vortices), the shear layer vortices, the remaining small-scale coherent/incoherent flow structures, the interactions between them, mean pressure contributions arising out of it, and further adding to the complexity is the body geometry/cross section.

The principal objective of this thesis is to finely characterise the wake identifying the physical mechanisms which drives the mean drag. For this, a bluff body is designed, as already mentioned, so as to focus only on the wake problem and to avoid/minimize the influence of complex phenomenon such as those linked to leading edge separation. The wake flow behind the bluff body is measured using Particle Image Velocimetry (PIV) technique and analyzed using the governing equations for mean momentum. A new method for the accurate estimation of mean pressure field, based on sparse-sensor measurements of pressure allows for closing the mean momentum equation and therefore to identify the dominant contributions to the mean drag through mean momentum budgets.

Another novelty of the study is the introduction of a method to estimate the pressure of the coherent structures, based on the triple decomposition using Proper Orthogonal

Decomposition (POD)[192], which further allows the closure of the equation governing the energy exchange between the mean flow and coherent stresses, both in a phase averaged and time-averaged sense. These new tools form the foundation to understand the dominant driving mechanism of drag. Once the physical driving mechanism for drag is identified for the case of natural flow, it is then disturbed/perturbed by the addition of turbulence in the free stream in order to understand how this disturbance influences the identified mechanism.

The thesis is structured as following:

- Chapter 2 presents the experimental setup describing the D shaped bluff body, measurement techniques and equipment, the flow parameters used in this study and the background flow characterisation.
- Chapter 3 introduces the new method for accurate mean pressure field estimation from the wake measurements obtained by the PIV technique and using sparse sensor-measurements of pressure.
- Chapter 4 introduces the natural/baseline wake flow behind the D-shaped bluff body, identify the contributions to the mean base pressure drag through integral mean momentum budgets, using the numerical tools developed in Chapter 3, and discusses on the principal driving factor of the dominant contributor to the mean base pressure drag.
- The contribution of the spatially coherent/incoherent structures to the mean base pressure drag is identified in Chapter 5. The novel method of coherent pressure estimation is introduced in chapter 5 which permits the closure of transport equations that helps understand the energy exchange mechanism, primarily between the mean flow and coherent structures.
- Chapter 6 discusses on the influence of increasing the flow Reynolds number on the mean base pressure drag and the energy exchange mechanism, identified in chapter 5. Further, the influence of flow perturbation, by the addition of background turbulence, and the effects of blockage are discussed in Chapter 6, using the novel tools developed in the thesis.
- Finally, conclusions are drawn in chapter 7 and future outlook and extensions of the current study are briefly discussed.

Chapter 2

Experimental Setup

Measurement Techniques - Introduction

The fundamental equations of fluid flow presents us with variables like velocity and pressure. Understanding and analyzing the flow behaviour requires the knowledge of these variables. The flow behind the bluff body involves fluctuating velocities and pressure. It can soon transition to a turbulent wake depending on the flow Reynolds number, wake inlet or the external flow conditions. The wake is then composed of a multitude of scales ranging from the size of the body down to the viscous Kolmogorov scales. The scales in this context refer to an average size of eddying motion. In practise, it is extremely difficult to obtain measurements resolving the smallest scales in both space and time. Therefore, simplified approaches which statistically reduces the flow into mean and time averaged fluctuating quantities, has to be adopted. Even then, a single measurement technique cannot be used to yield information both in space and time. This calls for other techniques to fill the gap and provide complementary information.

The primary measurement technique used in this study is the so-called particle image velocimetry commonly abbreviated as PIV. It provides a whole field of velocity measurements. Time-averaged PIV measurements are compared with those acquired by the point-wise hot wire anemometry technique to verify the acquired data. Further, pressure measurements are obtained by wall-mounted sensors and pitot tubes, which are also used to estimate an accurate mean pressure field in the wake.

The objective of this chapter is to provide a brief summary of the flow measurement techniques used in this study. The working principles are also briefly described, an understanding of which forms a prerequisite to obtain flow data of satisfactory quality.

2.1 Hot-Wire Anemometry

Hot wire anemometry is an inexpensive form of pointwise flow measurement technique used by the fluids community over the years. The technique is capable of measuring flow velocity with high resolution in time, making it an attractive option for obtaining measurements that are beyond the capabilities of conventional low-speed PIV systems and at a lower cost. However, its application in the very near-wake of a bluff body is limited because of its intrusive nature and inability to measure reverse flow velocities.

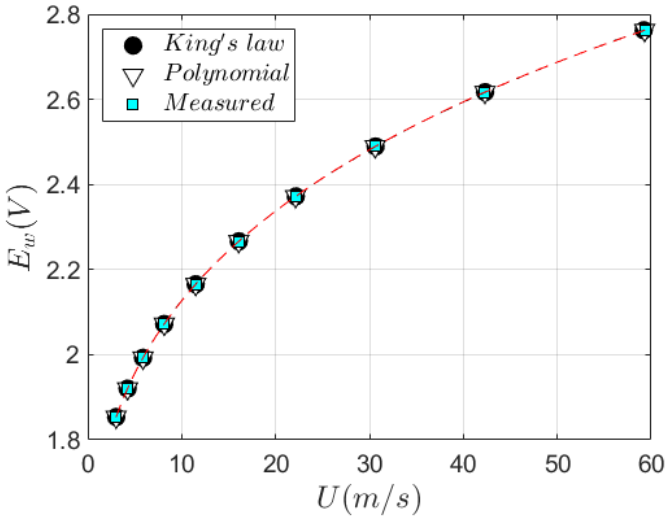

Figure 2.1: The calibration-curve of hot-wire. The squares represent the measured E_w for various reference velocities. The black circles and the inverted triangles represent the velocity estimated using the measure E_w with the King's law given by equation (2.1) and a fourth order polynomial given by the equation (2.2) respectively.

2.1.1 Operation and calibration

The operating principle of the Hot-wire anemometry is based on the concept of heat transfer from a small heated wire to the flow it is exposed to. For this purpose, the wire that forms the heating element is made up of material whose electrical resistivity depends on the temperature. The measurement of velocity is based on its relationship with the voltage across the sensor wire, the latter is temperature dependent and therefore on the heat transferred to the flow, known as King's law [30] which reads

$$E_w^2 = A + BU^n. \tag{2.1}$$

One may refer to [30] for an in-depth treatise on the working principle and derivation of the relation (2.1). The calibration procedure to determine the constants A and B requires the input of a flow with known velocity and preferably without turbulence. This can be done in the wind tunnel test section or by a dedicated calibrator(e.g., Dantec 90H02 flow unit). In this study, the dedicated calibration unit is used which generates a low-turbulence jet that is used as the velocity reference. The hot wire is aligned with the centre line of the jet nozzle and flush with the upper surface of the nozzle. A wide range of reference velocity is spanned, and the corresponding E_w is measured and recorded. The constants and the exponent of equation 2.1 are then determined by data-fitting. The exponent $n \approx 0.4306$ so obtained lies well within the optimal range reported in [30]. An alternative is to express the velocity as the powers of the hot-wire voltage E_w using a polynomial,

$$U = \sum_{n=0}^{N} A_n E_w^n, \tag{2.2}$$

as reported in the work of George et al. (1989) [60]. The best results reported in the literature [30] were for the solutions of polynomials of fourth order in E_w. Due to the simple nature and straightforward applicability, the polynomial form (2.2) is used in the

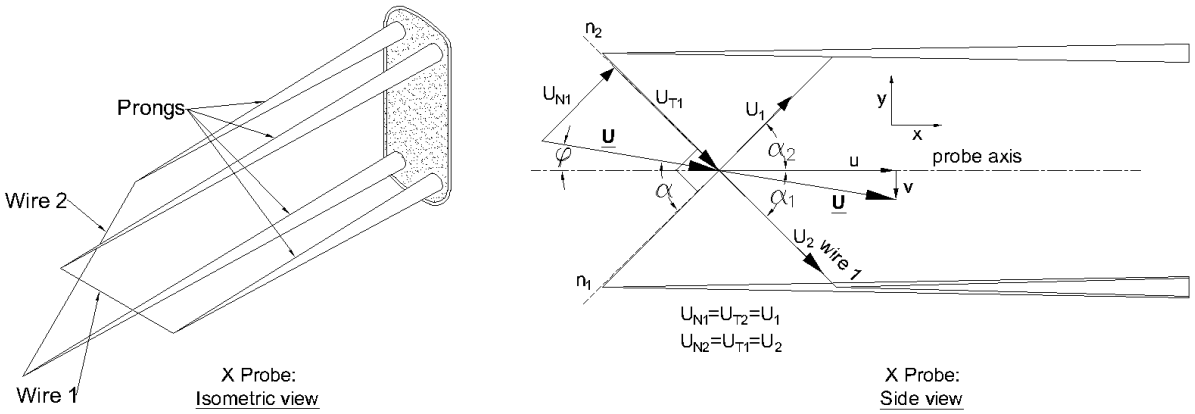

Figure 2.2: Typical arrangement of an X-Probe

present study for the calibration of hot wire. Figure 2.1 shows the calibration curves of the hot wire sensor for flow velocities in the range $0 - 60\ m/s$, in which both calibration methods seem equivalent. The error levels of the reference velocities remain below 0.5%, which is acceptable given the numerical errors that may be present.

The calibration is carried out at a particular ambient temperature and it is not actively maintained in the wind-tunnel. The operation of electrical machineries, changes in the external environment, surface friction, etc. can influence the ambient temperature whose variation can lead to errors in the measured velocities. Slight drift, however, can be compensated using temperature-correction laws, see for instance [80]. In order to minimise such errors, as a rule of thumb, the hot-wire was re-calibrated if the temperature exceeded $\pm 3^0 C$ from the initial ambient temperature at which calibration was carried out. The ambient temperature was monitored using an external thermometer.

Measuring two velocity components using X-wire probe

To measure two components of the flow, a Dantec $55P61$ X-wire probe is used in this study. The figure 2.2 shows a typical arrangement of X probe. It simply consists of two inclined wire-probes arranged closed together with a space in between them. It is assumed that the two inclined wires are in the same plane for signal-analysis purposes, however the thermal wake of one wire can interfere with the output of the other leading to erroneous measurements ([30] and references therein). Previous work (e.g., Jerome et al. (1971) has shown that thermal-wake interference can be minimised by placing the wires 1 wire-length apart. In addition, one may refer to Bruun (1996) [30] and the references therein for a detailed understanding of the interference caused by the stems and the prongs of the probe, and also the steps followed to minimise such disturbances.

As illustrated in figure 2.2, the two inclined wires of the probe are arranged so that an angle of 90 degree is maintained between their normals. Conventionally, the hot wire responds only to the velocity magnitude and not to its direction.

The probe is installed such that the probe axis is aligned with the streamwise velocity in the laboratory coordinate system indicated by (x, y) in figure 2.2. The conversion from the wire-coordinate system (axes aligned with the wires) to the laboratory co-ordinate system can be carried out as,

$$u = U_1 cos(\alpha_2) + U_2 cos(\alpha_1), \quad \& \quad v = U_1 sin(\alpha_2) - U_2 sin(\alpha_1). \tag{2.3}$$

Since the hot wire velocity-voltage calibration is carried out with the velocity vector aligned with the probe axis, U_1 and U_2 can be found by solving,

$$U_{1cal}^2\left(1+k_1^2\right)cos^2(90-\alpha_1) = U_1^2 + k_1^2U_2^2 \quad \& \quad U_{2cal}^2\left(1+k_2^2\right)cos^2(90-\alpha_2) = k_1^2U_1^2 + U_2^2. \tag{2.4}$$

Hot-wire anemometry remains, however, a pointwise measurement. With a single hot-wire probe, it is possible only to measure the velocity at a single point of interest at a specific time. Yet, the high response of the hot-wire sensor to the fluctuating velocities makes it an ideal tool to obtain time resolved velocity measurements.

2.2 Particle Image Velocimetry (PIV)

The technique of PIV is used for the whole field measurement of velocity, unlike the pointwise measurement carried out by hot wire anemometry. It is an optical flow measurement technique where the velocity of particles, that faithfully follow the flow, are measured and is therefore known as an indirect mode of measurement. The following section shall briefly introduce the velocity measurement using the PIV technique.

2.2.1 Working principle

The method simply consists of imaging a set of particles that trace the flow at two closely spaced time instants, i.e., at time t and $t+\Delta t$. The knowledge of their positions at these two instants forms the displacement vector which when divided by the time interval Δt gives the velocity vector and is given by,

$$\mathbf{u} = \frac{\mathbf{x}_A - \mathbf{x}_B}{\Delta t}. \tag{2.5}$$

The region of interest of the seeded flow is illuminated twice by a thin laser sheet, separated in time by Δt. The time duration of exposure of the particles to the illumination has to be significantly smaller than its displacement, so that the particles appear as frozen spots rather than as streaks. The laser sheet is formed by shaping the circular cross section beam delivered by the laser light source by means of cylindrical and spherical lenses. The light sheet so generated has to be thin otherwise it risks the particles external to the sheet being illuminated by the laser and contributes to the measurement noise. Furthermore, the generated light sheet has to have sufficient energy at each pulse, allowing the scattered light from the particles to be detected by the imaging device.

The images are captured on a CCD (Charge Coupled Device) camera. The light falling on the pixels during the exposure time creates electrons that forms a charge which is then converted to voltage, amplified, digitized, transferred and stored in the computer memory for further processing. In each image, the particle is illuminated only once.

To estimate displacements, the image I_1 at time t is divided into a regular mesh formed by smaller regions defined by interrogation windows. For one of such window W of size $2K \times 2L$, after a short duration Δt, the particles should have moved by $\Delta\mathbf{x}$ in the same window of the second image captured at time $t+\Delta t$. If the light intensity of particles in W of I_1 and I_2 are represented as $f(i,j)$ and $g(i,j)$ respectively with $f(i,j) \neq g(i,j)$ due to movement, then an average particle displacement can be estimated using the statistical measure of cross-correlation and is given by,

$$C_{fg} = \frac{\sum_{i=-K}^{K}\sum_{j=-L}^{L}\left(f(i,j)-\mu_f\right)\left(g(i+\delta x, j+\delta y)-\mu_g\right)}{\sigma_f\sigma_g} = \frac{R_{fg}}{\sigma_f\sigma_g}, \tag{2.6}$$

where μ and σ^2 represent the average and variance of the intensity in the respective windows f and g. The location of the average displacement shall correspond to the location of the peak on the cross-correlation map formed by the equation 2.6. For two 1D functions of length N, the computation of the cross-correlation coefficient requires N^2 operations, whereas in 2D it increases to N^4 operations. This is computationally very expensive especially for a high-resolution image and when a large number of images have to be processed. Therefore, the Fourier theory, which reads

$$R_{fg} = \mathcal{F}^{-1}\left(F^{*}G\right), \tag{2.7}$$

where F,G, $\mathcal{F}^{-1}$ and the superscript $*$ represents the Fourier transform of $f(i,j)$, $g(i,j)$, the inverse Fourier transform, and the conjugate complex, respectively. It reduces the number of operations to $\mathcal{O}\left(Nlog_2N\right)$ operations for 1 dimensional and $\mathcal{O}\left(2N^2log_2N\right)$ for 2 dimensional signals (see for eg.: [14]). The first run with the initial window gives an integer estimate of the average particle movement on a large scale. The displacement estimate can further be improved by employing multiple runs where the estimate from the preceding run is used as a pre-shift for the smaller sized windows in the subsequent runs. A further subpixel refinement in displacement estimation is obtained by approximating the particle image distribution to be a continuous Gaussian-shaped function with its peak corresponding to the particle image centre (see, e.g.: [137]). For a velocity field in regions of high gradients, the deformation of windows based on the local gradients after the first run and prior to the subsequent runs provides improved results with better spatial resolution [71].

In order to obtain reliable velocity measurements of the fluid, the tracer particles have to fulfil certain criteria such that the fluid flow properties/velocities are not altered by it. In short, the tracer particles have to be inert to the surrounding fluid with its size small enough to respond instantaneously to changes in fluid flow and large enough for the scattered light to be of sufficient intensity for its detection.

The velocity lag of the particles with respect to the surrounding flow using Stokes' drag law for a continuously accelerating fluid and under the assumption ($D\mathbf{U}/Dt = d\mathbf{v}_p/dt$), where $\mathbf{v}_p$ refers to the velocity vector of the particle, reads [137, 184],

$$\mathbf{v}_p - \mathbf{U} = \frac{d_p^2}{18\mu}\left(\rho_p - \rho_f\right)\frac{d\mathbf{v}_p}{dt}, \tag{2.8}$$

where the subscript p refers to the particle and d_p refers to its diameter. Equation (2.8) serves as a guide to choose the tracer particle. The choice of neutrally buoyant particles, i.e. $\rho_f = \rho_p$ leads to the particle that follows the fluid flow accurately; however, it is difficult to find such particles for gaseous flows. Therefore, the particle size, given by its mean diameter d_p, can be very small for the velocity-lag to become negligible. In the present study, the mean diameter of the particles corresponds to $d_p \approx 1.2\mu m$ and is generated by the PIVTech seeding device utilizing olive oil as the seeding fluid.

A convenient measure of the particle's ability to faithfully follow the field is given by the Stoke's number, which is the ratio of the time response of the particles to the characteristic time-scale of the flow. According to Raffel *et al.* (2018) [137] and Tropea *et al.* (2007) [184], it is given by

$$Stk = \frac{\tau_p}{\tau_f} = \left(\frac{d_p^2\left(\rho_p - \rho_f\right)}{18\mu}\right)\frac{1}{\tau_f}, \tag{2.9}$$

where $\mu = 1.7894 \times 10^{-5} m^2/s$, $\rho_p = 917 kg/m^3$ and $\rho_f = 1.225 kg/m^3$ are the dynamic viscosity of air, the particle density (olive oil droplets) and air density at $15^o C$ respectively. The flow time scale τ_f is that which characterises the smallest scales the flow can have, and can be estimated by the Kolmogorov time scale, $\tau_\eta = (\nu/\epsilon)^{0.5}$, which represents the smallest scales at which the turbulent kinetic energy is dissipated into heat by the action of viscosity. Under the equilibrium hypothesis for a turbulent flow, i.e., when the produced turbulent kinetic energy is lost by viscous dissipation, τ_η scales as $Re^{-0.5}$, where $Re = ul/\nu$, u and l characterises the turbulent velocity fluctuations and the largest scale in the flow (e.g., integral length scale), respectively [174]. Ideally, the particle response time has to be much smaller than the smallest time scale of the flow. Then, the use of τ_η implies that changing flow conditions, such as fluid type and increase in Reynolds number, put additional restrictions on the particle response time and to the choice of tracer particles as well.

2.2.2 Wall-pressure measurements

The wall pressure measurements along the bluff body surface in the streamwise and spanwise directions were carried out by the miniature pressure scanners manufactured by Scanivalve. The scanner incorporates piezoresistive pressure sensors for measurements. The resistance of the piezoresistive strain gauges changes when strained and is typically attached to a diaphragm. The scanner was operated at a frequency of $800 Hz$ in order to distinguish the energetic peaks in the spectrum at least that occurs below $400 Hz$. Before measurements, for each set of experiments, the zero offset was performed at zero velocity inside the wind tunnel.

2.3 Experimental setup

2.3.1 Wind tunnel

The experiments to measure the velocity in the wake of the bluff body were carried out in the open type subsonic wind tunnel at the PRISME lab facility, Orleans. The maximum velocity of the attainable free stream is close to $50 m/s$ with zero blockage of the test section. The test section measured $2000 mm$ in length with a cross section of $500 \times 500 mm^2$, preceded by a contraction $16:1$, ensuring a uniform flow at the inlet. The inlet of the wind-tunnel is equipped with honeycomb structures that suppresses / dissipates any possible large scale turbulent structures before it reaches the inlet of the test section. The velocity in the test section is set by a tri-phase centrifugal fan whose speed is controlled by a potentiometer. The velocity is monitored by measuring the differential pressure across the contraction using a FC014 micro-manometer manufactured by Furnace Controls Ltd. The differential pressure is indicated in mm of water column and is converted to Pascal units for estimating the inlet velocity. The inlet velocity assuming zero friction losses in the contraction follows from the Bernoulli's principle as,

$$\Delta P_{in} = \frac{1}{2} \rho_{air} U_{inlet}^2 = \rho_{water} g h_{water}, \tag{2.10}$$

where h_{water} represents the height of the water column in millimetres directly obtained from the manometer reading. Being analogue, the lowest count of the manometer for $\Delta P_{in} \in (0, 10)$ mm H_2O and $\Delta P_{in} > 10$ mm H_2O is 0.1 and 1 mm H_2O respectively.

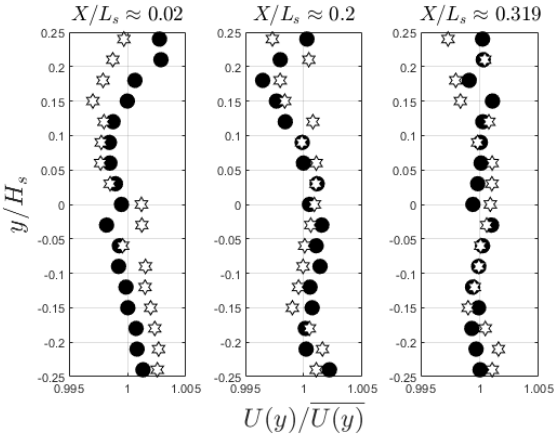

(a) Homogeneity of the mean velocity profile in the vertical direction.

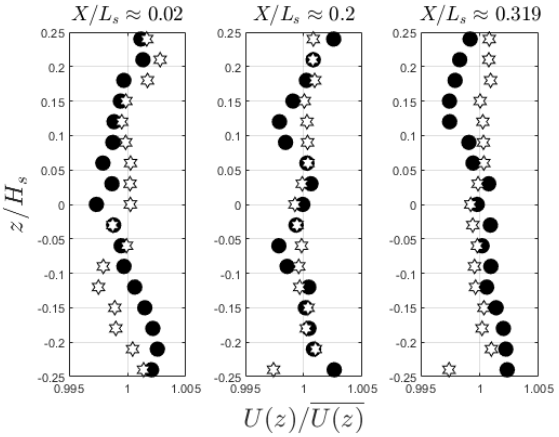

(b) Homogeneity of the mean velocity profile in the span-wise direction.

Figure 2.3: The streamwise mean velocity normalised by the spatial average of the profile measured at various location in the wind-tunnel test section. $L_s = 2000mm$ and $H_s = 500mm$ denotes the length and height of the test-section.

The uncertainty in the reading of an analogue device is usually half its least count, thus making the uncertainty due to the user setting as 0.05 and 0.5 $mm\ H_2O$ for $\Delta P_{in} \in (0, 10)$ $mm\ H_2O$ and $\Delta P_{in} > 10$ respectively.

The experiments are carried out for inlet velocities in the range $U_{inlet} \in (10, 30)$ and are set using a manometer. Once the wind tunnel is operational with the set velocity, the inlet velocity is precisely measured using the pressure scanner for each velocity measurement, by connecting the reference port of the pressure scanner to the stable static port at the inlet of the wind tunnel. Exception is only for the case while flow homogeneity of the wind tunnel is verified.

Verification of flow homogeneity

The single normal hot-wire probe mounted on a traverse is used to verify the flow homogeneity in the wind tunnel at three stations in the streamwise direction for the lowest and the intermediate inlet velocity used for the experiments $U_{in} \approx 10m/s$ and $U_{in} \approx 20m/s$ respectively. Figure 2.3 with the mean streamwise velocity measured along the vertical and spanwise directions at $40mm$, $400mm$ and $638mm$ from the inlet shows that the flow is homogeneous with variations as large as $\pm 0.5\%$. The prospective placement of the experimental bluff body model is at $X \approx 418mm$ from the test section inlet.

2.3.2 D-shaped bluff-body model

Figure 2.4 shows the details of the experimental model used in the study of bluff body wake. The leading edge of the body is circular in shape with a diameter of $h = 40mm$ followed a flat surface leading to a rectangular sharp base all the while maintaining the body height at $40mm$. The length-wise aspect ratio of the body length was chosen as $l/h = 4$. The objective was to limit the leading edge separation and to minimise its effect on the wake formed after the flow separates at the trailing edge.

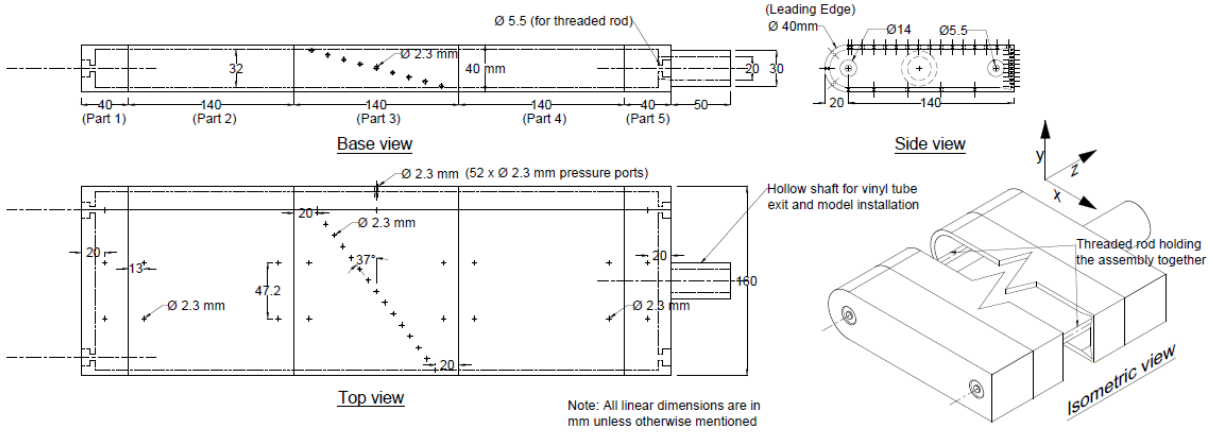

Figure 2.4: Details of the D shaped bluff body experimental model

The span-wise aspect ratio of the body (along z direction) is 12, chosen such that it fits the entire width of the wind-tunnel cross section. The body being long in the span-wise direction, it was fabricated by 3D printing in five parts labelled as *Part* 1 to 5 in the base view of the model in figure 2.4. The parts were fabricated such that each of them can be attached with the other through grooves and extrusions (not shown in the figure 2.4). The assembled parts are then held together using two $M5$ threaded rods that pass through two designated holes, one close to the leading and the other close to the trailing edges, respectively. Small holes of diameter $2.3mm \times 52$ no. are made on the body, included in the design while passed over to the 3D printer, to install the vinyl tubes for pressure measurement. The 52 vinyl tubes exit from the body through the hollow shaft provided at one end, which are then numbered using labels and then installed on the pressure scanner device. The length of the vinyl tubes is limited to a maximum of $1000mm$.The body is mounted in the middle of the cross section of the wind tunnel test section at $X/L_s \approx 0.21$, so that the hollow shaft remains outside of the test section and that the wake of the body is not disturbed by the measuring devices and its associated parts.

2.4 Parameters of the experiment

The experiments on the bluff body model are carried out by varying two parameters. The first parameter is the bluff body Reynolds number defined as,

$$Re_h = U_{in} h/\nu, \tag{2.11}$$

where h, U_{in} and ν refers to the height of the body, the inlet velocity at the inlet of the wind tunnel test section and the kinematic viscosity of air respectively. Re_h is varied in the range $Re_h \in (2.8 \times 10^4, 8.2 \times 10^4)$ corresponding to the inlet velocities in the range $U_{in} \in (10, 30)\, m/s$.

The second parameter is the level of free stream turbulence. Two sets of experiments varying the second parameter are conducted. The first set is with the presence of background turbulence existing in the wind-tunnel test section without any means of turbulence generation. The background turbulence level in this case was measured and found

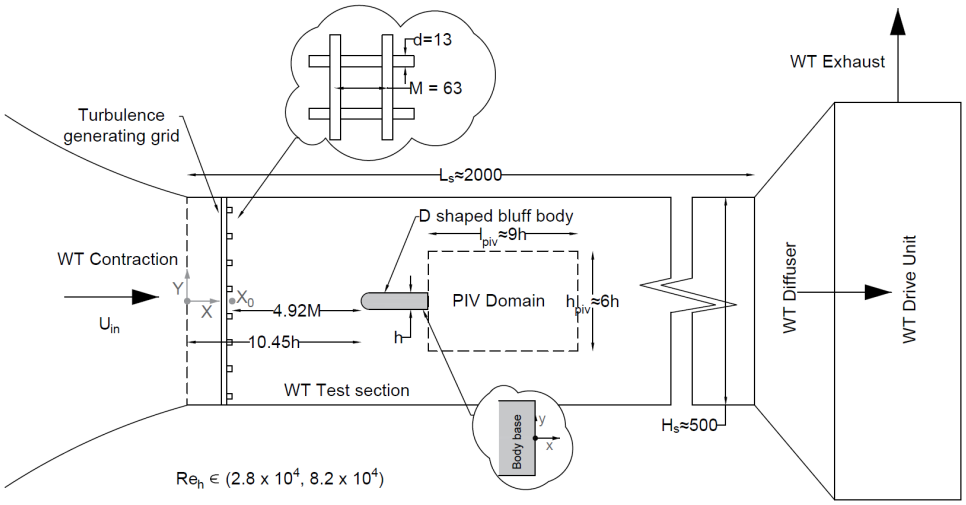

Figure 2.5: Illustration of the experimental setup. The abbreviation WT refers to wind tunnel, the inset cloud shows the dimensions of the regular meshed turbulence generating grid with d- the size of the bar and M referring to the mesh size. The wind-tunnel coordinate system is placed at the mid-point of the test section inlet and is denoted by (X, Y, Z), where Z is not explicitly shown. The bluff body is placed at approximately $10.45h$ from the inlet of the test section. L_s and H_s refers to the length and height of the test section. The test section being a square cross section, its width is also denoted by H_s. X_0 refers to the center of the turbulence generating grid in the streamwise direction. The reference port of the pressure scanner is connected to a static port close to the inlet of the test section and prior to the grid placement.

to be smaller than 0.1%. The second set of experiments are carried out at the Reynolds number specified in the range $(2.8 \times 10^4, 6.8 \times 10^4)$ in the presence of free-stream turbulence generated by a regular grid.

2.4.1 Characteristics of the flow in the presence of the grid

Turbulence generating grid is fabricated using square cross sectioned wooden rods of dimension $d = 13\ mm$ placed apart such that it forms a regular mesh of dimension $M = 63\ mm$. The solidity of the mesh, which is the ratio of its frontal area to the initial area without the mesh and given by $\sigma_M = (1 - \beta)$, where $\beta = (1 - \frac{d}{M})^2$ is the porosity of the grid, is found to be 0.37. The leading edge of the bluff body is installed such that it is approximately 4.9 mesh lengths away from the grid. The length of the body measures approximately 2.5 mesh length, thus keeping the trailing edge at 7.4 mesh lengths from the grid. The figure 2.6a shows the verification of the homogeneity of the mean flow in an upstream location close to the leading edge and at a location immediately downstream to the trailing edge of the body. These mean profiles were measured using a single normal hot wire probe with a low pass filter of $6kHz$ filtering all the smaller scales of the flow.

The mean velocity profile is highly irregular with a maximum positive and negative variations of 6% and 2% respectively from the inlet velocity, at $X_M/M \approx 4.6$. The velocity deficits due to the bars of the grid are clearly visible. The strong inhomogeneities smooths out moving further downstream but still exists at $X_M/M \approx 8.4$ as evidenced in figure 2.6a. The deviation from homogeneity is higher away from the centre-line of the flow field.

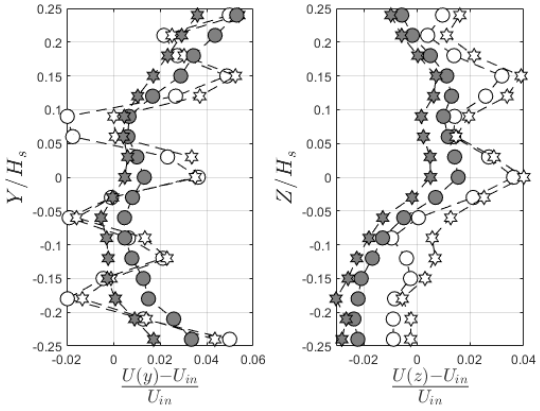

(a) Homogeneity of mean streamwise flow along the vertical Y and the span-wise Z directions. The white and the grey shaded symbols denote the streamwise location $X_M/M \approx 4.6$ and $X_M/M \approx 8.4$ respectively.

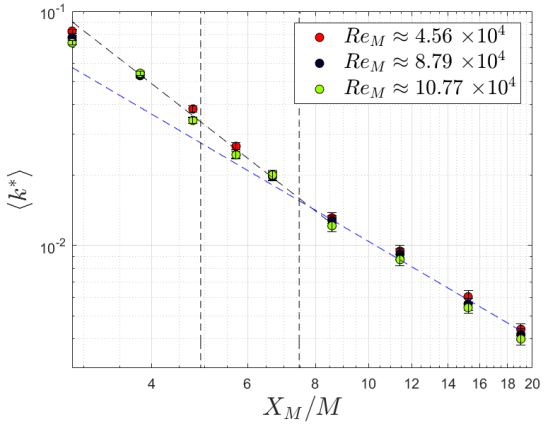

(b) Decay of kinetic energy along the streamwise direction. The dashed line denotes the limits of the leading and trailing edge of the bluff body.

Figure 2.6: Mean flow homogeneity (a) and the decay of kinetic energy (b) defined as $k = (\overline{u'^2} + \overline{v'^2} + \overline{w'^2})/2$, along the streamwise direction. The circles and pentagrams in (a) denotes the two inlet velocities of $U_{in} \approx 10\ m/s$ and $20\ m/s$ respectively at which data was acquired. X_M and H_s denotes the shifted streamwise coordinate, i.e. $X_M = X - X_0$, and to the height of the wind tunnel test-section respectively. The superscript $*$ and the angular brackets in (b) denotes normalization with the inlet velocity U_{in} and the spatial averages respectively. The uncertainty in spatial averaging is denoted by its average variance and represented as error bars in (b).

A span-wise deviation of the homogeneity in the mean velocity profile is also observed. The persisting mean strain implies the continued production of turbulence kinetic energy. The present study being focused on the near wake of the flow field, which is considered to extend $\pm 1.5h$ from the bluff body wake centerline, and not the far field in the transverse direction, the effects due to in-homogeneity in the far transverse direction is neglected. This is to say, no corrections to the inlet velocity are applied.

The figure 2.6b shows the decay of the kinetic energy generated by the grid. The measurement in this case is carried out using a hot-wire probe, capable of measuring three components of the flow, sampling the velocity signal at $60kHz$ to obtain a discrete signal of length 2^{20}. The peak of the produced kinetic energy, which falls in the range $X_M/M \approx 2$ to 3 (see [77] for example), is not visible in our data due to insufficient measurement points. Upon attaining the peak, it starts to decay. The solid lines correspond to a power law fit of the form $k^* = A\left(\frac{X_M - X_M^0}{M}\right)^n$, where X_M^0, n and A refers to the virtual origin, decay exponent, and the decay coefficient, respectively (see [187] for example). The virtual origin is set to zero here such that it coincides with the grid location. In order to perform the fit, logarithmic transform is applied to the power in order to have a first approximation of the power exponent and the decay coefficient. Further, a curve is fit using the non linear regression routine of Matlab 'nlnfit' which outputs the decay coefficient A and the power exponent n by performing iterative least squares estimation. The power law constants obtained for each case of Re_M are then averaged to perform the final fit shown by the solid lines in the figure 2.6b. The region after the

$U_{in}(m/s)$	Re_M	$L_x(m)$	$T_u(\%)$
10.58	4.56×10^4	0.0154	14
20.39	8.79×10^4	0.0151	14
24.97	10.77×10^4	0.0144	14

Table 2.1: Details of the incoming flow past the turbulence generating grid, with solidity $\sigma \approx 0.37$, at the location $X_M/M \approx 4.9$. Turbulence intensity is defined as $T_u = \sqrt{\overline{u'^2}}/U_\infty$.

peak that falls within at least 10 mesh lengths is classed as the near-field region, where the turbulent kinetic energy decay is faster (see [77] for example). This is evidenced in the figure 2.6b where the slope of the decay changes. The power law exponent changes from $n \approx -1.81$ to -1.36 and the decay coefficient changes from $A \approx 0.6$ to 0.24 from the near to the far field, respectively. It is within the near field region that our body is placed.

While studying the effects of free-stream turbulence on the bluff-body wake, the most often considered length scale is that of the largest energy-containing scales represented by the integral length scale (see, for example, [19, 82]) and is given by

$$\mathcal{L} = \int_0^\infty \rho(\Delta x) d(\Delta x), \tag{2.12}$$

where $\rho(\Delta x) = \overline{u'(x)u'(x+\Delta x)}/\overline{u'^2(x)}$ and τ refers to the auto-correlation coefficient and the spatial lags in computing the auto-correlation coefficient respectively. Though the upper limit of integration is specified to be at infinity, for practical purposes this limit is taken to be the first zero crossing of the auto-correlation coefficient.The values are reported in table 2.1.

2.5 Data acquisition

The experiments are carried out in the wind tunnel with varying parameters, as briefly explained in section 2.4. Principally, the PIV technique and the hot wire anemometry using the 'X probe' are used to acquire velocity data in the bluff body wake, such that one complements the other. The pressure measurement is carried out by the pressure sensors through vinyl tubes installed on the body.

2.5.1 Velocity data acquisition using the hot-wire 'X probe'

Referring to the figure 2.5, the origin of the body coordinate system (x, y, z) is located at the mid-point of the base of the body to denote streamwise, transverse, and spanwise directions, respectively. The Re_h of the flow is set using the manometer in the range specified in section 2.4. Profiles of 2 components of velocity were acquired at various locations in the wake through point-wise measurements, details of which are given in table 2.2. Statistically well converged data was acquired which was further processed in the commercial software package MATLAB.

2.5.2 Velocity field acquisition using the PIV technique

The PIV velocity field measurements are carried out using a Quantel Evergreen double pulsed monochromatic Neodym-YAG laser operating at a wavelength of 532 nm, with a

X probe measurements	x^*	y^*	Δx^*	Δy^*	Acquisition time (s)
Transverse profile $(u(y,t), v(y,t))$	3,6,9	-3:3	-	0.125 $\{-0.5 \leq y^* \leq 0.5\}$ 0.25 $\{-0.5 > y^* > 0.5\}$	$\geq 10^4$ $\mathcal{T}_x$
Streamwise profile $(u(x,t), v(x,t))$	2:9	0	0.375	-	$\geq 10^4$ $\mathcal{T}_x$

Table 2.2: Details of hot wire measurements of velocity in the wake of the bluff body. The superscript $*$ denotes normalization with the body-height h and $\mathcal{T}_x$ denotes the integral time-scale of the longitudinal fluctuations estimated at the wake centerline.

set of integrated hard-mounted optics which transforms the cylindrical laser beam into spatially aligned thin laser sheets. The flow is seeded with fine droplets of olive oil. Time-scale of the smallest fluctuation, Kolmogorov time-scale τ_η, is estimated using the velocity measurements acquired by hot-wire anemometry, following local isotropy assumptions (see [174]). The Stokes number (2.9), for an average diameter of olive oil droplets of $1.2\mu m$, estimated along the wake centre line at $x^* \approx 2$ & 8 for the range of Re_h used, is found to be much less than 0.05, indicating that the droplets indeed follow the flow faithfully. Labview software is used to programme the National Instruments NI 9402 input/output module to generate two low voltage TTL signals of different frequency to trigger PIV and wall pressure acquisition simultaneously. The TTL trigger signal of 0.5 Hz generated for PIV acquisition is used as an external trigger connected to the TSI Model 610035 LASERPULSE Synchronizer programmed through the INSIGHT $3G$ software. The synchroniser controls firing of the lasers and the image capture by the camera. IMPERX Bobcat 2.0 $B6620$ CCD camera of 29 Mpx, with a bit-depth of 16 bits, is used to capture the instantaneous position of the illuminated particles in the flow. Acquisition was carried out in sets of 602 seconds to minimise the effects of thermal noise due to camera overheat. The measurements are restarted after a few minutes to allow the camera to cool down. The TTL signal for triggering the PIV is recorded in order to obtain the time-stamp of individual velocity field measurements. The second TTL signal of 800 Hz is used to trigger the pressure scanner which acquires the pressure signal at 800 Hz. The timestamp of the pressure signal in millisecond accuracy is obtained in the output file from the pressure scanner. A total of 5000 image pairs were captured in order to obtain converged statistics for double-decomposed (mean and fluctuating) fields, as well as triple-decomposed (mean, coherent and incoherent signal) fields. The time interval between the two laser pulses were set so that the maximum particle displacements of 10 pixels were obtained. This ensures that the low velocity regions are represented with a sufficiently high pixel displacement in order to be captured by the cross-correlation algorithm. The consequence is that the overall dynamic range of the technique is increased, which depends on the maximum and minimum resolvable displacements.

Image pre-processing

Prior to the cross-correlation process to extract displacement information, the images are pre-processed to improve the signal-to-noise ratio. It is carried out in two stages.
In the first stage, the image is corrected for perspective mapping. The perspective mapping is used to refer to the situation when particles that are separated by a distance in the real life appears to be nearer or farther away from each other depending on the distance from the camera and its orientation with respect to the imaging plane. The correction procedure projects the captured image to a plane that is normal to the optical axis of the camera. It is achieved by capturing the image of a chequerboard with known square

size such that the pixels in the captured image can be mapped onto an image where the chequerboard should have been normally orientated with the optical axis of the camera. For the mapping, the four corner points of the captured chequerboard image are selected and the corresponding four corner's in the normally oriented image is specified with the knowledge of the dimensions of the chequerboard square. Further, the transformation matrix of the form,

$$\begin{bmatrix} x' \\ y' \\ 1 \end{bmatrix} = \begin{bmatrix} a & b & c \\ d & e & f \\ g & h & i \end{bmatrix} \quad \begin{bmatrix} x \\ y \\ 1 \end{bmatrix}, \tag{2.13}$$

where the (x', y') and (x, y) denotes the points in the normally oriented image plane and the captured image respectively. Usually, i in the transformation matrix is assumed to be 1. The linear system of equations so formed is solved in order to estimate the transformation matrix, which is then applied to transform the captured image. The procedure is explained in a simple manner in [163]. The projective transform is a linear transformation and cannot correct non-linear distortions (for example: radial distortion) due to the imperfections in imaging optics.
The radial distortion is corrected by using the model,

$$\begin{pmatrix} x_d \\ y_d \end{pmatrix} = L(r) \begin{pmatrix} \tilde{x} \\ \tilde{y} \end{pmatrix}, \tag{2.14}$$

where $L(r)$ is generally the distortion function of the form,

$$L(r) = 1 + \kappa_1 r^2 + \kappa_2 r^4 + \quad h.o.t, \tag{2.15}$$

and (x_d, y_d), $(\tilde{x}, \tilde{y})$ denotes the distorted and non-distorted image coordinates, respectively (see [69] for example). The lens distortion function (2.15) involves higher order terms $(h.o.t)$, but the choice was limited to second order for convenience. The coefficients κ in equation (2.15) are found by forming a system of equations by selecting a set of points (x_d, y_d) from the image and with the knowledge of its corresponding points in the non-distorted image $(\tilde{x}, \tilde{y})$. The resulting over determined system of equations are generally solved by employing a least squares method. Once the coefficients are found, an inverse geometric transformation can be applied to the image. The corrected image is shown in figure 2.7a where a horizontal straight line is also shown in order to visualise the effects of correction.
The second stage of image processing consists of high-pass filtering of the image by subtracting the same image convolved with a Gaussian smoothing kernel resulting in the image shown in figure 2.7b, using the MATLAB routine 'imgaussfilt'. The corrected images were then processed using the DPIV Software [104, 123] using multiple interrogation passes, the first and second passes using 64×64 px^2 and 32×32 px^2 respectively with 50% overlap.

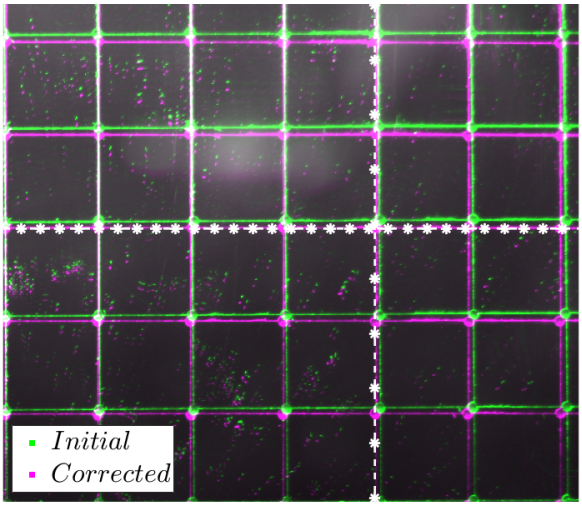

(a) The image resulting after the application of image corrections shown in magenta. A straight line at 0^0 to the horizontal axis is shown in white color to visualize the effects of correction. Only a portion of the image, where the effects of correction are maximum, is shown.

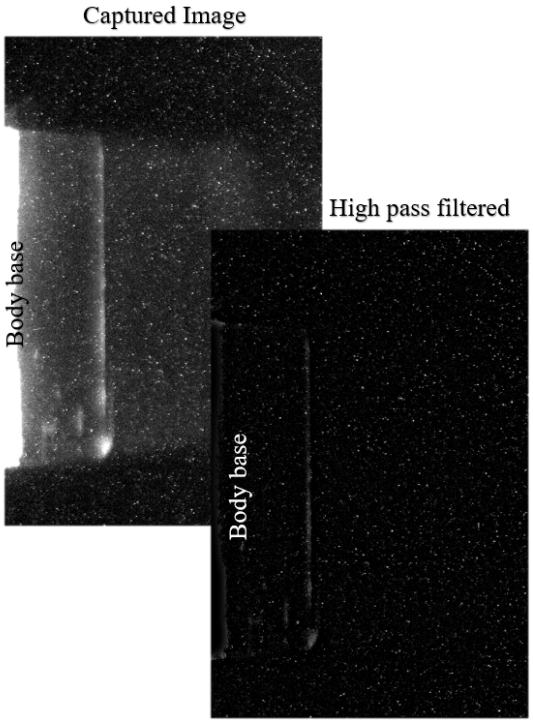

(b) A portion of the image close to the base-wall of the body, where laser reflections are high, prior and post high-pass filtering operation.

Figure 2.7

Chapter 3

Mean pressure field estimation based on planar PIV

3.1 Introduction - Mean pressure

Pressure plays an important role in the dynamics of fluid flows. It is linked to various physical flow phenomena such as the formation of coherent structures [50, 110], vorticity fluctuations [27, 136], wake topology of separated flows [146, 147, 164, 52], inception of cavitation [140, 96], aero-acoustics [85] to only name a few. Pressure is also a key component to obtain aerodynamic force estimated from near-field wake data for immersed bodies [186, 191, 43, 138]. Alternative approaches have been proposed to circumvent the requirement for pressure. An earlier example can be found in the works of Antonia & Rajagopalan [4] where the transverse momentum equation is used to approximate the pressure in the wake and estimate drag. But it fails in the near wake because of strongly non-parallel-shear component of the Reynolds stress tensor. A model to predict the mean-drag coefficient of bluff bodies in the absence of vortex shedding can be found in the works by Roshko [147] where a parameter characterizing the base suction is used to predict the drag coefficient. While these approximations are valid in specific cases, pressure still plays an important role in the physical examination of flow in wake regions. The role of mean pressure is especially evident from the mean-momentum and energy equations where it is responsible for the transport of momentum as well as energy respectively [131]. A review of some applications of pressure can be found in the work by van Oudheusden 2013[190]. The estimation of pressure has been conventionally carried out by sensors either mounted on surfaces or by Pitot-type probes. While the reliability and accuracy is high, depending on the sensors used, their presence may disturb the flow field. In addition, the achievable spatial resolution is often limited. This becomes undesirable while studying complex flow phenomena such as bluff body wakes, inception of cavitation among others. However, the advent of PIV offers a solution to estimate pressure from the two-dimensional and three-dimensional experimental PIV velocity fields using flow-constitutive equations. PIV is becoming increasingly popular with the accessibility of robust algorithms [190]. Estimating pressure solely based from velocity data in incompressible flows remains challenging since pressure requires both speed and acceleration locally with a high level of precision, which is restricted by the technology available to perform such measurements. Therefore, accurate pressure estimation, even calculated from mean-field quantities can be difficult to achieve. In particular, turbulent flows such as shear-dominated flows may prove to necessitate large amounts of snapshots to obtain well-resolved velocity fields. While this

can be commonly achieved from planar PIV, it can become prohibitively expensive for tomographic three-dimensional applications. In this scope, several methods have been developed to improve the accuracy of pressure reconstruction from experimental data.

Pressure estimation can be sub-divided by means of equations used, algorithms and the framework in which the pressure is computed (Eulerian and Lagrangian). While more details can be found in the review paper by Oudheusden [190], it is summarized to provide an overall insight to the reader. On the basis of equations, the pressure field is generally estimated in two ways [190]. The first method estimates the pressure gradient using the velocity derivatives in the Navier-Stokes (NS) equations subsequently integrating it in space. It requires the knowledge of, at least, one value of pressure in order to eliminate the constant arising from the integration (e.g. [15]). This method is known to suffer from the error propagation based on the integration path and several works have been conducted to minimize the path dependency and consequently the errors therein [95, 39, 88, 183, 189, 138]. Very recent works show that this method is akin to a least-squares approximation and shows very promising potential to time-resolved measurements [79, 97]. The second method solves a second-order partial differential equation, also known as the Poisson problem for pressure, which is obtained by applying the divergence operator to the momentum equations [66, 131, 190]. The boundary conditions utilised to solve the Poisson problem are either Dirichlet (solution specified at the boundary), Neumann (solution gradient specified at the boundary), or of mixed type (Dirichlet & Neumann). The Poisson formulation has been used by several authors to estimate mean, as well as instantaneous pressure from turbulent flows [66, 62, 44, 188]. It was used to estimate pressure for load estimation on immersed bodies [103, 26] as well as in the domain of aeroacoustics [85]. Details of both the methods can be found in the review paper by Oudheusden [190]. For both formulations, different approaches or algorithms were proposed by several authors (see for instance [95, 183, 79]). These methods were extended to compressible regime of flows (e.g. Oudheusden [189]), Ragni *et al.* [138]. Recent developments include fast algorithms based on FFT integration of pressure gradient proposed by Huhn *et al.* [73] and the spectral decomposition based pressure-gradient integration algorithm by Wang *et al.* [194].

Although various algorithms and approaches exist to reduce the errors in the estimated pressure field, the quality of the estimation essentially depends on the intrinsic quality of the velocity field used to compute pressure. Since velocity fields reconstructed using PIV algorithms inherently introduce noise (see [137, 176, 201]), the error propagates inherently in the pressure field [117, 118, 190, 44, 102]. A brief review on some of the factors affecting the accuracy of estimated pressure (resolution, flow specification, out of plane components etc.) can be found in the work by Oudheusden [190]. Guidelines on the type of pressure solvers to be used based on error sensitivity analysis were provided by McClure *et al.* [102]. A comparative assessment of the methods and algorithms for PIV-based pressure estimation was carried out by Charonko *et al.* [35] where the estimation accuracy depends, for instance, on the type of flow, resolution, and form of equation used. They concluded that there exists no universal method for pressure estimation, but it was flow dependent. Their work suggests that the use of conservative form of Poisson equation is much less sensitive to noise, specially for external flows such as those of immersed bodies.This is especially relevant to the present study concerning bluff-body wakes.

The low-pass filtering effect of Poisson equation and the finite difference scheme was noted by Oudheusden [190] implying that the low-frequency errors compared to their high-frequency counterparts from PIV data has to be minimized. In a recent work by

Pan *et al.* [117], a guideline on the optimal spatial resolution for the Poisson solver is proposed to limit the error propagated. A notable work commenting on the error propagation dynamics of PIV Poisson-based pressure estimation has been carried out by the same author [118]. Different factors such as the geometry of the domain and the type of boundary conditions was found to have a considerable effect on the estimated pressure field. The essence of this work emphasizes the importance of boundary condition in obtaining an accurate pressure estimate. They noted that the Neumann type of boundary conditions is prone to errors and is to be avoided wherever possible. However, it becomes mandatory in PIV domain focusing on rotational flow regions.

In this light, our current work aims at minimizing the error propagated to the estimated pressure field using sparse pressure sensors available from the experiment. To the best of our knowledge, only a single study considered the use of sparse measurements to improve the pressure estimated from PIV. In fact Wang *et al.* [194] essentially used sensor measurements to set the unknown constant, arising from the definition of the pressure problem itself. In this work, we consider a different approach and use reliable and accurate measurements from such sensors to correct for the whole pressure field. The method is based on the concept of optimal control where the Poisson model for the pressure is used to compute an optimal correction to the pressure field estimated from the PIV. Although optimal control was applied to numerous optimization problems (see for instance [93, 182, 67]),a formulation to correct the pressure estimated from PIV-based velocity fields using sparse reliable pressure measurements is first reported in this study. The method proposed hereafter is validated using a synthetic mean flow field and applied to experimental data. It does not involve any dependence on numerical simulation data and is computationally inexpensive. The sensitivity of the method tested against various types of noise shows that it is robust and produces an unbiased error minimizer. The only requirement for its application is the presence of at least one pressure measurement on the boundary, near the computational domain, which can normally be obtained using surface-mounted or Pitot-type probes.

3.1.1 Theoretical background - Mean pressure estimation

The Poisson approach of pressure estimation is used in this study to estimate the mean pressure from a 2D mean flow [131]. The mean pressure gradient from the Reynolds Averaged Navier-Stokes (RANS) equation given by

$$\frac{\partial}{\partial x_j}\left(P\delta_{ij}\right) = -\rho\left(\frac{\partial}{\partial x_j}\left(U_iU_j - 2\nu S_{ij} + \overline{u_iu_j}\right)\right), \tag{3.1}$$

where P, U, ν, S_{ij} and $\overline{u_iu_j}$ denotes the mean pressure, mean flow velocity, fluid kinematic viscosity, mean strain rate and the Reynolds stress components respectively, undergoes a transformation with the divergence operator to yield a second-order Poisson equation for pressure as

$$\frac{\partial}{\partial x_i}\left(\frac{\partial}{\partial x_j}\left(P\delta_{ij}\right)\right) = -\rho\frac{\partial}{\partial x_i}\left(\frac{\partial}{\partial x_j}\left(U_iU_j - 2\nu S_{ij} + \overline{u_iu_j}\right)\right). \tag{3.2}$$

It is to be noted that equations (3.1) and (3.2) are in their conservative form following the advice of Charonko *et al.* [35] with respect to its robustness to error propagation. Therefore the equations for mean pressure estimation can be formulated from (3.2) and

(3.1) respectively in a convenient form as

$$\Delta P = f\left(U, \overline{u_i u_j}\right) \;\; in \;\; \Omega \tag{3.3}$$

$$\nabla P \cdot n = g\left(U, \overline{u_i u_j}\right) \;\; on \;\; \Gamma \tag{3.4}$$

where Δ and ∇ denotes the Laplacian and gradient operators respectively, Γ and Ω represent the computational boundary and domain respectively, and n is the unit normal to the boundary. The right hand side (RHS) of the Poisson equation (3.3) shall be referred as 'source term' hereafter. The second order Poisson equation requires boundary conditions in order to solve for a unique solution. While the pressure specified on the boundary using Bernoulli's equation (Dirichlet boundary) is limited to irrotational flow regions which is seldom not the case with experiments, the pressure gradient (Neumann boundary) is always directly estimable from the velocity fields. Therefore, the current study focuses on the Poisson approach with Neumann boundary conditions because of its applicability for a wider range of experiments.

As a consequence of solving the second-order Poisson equation with Neumann-type boundary conditions on all boundaries, the computed pressure is defined up to a constant [131]. Furthermore, with such boundary conditions, the compatibility condition given as

$$\int_{\Omega} f\left(U, \overline{u_i u_j}\right) \; d\Omega = \int_{\Gamma} g\left(U, \overline{u_i u_j}\right) \; d\Gamma \tag{3.5}$$

must be satisfied for the solution to be unique up to a constant, such that the computed pressure given by $P_c(x, y) = P_{true}(x, y) + K$ holds true and where K is a constant. Note that the compatibility condition naturally follows from Gauss's divergence theorem. This is the ideal case but restricted to noise-free data. However in real PIV experiments, the velocity fields obtained will always be contaminated by noise [137, 201, 176] and thus (3.5) is hardly ever verified in such circumstances. As such, the equation for computed pressure writes

$$P_c(x, y) = P_{true}(x, y) + K + \epsilon(x, y), \tag{3.6}$$

where $\epsilon(x, y)$ represents the error propagated from the noisy PIV velocity fields.

In the present work, pressure is computed using a spectral decomposition method in which the solution is approximated by a linear combination of orthogonal basis functions. This method is used for a two-dimensional flow in the current work, but can be easily extended to three-dimensional flows. The Poisson operator is diagonalized and inverted in the spectral space to yield the solution. The numerical scheme adopted to compute the derivatives is of second order. This decomposition method is adopted from [130] and a simple implementation can also be found in [180, 122]. The details of this method is provided in the appendix.

3.1.2 Optimal control approach

Satisfying the compatibility condition (3.5) while specifying the Neumann boundary may not be likely when the data contains noise. The constant K arising from the pressure estimation (3.6) can be eliminated by a single known pressure measurement but the residual error remains. The minimization of these errors are addressed in the proposed method.

The optimal control approach corrects the Neumann boundary while minimizing a quadratic cost functional. The quadratic cost functional is formulated as the difference

between estimated and experimentally available pressure measurements. The approach is developed to utilize the available sparse pressure measurements on the boundary to correct the estimated pressure field. These measurements can be conveniently extracted using surface mounted or Pitot-type probes in a typical PIV experiment. The pressure being measured on the boundary, the cost functional to be minimized is along the boundary and is formulated as

$$\mathcal{J}(P,\varphi) = \frac{1}{2}\int_{\Gamma} H\left(P_c - P_{true}\right)^2 d\Gamma + \frac{\gamma}{2}\int_{\Gamma}\varphi^2 d\Gamma. \tag{3.7}$$

Here, $\varphi \in \mathbb{R}$ is the control that is applied on the boundary to minimize the cost functional. It can be viewed as a forcing or a correction term applied on the boundary to drive the estimated pressure close to the measurements. $\gamma > 0$ can be viewed as a constant which quantifies the effort to apply the control. P_c denotes the computed pressure by the solver, P_{true} refers to the true value of pressure (e.g. measured by a probe), Γ represents the boundary of the domain and H is a Boolean matrix with value 1 where P_{true} exists and 0 otherwise. The state constraints governing the minimization problem can be rewritten as

$$\Delta P = f\left(U, \overline{u_i u_j}\right) \quad \text{in} \quad \Omega, \tag{3.8}$$

$$\nabla P \cdot n = g\left(U, \overline{u_i u_j}\right) + \varphi \quad \text{on} \quad \Gamma, \tag{3.9}$$

which are the mean pressure Poisson equation and Neumann boundary conditions respectively. The control φ appears in (3.9) with the aim to correct Neumann boundary conditions.

The formal Lagrange multipliers method [182] is used to augment the cost function (3.7) together with the state constraints (3.8) and (3.9) using co-state variables known as Lagrange multipliers, thus forming a Lagrangian function written

$$\mathcal{L}(P,\varphi,\lambda^+,\varphi^+) = \mathcal{J}(P,\varphi) - \langle \Delta P - f(\overline{U}, \overline{u_i u_j}), \lambda^+ \rangle_{\Omega} - \langle \nabla P \cdot n - g(\overline{U}, \overline{u_i u_j}) - \varphi, \varphi^+ \rangle_{\Gamma}. \tag{3.10}$$

The angle bracket $\langle \cdot, \cdot \rangle_{\Omega}$ in (3.10) represents inner products defined by

$$\langle f_1, f_2 \rangle_{\Omega} = \int_{\Omega} f_1 f_2 \, d\Omega,$$

while $\langle \cdot, \cdot \rangle_{\Gamma}$ represents inner products defined by

$$\langle f_1, f_2 \rangle_{\Gamma} = \int_{\Gamma} f_1 f_2 \, d\Gamma,$$

and the additional variables λ^+ and φ^+ are the Lagrangian multipliers. The problem reduces to minimizing $\mathcal{L}(P,\varphi,\lambda^+,\varphi^+)$, such that its derivative with respect to P and the control φ vanish, that is

$$\mathcal{D}_P \mathcal{L} = 0, \tag{3.11}$$

and

$$\mathcal{D}_{\varphi} \mathcal{L} = 0, \tag{3.12}$$

where $\mathcal{D}$ represents the Fréchet derivative with respect to the variable. From equation(3.11), the adjoint-state equations for pressure is derived as

$$\Delta \lambda^+ = 0 \quad \text{in} \quad \Omega, \tag{3.13}$$

$$\nabla_n \lambda^+ = H(P_c - P_{true}) \quad \text{on} \quad \Gamma, \tag{3.14}$$

$$\lambda^+ = -\varphi^+ \quad \text{on} \quad \Gamma. \tag{3.15}$$

Using (3.12), the gradient of the cost function writes

$$\nabla_{\varphi}\mathcal{J} = \gamma\varphi - \lambda^{+} \quad \text{on} \quad \Gamma. \tag{3.16}$$

Setting (3.16) to zero leads to the optimal solution for the control given as

$$\varphi = \frac{\lambda^{+}}{\gamma} \quad \text{on} \quad \Gamma. \tag{3.17}$$

A first guess $K_{est.}$ of constant K is computed using the available P_{true} as

$$K_{est.} = \frac{1}{N}\sum_{i=1}^{N} P_{c,i} - P_{true,i}, \tag{3.18}$$

where N represents the total number of available pressure measurements. It is then subtracted from the computed pressure P_c prior to the application of control and is updated in an iterative manner. The Neumann boundary is corrected until the $P_c - K_{est.}$ converges to P_{true}, or when $|P_c - K_{est.} - P_{true}| < \varepsilon$. The values of ε where chosen to be 10^{-4} for synthetic data while 10^{-2} was more appropriate for experiments and corresponds to the uncertainty of the sensors.

3.1.3 Divergence correction for two-dimensional velocity field

Turbulent flows are known to be rotational and three dimensional. However, the flow over a two dimensional body at high Reynolds number can be made statistically two dimensional using Reynolds averaging provided there is no external disturbances. In a typical two-dimensional two-component (2D-2C) PIV experiment, the acquired velocity field is generally contaminated with noise making it non-divergence free. The impact of the out of plane components in a 2D velocity field on pressure estimation has been studied by many authors and a few can be found in the references [45, 35, 102, 103]. Also, the inherent measurement errors can lead to erroneous estimation of velocity gradients [56]. The velocity gradient directly influences the error level in the source and boundary terms [117] and hence affect the pressure estimate. As such, it is of interest to compute a divergence-free velocity field to reduce the accumulated error while estimating the total mean pressure. Statistically 2D flow implies a null mean spanwise velocity component and hence the resulting pressure estimation can be referred as 'total' and not 'planar' pressure.

In this section, a divergence-free correction based on the Helmholtz decomposition is proposed. Any smooth vector field may be decomposed as the sum of gradients of a scalar potential and curl of a vector potential, that is

$$\mathbf{U} = \nabla\phi + \nabla \times \psi. \tag{3.19}$$

Here the vector potential ψ is divergence free by construction. For an incompressible irrotational flow, the curl of the vector potential vanishes whereas for an incompressible rotational flow, the gradient of the scalar potential is zero. Thus, for a two-dimensional incompressible rotational flow, with velocity vector field $\mathbf{U} = (U, V, 0)$, the scalar potential part vanishes and the vector potential becomes $\psi = (0, 0, \psi)$. Hence the velocity components are given by

$$(U, V, 0) = \left(\frac{\partial\psi}{\partial y}, -\frac{\partial\psi}{\partial x}, 0\right), \tag{3.20}$$

where the vector potential ψ becomes the streamfunction. Using vector identities equation (3.19) can be rewritten as

$$\nabla \times \mathbf{U} = -\Delta\psi. \tag{3.21}$$

The new velocity vector is found, solving the Poisson equation for stream function ψ (3.21), with Neumann boundary conditions (3.20).

To summarize, the divergence correction for the velocity field is accomplished in three steps:

1. Acquire the mean velocity fields for an incompressible 2D flow by PIV experiment,
2. Solve the Poisson equation for the streamfunction (3.21) using Neumann boundary condition (3.20),
3. The new mean 2D velocity field vector is found using (3.20), such that $(U_{new}, V_{new}, 0) = \left(\frac{\partial\psi}{\partial y}, -\frac{\partial\psi}{\partial x}, 0\right)$

Whence the reconstructed mean velocity field is divergence free. i.e., $\nabla \cdot \mathbf{U}_{new} = \nabla \cdot \nabla \times \psi = 0$. Note that this correction only applies for flow over a two-dimensional body. A pseudocode of the pressure correction strategy is presented in Algorithm 1.

Algorithm 1: Pressure reconstruction

Input: PIV Velocity fields $\mathbf{U}_{piv}$
Output: Accurate pressure field P

1. Retrieve divergence free mean velocity field $\mathbf{U}^0$;

   Solve for streamfunction ψ;

$$\Delta\psi = -\nabla \times \mathbf{U}_{piv}\ , \quad \left(\frac{\partial\psi}{\partial y}, -\frac{\partial\psi}{\partial x}\right) = \mathbf{U}_{piv} \tag{3.22}$$

   New velocity field $\mathbf{U}^0$;

$$\mathbf{U}^0 = \left(\frac{\partial\psi}{\partial y}, -\frac{\partial\psi}{\partial x}\right) \tag{3.23}$$

2. Solve for initial pressure guess P^0;

$$\Delta P^0 = f(\mathbf{U}^0), \quad \nabla P^0 \cdot n = g(\mathbf{U}^0). \tag{3.24}$$

3. Apply Optimal control;

   Initialize $j = 1$, set $\gamma > 0$, and ϵ=10^{-2} (i.e. where ϵ is the relative sensors' uncertainty);

   Compute the cost function $\mathcal{J}^j$;

   while $\mathcal{J}^j > \epsilon$ **do**

   Solve for the adjoint state λ^+;

$$\Delta\lambda_j^+ = 0, \quad \nabla\lambda_j^+ \cdot n = H\left(P^{j-1} - P_{true}\right). \tag{3.25}$$

   Set control $\varphi^j = \lambda_j^+/\gamma$;

   Update pressure;

$$\Delta P^j = f, \quad \nabla P^j \cdot n = g + \varphi^j. \tag{3.26}$$

   Update the constant and pressure;

$$K_{est,j} = \frac{1}{N}\sum_{i=1}^{N} P^j - P_{true,i}, \quad P^j = P^j - K_{est,j}, \tag{3.27}$$

   $j = j + 1$;

   Update $\mathcal{J}^j$;

   end

3.1.4 Test case description

Synthetic data generation

Synthetic flow fields are used to validate the method proposed in the section 3.1.2. The database is generated using the ANSYS Fluent software package, for a prototype 2D flow over a D-shaped bluff body. Figure 3.1 shows the bluff body used for the simulation. The body is constructed with a circular leading edge and a rectangular base such that the body height d measures 40mm with a lengthwise aspect ratio of 4. The x and y axis represent the streamwise and transverse directions respectively. A structured mesh is generated using the ANSYS meshing tool with a maximum and average skewness of 0.59 and $1.25 \cdot 10^{-2}$ respectively. The minimum orthogonal quality of the mesh is 0.95 with an average value of 0.99. The domain extended $7d$ upstream from the leading edge, transverse extent of $7d$ from the top and bottom surface of the body and $20d$ from the trailing edge or base of the body.

The planar, two-dimensional flow domain was simulated using a transient pressure based solver with an absolute velocity formulation and using the $k-\omega$ SST turbulence model [55]. The fluid was set to 'air' with a dynamic viscosity and density of $\mu = 1.789 \cdot 10^{-5}$ kg/ms and $\rho = 1.225$ kg/m^3 respectively. The Reynolds number based on the body height defined as

$$Re_d = \frac{\rho U_\infty d}{\mu}, \tag{3.28}$$

where U_∞ is the inlet free-stream velocity, is set to $5.5 \cdot 10^4$ at the inlet. The outlet is specified to be 'pressure outlet' with gauge pressure set to 0. Turbulence at the inlet and outlet is specified using turbulence intensity (5%) and viscosity ratio (10). Symmetric flow condition was imposed at the transverse boundaries of the domain and 'no slip' conditions imposed at the bluff body wall. A SIMPLE scheme of pressure-velocity coupling was used with a second-order spatial discretization and second-order implicit transient formulation. The gradients are evaluated using the 'least-squares cell based' method (see [55] for details). Default values set by Fluent were used for the under-relaxation factors in solution controls. The convergence criteria given by the scaled residuals were set to 10^{-6}. The time step chosen for the simulation is 0.001 seconds which when normalized using the free-stream velocity and the body height gives $t^* = 0.5$, where the superscript $(*)$ denotes a normalized quantity and the same convention is adopted for further discussions. The flow was simulated for 1000 time steps with a maximum of 300 iterations per time step.

The origin of the coordinate system is defined at the mid height of the bluff-body base [See figure 3.1] and the coordinates are normalised with the body height d. The synthetic instantaneous flow fields extracted every four time steps are interpolated onto a uniform rectangular grid with extents $x^* \in [0, 6]$, $y^* \in [-1.5, 1.5]$ and uniform spacing of $dx^* = dy^* = 0.025$ in the streamwise and transverse directions. The flow is then time-averaged in a RANS sense to obtain the mean flow fields. The goal is to assess the performance of the proposed pressure correction schemes and is not to serve as reference data for comparison with experiments, especially since RANS model is a low fidelity model and suffers from inaccuracies in the prediction of complex flow fields (see for instance [74]).

Noise addition to synthetic data

The synthetic mean velocity and Reynolds stress fields generated in §3.1.4 are modified with the addition of different types of noise since the Poisson solver and the numerical

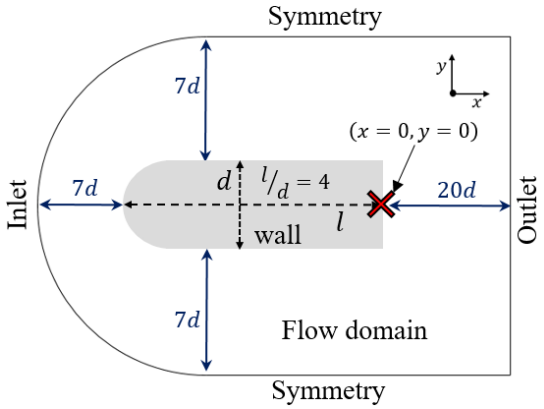

Figure 3.1: Sketch of the bluff body and flow domain used for simulation. The shaded region represents the D-shaped bluff body while the continuous lines represent the boundary of the computational domain.

scheme are sensitive to the noise color (see [45, 56] for instance). Therefore, two types of noise are selected based on their spectral energy content. The first one shall be referred to as 'Noise I' with a higher low-frequency spectral energy and the second one is 'White noise' with a uniform spectral energy distribution. Addition of two types of noise shall be tested separately to examine the sensitivity and robustness of the proposed method. The error levels are estimated by the L_∞ norm defined as

$$\epsilon_\infty = \max\left(\mid \epsilon_1 \mid, \mid \epsilon_2 \mid, ..., \mid \epsilon_n \mid\right), \tag{3.29}$$

where ϵ denotes the difference between the exact and estimated value, to quantify the maximum error level. The L_2 norm defined as

$$\epsilon_2 = \frac{\sqrt{\sum_{k=1}^{N} \mid \epsilon \mid^2}}{\mid \Omega \mid}, \tag{3.30}$$

where, $\mid \Omega \mid$ represents the region of the domain over which the norm is computed, to quantify the root mean square error level. The noise level input to the velocity and Reynolds stresses and the corresponding error level in the pressure estimation are given in the Table 3.1.

These noise levels were chosen independently and arbitrarily high to witness sufficient departure from the reference pressure field. It also represents the pressure error levels resulting from a combination of flow field uncertainties introduced by the computational methods or algorithms used for velocity reconstruction (see for instance [35]). The resulting noise-contaminated flow fields are input to the Poisson solver to compute 'Noisy' pressure.

3.1.5 Results based on synthetic data

Pressure solver

Mean velocity and Reynolds stress fields are input to the pressure solver to compute pressure. Figure 3.2 shows the evolution of the pressure coefficient, defined as

Noise level input (%)						Output error (%)	
		U_i		$\overline{u_i u_j}$		C_p	
	Noise type	ϵ_∞	ϵ_2	ϵ_∞	ϵ_2	ϵ_∞	ϵ_2
a	Noise I	16	12	7	5	39	12
b	White	5	2	2	1	27	10

Table 3.1: Input noise level and output error level

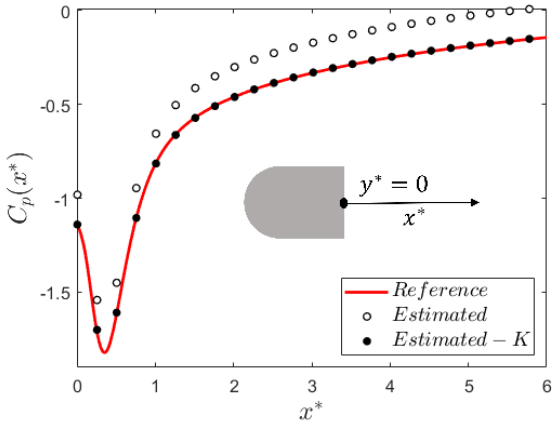

Figure 3.2: Evolution of the mean C_p along the wake centerline at $y^* = 0$. 'Reference' represents the pressure directly obtained from the turbulent solver and 'Estimated' represents the pressure computed using the synthetic flow fields.

$$C_p = \frac{P}{1/2 \rho U_\infty^2}, \tag{3.31}$$

along the wake centerline. The verification of the compatibility condition (3.5) shows that the pressure is uniquely defined up to a constant K. On subtraction of the constant K, computed using a single value of reference pressure, from the whole pressure field the estimated pressure profile is seen to match the reference (see figure 3.2). The maximum error level defined by equation (3.29) is found to be less than 0.2% percent which is attributed to the accuracy of the numerical scheme.

Thus in a scenario where pressure is estimated using Poisson pressure equation and Neumann boundary conditions, a unique solution of pressure estimate can be retrieved, using a single known pressure value, subject to satisfying the compatibility condition.

Pressure correction

In order to mimic experimental data, noise is added as described in 3.1.4. In the following sections, the results of optimal control applied to the 'Noise I' contaminated data shall be presented as figures whereas the results in the case of 'white noise' contaminated data shall be quantified.

Comparing the noisy pressure estimate (●) from figure 3.3 to the noise-free pressure estimate (○) in the same figure, pressure is not only offset by a constant. In this situation, the constant K cannot be eliminated using a single known pressure measurement and residual errors remain (see eq. (3.6)) and contaminate the whole pressure field. In this context, the optimal control minimizes simultaneously the offset and the residual errors through the Neumann boundary condition. The only requirement for this approach is

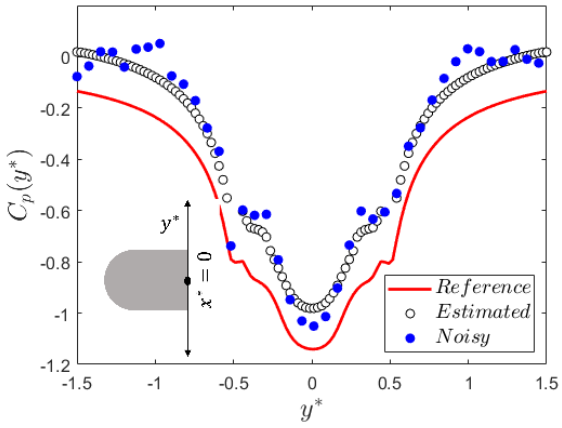

Figure 3.3: Profile of C_p along the boundary at $x^* = 0$. 'Noisy' represents the pressure computed from the synthetic mean flow fields corrupted with noise. (See §3.1.4) .

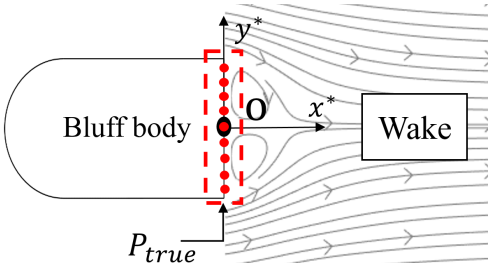

Figure 3.4: Probe locations P_{true} in a typical PIV experiment in the bluff body wake. The solid circles represents the pressure sensors. The dashed rectangle represents the region over which the control is applied.

the availability of, at least, one pressure measurement P_{true}. From an experimental point of view, P_{true} is readily available from wall-mounted pressure taps, but remains sparse compared to the spatial resolution of the PIV.

In order to apply the optimal control, few virtual pressure measurements (P_{true}) are used at the base of the bluff body, similar to the wind-tunnel experiment (see figure 3.4). These measurements are sparse with the mean spacing being $0.092d$ compared to the spatial resolution $0.025d$ of the synthetic data.
In the following discussion, the control is applied on two different pressure fields named as 'φ *App.* 1' and 'φ *App.* 2'. The details of their generation are as follows.

- φ *App.* 1 : 'Noise I' is added to Synthetic mean flow fields. It is then input to the pressure solver.

- φ *App.* 2 : 'Noise I' added to Synthetic mean flow fields. Further, divergence correction is applied to the resulting mean velocity field. Finally the divergence corrected mean velocity field U_i (see §3.1.3) and the noisy Reynolds stress fields $\overline{u_i u_j}$ are input to the pressure solver.

The value of the constant γ in (3.7) was chosen based on trial and errors in order to ensure a fast convergence of the algorithm. For this particular problem, a value of $1 \cdot 10^{-4}$ was used.

Figure 3.5 shows that the control minimises the error drastically on the boundary.

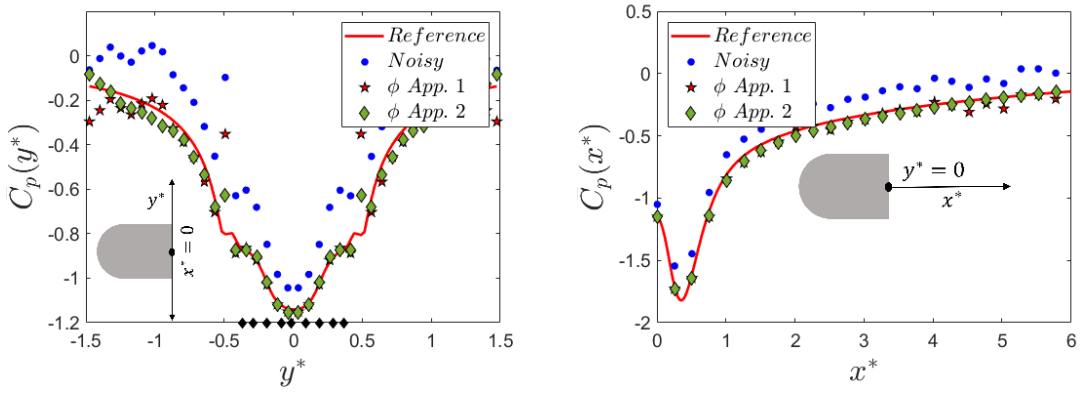

(a) (b)

Figure 3.5: Comparison of reference C_p to the control (φ) applied and the noise contaminated C_p along the inlet boundary (a) and the wake centerline (b). The black diamonds on the inlet boundary (a) represents the location of sensor pressure measurements (P_{true}).

Although the measurements are sparse, the correction by the control is not only limited to the location of the measurements but also to the nearby boundary locations. A matching fit to the reference C_p is observed for both the pressure fields 'φ *App.* 1' and 'φ *App.* 2' on the region of the boundary in the vicinity of the measurements (see figure 3.5a). Moving away from the boundary, the corrected pressure profile 'φ *App.* 1' does not match the reference but is shifted by a constant.

While the control fits the boundary to the reference in the vicinity of P_{true}, the effect is limited in the distant region. Additional wall measurements P_{true} may prove to be an effective solution. However, the error is negligible. Moreover, in a wind-tunnel experiment, this additional P_{true} obtained by Pitot sensors may disturb the flow and hence may be avoided. The error levels (see table 3.2) indicate that although a good match with the reference is observed (see figure 3.5) the maximum error (ϵ_∞) remains higher in case of 'φ *App.* 1'. These higher levels are caused by the high-frequency peaks, passed from the original noisy C_p. This is confirmed by examining the corresponding *rms* error level in table 3.2. The best results are seen for 'φ *App.* 2' where the pressure field is estimated using the divergence corrected mean velocity field along with the noisy Reynolds stresses. It is observed that the divergence correction of velocity field indirectly smooths the pressure field. In order to have a better insight, it would be worth examining the effect of noise in the source term for each case.

Figure 3.6 compares the source term estimated from Noisy and divergence corrected (Div. corrected) velocity fields which leads to the cases 'φ *App.* 1' and 'φ *App.* 2' respectively. The source term is normalized using the body height (d) and the free-stream dynamic pressure ($\rho U_\infty^2/2$). The error levels are quantified to be 255% (ϵ_∞) and 105% (ϵ_2) for the Noisy source term whereas it drastically reduces to 105% and 14% respectively on applying the divergence correction to the velocity fields.

According to Pan *et al.* the error level in the source term is directly influenced by the velocity gradients [117] which amplifies the noise [56] and can become very large. This explains the error levels in the source term even though the input noise level is considerably lower (see table 3.1). Further, the spatial high-frequency content of the errors in the source term is attenuated by the pressure Poisson solver through its low-pass filtering effect [66, 45]. This process outputs the pressure coefficient solution C_p contaminated

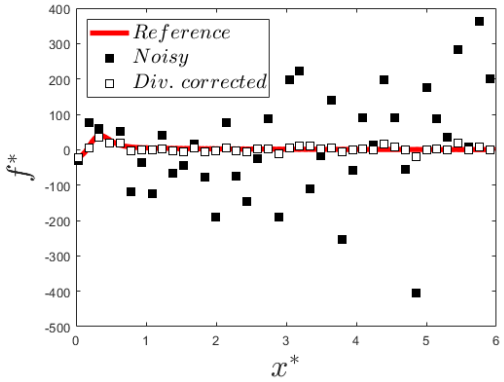

Figure 3.6: Evolution of non dimensional source term along the wake centerline $y^* = 0$

Error level in C_p (%)					
		φ *App.*1		φ *App.*2	
	Noise type	ϵ_∞	ϵ_2	ϵ_∞	ϵ_2
a	Noise I	24.9	4.8	9.8	2.8
b	White	17	4.4	7.7	4.2

Table 3.2: C_p error level obtained after pressure correction.

by noise, shown in figures 3.3 and 3.5 respectively with a considerable lower error level compared to the source term. Applying the control further reduces the error level by limiting the error propagated from the Neumann boundary giving the pressure field 'φ *App.* 1' shown in figure 3.5.

In case of 'φ *App.* 2', the noise contaminated velocity field undergoes filtering by the numerical scheme and the Poisson solver [56, 45] involved in enforcing divergence free condition (see §3.1.3). The process fits a second-order smooth surface on to the noisy velocity fields. This ensures minimum noise amplification and better derivative estimations thus leading to a smoother source term as shown in figure 3.6. The residual peaks observed are further filtered by the pressure Poisson solver to output a smooth pressure field. In the final step, the optimal control corrects the boundary and minimises the global error in the pressure field.

The results indicate that the optimal control acts not only on the points where P_{true} is available but also on its nearby locations. This effect can be simply explained by the harmonic nature of the formulated control. (i.e. satisfying Laplace equation $\Delta\varphi = 0$). Intuitively, this means that the average variation of the function at a point with respect to its neighborhood is zero. Also, the properties of harmonic functions shows that these are smooth and infinitely differentiable functions. As such, the control peaks at the location of P_{true}, due to the boundary conditions involved in solving for it, and also spreads to the neighborhood. This can also mean that for a high magnitude of pressure gradient along the length of the boundary, the distribution of true pressure measurements P_{true} determines the extent of optimal control effect.

From the preceding results and discussions it is seen that the divergence correction indirectly acts as a source term corrector and the optimal control approach minimises boundary error propagation. The results also shows that the control is unbiased to the type of noise. Although the low-pass filter properties of the Poisson solver [45] do not filter low-frequency errors, the control acts in a different way and is able to compensate for the

remainder of the error. Although Neumann boundary conditions are not recommended (see [117]), it is mandatory in case of experiments focusing on rotational regions of the flow. The optimal control approach is attractive in such cases subject to the availability of a few reliable pressure measurements. An accurate near field pressure estimate would mean that the approximations for pressure (e.g: [4, 26]) can be avoided to estimate drag of immersed bodies.

The optimal control approach can be naturally extended to instantaneous flow fields acquired using low-speed planar PIV. The source term to determine the instantaneous pressure field is independent of time derivatives and the time dependent information is required only to specify boundary conditions (see for instance [190]). In this framework, the multi-directional integration approach introduced by Liu & Katz [95, 97] to solve for the pressure problem may represent an interesting alternative to obtain an accurate instantaneous pressure field. The data assimilation methods such as those proposed by He *et al.* [68] can also prove valuable in this regard. But, these methods involve large computational efforts. The present approach can be beneficial when combined with the Taylor's hypothesis approach proposed by de Kat *et al.* (2012)[44]. As such, the optimal control may be used to reinforce these weaknesses (see [188]) and improve the detrimental effect of noise associated with time-dependent PIV measurements. However, the 2D divergence correction to correct the source term may not be applicable in such cases as the flow may be inherently three dimensional. The situation is made more difficult because of the unknown third velocity component. In such cases, to avoid noise amplification while estimating source terms, one may filter the velocity fields using typical low-pass filters or use hybrid derivative estimation schemes (see [51]) which offers a better trade-off between error and precision. Further, estimating instantaneous pressure field [95], the local acceleration which is the only remaining unknown in the 2D NS equations, may be estimated. Although the method seems attractive for instantaneous fields, the number and location of sensors to obtain P_{true} in order to optimally correct the boundary, is not known and remains to be investigated.

3.1.6 Application to wind-tunnel experimental data

The following section demonstrates the application of mean-pressure correction methods discussed in §3.1.2 and §3.1.3 on experimental data. The method is applied on PIV measurements of a two-dimensional mean flow over a D-shaped bluff body in operating conditions similar to that of the numerical simulation (see §3.1.4). Sparse pressure measurements available at the bluff body base (see figure 3.4) are used to apply the pressure correction and the extent and quality of the correction is analysed as a function of the domain size.

Bluff body flow - Experimental setup and procedure

The low-speed PIV experimental setup uses a TSI PIV systems depicted in figure 3.7. The D shaped bluff body described in §2.3.2 is used for the experiments. The bluff body was installed at approximately $14d$ from the inlet of the test section, where d is the height of the body. The background turbulence level in the test section was measured by a hot-wire anemometer and found to be less than 0.5%. The flow seeded with olive oil droplets was illuminated by a double-pulsed Nd:YAG laser with a pulse delay short enough to limit the in-plane movement to a quarter of the interrogation window size. Up to 2500 flow image pairs were acquired using the INSIGHT 4G-2DTR Data Acquisition

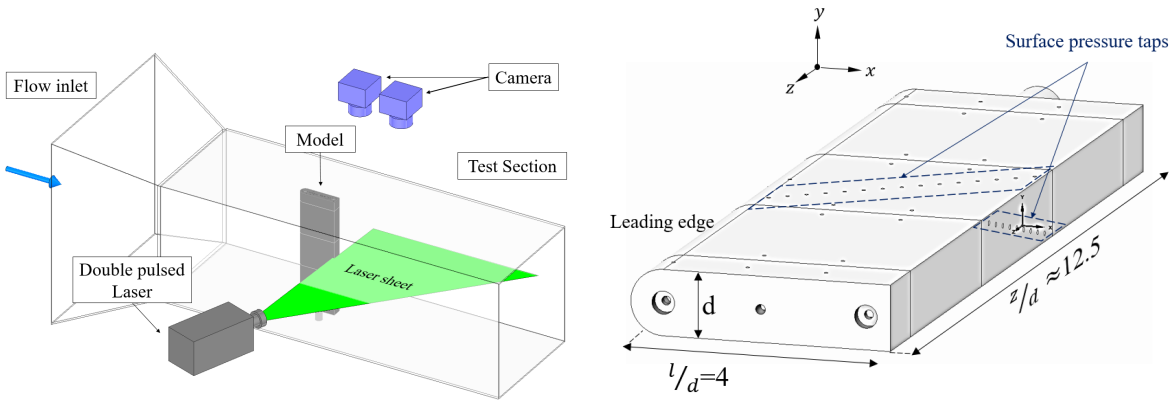

(a) Schematic of the experimental setup

(b) Bluff body model

Figure 3.7: Schematic of the experimental setup (a) and the D shaped bluff body model (b)

software package at a rate of 7.25 Hz, located sufficiently far apart in time to recover time-uncorrelated data sets to obtain turbulent quantities. Two CCD cameras of 4 Mpx each were synchronized with the laser using a TSI LaserPulse Synchronizer Model 610036. The cameras were aligned with an overlap of approximately 25% of the length of a single image, ensuring the continuity of the flow captured. A laser engraved checkerboard was used to calibrate both cameras, to correct the acquired images for perspective [167]. The common region of both the perspective corrected checkerboard images were found using a simple cross correlation. The overlapping region from both the images are then blended using a weighing function and then stitched together. The setting used to stitch the checkerboard images were then carried over to stitch each of the 2500 PIV image pairs. The corrected and stitched images are then processed using DPIVSoft software [104, 123], using multiple passes of interrogation with the final interrogation window size being 32 $\times$ 32 px^2 with a 75% overlap, resulting in a vector resolution of $0.014d$. From the boundary layer theory for flat plates [152], one may note that the length of the body is insufficient for the laminar boundary layer transition. Hence, Blasius approximations can be used to compute the displacement thickness and to express the vector field resolution in terms of this smaller length scale. The estimated displacement thickness prior to separation could be indicative of the shear layer thickness at separation and hence would give better insight into the vector field resolution. As such, the vector field resolution reported in terms of displacement thickness is $\approx 0.97\delta_1$, where δ_1 represents the displacement thickness. Finally, the Reynolds number of the flow was set to $Re_d \approx 5.5 \cdot 10^4$. The mean velocity fields and the Reynolds stress fields obtained from the PIV experiments are input to the solver to compute a first approximation of the pressure. The experiment setup described here is different than that used for the physical analysis. The reason is that the current set of experiment is higher in uncertainties than that described in the 'Experiment Setup', with the data later found to be corrupted due to insufficient dt between the laser pulses, resulting in noisy mean fields and consequently to a noisy pressure field. The noisy pressure estimated from these data sets makes it suitable for the application of the adjoint method, in order to show that a clean estimate of pressure can be obtained from a noisy data using the proposed method.

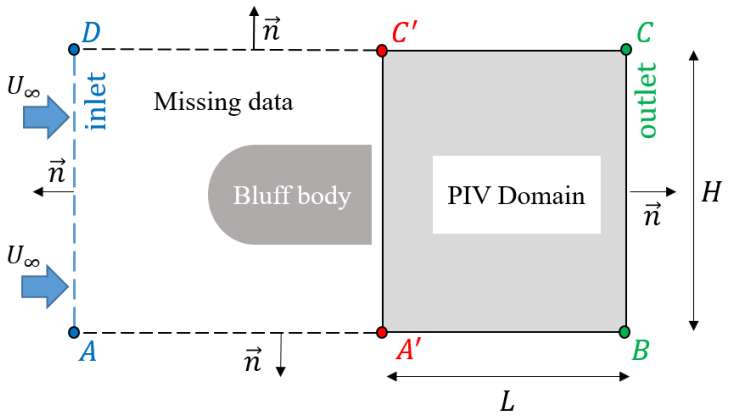

Figure 3.8: Control volume (CV) for momentum balance. L and H represents the streamwise and the transverse extent of the closed Control volume $A'BCC'A'$.

3.1.7 Computation of Drag and comparison between two independent estimates

Methodology

The mean pressure is estimated from the pressure Poisson equation which is derived from the mean momentum equations (RANS). Therefore, momentum is always conserved on any arbitrary control volume inside the domain. In an experiment, verification of momentum conservation cannot be considered as a tool to examine the accuracy of the pressure estimate. Alternatively, the drag coefficient from two independent sources are compared in order to obtain an estimate of the uncertainty in the pressure measurements. At this point, it is worth noting that uncertainties in drag estimation can be due to the uncertainties in the pressure field as well as the non divergence-free velocity field [103].

The drag of a bluff body in a high-Reynolds number flow is dominated by pressure forces (see for e.g: [38]). This is verified from the synthetic database generated in §3.1.4 where the total drag is composed of 95% of pressure drag and a negligible 5% for the viscous drag. In an experiment, a good estimate of the drag coefficient (C_d) can be obtained using the measurements from the surface pressure taps mounted on the body and is defined as

$$C_d^{\mathrm{I}} = \int_{Surface} C_p \ (\hat{n} \cdot \hat{i}) \ dA^*, \tag{3.32}$$

where $\hat{n}$ is the unit normal vector to the surface with area dA and $\hat{i}$ is the unit vector in the direction of the free-stream flow. An equivalent way to estimate the drag coefficient is by evaluating the momentum budget on an arbitrary Control Volume (CV) enclosing the body under consideration, for instance given in Figure 3.8 (see [4] [88] [43]). The origin of the coordinate system is at the mid point of the body base, depicted in figure 3.1. The PIV experiment being conducted at the wake, information upstream the PIV domain is not available and is represented by the domain bounded by dashed lines in figure 3.8. Applying the momentum budget, the equation for C_d reads

$$C_d^{\mathrm{II}} = 4 \int_{DC} (1 - U^*) V^* dx^* + 2 \int_{BC} (1 - U^*) U^* dy^* - \int_{BC} C_p dy^* - 4 \int_{DC} \overline{u'v'}^* dx^* - 2 \int_{BC} \overline{u'^2}^* dy^*, \tag{3.33}$$

Since, the upstream data is not available, we use the following approximations:

- the flow is advected with a constant velocity U_∞ along the lateral sides (DC' & AA'), and
- free-stream turbulence in these regions is assumed to be null.

The momentum budget hence writes

$$C_d^{\mathrm{II}} \approx 4\int_{C'C}(1-U^*)\,V^*dx^* + 2\int_{BC}(1-U^*)\,U^*dy^* - \int_{BC}C_p dy^* - 4\int_{C'C}\overline{u'v'}^*dx^* - 2\int_{BC}\overline{u'^2}^*dy^*. \tag{3.34}$$

Both the independent drag estimates given by equations (3.32) and (3.34) must coincide. Comparisons are conducted where the former is treated as the reference and the latter is used to obtain the error in the estimated pressure.

Results and discussions

In order to compute C_d from PIV data, pressure is required. It is estimated following the Poisson approach with Neumann boundary conditions. Verifying the compatibility condition, a difference of 17% was found between the normalised source term and boundary term contributions, where the normalisation is with respect to the free-stream dynamic pressure $\left(\frac{1}{2}\rho U_\infty^2\right)$. This indicates the presence of residual errors (see equation (3.6)) which might arise from both the source and boundary terms.

In the following discussions, two cases shall be discussed. The first case referred as 'Original' hereafter considers the pressure field estimated without application of corrections. In this case, the constant K_{est} is estimated using a pressure measurement at the wall. In a typical PIV experiment without wall treatment for laser-light reflections, obtaining near-wall PIV measurements is not trivial. This is particularly true in the case of our experimental data where a near-wall region equivalent of 18% of the body height d is overexposed with laser reflections. To recover the pressure estimate close to the body base, a second-order polynomial of the form

$$P(x) = ax^2 + bx + c,$$

is used to extend the estimated pressure corresponding to the location of the reference base-pressure measurement. The polynomial coefficients are found with the conditions

$$\frac{\partial}{\partial n}P(0) = 0 \quad , \quad P(x_1) = P_c \quad \text{and} \quad \frac{\partial}{\partial n}P(x_1) = k_1 \quad \text{on} \quad \Gamma.$$

where x_1 represents the location on the computational boundary Γ. The constant K_{est} is computed as the difference between the P_{true} at the wall and the polynomial extended pressure estimate (see figure 3.9).

In the second case which shall be referred to as 'φ Applied' hereafter, the pressure is estimated with the application of pressure corrections discussed in §3.1.2 and §3.1.3. As a first step, the mean velocity fields are divergence corrected. The corrected mean velocity fields together with the Reynolds stress components are used to estimate the pressure field. The polynomial is used to extend the pressure estimate to the wall at 9 locations corresponding to the location of the 9 base-pressure measurements.

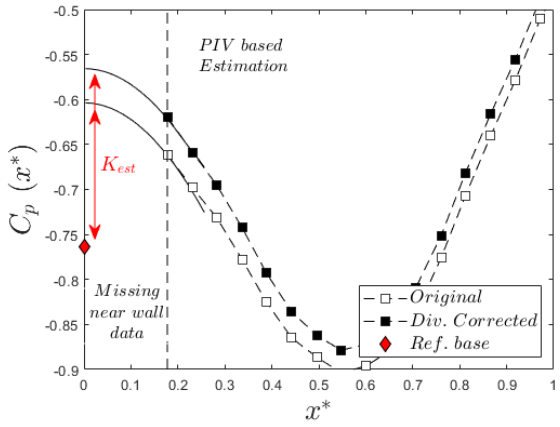

Figure 3.9: Sketch of the near-wall polynomial interpolation. The continuous black line represents the polynomial interpolation. 'Original' and 'Div. corrected' refer respectively to the pressure field estimated without and with corrections.'Ref. base' represents the reference pressure obtained from the wall-mounted sensors and the red arrows represent the constant K_{est}.

Difference in the extension is clearly visible in figure 3.9 between both cases, where the constant K_{est} also differs. These differences can have implications on the estimated drag. The smooth velocity fields obtained on applying the divergence correction indirectly corrects the source term and improves the pressure estimate as demonstrated in §3.1.5 and is thus expected to perform better.

Figure 3.10b compares the maximum deviation of estimated C_d from the reference, represented by δC_d defined as

$$\delta C_d = \frac{C_d^{\mathrm{II}} - C_d^{\mathrm{I}}}{C_d^{\mathrm{I}}} \times 100. \tag{3.35}$$

The CV chosen is a simple square such that $L^* = H^*$ and its size is progressively increased until either one of the CV extents reaches the domain extent and is schematically illustrated in figure 3.10a. The error in C_d is estimated using equation (3.35) for each CV and the results are presented in figure 3.10b.

The C_d obtained from the simulations shows that the contribution of viscous drag is only 5% to the total drag. From Schlichting (1960) [152], the critical Reynolds number based on the streamwise distance, for a flat plate, is $Re_{x_p} \approx 3.2 \cdot 10^5$. The surface of the body being equivalent to that of a flat plate, it is noted that this critical Re_{x_p} is never achieved for the present case, where x_p is the streamwise distance measured from the leading edge of the body. This is verified by experimental measurement of boundary layer close to the body base at $-1.5 < x^* < -1.3$ where the streamwise pressure gradient $\frac{\partial P}{\partial x_p} \approx 0$. The boundary layer is found to be laminar with a shape factor $H \approx 2.3$. Hence, invoking the Blasius approximation, one finds that the viscous drag stays well within 5% of the total drag. Since the reference C_d from equation (3.32) constitutes only the pressure drag, a 5% uncertainty region, shaded in red color, is provided in figure 3.10b to account for the viscous drag.

Figure 3.10b shows the error in C_d estimate which is under-predicted by approximately 10% in the region close to the body. The error substantially increases with the CV size for the 'Original' case, where the pressure is estimated without any corrections. The

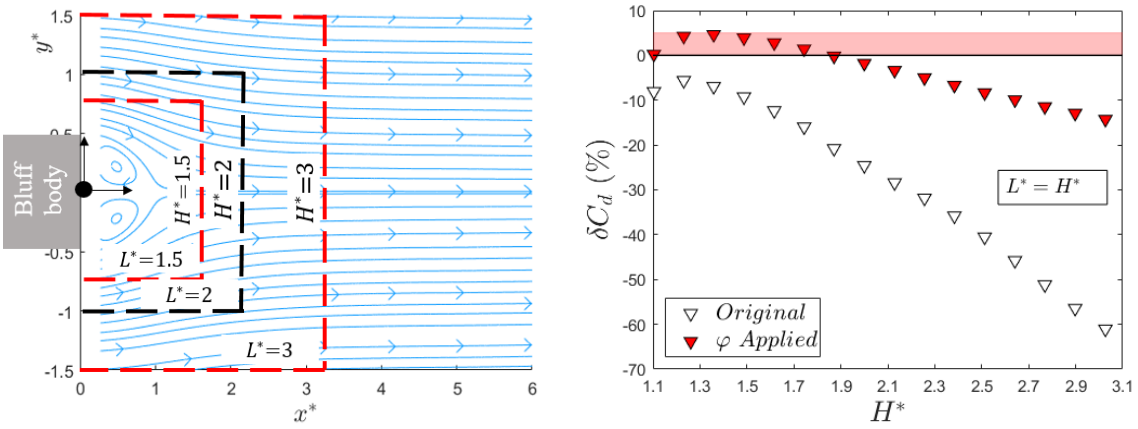

(a) (b)

Figure 3.10: Choice of CV for computing C_d (a) and the corresponding error estimate in C_d (b). The dashed line in (a) represents the boundary of CV. The red shaded region in (b) represents the additional 5% in drag coefficient attributed to viscous drag.

implementation of pressure corrections significantly improves the C_d estimate both in the near as well as far fields. The improvement is specially relevant in the region within $L^* \approx 1.7$ which is proportional to the region over which P_{true} is available for control application (see figure 3.4). Also in this region, the error remains within the 5% bound which accounts for viscous drag. The deteriorating accuracy with the increasing CV size beyond $L^* \approx 1.7$ is connected to the limitation of control as demonstrated with the synthetic data in §3.1.5. If further accuracy for pressure is required in the far field, one may require additional P_{true} to be made available from sensors. It is also worth noting that in the far field, one may also use approximations for pressure such as those given by Antonia *et al.* (1990) [4], provided that the Reynolds shear stress term $\overline{uv}$ decays to zero.

In order to further investigate the regions over which C_d estimate is reasonably good and for those where it shows large deviations, two CV with different heights $H^* = 1.4$ and $H^* = 3$ are selected based on the observations from figure 3.10b and correspond to the former and latter regions respectively. The choice of CV and the corresponding C_d error estimate are presented in figures 3.11a and 3.11b respectively. It is seen that the pressure field without any corrections, introduces large errors in C_d estimates while the CV size extends far from the body ($H^* = 3$), also observed in figure 3.10b. As discussed in §3.1.5, one of the reasons for the high-error level can be due to the derivative effect [56] which subsequently affects the estimation of velocity gradients in the source term and consequently propagates to the pressure field [117]. Also, the equation for C_d (3.34) is derived such that the momentum on the upstream inlet side is approximated using the momentum flux along the lateral side and the outlet such that the mass is conserved (see equation (3.33)). This implies that mass imbalance which may be caused from three-dimensional flow features, statistical convergence issues, experimental errors etc. can lead to an erroneous C_d estimate (see [103] for instance). For the experimental case prior to the application of pressure correction schemes, the residual of the mass balance is found to be 4% for a CV of size $H^* = 3$. Therefore, the corrupt C_d estimate observed for '*Original*' in figure 3.11b is a combined effect resulting from experimental errors, imbalance of mass and corrupted pressure field.

According to Pan *et al.*[117], the error contribution from the source term is higher

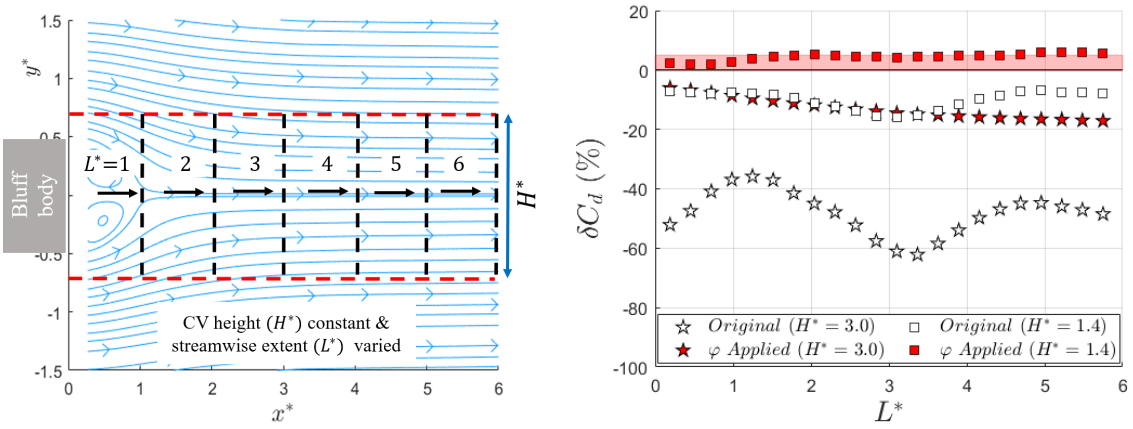

(a) (b)

Figure 3.11: Choice of CV size for computation of C_d (a) and C_d computed with a constant CV inlet height H^* and a varying outlet location L^* (b). The red and black dashed line in (a) represent the extent of H^* and L^* respectively.

with a larger domain area, where the area is normalised by the body height. The non-dimensional area of the domain used for pressure estimation in this study corresponds to $A^* \approx 18$ implying a higher error contribution from the source term. Further, the aspect ratio in this study corresponds to $\alpha \approx 0.5$ deviating from the recommended value of 1 by Pan *et al.*[117] and thus increasing the contribution of the Neumann boundary to the error propagation. Therefore, the errors introduced in the 'Original' pressure field arise from the combined effect of source and boundary errors, and are expected to be the principal reasons for the erroneous estimates of C_d observed in figures 3.10b and 3.11b.

The improvement of C_d estimate on implementing pressure correction schemes is especially relevant for the large CV with $H^* = 3$ in figure 3.11b, where the mean error reduction is approximately 35%. As demonstrated in §3.1.5, the limitation of the control is such that the C_d estimate improves only in the region closer to the region where the control is applied. Further, the streamlines in figure 3.11a indicate almost free-stream conditions when moving away from the body. This implies lesser velocity gradients and consequently reduces the expected errors in the Neumann inlet boundary[117]. Thus additional measurements P_{true} are not necessary in such far regions. Therefore, a good C_d approximation within 10% error is observed although the CV extent is farther downstream from the control applied region.

For a mean flow around a bluff body, the near wake which comprises of the entire recirculation region [202] is of fundamental importance and is of particular interest to understand the interplay between the recirculation zone and its surrounding environment (see for e.g: [18]). Figure 3.11b shows the errors in C_d estimate with a smaller CV of size $H^* = 1.4$. In this case, it is worth noting that the lateral sides of the CV approximately runs through the shear layer emanating from the body base. Although this region is highly susceptible to measurement errors [137, 201], a reasonably good C_d estimate is obtained prior to the correction schemes, especially close to the body base within $L^* = 1$. However, the error is not consistent and the maximum deviation reaches close to 20%. On implementation of pressure corrections, the C_d estimated with the smaller CV ($H^* = 1.4$) shows good agreement, especially closer to the body base where the control is applied.The deviations remain within the shaded region with slight deviations observed

further downstream. But, the maximum error remains approximately within 6%. The obvious reason for this slight deviation is the limitation of the control as demonstrated in §3.1.5.

As the uncertainties in C_d can be attributed both to the velocity and pressure field, it is difficult to quantify the error levels in pressure field through C_d comparisons. Nevertheless, the drag estimate is observed to be significantly improved on application of pressure corrections schemes, shown in figures 3.10b and 3.11b. The control (φ) acts not only to limit the errors propagated from the boundary where P_{true} is available but also corrects the nearby regions as demonstrated with synthetic data (see §3.1.5). A better estimate in near-wake pressure is obtained and is reflected in the C_d computed in the near wake. The source term indirectly corrected by the smooth divergence free velocity fields reduces the global uncertainties in the pressure field and is reflected through a relatively better estimate in C_d with the larger H^*. The limitation of the control is the reason for a relatively higher error level with a large H^* compared to the smaller CV as shown in figure 3.10b. Better accuracy may be achievable using additional P_{true}, but the optimal locations and numbers of probe has to be determined in order to design the experiment in such a way that an accurate whole field pressure is obtained with minimal flow intrusion and efforts. This remains a topic for further investigations.

The near wake of the bluff body being of considerable importance, improved accuracy must be achieved compared to the far field and is attainable using the conveniently available base pressure measurements as demonstrated in the previous discussions (see figure 3.10b and 3.11b). As such, additional P_{true} may be avoided, but becomes mandatory if good accuracy is desired over the far field. One may also use Bernoulli's equation to approximate P_{true} on the boundary to improve far-field pressure estimate but this estimate has to be computed along a streamline and the computational domain deformed to follow this particular streamline.

3.1.8 Conclusion

In this section, a method is derived for accurate total pressure reconstructions combining intrusive and non-intrusive sparse pressure sensors which can be included in an experimental setup at a minor cost. A Helmholtz-based divergence correction for two-dimensional flows is also applied. The methodology is validated using a noisy synthetic pressure field in the wake of a D-shaped bluff body. The results show more than 70% reduction in error level by using only the virtual pressure measurements from the body base. The control approach shows less sensitivity to different types of noise making it a robust error minimizer. Further, the approach is implemented on a matching PIV wind-tunnel experiment data, comparing the drag estimates from two independent methods. In particular, the drag coefficient is estimated with less than 5% error when using appropriate control volumes. The results show that the divergence correction combined with the optimal control approach using only sparse pressure sensors from pressure taps located at the bluff body base, provides an accurate pressure field.

It is worth noting that the present approach could become particularly relevant for the estimation of pressure in a time-dependent setting. While the present analysis is focused on steady mean flows, allowing for a first evaluation of the technique with a minimum number of assumptions, the method naturally extends to time-dependent flows, provided that the flow acceleration can be obtained. Methods including quadruple laser exposure technique [95] might strongly benefit from the present method where noise from the

boundaries is expected to increase compared to well-converged mean flows. As such, the optimal control method can be adapted to the omnidirectional integration method where the control would have to be adapted to Dirichlet-type boundary conditions, providing a minimizer for instantaneous pressure measurements. The CFD-based data assimilation methods [93, 68] to retrieve the instantaneous pressure field presents an interesting alternative, but is probably more suitable for off-line applications. The present method can be applied for real time applications since the Poisson equation can be solved within 0.5 seconds on a single core machine, for instance using optical flow techniques that allow real time planar velocity measurements (see [58]). Finally, the present method is independent of the way of solving the Poisson problem and therefore applies to most solvers already proposed in the literature (see for instance [124] for an application in the case of the near wake behind an Ahmed Body).

Chapter 4

Mean flow characterisation and the driving mechanism of mean drag

Introduction

The chapter is organised into two parts. The objective of the first part is to present the main features of the bluff body wake under study. The second part of the chapter focuses on understanding the mechanism that drives the drag in the very near wake.The flows shall be differentiated by the Reynolds number based on the body height $Re_h = U_{in}h/\nu$, varied in the range specified in the details of the Experiments. The baseline flow without any external perturbations such as free-stream turbulence shall be presented first, serving as a reference case.

4.1 Characterisation of the mean flow - Introduction

The flow meets the body at it's leading edge where it separates and reattaches further downstream developing into a boundary layer. Further, the developing boundary layer separates at the trailing edge of the body due to it's sharp edge. The separated flow is principally characterized by the free shear layer that develops on either sides of the body and the region of recirculating flow that is enclosed by these shear layers.

4.1.1 Boundary layer

It is well understood that the nature of the boundary layer at separation forms the inlet conditions to the wake. The state of the boundary layer and it's thickness has been reported to significantly influences the near wake topology. For example, [159] reports a decrease in the vortex shedding frequency and a widening of the corresponding spectrum when the boundary layer changes it's state from laminar to turbulent. A thick turbulent boundary layer is seen to increase the organization of the shed vortices, decrease it's strength and lead to a reduction in the base pressure drag [48]. With the decrease in thickness of the turbulent boundary layer, the effective diffusion length between the boundary layers on either sides of the body at separation decreases, shrinking the wake and increasing the base pressure [148]. Whereas [181] reports a higher drag for the thinner laminar boundary layer due to a larger mean velocity gradient $\partial U/\partial y$ in the ensuing shear layer.

In order to reduce the complexity of the developing wake and to have one less parameter, the state of the boundary layer is maintained such that the transition to turbulence is avoided as best as possible. For the bluff body of height $h = 40\ mm$ and a length-wise aspect ratio of 4, the boundary layer developing over it's surface can be compared to the case of the flat plate. Since the background turbulence level is very low $< 0.1\%$, the state of the boundary layer can simply be understood by considering the critical Reynolds number, based on the streamwise distance from the leading edge, $Re_{x_{tr}}$ of the flat plate(see [152]). For the experiments conducted without the addition of free-stream turbulence, the Re_x at separation, for the bluff body, remains far from the critical Reynolds number $Re_{x_{tr}}$. This holds even for the highest Re_h tested without FST.

However, the addition of FST complicates the determination of the state of the boundary layer and it's transition location without any boundary layer measurements. A satisfactory and reliable prediction of the transition location of the boundary layer in the presence of free-stream turbulence is a question yet to be answered, due to it's intrinsic complex nature (see [57, 151] and the references therein). As briefed in [57], the complex nature is due to the difference in the forcing by the decaying turbulence, with growing length-scales, on the growing boundary layer. The integral length scales of the incoming turbulent flow has been shown to advance or progress the transition location depending on the level of the turbulence intensity present (see for example [81, 57, 151]). The empirical model proposed by [57] to predict the onset of transition of boundary layer in the presence of free-stream turbulence, with the knowledge of only three parameters, i.e the integral length-scale and the turbulent intensity at the leading edge, though developed at low $Re_{L_x} = U_{in}L_x/\nu$, tells us that the maximum Re_x attainable in the case of our body surface is far from the transition Reynolds number $Re_{x_{tr}}$. This being the case, the boundary layer developing over the body-surface is expected to be laminar in the entire range of Re_h in the presence of free stream turbulence.

4.1.2 Mean velocity fields - Baseline flow

Figure 4.1 shows the fields of streamwise and transverse velocity fields of the baseline flow at the lowest Re_h. Here, the term 'Baseline flow' shall be used to refer to the cases of bluff body flow without the addition of FST. The flow being almost symmetric, only one of the symmetric planes are shown. The superscript asterisk is used to denote normalization using the inlet velocity U_{in}, body height h and the density ρ wherever applicable. The boundary layer after separation develops into a free-shear layer whose upper limit is demarcated by a black solid line defined as $U^*(x^*, y^*_{sl}) = 0.95U^*_{max}(x^*)$. The colormap in figure 4.1 for the streamwise velocity U^* shows a strong shear that exists close to the separation which then weakens on moving downstream. The shear layer from both the sides of the bluff body grows by entraining fluid from the external flow and merges downstream marking the end of the recirculating flow region enclosed by it. The growth of shear layer by entrainment can be visually seen in the velocity field in figure 4.1 where there is a strong positive V^* oriented towards the geometric wake centerline of $y^* = 0$. The merging occurs in figure 4.1 where the streamlines, that separates the recirculating flow from the external flow, converges towards the wake interior after separation. The dashed line in figure 4.1 demarcates a portion of the recirculating flow region containing negative streamwise velocities and is defined as the isoline of $U^* = 0$, following the convention

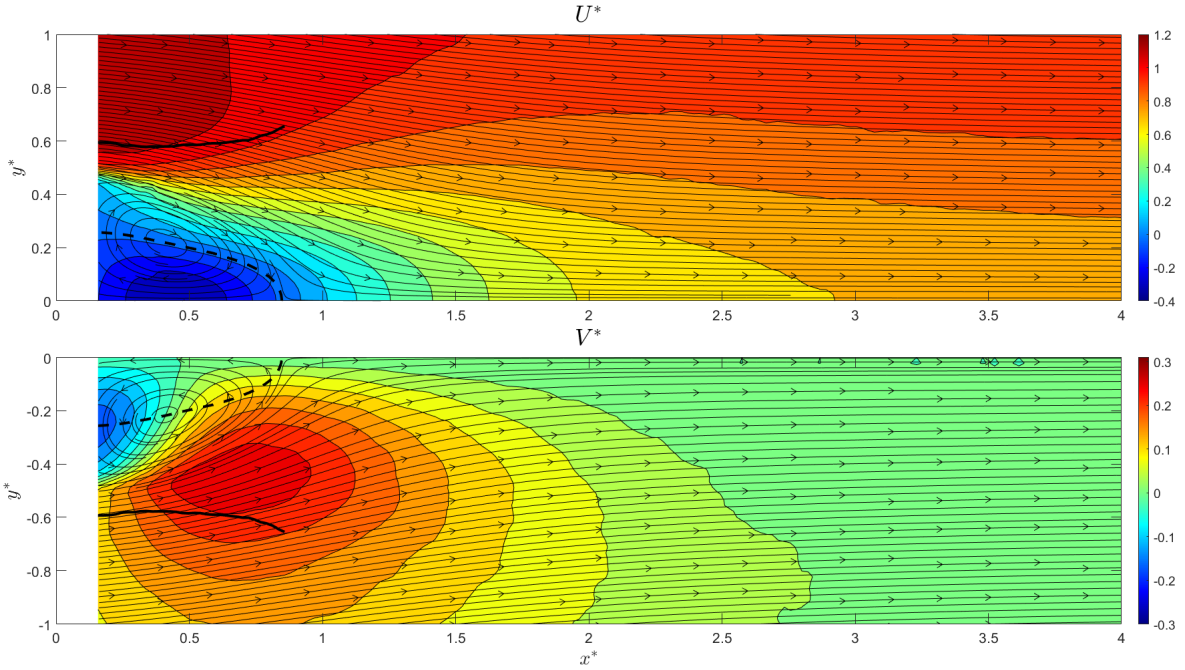

Figure 4.1: The streamwise mean velocity U^* (top) and the transverse mean velocity V^* (bottom) at $Re_h \approx 28 \times 10^4$. The superscript asterisk * denotes normalization by the inlet velocity U_{in} and the body height h.

used by [165]. The minimum of the streamwise velocity U^* exists within the wake bubble along the geometric wake centerline which then decays downstream represented by the changing colors in figure 4.1. Typically, in the far wake, the mean wake is represented by a function,

$$f(\zeta) = \frac{U_{max}(x) - U(x,y)}{U_s(x)} = \frac{U_{max}(x) - U(x,y)}{U_{max}(x,y) - U(x,0)}, \tag{4.1}$$

where $U(x,0)$ and $U_s(x)$ represents the minimum steam-wise velocity along the geometric centerline of a symmetric wake. The variable $\zeta = {}^{y}/_{y_\delta}$ in equation (4.1) is the transverse direction normalized by the wake width y_δ, where wake width is defined such that $f(\pm 1) = 0.5$ (see [131]).

Figure 4.2b shows the decay of the velocity deficit along the streamwise direction. In the region very close to the body $x^* < 1$, the velocity deficit increases reaching a peak value close to the center of the wake bubble defined by $U = 0$. Most of the contribution to the shape of the evolution of velocity deficit comes from the minimum streamwise velocity $U^*(x^*, 0)$, shown in figure 4.2, at the geometric wake centerline. The magnitude of $U_{max}(x^*)$ reaches a maximum value at separation, due to the blockage offered by the body to the flow, which then relaxes and tends to the free-stream velocity as the flow decelerates downstream. The minimum velocity in the wake is found to be set by the Re_h in the current study and remains at $U^*_{min} \approx -0.308 \pm 0.0058$ as shown in figure 4.2a. The velocity gradient in the wake can be said to scale as $\partial U^* \sim U^*_s$. Then, the velocity deficit is scaled by it's maximum value which occurs along the geometric centerline of a symmetric wake denoted by $U^*_{s_{max}}$ and it scales as $U^*_{s_{max}} \sim U^*_{sl} - U^*_{min}$, where $U^*_{max} \sim U^*_{sl}$ and U^*_{sl} denotes the maximum streamwise velocity that occurs at the edge of the shear layer at separation.

After reaching the peak the velocity deficit undergoes a fast decay which exists at $0.5 \leq x^* \leq 2$ in figure 4.2b. This region is found to evolve as $U^*_s(x^*) \sim ce^{ax^*}$, showing good

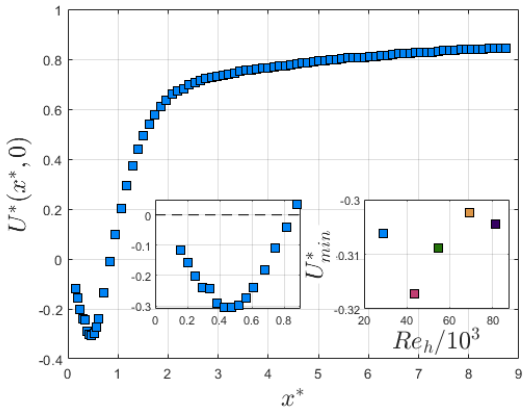

(a) Evolution of the streamwise velocity along the wake centerline. The inset on the left and right shows a close-up of the centerline streamwise velocity close to the body within the recirculating flow region and the variation of the it's peak value with Re_h.

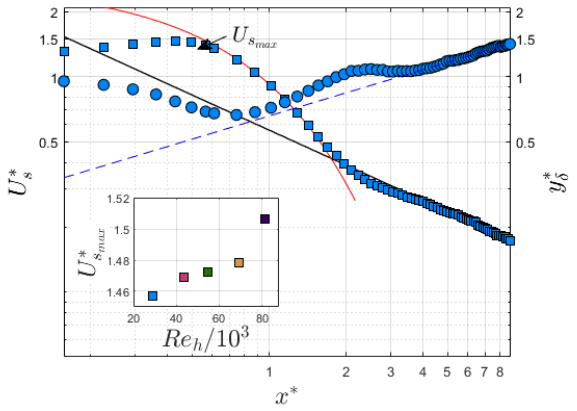

(b) The decay of mean velocity deficit in the wake represented by square symbols and the evolution of wake width represented by circular symbols. The straight lines in the log plot represents fits of the form $y = A(x - x_0)^n$ whereas the curved line is of the form $y = ce^{ax}$.

Figure 4.2

agreement fit to the data with an error less than 0.3% for all cases of Re_h, represented by red solid line in figure 4.2b. The constant a is negative for a decaying wake. The decay rate of the velocity deficit in the region scales as $dU^*_s(x^*)/dx^* \sim c_1 e^{ax^*}$. The coefficient c_1 is found to decrease with the Re_h implying a faster decay of the velocity deficit in this region. The entrainment hypothesis introduced by G.I. Taylor in this context relates the mean flow towards the wake to the characteristic velocity scale of the wake denoted by U_s here. This is to say that the increase in $U^*_{s_{max}}$ with Re_h is an indication of increased transport of mass/mean-momentum towards the wake centerline.

When the velocity deficit has decayed sufficiently such that the ratio U^*_s/U^*_{max} tends to zero, the wake is said to reach a self-similar state, depending on the wake-generator, and can be described simply by the velocity scale $U^*_s(x)$ and the length-scale y^*_δ (see Pope [131] for details).Further, achieving self-similarity has the consequence that the product $U_s(x)y_\delta(x)$ be independent of x in-order for the momentum deficit to be conserved, displaying a growth rate of x^n with $n = 0.5$ and $n = -0.5$ for $y_\delta(x)$ and $U_s(x)$ respectively [131]. Within the streamwise extent of our domain, this product was not found to be constant and decreased with the streamwise distance. Nevertheless, the curve-fit of the form $y = A(x - x_0)^n$ was performed on the evolution of wake-width and the velocity decay, sufficiently far from the body, with the starting point selected by specifying a threshold for $\frac{d}{dx}(U_s(x)y_\delta(x))$. The exponents so obtained are $n = -0.543 \pm 0.0175$ and $n = 0.321 \pm 0.0455$, for the decay of the velocity deficit and the evolution of wake-width respectively, which are far from the theoretical predictions. It is to be noted that for a robust fit of the form $y = A(x - x_0)^n$, the virtual origin x_0 set to zero.

Mean shear layer

The laminar boundary layer developing over the surface of the body separates at the base of the body which then evolves as a free shear layer. The upper boundary of the shear layer is represented by a black solid line in figure 4.1. It is characterized by a region of intense transverse gradient of mean streamwise velocity ($\partial U/\partial y$) and develops between the external flow and a recirculating flow region. The figure 4.3a shows the profile of mean streamwise velocity close to the separation point. The dividing streamline $\psi = 0$ passes approximately through the center of the region of intense mean shear ($\partial U/\partial y$), and this region is seen to overlap with a portion of the recirculating flow region. The recirculating flow region consists of the backflow region, where the streamwise velocity is negative, and the portion immediately above bounded by the dividing streamline $\psi = 0$. From the figure 4.3a, the lower velocity side of the shear layer, below $\psi = 0$ line, has a direct influence on the recirculating flow whereas the higher velocity side of the mean shear layer is primarily concerned about the interaction with the external flow.

The characteristics of the mean free-shear layer is significantly different from it's classical counterpart 'the mixing layer', where the development of the thickness of the latter is found to be linear with the downstream distance (see for eg.: [21]) whereas it is non-linear for the former. Numerous differences were noted in other studies as well (see for eg.: [33]). Since the intention is not to compare but to say that the separated shear layer in the wake of the bluff body is significantly different from it's classical counterpart, due to the complex nature of interactions with the recirculating flow region and the separated shear layer that develops from the diametrically opposite side of the bluff body on the trailing edge, further discussions on mixing layer is avoided.

Following [41], the measure of the shear layer thickness is typically computed using the vorticity thickness defined as,

$$\delta_w(x) = U_s(x)/max\left(|\partial U/\partial y|\right), \tag{4.2}$$

Note that equation (4.2) takes into consideration the back-flow in the near wake (see figure 4.1 and 4.3a). The evolution of vorticity thickness is shown in figure 4.3b, until the streamwise location of recirculation region where the mean shear layers from the top and bottom trailing edges merge together. From figure 4.3b, at-least three regions can be readily identified. The first region close to the body between $0 \leq x^* \leq 0.1$, where the vorticity thickness remains roughly a constant, followed by the second region where the thickness evolves exponentially i.e. $\delta_w^* \sim exp(cx + d)$, and connects the third region where the thickness evolves in a logarithmic fashion i.e., $\delta_w^* \sim log(ax^{*b})$. Most of the evolution in this region is dominated by the exponential growth i.e. a region covering $0.05 \leq x^* \leq 0.45$, after which the log-growth, covering a relatively shorter domain $0.45 \leq x^* \leq 0.65$, takes over before the shear layers merge. The growth of the shear layer in the log region i.e., $d\delta_w^*/d\left(log(x^*)\right) = b$ is found to decrease with Re_h A potential length-scale which marks the transition from the first to the third region, denoted by l_p^* in figure 4.3b, though not monotonically, is found to increase with the Re_h (see inset of figure 4.3b).

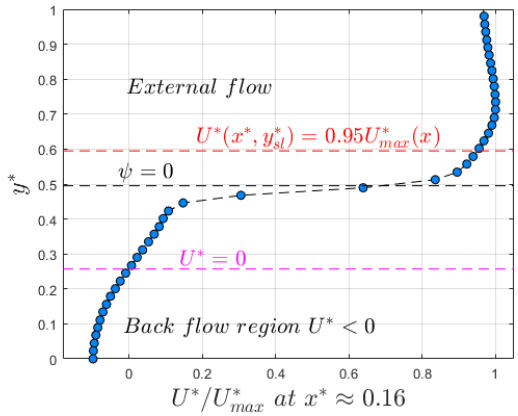

(a) The profile of streamwise velocity U close to the separation at $x^* \approx 0.16$, normalized by it's maximum value.

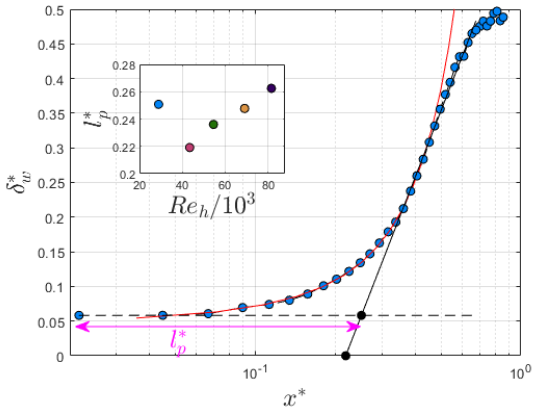

(b) Evolution of vorticity thickness along the streamwise direction.

Figure 4.3

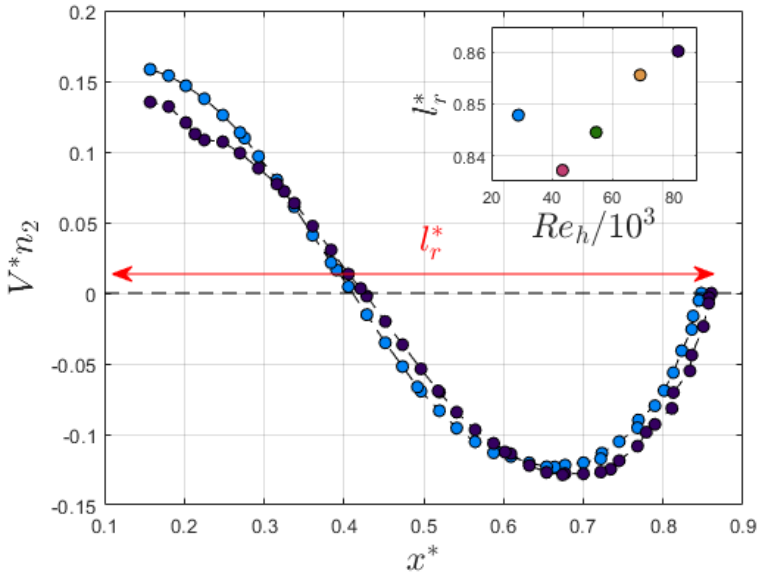

Figure 4.4: Evolution of local mass flux along the recirculating flow region interface (rri) defined by the isoline $U = 0$. The *rri* is taken at the upper half of the symmetric wake.

Recirculating flow region

The mean shear layer formed after the separation of flow at the trailing edge of the body encloses a region of low momentum where the flow recirculates. It is characterized by a nearly constant pressure in the transverse direction and it is within this region that the minimum wake-pressure can be found [202]. The extent of the recirculating flow region is denoted by l^*_r and has been the subject of several studies in the past because of it's observed variation with the drag (See for example [146, 120, 99, 147]). For example, Roshko (1993) [147] proposed a model linking the increase in bubble length to a drag decrease, based on the streamwise momentum budget along the wake bubble enclosed by the dividing or zero streamline. A recent study on the sensitivity of the drag to modifications

in the near wake by means of control cylinder by Parezanovic (2012) [120] reports the inverse relationship between drag and the recirculation region length. Similar conclusion is also reported by Mariotti (2015) [99] that a direct correlation between the length of the recirculating flow region and the base pressure drag. Further, l_r has been established as an important length-scale which scales the evolution of shear layer [165] or the evolution of quantities in the wake [109, 195]. For example, Wang *et al.* (2019) [195] was able to successfully scale the evolution of velocity deficit and the wake width of bluff bodies with varying geometries.

Generally, the recirculating flow region is defined in two ways. The first one considers the entire recirculating flow region and is defined by the area enclosed by the dividing streamline or by stream function $\psi = 0$ [13, 109]. The second manner is simpler to implement than the first and is defined as the area enclosed by the isoline of zero mean streamwise velocity $U = 0$ [109, 165]. The second definition does not completely enclose the recirculating flow but captures only the back-flow region where the mean streamwise velocity is negative.

Closer to the body, from figure 4.3a, the lower velocity side of the shear layer overlaps with a portion of the recirculating flow region. The former is known to influence the properties of the latter (see [165] and references therein). Figure 4.4 shows the evolution of local mass flux $\mathbf{U} \cdot n$, where the local normal n is obtained from the co-ordinates of the recirculating flow region interface (rri) defined by the isoline $U = 0$. The extent of the recirculation region is denoted by a length-scale l_r^*. The negative mass flux indicates mass entering the recirculation region whereas the positive indicates mass exit. The region of mass exit from the wake bubble is characterized by a negative vertical velocity V^* in figure 4.1 oriented away from the geometric wake centerline. At equilibrium, the mass that enters the recirculation region is the same as the mass that exits the recirculating flow region and hence conserving it [34]. This is not completely evident from figure 4.4 due to the missing data very near to the wall. It is verified that the mass that enters the rri is then completely balanced by the mass that exits through a portion of the rri close to the body and through the inlet side of the control volume bounded by rri. The value of l_r^* observed in the range $0.83 \leq l_r^* \leq 0.865$ agrees well with the $l_r^* = 0.82 \pm 0.04$ reported in the experiments of [120]. It increases with Re_h except for the lowest Re_h, shown in the inset of figure 4.4.This trend is similar to that displayed by l_p^* in the insets of figure 4.3b, indicating a possible link between them, which will be described later in the chapter 6.

4.1.3 Reynolds stress fields - Baseline flow

Figures 4.5 and 4.6 shows the Reynolds stress fields for the lowest Re_h in case of baseline flow fields. The Reynolds normal stress $\overline{u'^2}^*$ field in figure 4.5 displays a two lobed structure at either sides of the geometric wake centerline reaching a peak of approximately 0.15 at $y^* \approx \pm 0.3$ and are symmetric. Most of the $\overline{u'^2}^*$ is contained within the upper limit of the mean shear layer, demarcated by the black solid line, and the mean rri, demarcated by the black discontinuous line. The peak of $\overline{u'^2}^*$ is contained within the recirculating flow region demarcated by the dividing stream line ($\psi = 0$).

The Reynolds shear stress in figure 4.6a is largely composed of two lobe shaped structures and are anti-symmetric. Considering the upper wake, i.e $y^* \geq 0$, the negative peak

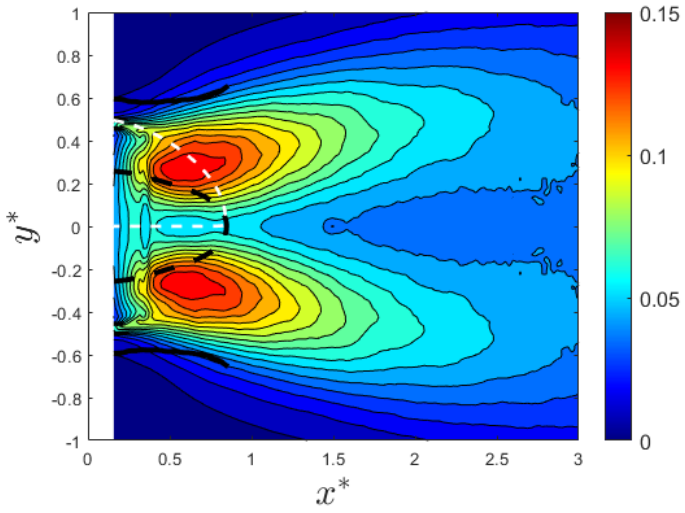

Figure 4.5: Streamwise Reynolds stress field for $Re_h \approx 2.8 \times 10^4$. The black solid line, the discontinuous black line and the discontinuous white denotes the upper edge of the shear layer, the rri and the dividing stream line ($\psi = 0$) respectively.

of $\overline{u'v'}^*$ is reached outside of the recirculating flow region, whereas it's positive peak is contained within the back-flow region. Unlike $\overline{u'^2}^*$, $\overline{u'v'}^*$ seems to be completely contained within the mean shear layer and due to a symmetric flow, it is zero along the geometric wake centerline ($y^* = 0$). Overall, the structure of the Reynolds stress fields are similar to that of the cylinder wake reported in [29]. However, the lobe shaped structures of $\overline{u'^2}^*$ and $\overline{u'v'}^*$ are oriented towards the wake centerline in [29] whereas it seems to orient away from the wake, probably due to the difference in nature of the separation in both the flows. The intensity reported in [29] is even higher than that of our case, for example the maximum value of $\overline{u'^2}^*$ in [29] reaches approximately as high as 0.35, whereas it is limited to approximately 0.15 in our case (from figure 4.5) . It is to be noted that the our present study is limited to $Re_h < 10^5$ and the blockage ratio is much lesser than that reported in [29], probable cause of decreased intensities of Reynolds stresses.

The Reynolds vertical normal stress $\overline{v'^2}^*$ in figure 4.6b displays a single lobed structure, reaching peak values near the end of the recirculating flow region at the geometric wake centerline. Note that it's peak value is significantly higher than that of $\overline{u'^2}^*$. Figure 4.7 shows the turbulent kinetic energy, defined as $k = \left(\overline{u'^2}^* + \overline{v'^2}^*\right)/2$ displaying a single lobed structure. The peak of k is reached near the end of the recirculating flow region, with $\overline{v'^2}^*$ taking up the dominant role similar to that reported in [193]. Local peaks are observed near the rri and k locally spikes on the dividing streamline. This observation is slightly different to that of the k field in [193], where local peaks in k, close to the body, are observed on the dividing streamline. Figure 4.8 shows the profile of Reynolds normal stresses obtained by PIV as well as Hot wire experiments. Both the hot wire and the PIV measurements are in agreement with each other for $\overline{u'^2}^*$. In case of $\overline{v'^2}^*$, at $x^* \approx 3$, there is a slight disagreement between the hot-wire and PIV measurements with hot-wire measuring approximately 7% lesser value compared to that of the PIV measurement. This is to be expected because of the limited angular sensitivity of the hot-wire in the near wake. From the PIV instantaneous fields, it is seen that the instantaneous flow angles can reach

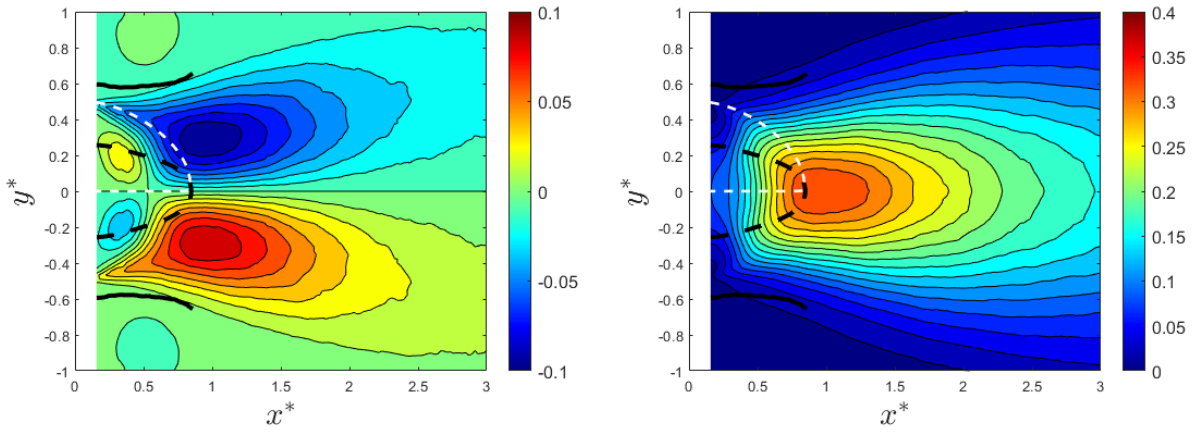

(a) (b)

Figure 4.6: Reynolds stress fields $\overline{u'v'}^*$ (a) and $\overline{v'^2}^*$ (b) for $Re_h \approx 2.8 \times 10^4$.

as high as 80^o at $x^* \approx 3$, whereas the hot-wire saturates approximately between $\pm 30^o$ and $\pm 35^o$, and hence the discrepency in the $\overline{v'^2}^*$ values.

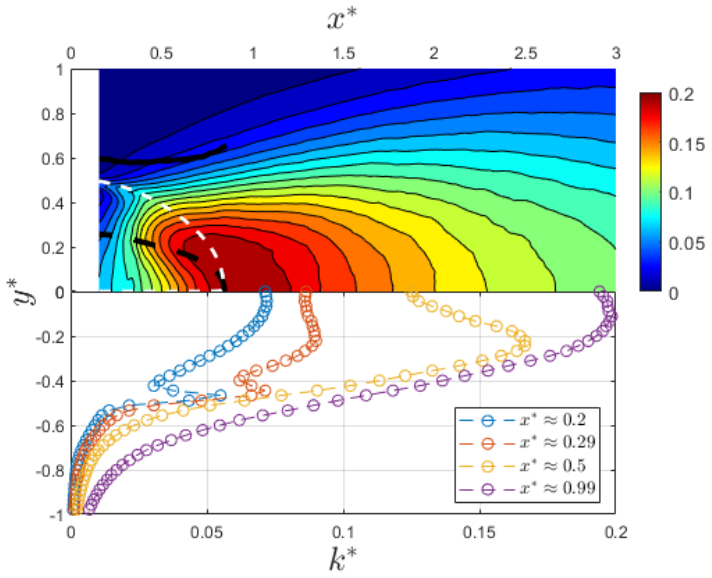

Figure 4.7: Turbulent kinetic energy field, and profiles at various downstream locations in the wake for $Re_h \approx 2.8 \times 10^4$.

Finally, the figure 4.9 shows the field of production of turbulent kinetic energy defined as $\mathcal{P}_k = -\overline{u_i u_j}\frac{\partial U_i}{\partial x_j}$. The general structure is similar to that of the circular cylinder wake in [29], however the intensities differ in magnitude. Near the body, it peaks close to the center of the shear layer at the dividing streamline, and remains within the vicinity of the dividing streamline further downstream. The peak of the production occurs close to the body, due to the intense mean shear, and close to the end of the recirculation region due to the intense $\overline{v'^2}^*$ acting along with the vertical velocity gradient $\partial V/\partial y$. The production is negligible in the first half of the recirculating flow region, approximately between $0 \leq x^* \leq 0.5$, which then rises to its peak value in the second half. It is interesting to note that the upper extent of the shear layer correctly wraps around the

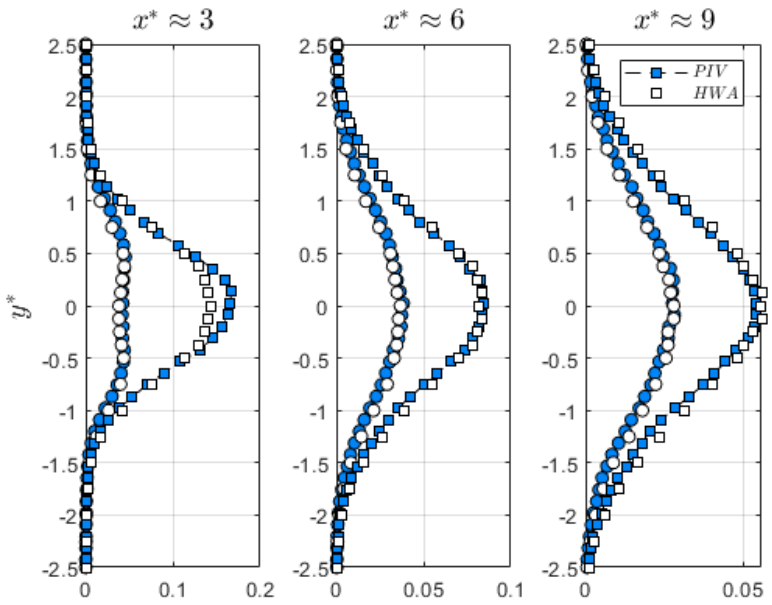

Figure 4.8: Comparison of Reynolds normal stresses, $\overline{u'^2}^*$ (circles) and $\overline{v'^2}^*$ (squares) at various downstream locations in the wake, measured by PIV and hot-wire experiments for $Re_h \approx 2.8 \times 10^4$.

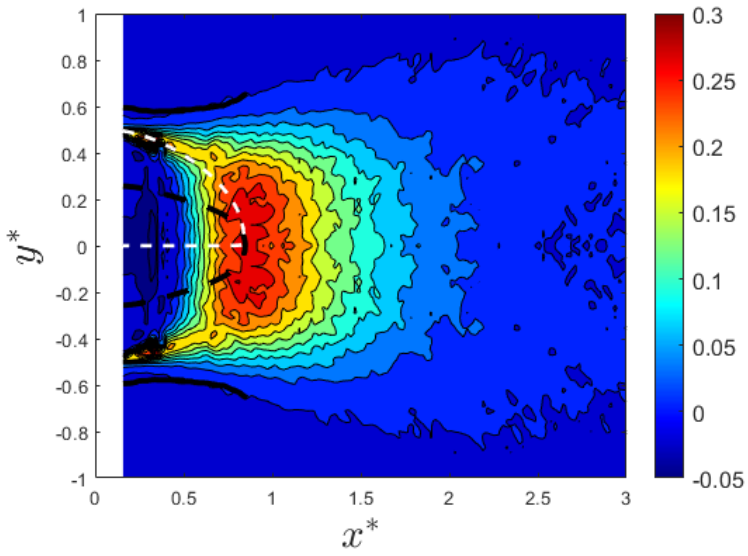

Figure 4.9: Field of turbulent kinetic energy production for $Re_h \approx 2.8 \times 10^4$.

production in the near wake. However, certain amount of k^* is leaked out of it, suggesting that the upper extent, defined only based on the mean streamwise velocity profile, may not be considered as an interface that separates the external irrotational flow from the wake.

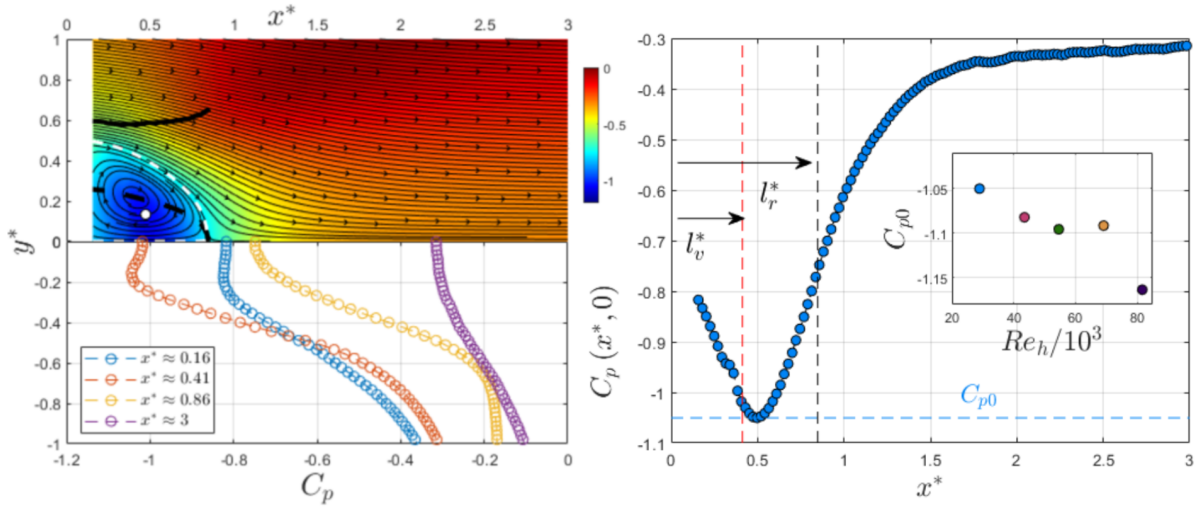

Figure 4.10: $C_p(x^*, y^*)$ field at $Re_h \approx 2.8 \times 10^4$ (left) and its evolution along $y^* \approx 0$ (right). C_{p0} denotes the minimum C_p along $y^* \approx 0$. l_r^* and l_v^* represents the extent of the recirculation region and center of the recirculating vortex respectively.

4.1.4 Mean pressure field

Pressure is an important quantity relating to the dynamics of fluid and to the force exerted by it on a body [66, 15, 191, 103, 190] and its importance is stressed in Chapter 3 briefly reviewing the studies in this regard or the alternative approaches to circumvent it's requirement. The following section however, discusses on the features of the wake pressure field estimated using the approach discussed in Chapter 3. Figure 4.10 shows the coefficient of the mean pressure field. The profiles at $x^* \approx 0.16, 0.41, 0.86, 3$ corresponds to the location close to the body, the center of the recirculating flow vortex, end of the recirculation region and farther downstream. Globally, the minimum pressure region in the wake is localised within the recirculation region with its global minima indicated by a solid white circle in figure 4.10. Close to the point of separation at $y^* \geq 0.5$, one may see an adverse pressure gradient, i.e, the C_p rises, causing the flow to decelerate and expand downstream to fill the space, after separation. As one moves towards the wake along the vertical direction, i.e $y^* < 0.5$, the pressure dips to a lower value, following which it starts to rise, as shown in figure 4.10.

Along the geometric wake centerline, the C_p with a value of -0.8 at the body base dips to a minimum of approximately -1.05 close to the streamwise location of the recirculating vortex center. The pressure rises gradually after reaching a minimum along the centerline in figure 4.10. The growth rate changes indicated by an inflection point close to l_r, which marks the decay of pressure gradient and hence the flow recovers. Farther downstream, after $x^* \approx 1.5$, the pressure recovery is seen to be considerably slower. Further, within the back flow region the pressure remains roughly a constant in the vertical direction.

Contributions to the mean pressure

It is already known that the pressure in the far wake can be approximated by the vertical normal Reynolds stress $\overline{v'^2}$, valid only where the Reynolds shear stress is negligible [4, 131]. Recent studies by [26] in the wake of an oscillating airfoil reports that this assumption is indeed true in the near wake. This is verified in figure 4.11 at various loca-

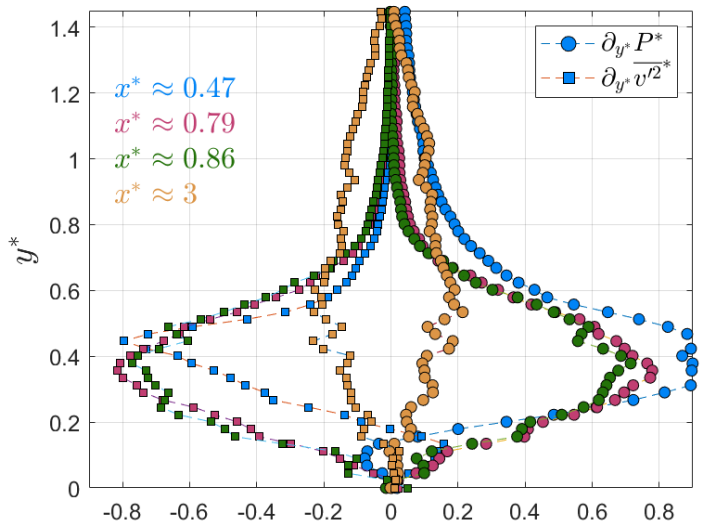

Figure 4.11: Verifying the balance of pressure at various downstream locations such as at the streamwise location of C_{p0}, close to l_r^* at $x^* \approx 0.79$, at $x^* \approx l_r^*$ and at $x^* \approx 3$.

tions in the near wake and farther downstream, where except at the streamwise location of C_{p0}, the pressure is balanced by $\overline{v'^2}$. Then, near and beyond l_r^* it follows that,

$$\partial_{y^*} P^* \approx -\partial_{y^*} \overline{v'^2}^*. \tag{4.3}$$

Equation (4.3) when integrated from $y^* = 0$ to ∞ gives the established relation [4, 131],

$$P^* \approx -\left(\overline{v'^2}^* - \overline{v'^2}^*_{FST}\right) + P^*_{FS}. \tag{4.4}$$

The subscript FS and FST denotes free-stream condition and free stream turbulence respectively, where, $P^*_{FS} \approx \left(1 - U^*_{FS} + \Delta\overline{u'^2}^*_{FS}\right)/2$, from the Bernoulli's equation. Equation (4.4) does not hold very close to the body and hence a different approach is necessary.

The mean flow content of the Poisson equation for pressure, using the divergence condition of the two dimensional velocity fields, may be simplified to,

$$\Delta P^* = \underbrace{-2\left(\frac{\partial U^{*\,2}}{\partial x^*} + \frac{\partial V^*}{\partial x^*}\frac{\partial U^*}{\partial y^*}\right)}_{\Delta P^*_M} \underbrace{-\frac{\partial^2(\overline{u'^2}^*)}{\partial x^{*2}}}_{\Delta P^*_{uu}} \underbrace{-\frac{\partial^2(\overline{v'^2}^*)}{\partial y^{*2}}}_{\Delta P^*_{vv}} \underbrace{-2\frac{\partial^2(\overline{u'v'}^*)}{\partial x^* \partial y^*}}_{\Delta P^*_{uv}}, \tag{4.5}$$

meaning that the mean flow contribution to the mean pressure is caused by the mean velocity gradients. Along the wake centerline owing to the wake symmetry, the mean strain terms are zero. The streamwise velocity exhibits a local minima along the centerline (figure 4.2a) and roughly coincides with the local minima of the pressure (figure 4.10), such that $(\partial U^*/\partial x^*) \approx 0$. Therefore, on the centerline,

$$\Delta P^* \approx -\left\{\partial^2/\partial y^{*2}\left(\overline{v'^2}^*\right) + 2\partial^2/\partial x^* \partial y^*\left(\overline{u'v'}^*\right)\right\}, \tag{4.6}$$

implying that the pressure minima is solely caused by the Reynolds transverse normal and shear stresses. Verifying equation (4.6) is difficult with the experimental data, because of

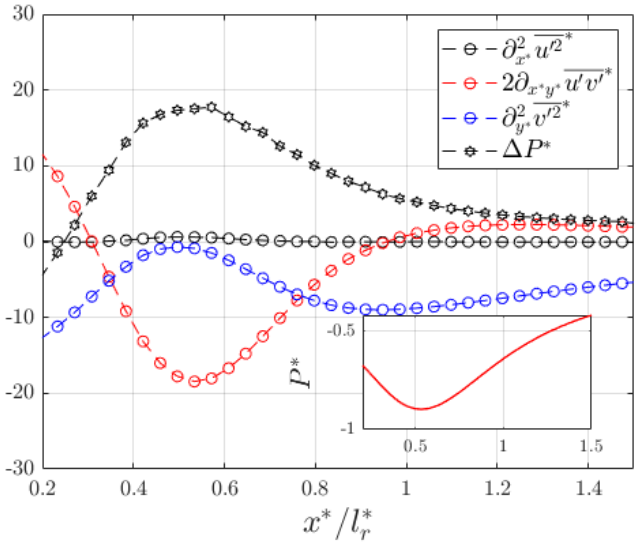

Figure 4.12: Balance of the pressure Poisson equation (4.5) using only the Reynolds stress terms. The inset shows the profile of non-dimensional pressure P^* evolving along the streamwise coordinate normalized by l^*_r.

the second derivative operation amplifying any noise present in the data. Therefore, the synthetic RANS data from Chapter 3 is used in order to qualitatively understand the role of the Reynolds stresses in forming the pressure minima.

Figure 4.12 shows the balance of equation 4.5 using the Reynolds stress terms only. Confirming the assumption near $x^*/l^*_r \approx 0.5$, that $\partial^2/\partial x^{*2}\left(\overline{u'^2}^*\right) \approx 0$, the pressure minima appears to be primarily due to the Reynolds shear stress. From figure 4.6a in the upper half of the wake, the Reynolds shear stress close to the body is positive and implies an out-flux of momentum away from the wake centerline. Moving downstream along the centerline, roughly after the center of the recirculation region, the sign changes implying a mean inward momentum flux due to fluctuations. Moving farther along the centerline, as implied from the inset of figure 4.12, it is $\partial^2_{y^*}P^*$ that becomes important due to the local minima formed by the pressure profile in the vertical direction (see figure 4.10). The role of Reynolds shear stress is non negligible until at least 80% of the recirculating flow region after which it is mostly the Reynolds vertical normal stress that plays a major role as is evident from the figure 4.11.

We may alternatively split the solution of pressure based on the contribution from the mean field and the various Reynolds stress components. The Poisson operator being a linear operator, we may write the solution of pressure as a sum comprising of the mean and the Reynolds stress components as shown in equation (4.5) [131]. The source term is solved with Neumann boundary conditions split in the same manner as equation (4.5). For example, the source term due to mean flow is solved as,

$$\partial^2/\partial x_i^2\left(P^*_M\delta_{ij}\right) = -\partial/\partial x_i\left(\partial/\partial x_j\left(U_iU_j\right)\right), \tag{4.7}$$

with the Neumann boundary condition, $\partial/\partial x_i\left(P^*_M\delta_{ij}\right) = -\partial/\partial x_j\left(U_iU_j\right)$. The constant is eliminated by comparing with P^*. Only the pressure due to the mean flow P^*_M is expected to be non-zero in the free-stream, whereas the constant shift for the pressure due

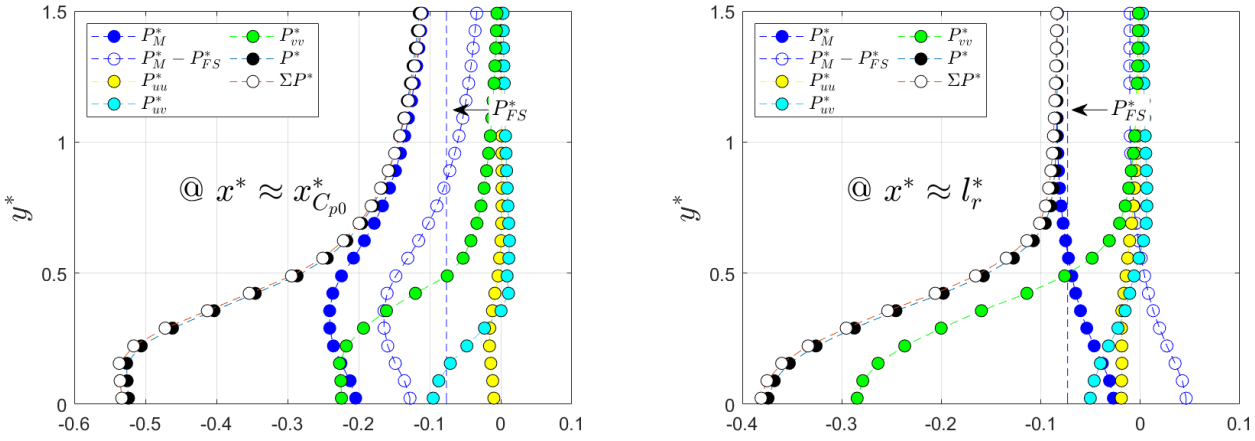

(a) (b)

Figure 4.13: Decomposition of pressure, where $P^*_M, P^*_{uu}, P^*_{uv}, P^*_{vv}, P^*$ and ΣP^* represents the pressure due to mean flow, $\overline{u'^2}^*$, $\overline{u'v'}^*$, $\overline{v'^2}^*$, corrected pressure (from the optimal control algorithm) and the sum $\Sigma P^* = P^*_M + P^*_{uu} + P^*_{uv} + P^*_{vv}$ respectively .

to Reynolds stresses is zero since the Reynolds stresses are zero in the free stream. Figure 4.13 shows the pressure decomposition based on the solution of equation (4.5) at two streamwise locations. As expected, slight differences exist between ΣP^* and P^*. From figure 4.13a, P^*_{FS} representing the free stream pressure causes an overall shift in P^*_M. The dip in P^*_{FS} due to the blockage induced by the body, drives the flow in the free stream and hence is subtracted from P^*_M in order to obtain the contribution from the mean flow deformations to the mean pressure.

At the streamwise location of minimum pressure, most of the integral contribution to the mean pressure comes from $\overline{v'^2}^*$ arising from the cross-stream mixing, followed by the mean-flow deformations $P^*_M - P^*_{FS}$. Moving transversely towards the wake core, the mean flow pressure contribution peaks at the location of maximum mean shear. Within the wake core, most of the pressure profile is due to $\overline{v'^2}^*$, consistent with the observations in figure 4.11. Moving further downstream, at $x^* \approx l^*_r$ in figure 4.13a, the pressure due to mean flow deformations $P^*_M - P^*_{FS}$ tends to increase the pressure P^*. At this location, most of the pressure contribution comes from $\overline{v'^2}^*$, as observed in figure 4.11.

4.1.5 Evolution of pressure and momentum exchange process along the centerline

The evolution of pressure can be understood from the balance of streamwise momentum at the centerline, (see figure 4.14) Note that the source/ sink of momentum in this case is the drag force and it may only appear through a global momentum balance along a control volume enclosing the source/sink of momentum. The balance along the centerline, describes the local momentum exchange process for which the pressure forms the key component and its evolution depends on this exchange process.

The sink of momentum created by the drag force is transported by the terms in the local balance in figure 4.14. The largest contribution to momentum is through the Reynolds

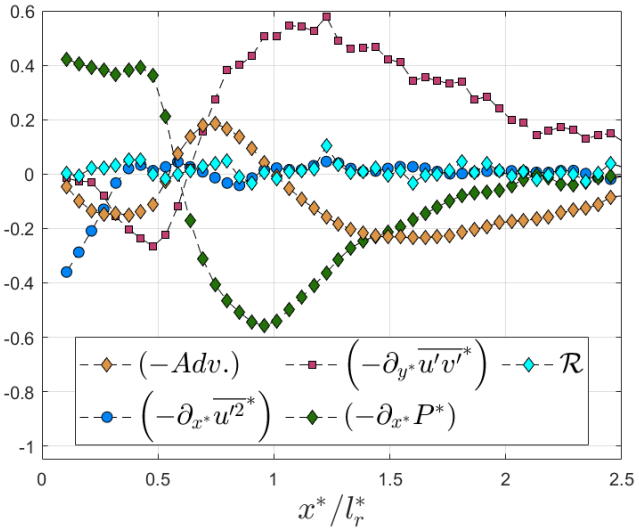

Figure 4.14: Evolution of the streamwise mean momentum budget along the wake centerline, along the streamwise direction scaled by the length of the recirculating flow region.

shear stress gradient, which is indicative of momentum-diffusion by the fluctuations peaking at l_r^* where $U = 0$. The pressure gradient is exactly balanced by the Reynolds shear stress gradient term, i.e,

$$\frac{\partial P^*}{\partial x^*} = -\frac{\partial \overline{u'v'}^*}{\partial y^*}. \tag{4.8}$$

It means that the pressure rise near $x^* \approx l_r^*$ is governed by the intensity of the Reynolds shear stress within the shear layer and reducing its intensity would be a possible strategy to increase l_r^* [165]. The momentum transported by the Reynolds shear stress decreases beyond l_r^*. The role of pressure gradient is dominantly to transfer the mean momentum upstream the recirculation region to the wake. Beyond l_r, the flow evolution is dominated by the Reynolds shear stress gradient which decays slowly compared to the pressure gradient.

From the momentum budget along the wake centerline, the evolution of pressure minima is seen to depend on the momentum transferred by the Reynolds shear stress gradient. The observations suggests that a reduction in the momentum transferred through the Reynolds shear stress gradient, while influencing the properties of the recirculating region may also reduce the amount of momentum fed upstream hence influencing the drag.

4.2 Budget of mean drag

The aerodynamic drag estimated using the integral momentum budget is a useful and a basic approach in order to identify contributions of various terms in the integral momentum transport equation. The budget are performed over three rectangular control volumes, shown in figure 4.15a:

- CV_L - Control volume with lateral sides approaching the free-stream flow,
- CV_S - Control volume with lateral sides close to the body,

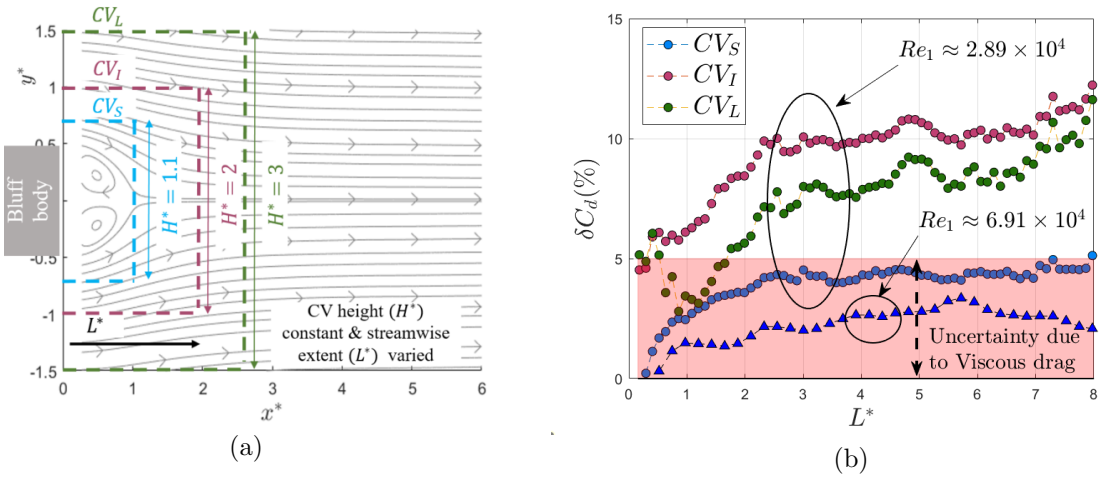

Figure 4.15: Estimate of δC_d (b), refer equation (3.35) in Chapter 3 for the definition, and the schematic of the control volumes (CV) used to estimate it (a). H^* and L^* represents the height and the location of the CV from the body base respectively.

- and CV_I - Control volume with lateral sides in between the CV_L and CV_S, with it's outlet displaced in the streamwise direction with a corresponding estimate of drag and compared with the measured drag is shown in figure 4.15b.

The approach is a useful metric, introduced in chapter 3, to quantify the accuracy of the estimated pressure. As briefed in Chapter 3, the viscous friction drag estimated using a laminar boundary layer accounts for a maximum of 5% of the total drag and hence shown as a shaded region in figure 4.15b corresponds to the viscous drag.

For the three cases of control volume, it is seen that the error in C_d estimate for the smallest control volume remains within the shaded uncertainty region. For the large and the intermediate control volumes, CV_L and CV_I respectively, the error remains roughly within the uncertainty region close to the body. As one moves the CV outlet downstream, the error is seen to increase but remains within 10% until $L* \approx 6$ after which it goes beyond 10%. The method for pressure estimation and the reason for increased error in δC_d with an increasing H^*, is detailed in Chapter 3. The error level remaining within 10% is considered to reflect an accurate pressure estimation and hence $L^* = 6$ is considered to be the limit until which the mean pressure is considered acceptable.

4.2.1 Requirement of flow similarity to perform integral budgets of momentum

In order to compare the integral budget between different flows, the chosen control volume has to be similar or of universal form for all the flows under consideration. In addition, the chosen CV should enclose the body such that the total drag force experienced by the body can be estimable. Similarity requires identification of length-scales. Alternatively, one may choose the physical boundary such as the streamline enclosing the recirculating flow region or the recirculating flow region defined by the isoline $U = 0$. The computation of the streamfunction depends on the resolution of the velocity fields, while the rri is relatively simple to define with lesser uncertainties than the former. However,

both of these choices can include only budget of the base pressure drag, which is largely sufficient as it forms the dominant contributor to the total drag.

Length scales

It has been known from the past studies that the recirculating flow region forms an important feature of the wake flows. For example, the length of the recirculating flow region scales the velocity deficit in the wake of bluff bodies with differing geometries [195]. In the studies of [165], the l_r^*, which in their study depends highly on the state and thickness of the incoming boundary layer prior to separation, has been found to be the most important lengthscale in the near wake which scales the development of the near wake. Earliest studies such as [91, 169, 1, 31] have also used this quantity in order to scale the evolution of quantities such as the static pressure in the near wake of either backward facing step flows or that of bluff bodies.

Figures 4.16a shows the evolution of the velocity deficit, normalized by the maximum velocity deficit, along the streamwise direction scaled by l_r^*. The normalized velocity deficit rises from 0.9 to the peak approximately at half the l_r^* for all the Re_h cases, after which it decays reaching 70% of the maximum at l_r^*. The data for all Re_h collapses perfectly until l_r^* after which a very small scatter is observed. It is to be noted that the maximum l_r^* variation with respect to the baseline Re_h is only 1.5% approx.
Figure 4.16b shows the evolution of the pressure deficit defined by

$$P_d^* = P^*(x^*, 0) - P_{FS}^*(x^*), \tag{4.9}$$

where the subscript FS denotes the free-stream. The evolution of the wake pressure deficit is scaled by its minimum value near half the l_r^*. As expected, the pressure deficit term decays faster than the velocity deficit. The figures indicate that the l_r^*, characteristic of the shear layer evolution, organises the flow field not only in the region after separation, but also a few l_r^*s away from it. Thus, any change in the shear layer evolution is expected to change the wake structure (see [165]).

The evolution of flow quantities such as the mean velocity deficit in figure 4.16a and the pressure deficit in figure 4.16b along the symmetric wake centerline is interesting as the influence of any transverse length scale is minimized or null. The dominant term that influences the evolution of flow according to figure 4.14 is the transverse variation of Reynolds shear stress term. Figure 4.17b shows the profiles of Reynolds shear stress at various streamwise locations in the similarity coordinate, i.e. in the streamwise direction normalised by l_r^*, varying along the vertical direction normalised by half the wake width y_δ^*. The peaks of the Reynolds shear stress in the near as well as the far wake align itself at the edge of the wake-width y_δ^*. Note that the wake width is a local length scale, and the alignment of Reynolds shear stress peaks near the edge of the wake width means that it scales the variation of flow in the transverse direction.

Figure 4.17a shows the mean streamwise velocity profiles, upstream $x^* \approx l_r^*$, centered at the shear layer and normalized by the vorticity thickness defined in (4.2). The velocity profiles collapse between $0.2 \leq U^* \leq 1$ within -0.5 to $+0.5$ in the normalized coordinates. Then, from profiles in figures 4.17b and 4.17a, while the wake width scales the large scale features of the flow, the vorticity thickness is localized in the shear layer.

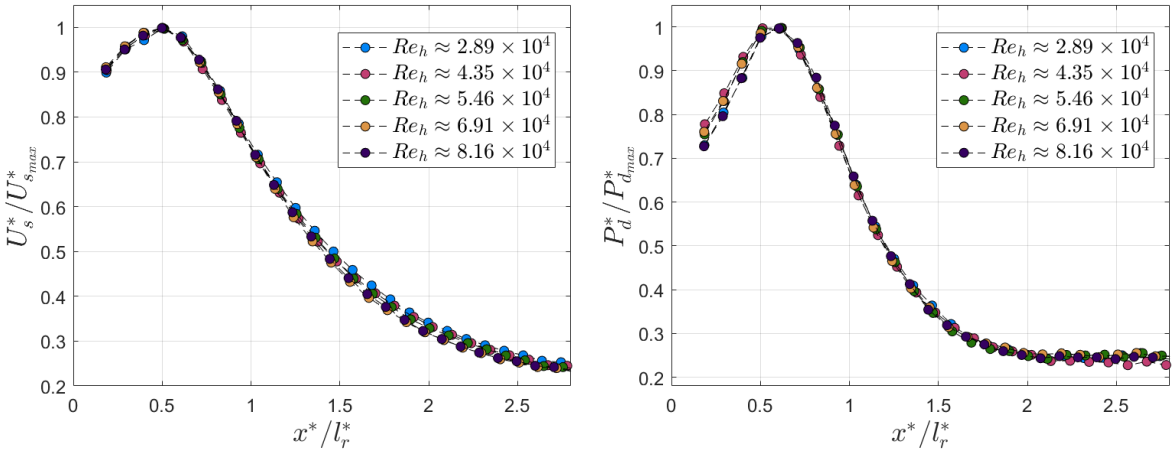

(a) (b)

Figure 4.16: Scaling the evolution of the mean velocity deficit (a) and the pressure deficit (b), using it's peak values, along the streamwise direction scaled by l_r^*.

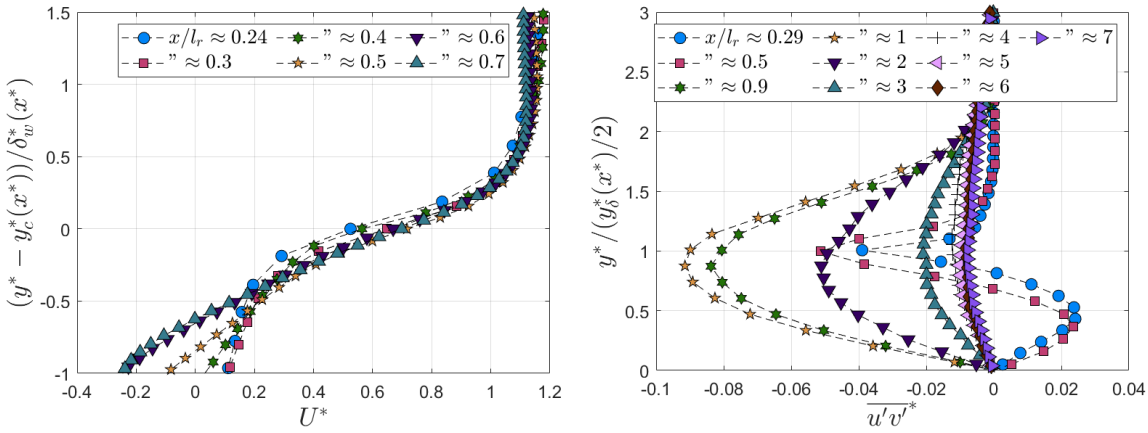

(a) (b)

Figure 4.17: The mean streamwise velocity profiles centered at the shear layer center and normalized by the local vorticity thickness δ_w^* (a) and the shear stress profiles, in the upper half of the symmetric wake, y^* scaled by the local wake width y_δ^*(a).

Figure 4.18 shows the evolution of wake width for different Re_h cases scaled by its minimum value found near l_r^*. The wake width drops from a higher value at separation to its minimum value close to l_r due to the presence of the recirculating flow region. Further, there is a linear increase, implying that the peaks of the Reynolds shear stress also evolves linearly in this region. It is seen that that l_r^* scales the evolution of the wake width, the magnitude of which is scaled by its characteristic value that occurs close to the end of the recirculating flow region. In [195], the wake width magnitude is scaled by the maximum thickness of the recirculating flow bubble (i.e. the lateral distance between the two separating streamlines). Since the wake width follows the recirculating flow bubble, then the characteristic lengthscale used in figure 4.18 should be equivalent to that of the recirculating flow bubble thickness used in [195].

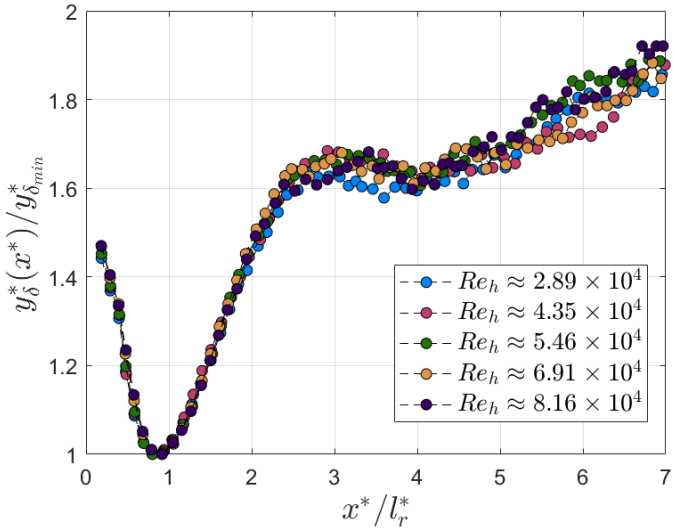

Figure 4.18: Evolution of the wake width $y_\delta(x^*)$ scaled by it's minimum value, $y^*_{\delta_{min}}$.

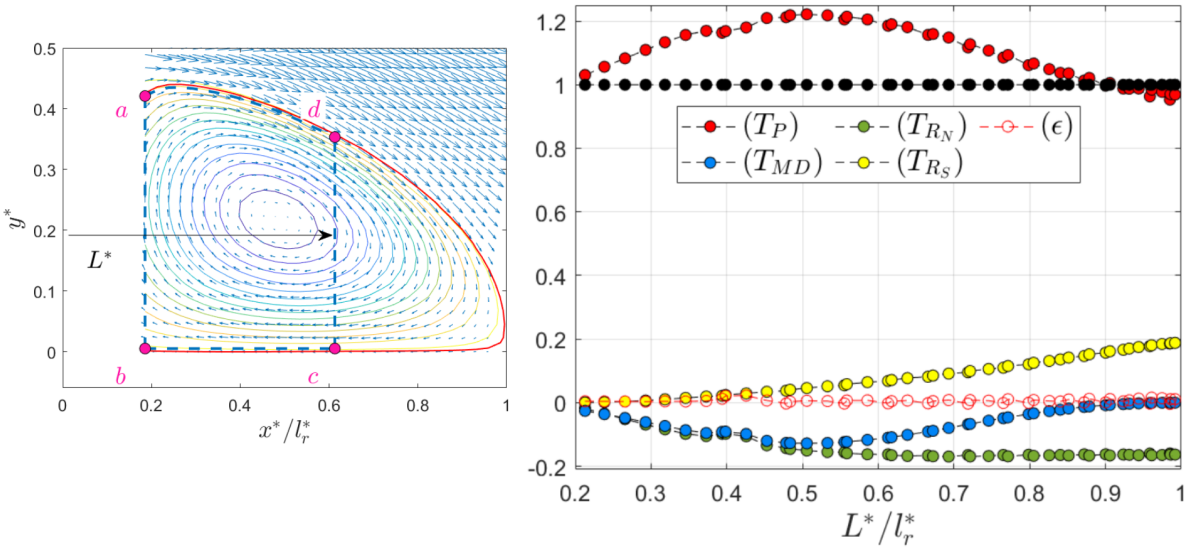

Figure 4.19: The control volume (CV) defined using the stream function $\psi = 0$ that encloses the recirculating flow region (left) and the budget of base pressure drag (right). Here, L^* refers to the streamwise location of the CV outlet and l^*_r forms the streamwise extent of the recirculating flow region.

4.2.2 Recirculating flow region - a universal choice of control volume

Figure 4.19 shows a control volume defined using the stream function $\psi = 0$ corresponding to the streamline forming the lateral side of the control volume, impermeable to mass or mean momentum transported by the mean flow. The inlet is fixed close to the body and the outlet location L^* varied in the streamwise direction. The momentum budget is performed at each location of L^*. Note that the performed budget is for the base pressure drag which forms the largest component of the total drag. The budget may be compared with any other bluff body flows since the CV definition is based on the common physical feature to all such flows. Note that the viscous contribution is neglected. The

integral momentum budget along the CV defined in figure 4.19 reads,

$$\underbrace{2\int_{\Gamma} U^*\left(\mathbf{U}^*\cdot\mathbf{n}\right)ds^*}_{t_{MD}}\underbrace{-2\int_{\Gamma}\overline{u'^2}^*n_x ds^*}_{t_{R_N}}\underbrace{-2\int_{\Gamma}\overline{u'v'}^*n_y ds^*}_{t_{R_S}}\underbrace{-\int_{\Gamma}C_p n_x ds^*}_{t_P}\approx\underbrace{-\int_{ab}C_p dy^*}_{t_P^{base}}, \tag{4.10}$$

$$t_P^{base}\approx\left(T_P+T_{R_N}+T_{R_S}+T_{MD}\right)\times t_P^{base},$$

whose contributions are shown in figure 4.19, with a residual ϵ close to zero indicating the quality of the PIV measurements and the estimated mean pressure. In equation (4.10), n_x and n_y represents the streamwise and vertical component of the unit normal vector to the streamline computed as,

$$\hat{\mathbf{n}}=(dy/ds)\hat{i}-(dx/dy)\hat{j}, \tag{4.11}$$

by the rotation of unit tangent vector by 90 degrees in the clockwise direction since the sense of integration around the CV is in the anti clockwise direction.

At $L^*\approx 0.2l_r^*$, the budget is dominated by pressure. All the remaining terms are zero. As the outlet L^* is displaced further downstream towards the center of the re-circulating bubble, $T_{MD}\approx 12\%$ reaches a peak due to the intense backflow. T_{R_N} also reaches a peak $\approx 12\%$ here, because $\overline{u'^2}^*$ reaches a peak within the recirculating flow region, shown in figure 4.5. T_{R_N} and T_{MD} tend to reduce the base-pressure drag which is compensated by T_P which peaks near the center of the recirculation region. As L^* is displaced further downstream, the outlet term contributions decreases and tends to zero due to decreasing size of the outlet. This is compensated by the corresponding terms acting on the lateral side of the CV. The lateral side being a streamline, the contribution of the mean momentum along it is null causing T_{MD} to decrease to zero beyond $L^*\approx 0.5l_r^*$.

Now, if the budget in equation (4.10) is written as,

$$1-\left(T_P^{(o)}+T_{MD}+T_{R_N}^{(o)}\right)=T_P^{(c)}+T_{R_N}^{(c)}+T_{R_S}, \tag{4.12}$$

where the superscript (o) and (c) represents the terms split into contributions from the outlet and the lateral side respectively, then the $R.H.S$ of equation (4.12) is a sink or source of momentum depending on the sign. Figure 4.20 shows the evolution of the terms on the $R.H.S$ of equation (4.12). All terms are close to zero within $L^*<0.3l_r^*$. The contribution from $T_{R_N}^{(c)}$ falls keeping the overall contribution of Reynolds normal stress a constant beyond $0.5l_r^*$. It is roughly balanced by the rise in T_{R_S}, same term as in figure 4.19. The contribution of the Reynolds shear stress to T_{R_S} saturates beyond $0.9l_r^*$ as the lateral side of the contour tends to reach the wake centerline. Splitting the contributions of T_P and T_{R_N} into those in equation (4.12) may not bring any new information than already shown in figure 4.19. However, it may shed light on the curvature effect of the recirculating flow bubble. For example, from the streamwise momentum balance along the centerline in figure 4.14, it is understood that the intensity of the Reynolds shear stress is crucial in determining l_r^* and this is supported by several studies [165, 120, 181]. In that case, this would cause an increase in magnitude of $T_{R_N}^{(c)}$ and $T_P^{(c)}$ as well (see equation (4.7) and figure 4.13) , and tend to increase the base pressure drag [120, 181].

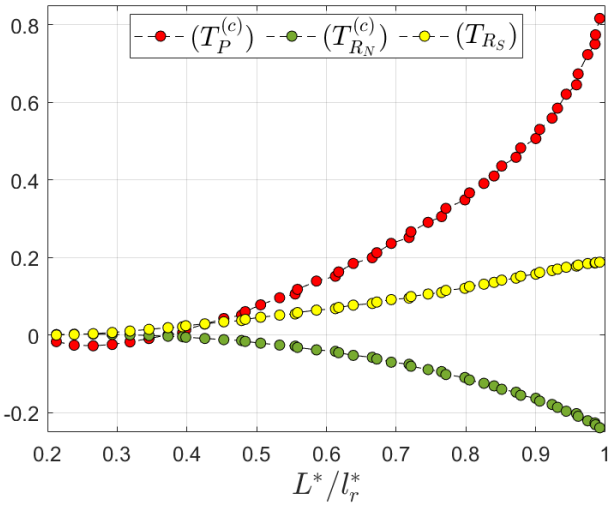

Figure 4.20: Contributions of the Reynolds stresses and the mean pressure to the base pressure drag while acting along the walls of the CV defined by the streamline $\psi = 0$

It is clear that the dominant contribution to the drag in the near wake comes from the pressure. Globally, the Reynolds streamwise normal stress and the mean momentum act to decrease the drag whereas the Reynolds shear stress increase it.The Reynolds shear stress contribution diminishes if a relatively larger CV is considered, whereas the Reynolds normal stress contribution is not affected significantly implying that the role of the former is to redistribute the momentum, while the latter always remain a sink. In addition, decomposing the mean pressure shows that it is driven primarily by the mean flow deformation close to the body, whose intensity is high in the separated shear layer, whereas near l_r^* the role switches to the Reynolds transverse normal stressAll these observations points to the significant role of Reynolds stresses, specially the normal components, in driving the drag and therefore it is necessary to understand its driving mechanism, more precisely the energy exchange mechanism or interplay between the mean flow and the Reynolds stresses.

4.3 Transport mechanism of Reynolds stresses

The Reynolds stress transport equation is given in equation (4.13). The numerical subscripts in the equation 4.13 represents the component of the Reynolds stress tensor.

$$\underbrace{U_k\frac{\partial}{\partial x_k}\left(\overline{u_i'u_j'}\right)}_{\mathcal{A}_{ij}} = \underbrace{-\left\{\overline{u_i'u_k'}\frac{\partial U_j}{\partial x_k}+\overline{u_j'u_k'}\frac{\partial U_i}{\partial x_k}\right\}}_{\mathcal{P}_{ij}} + \underbrace{\left\{\frac{\partial}{\partial x_k}\left(-\overline{u_i'u_j'u_k'}\right)\right\}}_{\mathcal{D}_{ij}}$$

$$+\overbrace{\frac{1}{\rho}\frac{\partial}{\partial x_k}\left(-\overline{p'\left(u_i'\delta_{jk}+u_j'\delta_{ik}\right)}\right)}^{\mathcal{D}_{ij}^p} + \underbrace{\frac{2}{\rho}\overline{p's_{ij}'}}_{\mathcal{PS}_{11}} - \underbrace{2\nu\overline{\frac{\partial u_i'}{\partial x_k}\frac{\partial u_j'}{\partial x_k}}}_{\varepsilon_{11}} + \underbrace{\nu\frac{\partial}{\partial x_k}\left(\frac{\partial}{\partial x_k}\left(\overline{u_i'u_j'}\right)\right)}_{(\mathcal{D}_{11}^{\nu})}, \tag{4.13}$$

$$\mathcal{A}_{ij} = \mathcal{P}_{ij} + \mathcal{D}_{ij} + \underbrace{\mathcal{D}_{ij}^p + \mathcal{PS}_{ij} - \varepsilon_{ij}}_{\mathcal{R}_{ij}} + \mathcal{D}_{ij}^{\nu},$$

where,

$$s_{ij}' = \frac{1}{2}\left(\frac{\partial u_i'}{\partial x_j}+\frac{\partial u_j'}{\partial x_i}\right) \tag{4.14}$$

is the fluctuating strain rate tensor. The left hand side of the equation (4.13) represents the net rate of increase or decrease of the Reynolds stress component, due to the spatial advection by the mean flow and it depends on the mechanism given on the right hand side ($R.H.S$) of the equation. The first term on the $R.H.S$, $\mathcal{P}_{ij}$, represents the production term for the Reynolds stress component which extracts energy from the mean flow by the action of the Reynolds stresses resisting the deformation by the mean flow gradients [59].It is similar in form to the complete production term, $\mathcal{P} = -\rho\overline{u_i'u_j'}\frac{\partial U_i}{\partial x_j}$ is responsible for energy exchange between the mean and fluctuating kinetic energy.

The terms $\mathcal{D}_{ij}$, $\mathcal{D}_{ij}^p$ and $\mathcal{D}_{ij}^{\nu}$ represent the diffusion of Reynolds stresses by the fluctuations, diffusion by the fluctuating pressure and the viscous diffusion respectively. These diffusion terms can be expressed in the divergence form while integrating over a control volume. They disappear while integrating over a large control volume, meaning that it cannot produce or destroy energy but merely redistributes the energy spatially and hence is considered a transport term. The term ε_{ij} is considered a dissipation (heat/entropy production) term since it is always positive, acting to remove energy from the fluctuations, due to its negative sign in equation (4.13).Finally, the term $\mathcal{PS}_{ij}$ is known as the pressure strain or the pressure redistribution term because its function is to re-distribute energy between the Reynolds stress normal components. This can be understood from the transport equation of fluctuating kinetic energy, where the pressure strain is zero due to the divergence-free nature of the velocity field, but is non zero in the transport equations of Reynolds stresses. However, for the transport equation of Reynolds shear stresses, the pressure strain term serves as a source or a sink term depending on its sign. The viscous diffusion term in equation (4.13) is neglected for the local balance since its contribution is negligible. In addition, the sum of terms $\mathcal{D}_{ij}^p$, $\mathcal{PS}_{ij}$ and $-\varepsilon_{ij}$ shall be represented by the residuals due to it's inaccessibility from the 2D planar PIV measurements.

4.3.1 Transport mechanism of streamwise Reynolds normal stress

The transport equation for Reynolds streamwise normal stress is derived from (4.13) and given in (4.15). Note that the third term of $\mathcal{D}_{11}$ is cancelled out since the flow is

statistically two-dimensional.

$$\underbrace{U\frac{\partial\overline{u'^2}}{\partial x}+V\frac{\partial\overline{u'^2}}{\partial y}}_{\mathcal{A}_{11}}=\underbrace{-2\left\{\overline{u'^2}\frac{\partial U}{\partial x}+\overline{u'v'}\frac{\partial U}{\partial y}\right\}}_{\mathcal{P}_{11}}\underbrace{-\left\{\frac{\partial}{\partial x}\left(\overline{u'^3}\right)+\frac{\partial}{\partial y}\left(\overline{u'^2v'}\right)+\cancel{\frac{\partial}{\partial z}\left(\overline{u'^2w'}\right)}\right\}}_{\mathcal{D}_{11}}$$
$$\underbrace{+\mathcal{D}^p_{11}+\mathcal{PS}_{11}-\varepsilon_{11}}_{\mathcal{R}_{11}}+\cancel{\mathcal{D}^\nu_{11}}^{\,0} \tag{4.15}$$

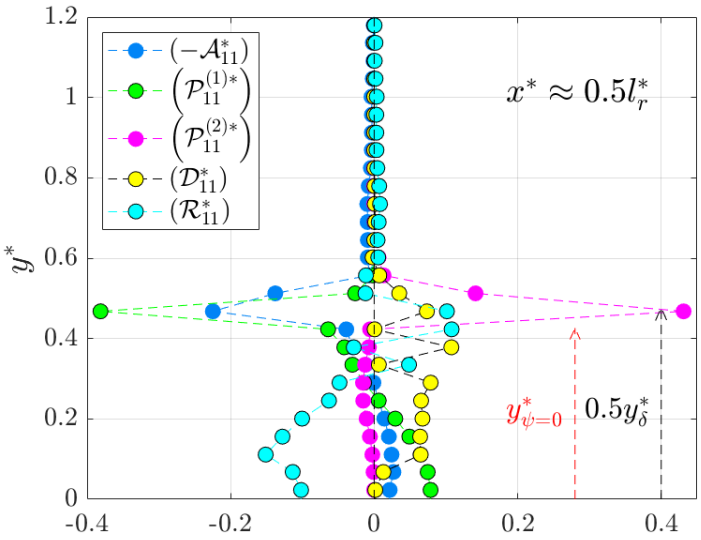

Figure 4.21: Local balance of the transport equation for the streamwise Reynolds normal stress performed close to the body after separation.

Figure 4.21 shows the local balance of the transport equation for streamwise Reynolds normal stress $\overline{u'^2}^*$ close to the flow separation point. The transverse extent of local wake width and the recirculating bubble width are marked by black and red arrows respectively. The transport of $\overline{u'^2}$ is zero in the region of external flow $0.6 \leq y^* < \infty$, beyond the width of the wake. It is toward the center of the mean shear layer, denoted by the wake width and the local height of the bubble, that the majority of the energy exchange takes place. Within the wake $0.4 \leq y^* < 0.6$, the major energy gain is due to the shear production $\mathcal{P}^{(2)}_{11}$ whereas normal production $\mathcal{P}^{(1)}_{11}$ tends to oppose it. Towards the wake centerline, the normal production shows a slight gain balanced by the residual. Since the role of diffusion is energy-redistribution, it can be thought as carrying the energy from the residuals, near the wake centerline, to elsewhere such as the shear-layer center here. However, it's magnitude is relatively small compared to the shear and normal production terms.

Towards the center of the recirculating flow region at $x^* \approx 0.5l^*_r$, in figure 4.22, the energy drained to $-\mathcal{A}_{11}$ is non zero over a larger transverse distance y^* relative to the terms in figure 4.21. Approaching the wake from the free stream, in the range $0.5 \leq y^* \leq \infty$, there is a gain in energy through $\mathcal{R}^*_{11}$ and $\mathcal{D}^*_{11}$ which is balanced by $-\mathcal{A}^*_{11}$. All the remaining terms are negligible here.Moving towards the wake centerline, there is a significant energy gain due to the shear production $\mathcal{P}^{(2)}_{11}$ peaking at $0.5y^*_\delta$. The residual $\mathcal{R}^*_{11}$ shows a sink in

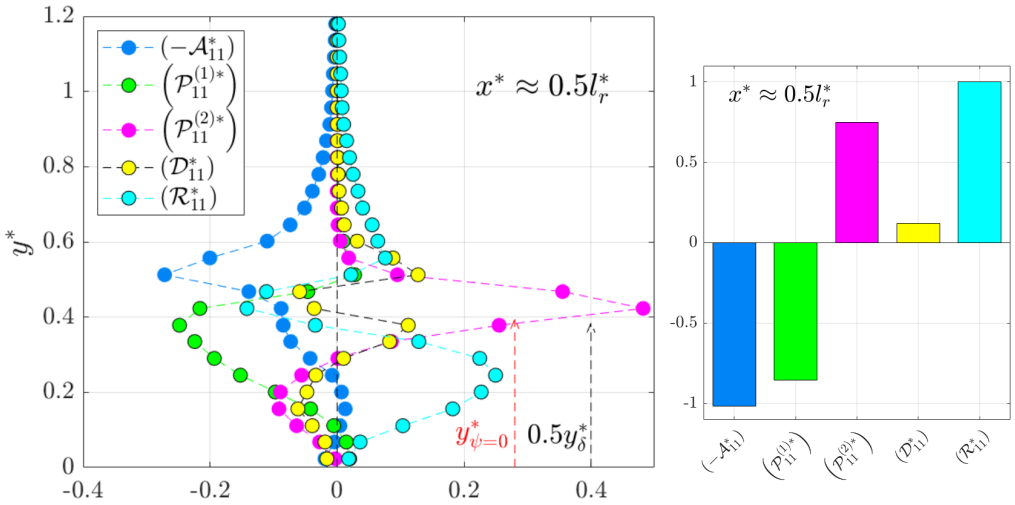

Figure 4.22: Local balance of the transport equation for the streamwise Reynolds normal stress performed close to the center of the recirculating flow region $x^* \approx 0.5l^*_r$. The average view is shown in the bar plot, where the terms are averaged in the transverse direction in the range $0 \leq y \leq \infty$ and then normalized by the highest gain term.

the range $0.3 \leq y^* \leq 0.5$. Note that the shear production $\mathcal{P}^{(2)}_{11}$, compared to the location close to separation in figure 4.21, is spread over a larger area attributed to the growing shear layer.

There is a significant sink of energy through the normal production $\mathcal{P}^{(1)}_{11}$, peaking at $0.5y^*_\delta$, opposing the shear production $\mathcal{P}^{(2)}_{11}$. Towards the wake centerline, the residual shows a significant energy sink balanced by the normal production. The shear production shows a sink, close to the centerline, due to the presence of positive $\overline{u'v'}^*$ within the first half of the recirculating flow region. $\mathcal{D}^*_{11}$ redistributes energy in the vertical direction, and hence it shows up as a negligible value in the bar plot of figure 4.22.

On average, the flow is driven by the residual terms. The averaged shear production $\mathcal{P}^{(2)}_{11}$ is comparatively lesser than the residuals, its local contribution is the highest, because it is highly localized close to the shear layer center and at this position, the shear layer is in the growing stage and hence it's thickness is expected to be small compared to its thickness at the end of the recirculating flow region (see figure 4.3).

At the streamwise location l^*_r in figure 4.23, similar to the case in figure 4.22, advection of $\overline{u'^2}$ is balanced by $\mathcal{R}_{11}$ within $0.6 \leq y^* < \infty$. The role of diffusion is the transverse energy redistribution which is why its spatial average is negligible, shown in bar plot of figure 4.23. There is a significant generation of energy by the shear production $\mathcal{P}^{(2)}_{11}$ which is the largest of all terms, and thus the highest spatially-averaged value in the bar plot of figure 4.23. Similar to the case in figure 4.22, the normal $\mathcal{P}^{(1)}_{11}$ opposes the shear production $\mathcal{P}^{(2)}_{11}$. The energy gained by the shear production is redistributed transversely by the diffusion $\mathcal{D}^*_{11}$. The loss in advection $\mathcal{A}^*_{11}$ towards the wake centerline can either be due to $\mathcal{R}^*_{11}$ or $\mathcal{P}^{(1)}_{11}$, but not $\mathcal{D}^*_{11}$ because of its redistribution role. However, the residual terms seem to be of primary importance in order to completely understand the underlying physical mechanism.

At separation, the laminar boundary layer along leads to an intense mean shear within

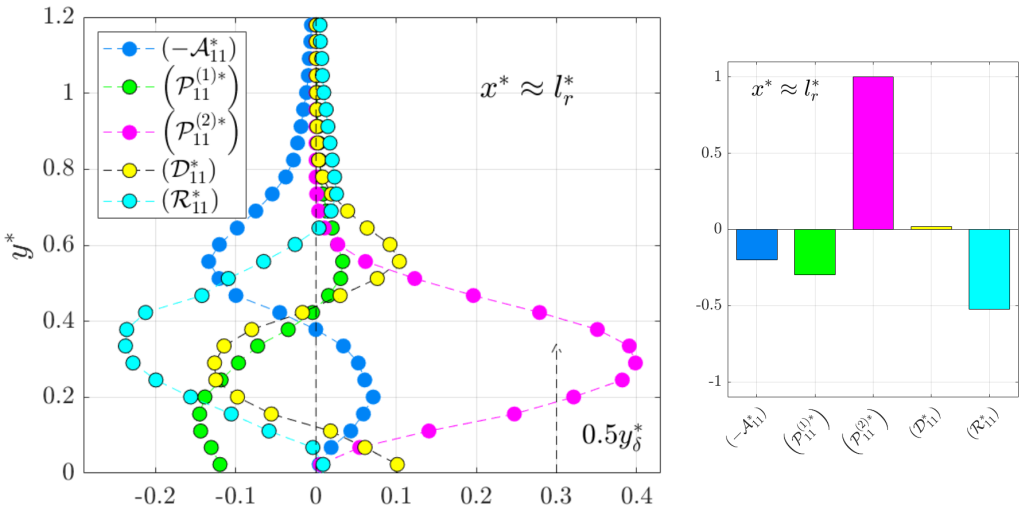

Figure 4.23: Local balance of the transport equation for the streamwise Reynolds normal stress performed close to the end of the recirculating flow region.

the separated mean shear layer. The Reynolds shear stress, which shows a peak corresponding to the location of maximum shear, while resisting this mean shear leads to an intense shear production $\mathcal{P}^{(2)}_{11}$ in figure 4.21. The drain in energy through $\mathcal{P}^{(1)}_{11}$ occurs slightly below the body height and is due to the $\overline{u'^2}$ which peaks close to this location as well as due to the intense positive $\partial U/\partial x$ due to the growing shear layer (see figure 4.24).

As the flow expands downstream the mean shear decreases. However, the Reynolds shear stress exerted onto the flow continues to grow in intensity until close to l^*_r. There is a small region close to the body, where the Reynolds shear stress remain positive due to the presence of the recirculating flow region, resulting in a sink by $\mathcal{P}^{(2)}_{11}$ (shown as a negative peak along the rri in figure 4.24). The diminished mean shear with the intensifying Reynolds shear stress contribution leads to a persisting and dominating energy gain through the production term $\mathcal{P}^{(2)}_{11}$ at l^*_r. Figure 4.24 shows the evolution of the normal as well as the shear production terms, where both are initially concentrated along the mean shear layer center and is smeared beyond $0.75l^*_r$ with the growing shear layer. The latter locally peaks roughly along the local wake-width whereas the former along the streamline $\psi = 0$.

4.3.2 Transport mechanism of transverse Reynolds normal stress

The transport equation for the transverse Reynolds normal stress is given in equation (4.16). The local balance of the transport equation is performed at two streamwise locations. These locations correspond to the maximum contribution of the pressure to the overall budget of drag in figures 4.19, i.e. near the center of the recirculating flow region, and at l^*_r where the Reynolds normal stress $\overline{v'^2}^*$ is seen to be a dominant driving factor

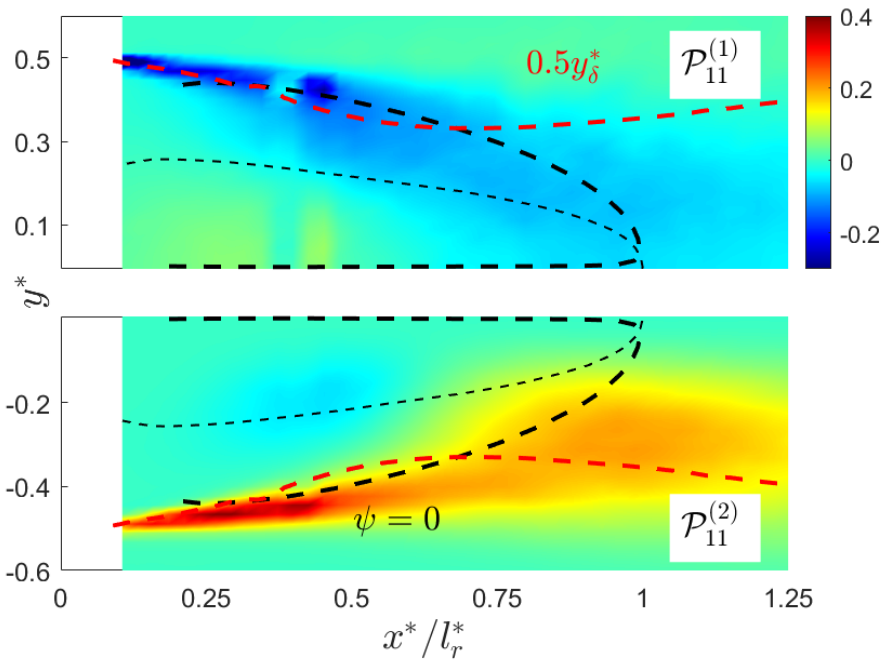

Figure 4.24: Colormap of the normal (top) and shear (bottom) production terms involved in the transport of Reynolds streamwise normal stress.

of mean pressure in figure 4.13b.

$$\underbrace{U\frac{\partial\overline{v'^2}}{\partial x}+V\frac{\partial\overline{v'^2}}{\partial y}}_{\mathcal{A}_{22}}=\underbrace{-2\left\{\overline{u'v'}\frac{\partial V}{\partial x}+\overline{v'^2}\frac{\partial V}{\partial y}\right\}}_{\mathcal{P}_{22}}\underbrace{-\left\{\frac{\partial}{\partial x}\left(\overline{v'^2u'}\right)+\frac{\partial}{\partial y}\left(\overline{v'^3}\right)+\cancel{\frac{\partial}{\partial z}\left(\overline{v'^2w'}\right)}\right\}}_{\mathcal{D}_{22}}$$
$$\underbrace{+\mathcal{D}_{22}^{p}+\mathcal{PS}_{22}-\varepsilon_{22}}_{\mathcal{R}_{22}}+\cancel{\mathcal{D}_{22}^{\nu}}^{0}, \tag{4.16}$$

Figure 4.25 shows the local balance of transport equation of $\overline{v'^2}^*$ at $x^* \approx 0.5l_r^*$, which also corresponds to the streamwise location of mean pressure minimum along the wake centerline. Along the vertical direction, approaching from the free stream, $-\mathcal{A}_{22}$ is balanced by the residual terms only. Moving towards the wake centerline, the net gain in energy due to the residual term is drained by the diffusion term. Note that the shear production $\mathcal{P}_{22}^{(1)}$ remains relatively small throughout the budget (see figure 4.26b). The highest gain in energy is the normal production $\mathcal{P}_{22}^{(2)}$ peaking close to the center of the mean shear layer (see figure 4.22 for the position of the mean shear layer-center). The shape of the curves of diffusion and the residual term behaves as if they redistribute the energy in the vertical direction. This should be the reason why their transverse spatial average is negligible in figure 4.25. The majority of the produced energy by $\mathcal{P}_{22}^{(2)}$ is then gained by the advection term.

Considering the normal production terms $\mathcal{P}_{22}^{(2)} = -2\overline{v'^2}^*\frac{\partial V^*}{\partial y^*}$ and $\mathcal{P}_{11}^{(1)} = -2\overline{u'^2}^*\frac{\partial U^*}{\partial x^*}$, the two-dimensional incompressible mean flow demands that the energy drained by the $\mathcal{P}_{11}^{(1)}$ during the transport of $\overline{u'^2}^*$, be at least partially be transferred to contribute to the transport of $\overline{v'^2}^*$. This can be found near the center of the recirculating flow region, where the energy extracted by the $\mathcal{P}_{11}^{(2)}$ from the mean flow is partially drained by the

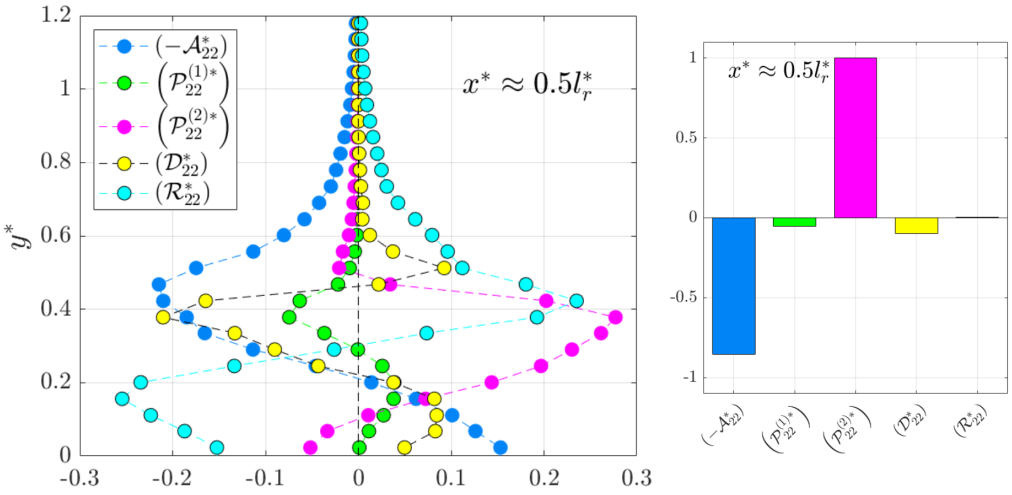

Figure 4.25: Local balance of the transport equation for the transverse Reynolds normal stress performed near the center of the recirculating flow region.

$\mathcal{P}_{11}^{(1)}$ which is subsequently injected to the transport of $\overline{v'^2}^*$ through $\mathcal{P}_{22}^{(2)}$, as shown in figure 4.26a where the sum of $\mathcal{P}_{11}^{(1)} + \mathcal{P}_{22}^{(2)}$ is close to zero. The gain due to $\mathcal{P}_{22}^{(2)}$ forms a sort of feedback mechanism, where the Reynolds stress $\overline{v'^2}^*$ resisting the deformation of the mean field through $\partial V^*/\partial y^*$ results in a net increase of $\overline{v'^2}^*$ through $-\mathcal{A}_{22}$.

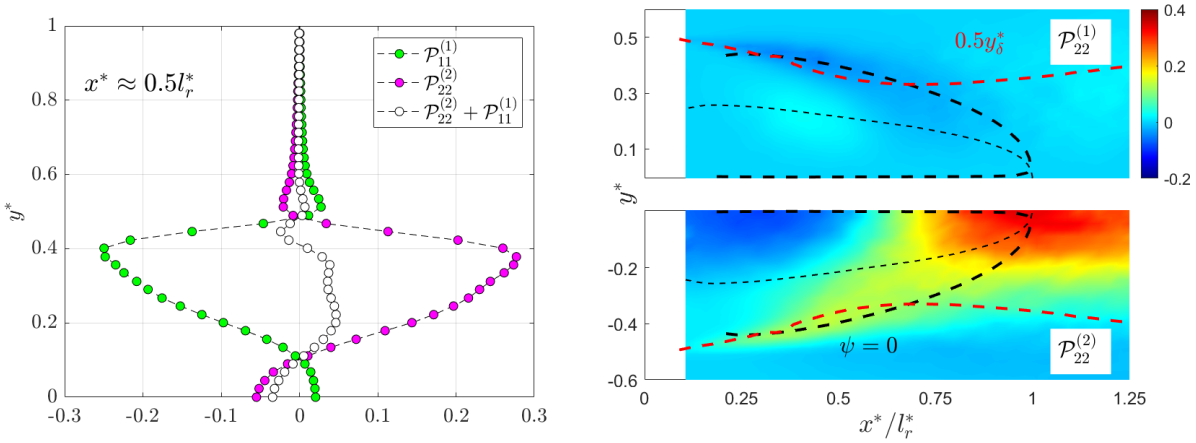

(a) (b)

Figure 4.26: Comparison of the production terms $\mathcal{P}_{11}^{(1)}$ and $\mathcal{P}_{22}^{(2)}$ in the transport of $\overline{u'^2}^*$ and $\overline{v'^2}^*$ respectively at the center of the recirculating flow region (a), and color-map of the normal (top) and shear (top) production terms involved in the transport of Reynolds transverse normal stress (b).

Figure 4.27 shows the local balance of $\overline{v'^2}^*$ transport near $x^* \approx l_r^*$, where $\overline{v'^2}^*$ is close to its maximum (see figure 4.6b). Approaching the wake from the free stream $0.4 \leq y^* \leq \infty$, the residual term remains negligible and the gain by the diffusion is balanced by the advection.Moving further towards the wake centerline for $0 \leq y^* < 0.4$, the diffusion switches to a sink along with the residual terms, which together balances the normal production $\mathcal{P}_{22}^{(2)}$. The advection $-\mathcal{A}_{22}$ becomes zero at $y^* \approx 0$, meaning that the transported $\overline{v'^2}^*$ reaches its maximum at this location. The peak V^* close to l_r^* in a

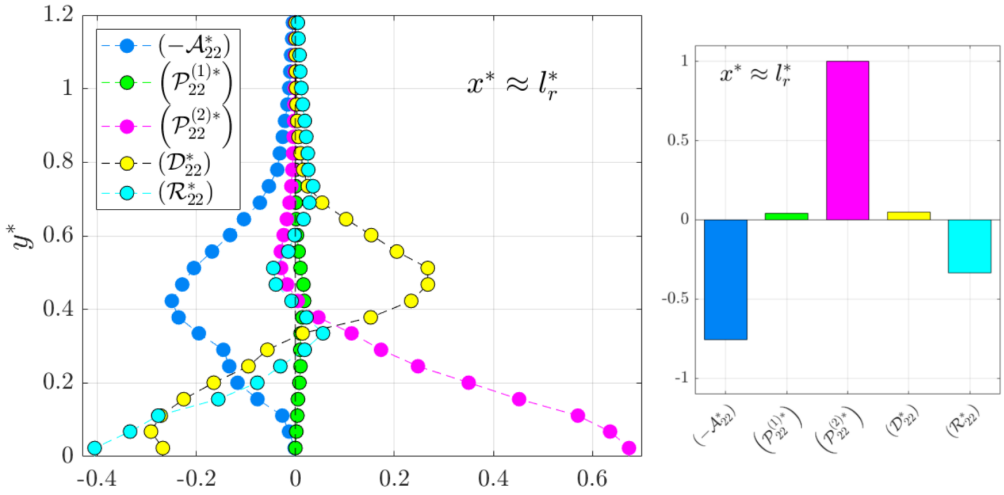

Figure 4.27: Local balance of the transport equation for the transverse Reynolds normal stress performed near the end of the recirculating flow region.

symmetric wake implies higher mean strain due to $\partial V^*/\partial y^*$, or $-\frac{\partial U^*}{\partial x^*}$ because the flow transitions from the recirculating flow to the wake, and thus $\overline{v'^2}^*$ resists this deformation which results in a gain in energy through $\mathcal{P}^{(2)}_{22}$.

The local balance and the spatial average show that the advection of $\overline{v'^2}^*$ is primarily driven by the normal production and the redistribution is due to the diffusion and the residual terms. The energy produced by the mean flow through the production terms $\mathcal{P}^{(1)}_{11}$ and $\mathcal{P}^{(2)}_{11}$, primarily in the growing shear layers, may be transferred inter-componently through the pressure strain terms. But, this information remains out of reach within the residual, the description of the physics remains incomplete. Further, a mechanism near $0.5l^*_r$ is noticed wherein the normal production $\mathcal{P}^{(1)}_{11}$, draining energy from shear production $\mathcal{P}^{(2)}_{11}$, transfers it inter-componently through the normal production $\mathcal{P}^{(2)}_{22}$.

4.4 Conclusion

The objective of this chapter was to characterize the mean flow and to understand the various contributions to the mean drag. The qualitative features of the mean fields such as those of Reynolds stresses or velocity fields were found similar to that reported in the literature. The minima of the mean pressure is found to be localized within the recirculation region due to the switching in momentum redistribution by the Reynolds shear stress. Decomposing the pressure showed that the mean flow deformations contribute significantly to the mean pressure especially within the mean shear layer during it's initial stage of growth whereas it is the transverse Reynolds normal stresses that drives it while approaching the end of the recirculation region. Performing integral mean momentum budget over the recirculation region reveals the physical mechanism of drag through the momentum exchange process. The mean pressure remains the dominant momentum source throughout the budget. The mean momentum and the streamwise Reynolds normal stress acts as a sink of momentum, with it peaks near the center of the recirculation region. The role of Reynolds shear stress is to redistribute the momentum balancing the sink by Reynolds normal stress near the end of recirculation region, while the transverse

Reynolds normal stress, though not explicit in it's contribution, acts as a key source for the mean pressure.

An attempt is made to identify the transport mechanism of Reynolds normal stresses.In case of the normal stress component, the energy is primarily produced within the growing shear layer due to the dominant shear production term, which is then redistributed by the residuals and the diffusion terms. In case of transverse Reynolds stresses, the energy production is dominant near the wake-centerline, by the normal production term, where the opposite side shear layers interacts and merges with each other. Further, near the vicinity of the center of recirculation region, the energy produced within the shear layer is transferred through the normal production terms of both streamwise and transverse normal stresses, from former to the latter. The description of the energy exchange mechanism however is incomplete due to the unresolved residual terms and this issue will be addressed in the following Chapter.

Chapter 5

Coherent and incoherent structures

5.1 Introduction

The objective of this chapter is to understand the contribution of the large scale coherent structures to the mean base-pressure. The chapter is organised into four parts. The objective of the first part is to present the method of flow decomposition used in this study and describe the main features of the large-scale coherent structures. The second part of this chapter focuses on isolating the contributions of the dominant coherent and the remaining incoherent structures to the mean drag. The third part introduces the method of estimating coherent pressure fields, also utilising a novel approach for estimating the temporal derivative of the coherent velocity fields from non-time-resolved data. Finally, the fourth part is focused on understanding the mechanism that drives the transport of coherent Reynolds stresses.

5.1.1 Coherent structures and incoherent motions decomposition

The wake of bluff bodies is dominated by large scale coherent structures. The term large scale is specified in order to focus on structures with size of the order of the height of the body, specifically on the von-Kàrmàn type vortex streets, observed in the bluff body wake (see the review by Williamson (1996) [200]. Several studies in the past aimed at attenuating such large coherent structures in order to reduce the drag force experienced by the body. For example, placing splitter plates, rigid [145] or flexible [158], along the wake centerline thereby interfering with the shear layer and disrupting the formation of large-scale vortices. Further examples include three dimensional forcing such as geometrical modifications of the bluff body. Examples include spanwise wavy leading edge [20], distorting shear layers in the spanwise direction and making it less susceptible to roll up into a von-Kàrmàn street [42], [148] interfered with the incoming boundary layer to affect the formation of the vortex street (see the review by Choi *et al.* (2008) [37]).

A recent study by Nedic *et al.* (2013) [113] reports both increased drag and vortex shedding increased, introducing a variety of turbulence lengthscales in the flow by means of fractal edged geometries. In the follow-up study by Nedic *et al.* (2015) [114], the effect of multi-scale fractal edges was found to redistribute the energy from the dominant mode of vortex shedding to a broad range of scales, which opened new alleys to study the role of vortex shedding in a turbulent bluff-body wake. However, the dominant terms in the

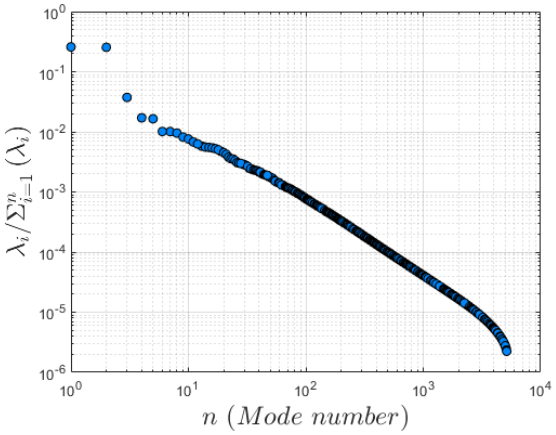

(a) Relative energy contribution of the POD modes for $Re_h \approx 2.8 \times 10^4$.

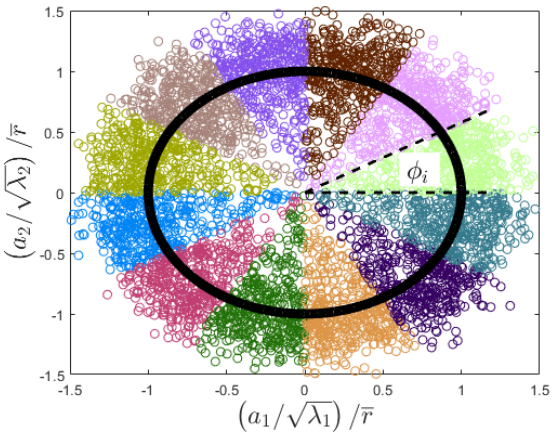

(b) POD time coefficients of the first 2 modes for approximately 5100 snapshots.

Figure 5.1: Modal energy contribution of POD modes (a) and the time coefficients of the first two modes (b). The color codes in (b) represent the flow split into 12 phases to sort the flow based on the time coefficients in (a_1, a_2) plane (a) and to phase average for the extraction of coherent structures.

transport of coherent motions have remained out of reach because the associated coherent pressure plays a major role in the momentum budget. In this chapter, pressure is calculated and analysed to obtain the coherent forces on the body and close the transport of coherent stresses in the near wake.

Following the work of Reynolds and Hussain (1972)[142], the fluctuating velocity is split between a coherent and incoherent motions. i.e.,

$$u = U + \tilde{u} + u'', \tag{5.1}$$

where $\tilde{u}$ and u'' denotes the coherent and incoherent part respectively. The aim is to analyse the fundamental transport equations that govern the coherent part in a complex flow geometry.

Coherent structure extraction

In the current study, the method proposed by van Oudheusden *et al.* (2005) [192] is used to compute spatially coherent structures in the flow field. The term 'spatially coherent' is used to emphasize that the obtained structures do not represent coherent structures that evolve temporally and spatially, instead it represents the spatial mode that captures most of the fluctuating or turbulent kinetic energy in the flow field (see for example [184] for the application of POD technique on velocity fields). Figure 5.1a shows the normalized spectrum of the POD modes. The first two modes represent approximately 51% of the total energy, that is mode 1 and 2 take up 25.82% and 25.42% respectively. The remaining is distributed into higher modes. This is similar to that reported in [192] or [29] where the first two modes capture the highest energy levels. But the magnitudes of the energy levels, compared to our case, are different. In the former study, the geometry is a square cylinder (blockage ratio 7%) experiencing massive separation at the leading edge with the mode 1 and 2 taking up 42 and 32% of the total energy at $Re_h = 1 \times 10^4$, and

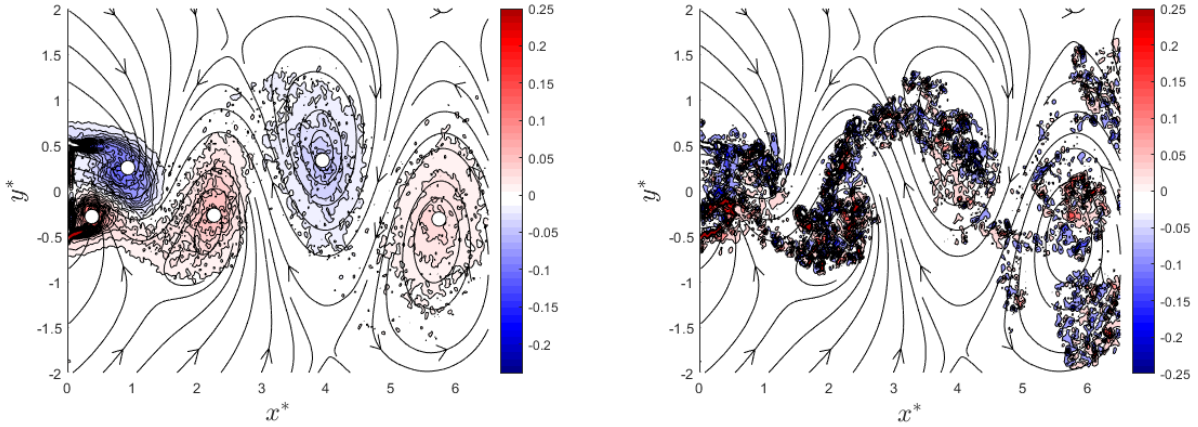

(a) Coherent vorticity $\tilde{\omega}_z$ at an arbitrary phase extracted using the POD technique, at $Re_h \approx 2.8 \times 10^4$.

(b) Incoherent vorticity ω_z'' at an arbitrary time and at the same phase as that of (a).

Figure 5.2: The coherent (a) and incoherent (b) spanwise vorticity . The coherent vorticity is computed at an arbitrary phase ϕ_1, while the incoherent vorticity is computed at an arbitrary time but occurs at the same phase ϕ_1 as that of (a). The white solid circles in (a) denotes the center of the vortex formation and the streamlines represents that which is seen by an observer travelling at U_{in}.

in our studies the Re_h and blockage ratio are similar but the massive leading edge separation is absent and the wake forms post separation of a laminar boundary layer. In the later study, the geometry is a circular cross section (blockage ratio 20%) with the mode 1 and 2 taking up more than 30 and 20% of the total energy respectively at $Re_h = 1.4 \times 10^5$.

According to [192], the time coefficients a_1 and a_2, of the first two modes with similar energy levels form an elliptic limit cycle:

$$\frac{a_1(i)^2}{2\lambda_1} + \frac{a_2(i)^2}{2\lambda_2} = r_i^2, \tag{5.2}$$

This is verified in this study in figure 5.1b, where the values are clustered on the edge of the (normalised) unit circle (see figure 5.1b, where the quantities $a_1/\sqrt{2\lambda_1}$ and $a_2/\sqrt{2\lambda_2}$ are normalized by the means of the local radii r_i). The unit circle is further split into 12 phases. Each phase is within $\pi/6$ rad. Further, the velocity fields are phase-sorted based on the time coefficient values in the (a_1, a_2) plane, for example the flow fields with the time-coefficients that fall in between the first angular section in figure 5.1b, demarcated by dashed lines, are sorted to form the first phase. The procedure is then repeated for the other 11 phases.

Figure 5.2a shows the coherent spanwise vorticity defined as $\tilde{\omega}_z = \partial\tilde{v}/\partial x - \partial\tilde{u}/\partial y$. Alternating vortices are denoted by red for positive and blue for negative magnitudes. The small intense vorticity bearing vortices close to the body becomes larger on moving downstream and the vorticity is diffused into the surrounding flow. The streamlines as observed by an observer travelling at the same speed as that of the inlet flow U_{in}, shows the vortex patterns clearly, similar to that reported in an earlier study [129]. Some qualitative features are also visible such as the quasi-instantaneous alleyway that penetrates into the

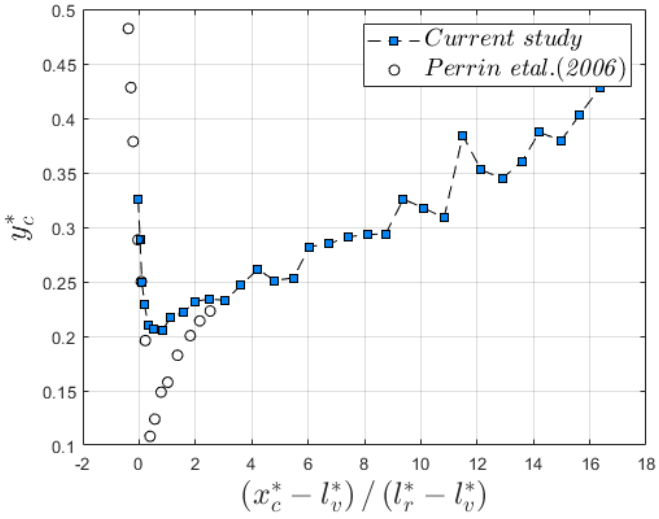

Figure 5.3: Trajectory of the alternating vortices. The squares and circles indicate indicate the current study at $Re_h \approx 2.8 \times 10^4$ and the results reported in [29] at $Re_h \approx 1.4 \times 10^5$ respectively. l_v^* and l_r^* represents the streamwise distance of the center of the mean recirculating flow vortex and the extent of the recirculating flow respectively.

wake interior that represents the transport of fluid from the irrotational flow region to and across the wake, induced by these coherent structures. Within the flow domain, the vortex centers are observed to be displaced laterally, and the size of the vortices becomes larger, entraining fluid from the free stream. A qualitative discussion on the entrainment mechanism by the vortices can be found in [119]. The rapid growth of the vortex street indicates a stronger entrainment which decreases further downstream due to decreased strength of the vortices. Overall, the discussion highlights the importance of the coherent structures observed, in the entrainment process. Figure 5.2b shows the incoherent vorticity computed as $\omega_z'' = \partial v''/\partial x - \partial u''/\partial y$ at an arbitrary time, but at the same phase as the coherent vorticity shown in figure 5.2a. Small eddying motions are clearly visible and the interactions between them are intense closer to the vortex center until approximately $x^* \leq 4.5$, after which it slowly begins to diffuse outwards from the vortex center. Further, the incoherent motions are seen to follow the path of the coherent structures, indicating that the coherent structures interact with the incoherent structures while transporting them.

Figure 5.3 shows the trajectory followed by alternating vortices during travel travel downstream. The vortices are detected by the $\Gamma(2)$ criterion following [64], defined as,

$$\Gamma(2) = \frac{1}{N}\Sigma_S \frac{\mathbf{PM} \wedge (\mathbf{U_M} - \mathbf{U_P})}{\|\mathbf{PM}\| \cdot \|\mathbf{U_M} - \mathbf{U_P}\|}, \tag{5.3}$$

where N is the number of points in a rectangular window within the PIV domain centered at $\mathbf{P}$ with $\mathbf{M}$ being the distance from the local center $\mathbf{P}$, $\mathbf{U_M}$ is the local velocity vector at $\mathbf{M}$ and $\mathbf{U_P} = \frac{1}{S}\int_S \mathbf{U} dS$ is the local convection velocity around $\mathbf{P}$. Vortex centers are identified as the weighted center of the vorticity (see [22]) or from the $\Gamma(2)$ function as

$$x_{i\Gamma} = \frac{1}{\int_S \Gamma(2)\, dx\, dy} \int_S x_i\, \Gamma(2)\, \mathrm{d}x\, \mathrm{d}y,\ (i = 1, 2) \tag{5.4}$$

where S refers to the area of the vortex, detected using some threshold values over the computed $\Gamma(2)$ values from equation (5.3).

Figure 5.3 shows that the vortices move towards the wake centerline, while forming, and then their centers starts to be displaced laterally during its growth by entrainment. The trajectory shows good agreement with the results in [29] at least in the initial stages of vortex formation in figure 5.3, when the origin shifted to the center of the recirculating flow and normalised by the extent of the recirculating flow region. One may also notice that in the initial stages, the vortex trajectory is scaled by the body height. Figure 5.3 further suggests the importance of l_v^* and l_r^* as potential length-scales.

Finally, it is to be noted that the POD methods computes orthogonal modes which are based on the energy content only. The temporal dynamics may be therefore partially lost in the process. Spatially uncorrelated structures may be contained within the large-scale structures embedded, thus obscuring its physical significance [207]. One may circumvent this problem by the conventional phase averaging technique, where a sufficiently time resolved reference signal is used [127], or more advanced methods, for example: based on Dynamic Mode Decomposition (DMD) [153], Spectral POD modes (SPOD) [179], or Optimal Mode Decomposition (OMD) [11] in a multi scale flow, to isolate the coherent structures at a specific frequency which is more representative of a single coherent structures.

Coherent and incoherent Reynolds stresses

Following the work of Reynolds and Hussain (1972) [142], the Reynolds stress terms can be split into coherent and incoherent contributions such that

$$\overline{u_i' u_j'} = \overline{\tilde{u}_i \tilde{u}_j} + \overline{\langle u_i'' u_j'' \rangle} + \cancelto{0}{\overline{\langle u_i'' \rangle \tilde{u}_j} + \overline{\tilde{u}_i \langle u_j'' \rangle}}, \tag{5.5}$$

where $\bar{\cdot}$ and $\langle \cdot \rangle$ represents time averaging and phase averaging respectively. Note that the last two terms result from the coherent-incoherent structure interaction. It was found to be negligible and is not taken into account in the following discussion. This can be the consequence of the triple decomposition used in this study where temporal periodicity is enforced using POD, resulting in coherent structures that are spatially uncorrelated with the remaining POD modes.

Figure 5.4 shows the topology of the coherent and incoherent stresses at a phase ϕ_1. The qualitative features are generally seen to be similar to those reported in an earlier study by Cantwell and Coles (1983) [32]. The coherent streamwise normal stress $\tilde{u}^2$ in figure 5.4a shows symmetry about the wake centerline and peaks away from the vortex center, close to its edges. The peaks observed are a result of positive and negative peaks of $\tilde{u}$ due to the local rotation of the vortices at this location.

The incoherent streamwise normal stress $\langle u''^2 \rangle^*$ shown in figure 5.4b follows the path of the shed vortices and displays a wavy structure, however these stresses are nor negligible close to the wake centerline nor exhibits symmetry unlike its coherent counterpart. As observed in [32], the $\langle u''^2 \rangle^*$ peaks close to the center of the vortices and the peaks are connected by thick strips of lower $\langle u''^2 \rangle^*$ close to the saddle point of the vortices. The amplitude levels of the coherent and the incoherent stresses in figures 5.4a and 5.4b are

approximately comparable, with the coherent component slightly higher than the incoherent part.

The coherent component of the Reynolds shear stress $\tilde{u}\tilde{v}$ in figure 5.4c displays an anti-symmetric behaviour. Unlike the coherent $\tilde{u}^2$ which displays peaks close to the top and bottom edges, the coherent $\tilde{u}\tilde{v}$ displays peaks close to the side-wise edges of the vortices where the saddle points are located. As observed in [32], there are regions of strong momentum influx towards the wake interior and regions where relatively weaker momentum outflux away from the wake observed with a thin layer separating the two. In addition and similar to that reported in [32], regions of high coherent shear stresses are also observed where the fluid from the external flow enters the wake, represented by alleyways between the stream lines directed towards the wake interior. The incoherent component of Reynolds shear stress $\langle u''v'' \rangle^*$ on the other hand displays a wavy structure similar to that of $\langle u''^2 \rangle^*$. Unlike the associated coherent part, the incoherent Reynolds shear stress components are mainly composed of regions with strong influx of momentum towards the wake interior. It tends to peak closer to the saddle points, similar to that observed in [32, 29]. The maximum magnitude of the coherent and incoherent component of the Reynolds shear stress appear to be closer in comparison. In addition, unlike the coherent part, the $\langle u''v'' \rangle^*$ does not display a region of strong outflux of momentum away from the wake interior in the region close to body.

Figure 5.4e shows the coherent component of the transverse Reynolds normal stress at phase ϕ_1. The peaks in $\tilde{v}^2$ appear as islands separated by small strips and displays symmetry about the geometric wake centerline. The peaks form away from the vortex center and close to its edges on the wake centerline due to the positive and negative peaks of $\tilde{v}$ arising out of local rotation of the vortices. In addition, these peaks are located at regions where the external flow penetrates to the wake. Comparatively, the peak values of $\tilde{v}^2$ appears to be more than twice that of $\tilde{u}^2$, in agreement with [32]. The incoherent component $\langle v''^2 \rangle^*$ in figure 5.4f of vertical Reynolds normal stress displays a wavy structure similar to that of $\langle u''^2 \rangle^*$. The amplitude of the wavy structure is similar closer to the body whereas it goes higher while moving down-stream. The $\langle u''^2 \rangle^*$ unlike $\langle v''^2 \rangle^*$ is spread over a relatively larger region. The $\langle v''^2 \rangle^*$ similar to $\langle u''^2 \rangle^*$ is observed to follow the path of the coherent structures and peaks closer to the vortex centers, whereas the incoherent Reynolds shear stress component is found to peak near the saddles, in agreement with the observations of [29, 32]. The magnitude of the peaks of $\langle v''^2 \rangle^*$ and $\langle u''^2 \rangle^*$ are found to be comparable, however with the former displaying slightly higher values and indicating anisotropy in the turbulent incoherent fluctuations.

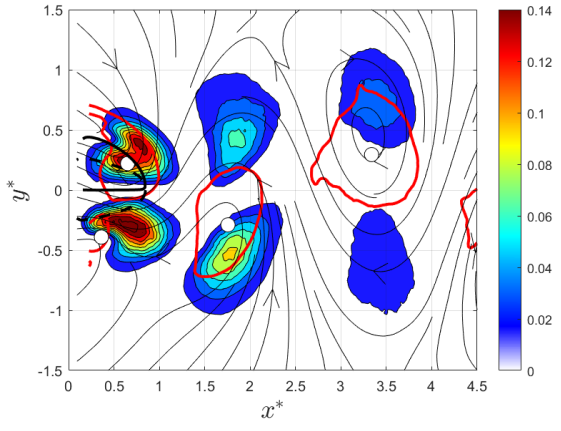

(a) $\tilde{u}^{2*}$.

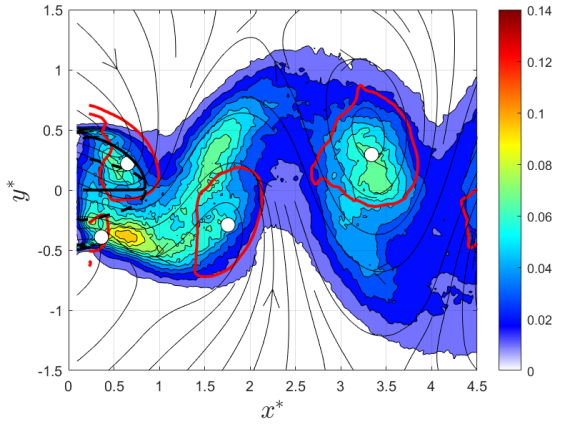

(b) $\langle u''^2 \rangle^*$.

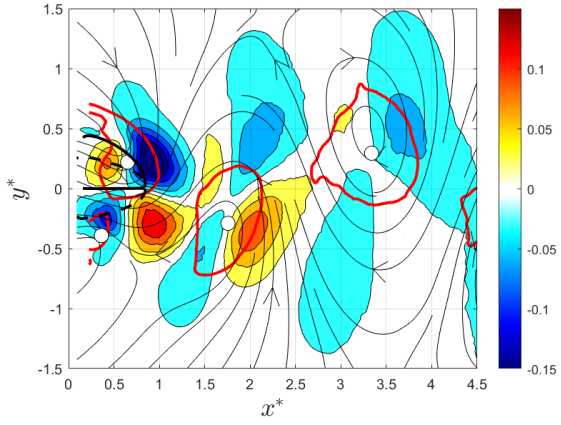

(c) $\tilde{u}\tilde{v}^*$.

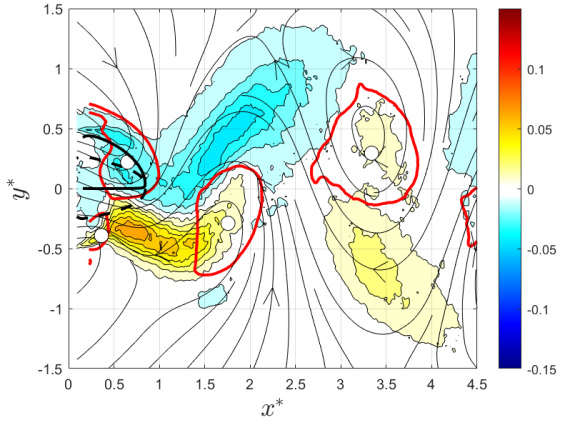

(d) $\langle u''v'' \rangle^*$.

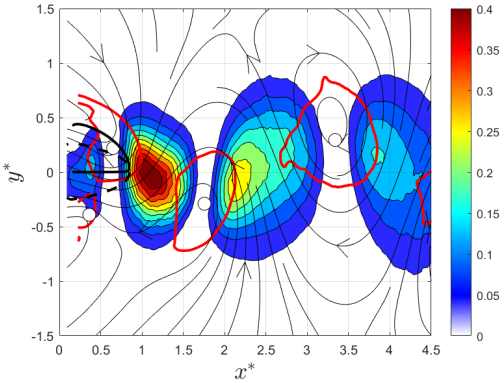

(e) $\tilde{v}^{2*}$.

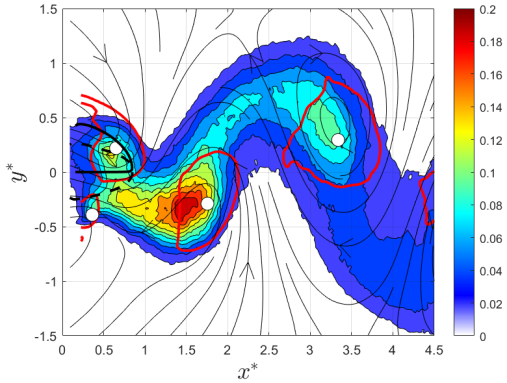

(f) $\langle v''^2 \rangle^*$.

Figure 5.4: Coherent and incoherent components of the total Reynolds stress fields at a single phase ϕ_1 for $Re_h \approx 2.8 \times 10^4$. Similar to figure 5.2a, the streamlines are that observed by an observer travelling at U_{in}. The red contours and white solid circles denote the vortices detected by the Gamma -2 criterion (5.3) and the vortex centers respectively.

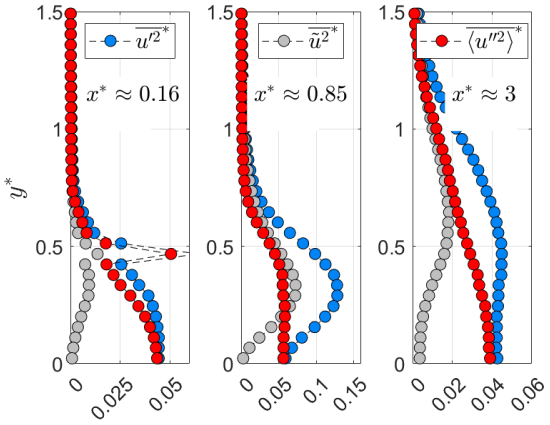

(a) $\overline{u'^2}^*$ profiles.

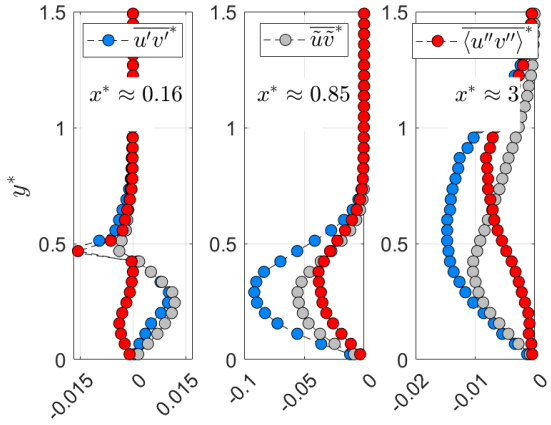

(b) $\overline{u'v'}^*$ profiles.

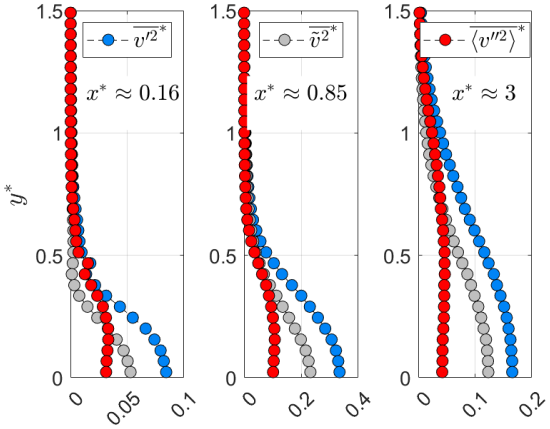

(c) $\overline{v'^2}^*$ profiles.

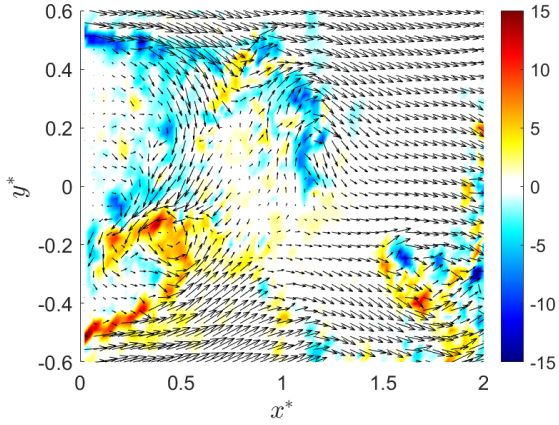

(d) Vorticity of incoherent structure convected by the mean field i.e. $\nabla \times (\mathbf{u} - \tilde{\mathbf{u}})$, at an arbitrary time within the phase ϕ_1 defined for the coherent structure.

Figure 5.5

Figure 5.5 shows profiles of Reynolds stress components split between coherent and incoherent part, based on equation (5.5). The wake being symmetric, only the profiles in the upper half is shown. The profiles of $\overline{u'^2}^*$ and $\overline{v'^2}^*$ profiles are symmetric whereas $\overline{u'v'}^*$ profiles are anti-symmetric as shown in figure 4.6a. The locations at which these profiles were taken corresponds approximately to (a) the region close to separation, (b) the end of the recirculating flow region at $x^* \approx 0.85$ where the normal and shear stresses reaches its maximum values and (c) a location farther away where the Reynolds stresses decay.

In figure 5.5a, close to the body at $x^* \approx 0.16$, $\overline{u'^2}^*$ is dominated by the incoherent stress. The coherent component is negligible and zero especially at the center. At $x^* \approx 0.16$ and roughly close to the center of the shear layer (see figure 4.3a), a peak in $\overline{u'^2}^*$ is observed. The incoherent stresses further increase and reach roughly a constant value close to the centre. In case of $\overline{u'v'}^*$, similar to that of $\overline{u'^2}^*$, it is dominated by the incoherent component at the transverse location close to the shear layer center and close to the body at $x^* \approx 0.16$. On moving further towards the center of the wake, the coherent component dominates the Reynolds shear stress and is positive indicating an out-flux of streamwise momentum

away from the wake.

In case of $\overline{v'^2}^*$ close to the body at $x^* \approx 0.16$ in figure 5.5c, similar to the other two Reynolds stress components, a peak close to the shear layer center, lesser in magnitude, is visible. Here, the incoherent stresses dominate. Towards the wake core, the incoherent component of $\overline{v'^2}^*$ rises to reach roughly a constant value and $\overline{u'^2}^*$ is dominated by the coherent component. The centerline values of $\overline{\langle u''^2 \rangle}^*$ and $\overline{\langle v''^2 \rangle}^*$, close to the body, are comparable. The peaks observed in the incoherent component of the Reynolds stresses relates to the signature of some high wave number energetic structure buried in the incoherent motions, quite similar to the peaks observed in the coherent Reynolds stress components (for example, the peaks in case of $\tilde{u}^{2*}$ due to the solid body rotation of the vortex structure in figure 5.4a). Figure 5.5d shows the vorticity of incoherent motion advected by the mean flow and estimated at phase ϕ_1. Closer to the body at the locations where the peaks in Reynolds shear and normal stresses exists, the signature of energetic structures, within the incoherent motions, in the shear layer are found in figure 5.5d represented by intense vorticity regions. It appears as a slight wavy motion. An eddying motion exists at $(x^*, y^*) \approx (0.5, -0.2)$ carrying the fluid towards the wake center. This streamwise location approximately corresponds to the center of the mean recirculating vortex. It is well known that an inflection point in the mean velocity profile such as in figure 4.3a forms a necessary condition for the appearance of instabilities according to Rayleigh's inflection point criterion [154]. In addition, the experimental results and observations made by previous studies mention the appearance of Kelvin-Helmholtz type instabilities (vortex rollup) occurring within the shear layer. For example, the flow visualization and spectral measurements in the wake reveal such structures which interacts with vortex shedding [197, 86], or in the studies of [139] where they observe traces of such structures in the spectra of velocity fluctuations [134]. The studies of [139] also concludes that such type of structures in the shear layer decides the initial development of the wake before vortex shedding dominate the flow. The observations and arguments from all these studies leads to a conclusion that the small scale structures in figure 5.5d, are associated with the secondary peaks observed in the incoherent part of the Reynolds shear and normal stresses in figures 5.5a, 5.5b and 5.5c at the location near separation, could possibly be the structures associated to Kelvin-Helmholtz instability typically observed in the shear layers (see [139] and the references therein).

Another striking feature of the Reynolds normal stress $\overline{u'^2}^*$ and shear stress $\overline{u'v'}^*$ profiles in figures 5.5a and 5.5b, near the streamwise end of the recirculating flow region, is that the double lobed structure observed in figure 4.5 is mainly due to the contribution from the coherent structures formed by the shear layer roll up. The symmetric pattern found in figure 5.4a together with the rotation of the coherent vortex structures leads to a negligible time averaged contribution of $\tilde{u}^2$ along the wake centerline, whereas the incoherent contribution is nearly constant while approaching the core of the wake. The normal stress $\overline{u'^2}^*$ is mostly dominated by the incoherent structures in the near wake, near the end of the recirculating flow region at $x^* \approx 0.85$, as well as farther downstream, at $x^* \approx 3$. In case of Reynolds shear stress, both the incoherent and coherent contributions are comparable in the near as well as farther downstream. In case of $\overline{v'^2}^*$, the upper hand is for the coherent component of the Reynolds stress in the near wake as well as farther downstream. Similar to that of $\overline{u'^2}^*$, the incoherent part of $\overline{v'^2}^*$ is approximately a constant close to the wake core and roughly twice higher than that of $\overline{\langle u''^2 \rangle}^*$. Whereas, farther downstream, the incoherent component of both the Reynolds normal stress com-

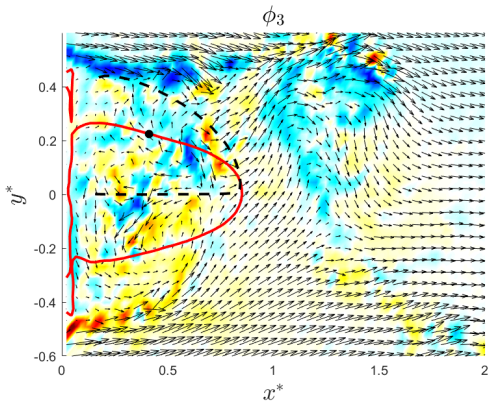

(a) $\nabla \times (\mathbf{u}' - \tilde{\mathbf{u}})$ at phase ϕ_3.

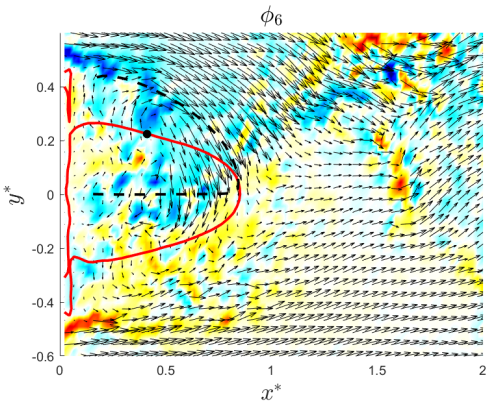

(b) $\nabla \times (\mathbf{u}' - \tilde{\mathbf{u}})$ at phase ϕ_6.

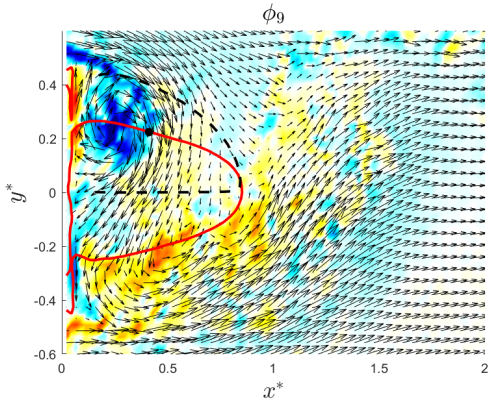

(c) $\nabla \times (\mathbf{u}' - \tilde{\mathbf{u}})$ at phase ϕ_9.

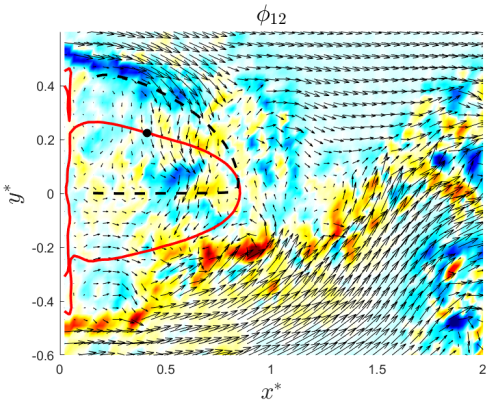

(d) $\nabla \times (\mathbf{u}' - \tilde{\mathbf{u}})$ at phase ϕ_{12}.

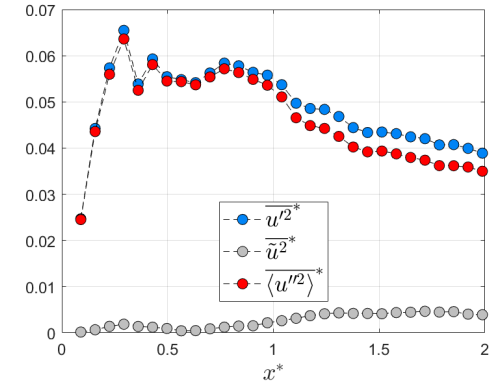

(e) Decomposition of $\overline{u'^2}^*$ along the wake centerline .

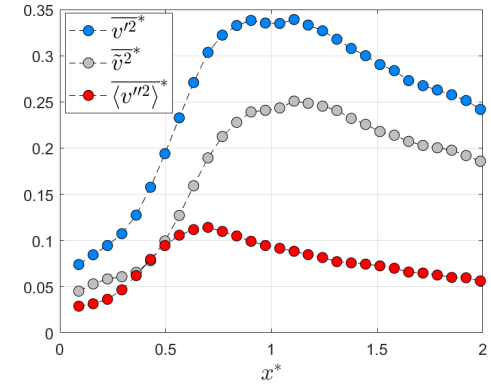

(f) Decomposition of $\overline{v'^2}^*$ along the wake centerline .

Figure 5.6: Vorticity of incoherent structure convected by the mean field i.e. $\nabla \times (\mathbf{u} - \tilde{\mathbf{u}})$, at an arbitrary time within the phase ϕ_3 (a), ϕ_6 (b), ϕ_9 (c), ϕ_{12} (d) defined for the coherent structure. The red solid line denotes the *rri* defined by the isoline $U = 0$. Decomposition of streamwise (e) and transverse (f) Reynolds normal stress respectively along the geometric wake centerline.

ponents approaches comparable values.

Finally, figures 5.6a to 5.6d shows the instantaneous vorticity of the flow field with the coherent structures, in the respective phases, removed. This reveals the vorticity due

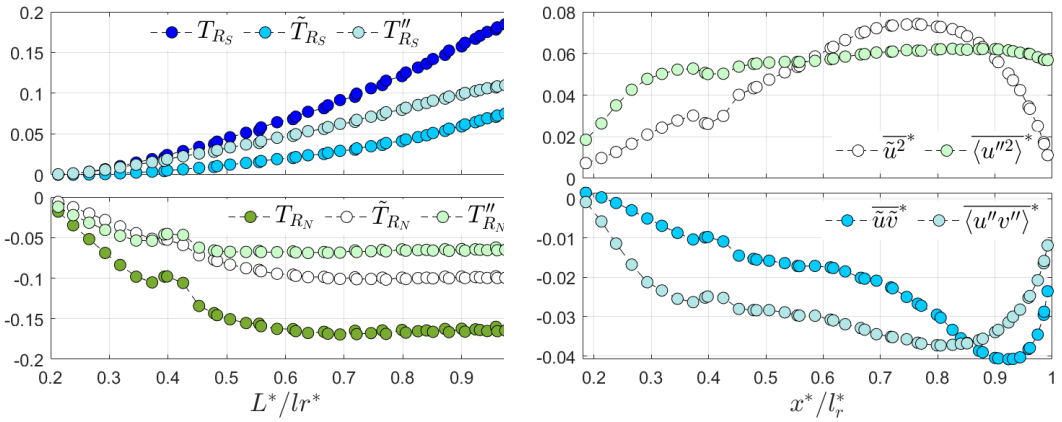

(a) (b)

Figure 5.7: Contributions of coherent and incoherent Reynolds stresses to the base pressure drag (a) and its evolution along the streamline $\psi = 0$ (b).

to incoherent structures advected by the mean flow field, similar to that of figure 5.5d. The purpose is to show the existence of energetic structures within the shear layer which are entrained in the recirculation region. These structures are known to interact with the Karman vortices (see for example [197]). The resulting incoherent Reynolds normal stress component $\overline{\langle u''^2\rangle}^*$ dominates along the centerline of the wake, displaying two peaks close to the center of the recirculating flow region where the influence of these incoherent structures in the shear layer remains strong. Similarly, $\overline{\langle v''^2\rangle}^*$ also reaches a peak close to the center of the recirculating flow region, due to the influence of energetic structures within the shear layer, that dominates within the incoherent structures. It is also seen that the magnitude of the peak of $\overline{\langle v''^2\rangle}^*$ is higher than that of $\overline{\langle u''^2\rangle}^*$. But this difference decreases farther downstream and the flow slowly tends an isotropic state in the wake.

5.2 Contributions of the coherent and incoherent structures to the mean base pressure drag.

The contributions of the streamwise Reynolds normal and shear stresses, split into the coherent and incoherent structures and their contributions to the time averaged base pressure drag is shown in figure 5.7a. The contributions from the coherent and incoherent structures are represented by the superscripts $(\tilde{\cdot})$ and $(\cdot'')$ respectively. Near separation, the coherent structures are in their forming stage. Their contributions to the Reynolds stresses are therefore negligible. Incoherent structures, on the other hand, are active near the shear layer center with a strong contribution to the Reynolds stresses. They grow faster that coherent structures within the streamwise extent of the first half of the recirculating flow region (see figures 5.5 and 5.6 and 5.7b). This causes a higher contribution of the incoherent structures to the Reynolds shear and normal stresses near separation, in figure 5.7a growing rapidly until $0.3l_r^*$ after which they roughly remains a constant throughout except for the incoherent shear stress which tends to zero near l_r^* as the streamline $\psi = 0$ reaches the wake centerline. Coherent structures grow relatively slowly gradually reaching a peak closer to l_r^* but tending to zero at l_r^* as the streamline touches

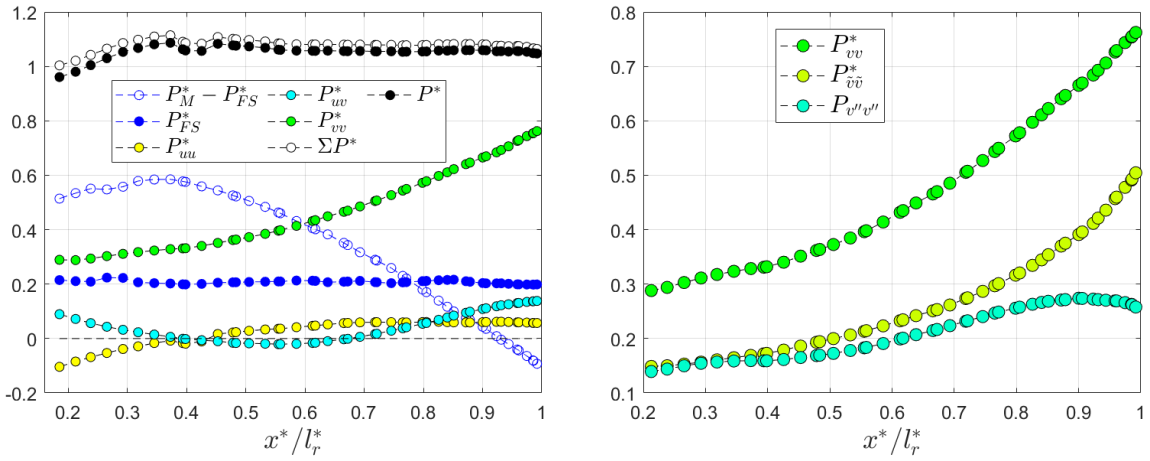

Figure 5.8: Decomposition of the mean pressure along the streamline defined by the stream function $\psi = 0$, which forms the lateral boundary of the CV shown in figure 4.19. All the terms are normalized by the spatially averaged base pressure. The description of the legends are same as that given in figure 4.13.

the wake centerline (see figure 5.7b). ${T''}_{R_N}$ reaches -7% near $0.4l^*_r$ after which it remains constant and $\tilde{T}_{R_N}$ grows to approximately -11% near the center of the recirculating flow region. For the Reynolds shear stress, its initial magnitude near separation is important since the transverse normal component n_y is the highest near separation and tends to zero as the bubble curves inward near l^*_r. Hence, the contribution of incoherent Reynolds shear stress is higher than that of its coherent counterpart and peaks at 11% while the latter peaks at 7% at l^*_r.

The mean pressure along the streamline, defined by $\psi = 0$, is also split and each part is shown in figure 5.8a. Note that the mean pressure here is normalised by the mean base pressure

$$\frac{1}{h^*} \int_{Base} P^* dy^*.$$

A marginal difference between the sum of pressure solutions represented by ΣP^* and the pressure reconstructed using the optimal control algorithm P^* can be seen, which is to be expected. The magnitude of the mean pressure P^*, along the streamline $\psi = 0$, is seen to be greater than or equal to the average base pressure of the body, however its magnitude remains approximately a constant.

The term P^*_{FS} which represents the free-stream pressure, primarily due to the blockage by the body and by the test-section wall boundary layer, remains a constant at 15% of the average base pressure. Near the body-base, the mean pressure due to $\overline{u'^2}^*$ and $\overline{u'v'}^*$ tends to cancel each other until $0.4l^*_r$, after which P^*_{uu} and P^*_{uv} remains negligible. Close to the end of the recirculating flow region, the P^*_{uv} peaks close to 15% of the average mean base pressure.

P^*_{vv} may further be split into coherent and incoherent contributions, along the streamline $\psi = 0$ (see figure 5.8b). Closer to the separation point, the 30% contribution of P^*_{vv} to the base pressure, is driven by 50% from coherent and incoherent structures. It remains roughly a constant until $0.4l^*_r$ after which the contribution of coherent structures

to P^*_{vv} increases owing to the developing coherent structures. The contribution from the incoherent structure also increases after $0.5l^*_r$ and peaks at $0.9l^*_r$ providing close to 30% of the base pressure.
The integral contribution of the mean pressure to the budget of the base pressure drag may also be decomposed but, conclusions are similar to that in figure 5.8a.

The average contribution to the base pressure drag between mean flow,coherent and incoherent structures, can be defined by,

$$I = \frac{1}{l^*_r} \int_0^{l^*_r} T \quad \mathrm{d}L^*, \tag{5.6}$$

where T represents the total contribution of a term at each L^*. For example, $I_{uu} = \frac{1}{l^*_r} \int_0^{l^*_r} (T_{R_N})\, \mathrm{d}L^*$ represents the total contribution of the streamwise Reynolds normal stress $\overline{u'^2}^*$ to the base-pressure drag in the budget performed in figure 4.19. The resulting integral contributions are shown in figure 5.9a. The direction of the arrows represent the source or sink of the base pressure drag. The mean pressure contribution acts to increase the mean base pressure drag with a dominant contribution of 112%. The streamwise Reynolds normal stress $\overline{u'^2}^*$ acts to reduce the mean base pressure drag, and hence the arrow pointing away from the main node Cd^{Base}, with an integral contribution of 13.6%, out of which 43% of I_{uu} comes from the incoherent structures and the remaining from the coherent part. The Reynolds shear stress tends to increase the base drag contributing up to 7.6% of the mean base pressure drag, out of which the incoherent stress dominates with 66% and the remaining 34% Reynolds shear stress comes from the coherent structures. The least contribution comes from the mean momentum term with only 5% of the mean base pressure drag. Note that the mean momentum term I_U tends to decrease the mean base pressure drag and hence it is shown with an arrow pointing away from the main node Cd^{Base}.

The dominant pressure contributions to the mean base pressure drag are split between its constituent building blocks and its integral contribution, using the definition given in equation (5.6), is shown in figure 5.9b. The least contributors to I_P is due to the mean pressure contributions arising from the Reynolds streamwise normal stress (2%) and from the Reynolds shear stress (8.9%). The blockage contributes up to 16% of the integral mean pressure contribution I_P. The contribution to I_P from the mean flow deformations, which is intense close to the body, due to a strong shear layer, and dies down while nearing the end of the recirculating flow region, contributes on an average 29% of the total I_P. The transverse Reynolds normal stress, though it does not contribute explicitly to the base pressure drag, acts through the mean pressure tending to increase the mean base pressure drag. The mean pressure due to the transverse Reynolds normal stress $\overline{v'^2}^*$ is the dominant one (44% of I_P on an average) driving the total mean pressure contributions I_P, out of which the effect of the large scale von-Kàrmàn like vortex shedding is the dominant one contributing upto 57% of the $I_{P_{vv}}$, whereas the incoherent structures, though not dominant, has a significant contribution of 43% of $I_{P_{vv}}$.

The simple integral momentum budget along the CV defined using the streamline $\psi = 0$ shows that the coherent structures as well as the incoherent ones has a significant contribution to the mean base pressure drag, both explicitly and implicitly through the Reynolds streamwise normal stress, the Reynolds shear stress and the mean pressure due

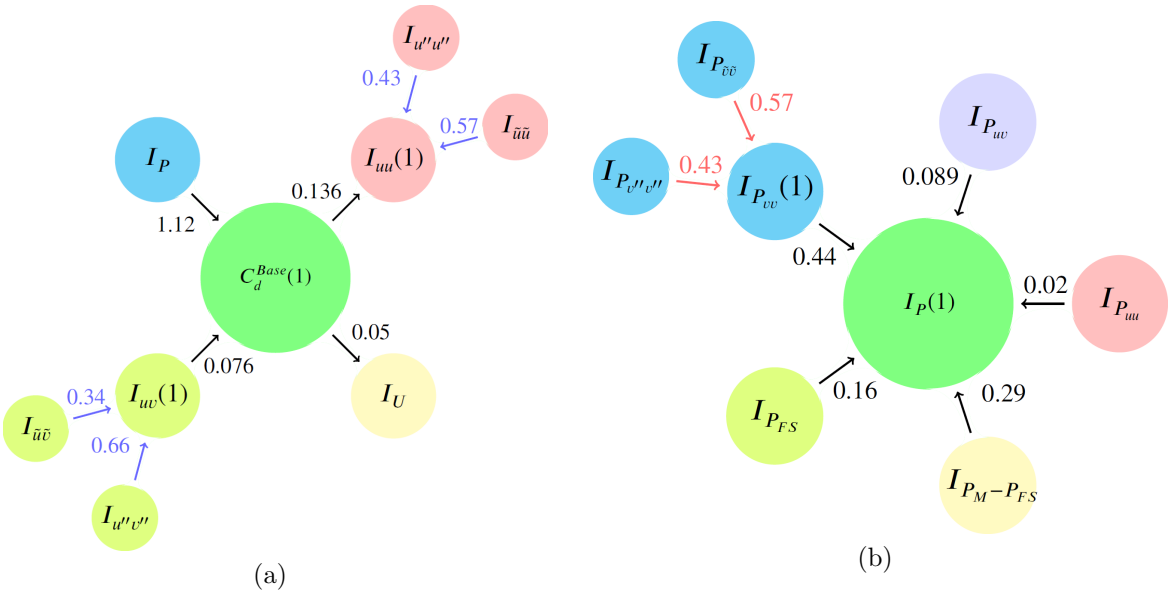

Figure 5.9: The integral contributions of Reynolds stress, pressure and the mean momentum to the base pressure drag, based on the integral momentum budget performed in figure 4.19 (a), the integral quantification of the constituent building blocks of the mean pressure contributions to the base pressure drag (b).

to the transverse Reynolds normal stress. Therefore, it is necessary to understand the mechanism that drives the coherent structures. The strategy is similar to that followed in section 4.3 but for the coherent Reynolds stresses in order to understand how energy from the mean flow is redistributed amongst the coherent Reynolds stress components. Further, this may reveal the mechanism by which energy is fed to the incoherent structures since it is believed that the coherent structures feed the incoherent ones [133, 149, 12]. However, it is to be noted that the method of triple decomposition followed, as briefly mentioned in section 5.1.1, extracting the coherent structures by ensemble averaging of instantaneous velocity fields in the corresponding phase-bin simplifies the transport equation since few terms becomes zero similar to that in equation (5.5).

5.2.1 Coherent Reynolds stress transport

The transport equation for the coherent Reynolds stresses reads:

$$\underbrace{U_k\frac{\partial\overline{\tilde{u}_i\tilde{u}_j}}{\partial x_k}}_{\tilde{\mathcal{A}}_{ij}} = \underbrace{-\left\{\overline{\tilde{u}_j\tilde{u}_k}\frac{\partial U_i}{\partial x_k}+\overline{\tilde{u}_i\tilde{u}_k}\frac{\partial U_j}{\partial x_k}\right\}}_{\tilde{\mathcal{P}}_{ij}} \overbrace{-\frac{1}{\rho}\frac{\partial}{\partial x_k}\left(\overline{\tilde{p}\left(\delta_{ik}\tilde{u}_j+\delta_{jk}\tilde{u}_i\right)}\right)}^{\tilde{\mathcal{D}}^{\tilde{p}}_{ij}} + \underbrace{\frac{2}{\rho}\overline{\tilde{p}\tilde{s}_{ij}}}_{\widetilde{\mathcal{PS}}_{ij}}$$
$$\underbrace{-\frac{\partial}{\partial x_k}\left(\overline{\tilde{u}_i\tilde{u}_j\tilde{u}_k}\right)}_{\tilde{\mathcal{D}}_{ij}}\underbrace{-\frac{\partial}{\partial x_k}\left(\overline{\langle u_i''u_k''\rangle\tilde{u}_j}+\overline{\langle u_j''u_k''\rangle\tilde{u}_i}\right)}_{\mathcal{D}''_{ij}}$$
$$-\underbrace{\left(-\overline{\langle u_i''u_k''\rangle\frac{\partial\tilde{u}_j}{\partial x_k}}-\overline{\langle u_j''u_k''\rangle\frac{\partial\tilde{u}_i}{\partial x_k}}\right)}_{\mathcal{P}''_{ij}}\underbrace{-2\nu\overline{\left(\frac{\partial\tilde{u}_i}{\partial x_k}\frac{\partial\tilde{u}_j}{\partial x_k}\right)}}_{\tilde{\varepsilon}_{ij}}+\underbrace{\frac{\partial}{\partial x_k}\left(\nu\frac{\partial}{\partial x_k}\overline{\tilde{u}_i\tilde{u}_j}\right)}_{(\mathcal{D}_{\nu_{ij}})},$$

$$\tilde{\mathcal{A}}_{ij} = \tilde{\mathcal{P}}_{ij} + \tilde{\mathcal{D}}^{\tilde{p}}_{ij} + \widetilde{\mathcal{PS}}_{ij} + \tilde{\mathcal{D}}_{ij} + \mathcal{D}''_{ij} - \mathcal{P}''_{ij} - \tilde{\varepsilon}_{ij} + \mathcal{D}_{\nu_{ij}} \tag{5.7}$$

where the subscript refers to the component of the Reynolds stress tensor. The interpretation of various terms are similar to that of equation (4.13). For instance, the left-hand side of equation (5.7) is the spatial transport of the coherent Reynolds stress $\overline{\tilde{u}_i\tilde{u}_j}$ in a time averaged sense, whereas the right hand side of the equation describes its mechanism. The term $\tilde{\varepsilon}_{ij}$ is expected to be extremely small, because the dissipation essentially takes place at the smallest scales (see for instance [132]). The viscous diffusion of the coherent Reynolds stress is seen to be extremely small and hence it shall not be shown in the balance plots. $\tilde{\mathcal{P}}_{ij}$ is similar to $\mathcal{P}_{ij}$ in equation (4.13) acting as a source term extracting the energy from the mean flow and injecting it to the coherent structures. The terms $\tilde{\mathcal{D}}^{\tilde{p}}_{ij}$, $\mathcal{D}_{ij}$ and $\mathcal{D}''_{ij}$ respectively, represent the turbulent diffusion of Reynolds stresses, due to coherent pressure, coherent and incoherent motions respectively, since its integral over a large control volume vanishes (see [142]), or in other words it merely redistributes stresses within the flow.

The pressure strain term $\widetilde{PS}_{ij}$, similar to $\mathcal{PS}_{ij}$, merely acts to redistribute energy within the Reynolds normal stress components. However, in the case of coherent Reynolds shear stress components, it may act as a sink or source causing a net rate of change of the Reynolds shear stresses. Finally the term $\mathcal{P}''_{ij}$, is a production term as the integral of it over a large control volume does not vanish, and it acts to extract energy from the coherent structures passing it on to the incoherent structures since this term is positive in the equation for transport of incoherent Reynolds stresses.

The mean flow being two dimensional, the mean spanwise component of the velocity is zero and hence, the advection term can be estimated accurately. Further, the mean two dimensional flow field eliminates the mean spanwise gradient of the mean spanwise velocity and hence the production term $\tilde{\mathcal{P}}_{ij}$ can be estimated accurately. Among the diffusion terms, if the coherent structures are predominantly two dimensional, then the spanwise gradient terms can be assumed to be very small. This is also the case for the production term $\mathcal{P}''_{ij}$. The pseudo-dissipation and the viscous diffusion terms, being negligibly small,

is not important such that the equation shall be in balance even if those terms are not included. Therefore, the only terms that remains are those with the coherent pressure in it, such as the coherent pressure diffusion $\tilde{\mathcal{D}}_{ij}^{\tilde{p}}$ and the coherent pressure strain $\widetilde{\mathcal{PS}}_{ij}$ terms, which may not be negligible.

In the following section, the method to compute the coherent pressure fluctuations from the 2D planar PIV velocity fields is discussed.

5.3 Pressure of coherent structures

The fluctuating pressure is an important quantity that determines the fluctuating forces experienced by the bluff body. However, the effect of fluctuating pressure on the mean drag is not well documented. The reduction of fluctuating pressure was found to lead to a reduced mean drag (see [40]) and therefore represents an important quantity for flow control purposes. Similar to the decomposition of the fluctuating velocity, the fluctuating pressure can also be decomposed between a coherent and an incoherent part. This allows for analysing flow fields in a phase-averaged sense. Similar to the mean pressure gradient, the coherent pressure gradient may also be estimated directly from the knowledge of coherent and incoherent velocity fields. This allows for performing a phase-by-phase local momentum budget and understand the mechanism responsible for its transport. However, the knowledge of coherent pressure rather than its gradient is still required to perform a global phase-by-phase momentum budget (along a control volume) in order to estimate the quasi-instantaneous drag force and to understand the role of various transport terms.

The mean drag force of the bluff body is due to contribution from various transport terms such as the mean momentum, the Reynolds stresses and mean pressure. The driving mechanism of mean momentum may be understood by performing local mean momentum budget at specific streamwise locations, for which the knowledge of mean pressure gradient, estimable directly from the PIV obtained velocity fields, is the only necessary information. In order to understand the driving mechanism of Reynolds stresses, attention has to be turned onto the Reynolds stress transport equation which permits identifying the mechanism of transport of individual Reynolds stress terms. This is unlike the turbulent kinetic energy budget equation, where it doesn't yield information on the transport of individual Reynolds stress terms. The budget of Reynolds stress transport requires the knowledge of certain terms such as diffusion due to the third component of fluctuating velocity, dissipation and the fluctuating pressure, for its closure. The dissipation in the near wake is typically found to be negligible in the near wake (see [132]). However, the residual terms including that due to fluctuating pressure and the third component of fluctuating velocity remains unknown.

An alternative is to split the Reynolds stresses into coherent and incoherent part and analyse the transport equations for both separately. Since it is the coherent structures that dominate a two-dimensional bluff body wake, the budget of coherent Reynolds stress transport can already reveal important driving mechanisms and may also shed light on the energy exchange between the coherent and the incoherent structures since the sink term in the coherent Reynolds stress transport equation acts as a source term in the incoherent Reynolds stress transport equation. In [12], where they study the interac-

tion of multiple coherent structures produced by multiple wakes of bluff bodies and the mechanism of energy transfer between them, it is speculated that the diffusion due to the coherent pressure along with the other residual terms could be an important contributor to the transport of coherent turbulent kinetic energy, however it was not estimated in their works and hence its contribution was not quantified. [149] observed that the fluctuating pressure plays an important role in the energy exchange between mean and fluctuating motion in the wake of a square cylinder at $Re \sim \mathcal{O}(10^2)$. Examining the transport equation for coherent Reynolds stress transport, one may notice that the coherent dissipation term is not important as the dissipation largely takes place at smaller scales or at the level of incoherent structures. If the coherent structures are predominantly two-dimensional in nature, we may notice that the only dominant terms that needs to be determined are those with the coherent pressure included in it. The estimation of coherent pressure should allow for the partial closure of the Reynolds stress transport equation.

This section focuses on estimating the coherent pressure from the knowledge of two dimensional velocity fields readily available from the PIV experiment.

5.3.1 Theoretical background and coherent pressure estimation

Similar to the mean pressure, we may estimate the coherent pressure by inverting the Poisson's operator for the coherent pressure. From the transport of coherent momentum, one may write the local gradient of coherent pressure as,

$$\frac{\partial}{\partial x_j}\left(\tilde{p}\delta_{ij}\right) = -\rho\left\{\frac{\partial \tilde{u}_i}{\partial t} + \frac{\partial}{\partial x_j}\left(\tilde{u_j}U_i + U_j\tilde{u_i} - 2\nu\tilde{s}_{ij} + \tilde{u}_i\tilde{u}_j + \langle u_i''u_j''\rangle - \overline{\tilde{u}_i\tilde{u}_j} - \overline{\langle u_i''u_j''\rangle}\right)\right\}, \tag{5.8}$$

where U, $\tilde{u}$ and u'' are the mean, coherent and incoherent velocities respectively. Applying the divergence operator to equation (5.8) results in a Poisson's equation for the coherent pressure given as,

$$\frac{\partial}{\partial x_i}\left(\frac{\partial}{\partial x_j}\left(\tilde{p}\delta_{ij}\right)\right) = -\rho\frac{\partial}{\partial x_i}\left\{\frac{\partial}{\partial x_j}\left(\left[\tilde{u_j}U_i + U_j\tilde{u_i}\right] + \left[\tilde{u}_i\tilde{u}_j + \langle u_i''u_j''\rangle - \overline{\tilde{u}_i\tilde{u}_j} - \overline{\langle u_i''u_j''\rangle}\right]\right)\right\}, \tag{5.9}$$

where the time dependency and the viscous term vanishes owing to the divergence-free velocity fields. The second-order source term formed by the Poisson's equation for the coherent pressure (5.9) can be solved using Neumann type boundary condition (5.8). However, it is to be noted that the boundary terms involve a time dependent term. The time derivative of the coherent velocity $\tilde{\mathbf{u}}(\mathbf{x}, \phi, t)$, while extracting the coherent structures based on a time resolved signal that indicates the phase of the periodic coherent signal, may be written as,

$$\frac{\partial \tilde{\mathbf{u}}}{\partial t} = \frac{\partial \tilde{\mathbf{u}}}{\partial \phi}\frac{\partial \phi}{\partial t} = 2\pi f\frac{\partial \tilde{\mathbf{u}}}{\partial \phi}, \tag{5.10}$$

where f is the frequency of the band-passed time resolved signal based on the phase averaging is carried out [190]. In the present set of experiments, phase averaging method based on a pressure signal sampled at a high frequency, sufficient to capture the dominant mode, was not successful. As such, the coherent structures in this study are obtained by a POD based method that represents phase averaging, where the phase selection is carried out based on the time coefficients of the first two modes with very similar energy levels

(see [192]). This method of phase averaging, suitable for flow data that are arbitrarily spaced in time, provides a fairly good representation of the well documented von-Kàrmàn vortex street. The disadvantage is that the time dependency of the coherent structure is lost. However, the time derivative may be approximated using equation (5.10) using the frequency information available from the pressure signals, since the dominant frequency captured by the pressure signal corresponds to the well documented von-Kàrmàn vortex street and the POD-based phase average extracts the spatially coherent modes that represents the von-Kàrmàn vortex street (see [128] for instance). Therefore, the time derivative of the coherent velocity $\tilde{u}_i$ at phase ϕ_i may be approximated using a second-order central difference scheme as,

$$\frac{\partial \tilde{u}_i}{\partial t}\mid_{\phi_k} = 2\pi f\left(\frac{\tilde{u}_i\mid_{\phi_{k+1}} - \tilde{u}_i\mid_{\phi_{k-1}}}{2\Delta\phi}\right) = fN_\phi\left(\frac{\tilde{u}_i\mid_{\phi_{k+1}} - \tilde{u}_i\mid_{\phi_{k-1}}}{2}\right), \tag{5.11}$$

where N_ϕ represents the number of phases that the periodic signal is split into. This is a first approximation of the temporal derivative. It can be further improved by considering the temporal derivative of spanwise vorticity, i.e.,

$$\frac{\partial \tilde{\omega}_z}{\partial t} = \frac{\partial}{\partial x}\left(\frac{\partial \tilde{v}}{\partial t}\right) - \frac{\partial}{\partial y}\left(\frac{\partial \tilde{u}}{\partial t}\right) = -\Delta\left(\frac{\partial \psi}{\partial t}\right), \tag{5.12}$$

where ψ is the streamfunction and $\tilde{\omega} = \nabla \times \tilde{\mathbf{u}}$. Rearranging the transport equation for the coherent momentum and representing the right-hand side of the time derivatives as,

$$\begin{aligned}
\frac{\partial \tilde{u}}{\partial t} =& -\left\{\tilde{u}\frac{\partial U}{\partial x} + \tilde{v}\frac{\partial U}{\partial y} + U\frac{\partial \tilde{u}}{\partial x} + V\frac{\partial \tilde{u}}{\partial y}\right\} - \frac{1}{\rho}\frac{\partial \tilde{p}}{\partial x} - \frac{\partial}{\partial x}\left(\tilde{u}^2 + \langle u''^2\rangle - \overline{\tilde{u}^2} - \overline{\langle u''^2\rangle}\right) \\
&- \frac{\partial}{\partial y}\left(\tilde{u}\tilde{v} + \langle u''v''\rangle - \overline{\tilde{u}\tilde{v}} - \overline{\langle u''v''\rangle}\right) + \frac{\partial}{\partial x}\left(2\nu\tilde{s}_{11}\right) + \frac{\partial}{\partial y}\left(2\nu\tilde{s}_{12}\right) = f_t(\tilde{u}) \\
\text{and} \\
\frac{\partial \tilde{v}}{\partial t} =& -\left\{\tilde{u}\frac{\partial V}{\partial x} + \tilde{v}\frac{\partial V}{\partial y} + U\frac{\partial \tilde{v}}{\partial x} + V\frac{\partial \tilde{v}}{\partial y}\right\} - \frac{1}{\rho}\frac{\partial \tilde{p}}{\partial y} - \frac{\partial}{\partial x}\left(\tilde{u}\tilde{v} + \langle u''v''\rangle - \overline{\tilde{u}\tilde{v}} - \overline{\langle u''v''\rangle}\right) \\
&- \frac{\partial}{\partial y}\left(\tilde{v}^2 + \langle v''^2\rangle - \overline{\tilde{v}^2} - \overline{\langle v''^2\rangle}\right) + \frac{\partial}{\partial x}\left(2\nu\tilde{s}_{21}\right) + \frac{\partial}{\partial y}\left(2\nu\tilde{s}_{22}\right) = f_t(\tilde{v}),
\end{aligned} \tag{5.13}$$

the problem is to solve the Poisson equation for the temporal derivative of the streamfunction in the interior of the domain, i.e.,

$$\Delta\left(\frac{\partial \psi}{\partial t}\right) = -\left(\frac{\partial}{\partial x}\left(f_t(\tilde{v})\right) - \frac{\partial}{\partial y}\left(f_t(\tilde{u})\right)\right), \quad in\ \ \Omega, \tag{5.14}$$

with Neumann-type boundary conditions,

$$\nabla\left(\frac{\partial \psi}{\partial t}\right)\cdot n = \begin{cases} \frac{\partial}{\partial x}\left(\frac{\partial \tilde{\psi}}{\partial t}\right) = -\frac{\partial \tilde{v}}{\partial t} = -f_t(\tilde{v}) \text{ on the transverse domain-boundaries,} \\ \frac{\partial}{\partial y}\left(\frac{\partial \tilde{\psi}}{\partial t}\right) = \frac{\partial \tilde{u}}{\partial t} = f_t(\tilde{u}) \text{ on the lateral domain-boundaries.} \end{cases} \tag{5.15}$$

Once the solution $\frac{\partial \psi}{\partial t}$ is found, the temporal velocity derivative can be estimated simply by the spatial derivative,

$$\frac{\partial \tilde{u}}{\partial t} = \frac{\partial}{\partial y}\left(\frac{\partial \psi}{\partial t}\right) \text{ and } \frac{\partial \tilde{v}}{\partial t} = -\frac{\partial}{\partial x}\left(\frac{\partial \psi}{\partial t}\right). \tag{5.16}$$

The advantage of estimating the temporal derivative of streamfunction to estimate the temporal derivative of velocities in equation (5.14) is that the coherent pressure information is not required in the interior of the domain, because $\nabla \times \nabla \tilde{p} = 0$. But, the coherent pressure information is required at the boundary. Therefore, a first estimation of the pressure is carried out by solving the Poisson equation for coherent pressure (5.9) and by specifying boundary conditions that involve the temporal derivative of velocities, approximated using the finite difference estimation (5.11). Further, this first estimate of coherent pressure is used to recompute the temporal derivative of velocity, using the equation (5.16), which is then input to the coherent pressure solver in order to re-estimate the coherent pressure. The vectors of temporal velocity derivatives estimated using equation (5.16) are divergence free by construction and are based on the assumption that the coherent velocity fields are 2D.

The assumption of coherent structures being predominantly two-dimensional in nature is also used, in order to compute the source and the boundary terms for estimation of coherent pressure. The PIV experiment in this study being planar, the only velocity components obtained are the streamwise and the transverse ones. This leads to certain missing terms while computing the source and the boundary terms. For example, considering the source term, we may simplify the first set of terms on the right hand side of equation (5.9) in the square brackets, using zero divergence condition of the coherent velocity fields, as,

$$\Delta\tilde{p}_{Mc} = -2\rho\left\{\frac{\partial U}{\partial x}\frac{\partial \tilde{u}}{\partial x} + \frac{\partial V}{\partial y}\frac{\partial \tilde{v}}{\partial y} + \frac{\partial U}{\partial y}\frac{\partial \tilde{v}}{\partial x} + \frac{\partial V}{\partial x}\frac{\partial \tilde{u}}{\partial y}\right\}, \tag{5.17}$$

where it is free of any three-dimensional effects. Expanding the second set of terms on the right-hand side of the equation (5.9),

$$\begin{aligned}\Delta\tilde{p}_{Rs} = -\rho\Bigg\{&\frac{\partial^2}{\partial x^2}\left[\tilde{u}^2 + \langle u''^2\rangle - \left(\overline{\tilde{u}^2} + \overline{\langle u''^2\rangle}\right)\right] + 2\frac{\partial^2}{\partial x\partial y}\left[\tilde{u}\tilde{v} + \langle u''v''\rangle - \left(\overline{\tilde{u}\tilde{v}} + \overline{\langle u''v''\rangle}\right)\right]\\ &+2\frac{\partial^2}{\partial x\partial z}\left[\tilde{u}\tilde{w} + \langle u''w''\rangle - \left(\overline{\tilde{u}\tilde{w}} + \overline{\langle u''w''\rangle}\right)\right] + \frac{\partial^2}{\partial y^2}\left[\tilde{v}^2 + \langle v''^2\rangle - \left(\overline{\tilde{v}^2} + \overline{\langle v''^2\rangle}\right)\right]\\ &+2\frac{\partial^2}{\partial y\partial z}\left[\tilde{v}\tilde{w} + \langle v''w''\rangle - \left(\overline{\tilde{v}\tilde{w}} + \overline{\langle v''w''\rangle}\right)\right] + \frac{\partial^2}{\partial z^2}\left[\tilde{w}^2 + \langle w''^2\rangle - \left(\overline{\tilde{w}^2} + \overline{\langle w''^2\rangle}\right)\right]\Bigg\},\end{aligned} \tag{5.18}$$

where all the time-averaged cross Reynolds stress terms involving the third dimensional velocity component $\tilde{w}$ or w'' is zero owing to the two-dimensional mean flow (see [128]). Due to the time averaged mean two-dimensional flow, the spanwise variation of spanwise normal Reynolds stresses $\overline{\tilde{w}^2} + \overline{\langle w''^2\rangle}$ also has to be null. The phase averaged contribution of cross Reynolds stress terms involving the third dimensional velocity component need not be zero (see [208]). These terms are not accessible by the conventional two-dimensional planar PIV. Further, assuming a two dimensional dominant mode, their spanwise gradients are assumed to be zero. Owing to these assumptions, we are finally left with three terms from equation (5.18) as,

$$\begin{aligned}\Delta\tilde{p}_{Rs} = -\rho\Bigg\{&\frac{\partial^2}{\partial x^2}\left[\tilde{u}^2 + \langle u''^2\rangle - \left(\overline{\tilde{u}^2} + \overline{\langle u''^2\rangle}\right)\right] + 2\frac{\partial^2}{\partial x\partial y}\left[\tilde{u}\tilde{v} + \langle u''v''\rangle - \left(\overline{\tilde{u}\tilde{v}} + \overline{\langle u''v''\rangle}\right)\right]\\ &+\frac{\partial^2}{\partial y^2}\left[\tilde{v}^2 + \langle v''^2\rangle - \left(\overline{\tilde{v}^2} + \overline{\langle v''^2\rangle}\right)\right]\Bigg\}.\end{aligned} \tag{5.19}$$

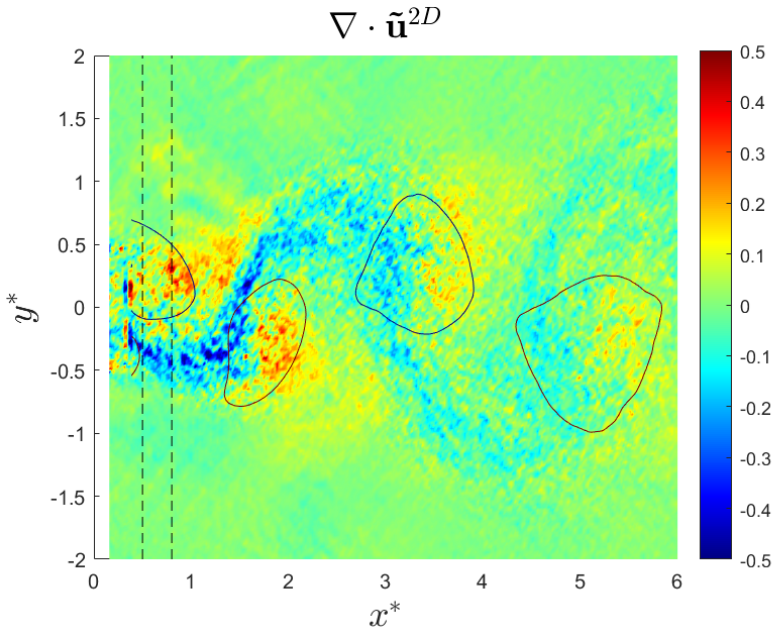

Figure 5.10: Divergence of the coherent velocity fields at phase ϕ_1.

Similarly, for the boundary terms involving the pressure gradient terms, the spanwise gradients of the phase and time averaged cross stream Reynolds stress terms involving the third dimensional velocity component, are assumed to be zero. Finally, the boundary condition projected along the normal of the planar surface written as,

$$\frac{\partial \tilde{p}}{\partial z} \approx -\rho \left\{ \frac{\partial \tilde{w}}{\partial t} + \frac{\partial}{\partial x}\left(U\tilde{w} + \tilde{u}\tilde{w} + \langle u''w''\rangle\right) + \frac{\partial}{\partial y}\left(V\tilde{w} + \tilde{v}\tilde{w} + \langle v''w''\rangle\right) \right\}, \tag{5.20}$$

where the two-dimensional assumption is again used to remove the spanwise variation of phase averaged cross stream Reynolds stresses, the terms involving mean spanwise velocity W, and the time averaged cross stream Reynolds stresses - found to be zero in the cylinder wake by [128]. The spanwise coherent velocity shows a pattern similar to that of $\tilde{u}$ in [208] but is out of phase with respect to $\tilde{u}$. This implies that the remaining terms in equation 5.20 is non zero. The terms contributing to the spanwise coherent pressure gradient, though not accessible in this study, is written in order to emphasize that the three-dimensional effects may not be negligible. However, if the flow is really two dimensional and since we are estimating pressure on a very thin plane, then the terms in equation (5.20), that forms the Neumann boundary condition in the spanwise direction $\left(\frac{\partial \tilde{p}}{\partial z}\right)$, gets cancelled out because of the surface normal that points in the opposite directions, i.e. in $+z$ and $-z$ directions respectively. We may verify the assumption of two dimensional modes by estimating the two-dimensional divergence of the coherent velocity fields. Figure 5.10 shows the divergence computed using the coherent streamwise and transverse velocity field at phase ϕ_1. The residual resulting from the divergence operation seems to be mild (lower than unity) especially in the near-wake region, close to the body until at least $x^* \approx 2$. The PIV obtained velocity fields inherently contain noise. Even though the phase averaging reduces the noise levels, it may still be present and the derivative operation can amplify the noise level present [56].

Figures 5.11a and 5.11b shows the coherent streamwise and transverse velocity profiles, and the $2D$ divergence at the streamwise locations of $x^* \approx 0.5$ and $x^* \approx 0.8$. Note

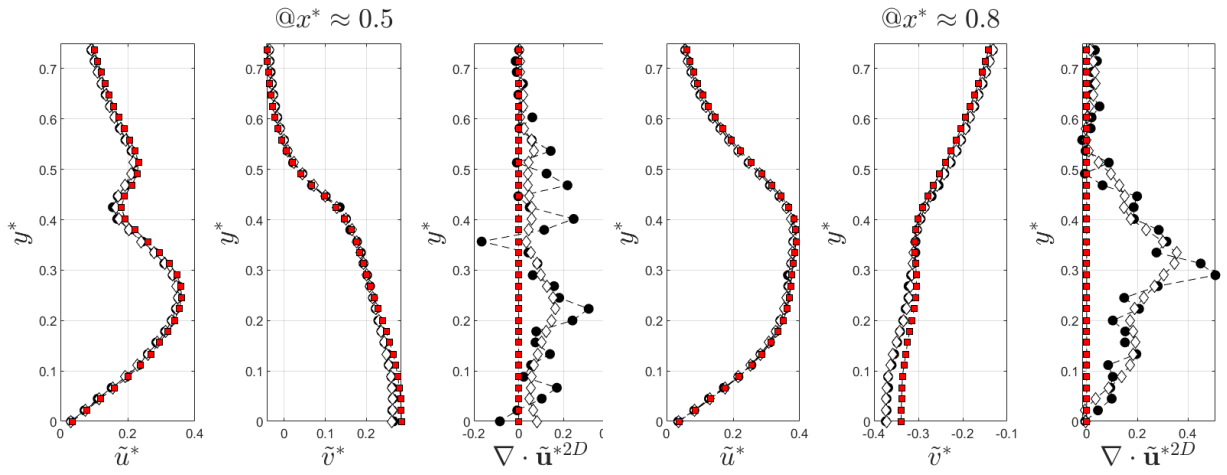

(a) (b)

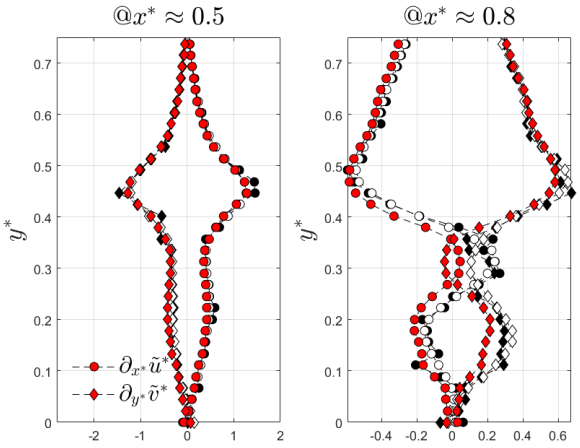

(c) Terms of the divergence operation on the coherent velocity vector $\tilde{\mathbf{u}}$.

Figure 5.11: Comparison of the components of the velocity vector (a) and (b), where the circular black, white diamonds and the red squares represents the original, smoothed and the divergence corrected velocity profiles at streamwise locations of $x^* \approx 0.5$(a) and $x^* \approx 0.8$(b) marked by dashed lines in figure 5.10. The smoothing is carried out by a Savitzky-Golay type filter for 2D data. The corresponding residual of the divergence operation is shown on the third subplot. (c). The individual terms resulting from the divergence operation on the coherent velocity vectors.

that these locations approximately correspond to the edge and the center of the forming vortices respectively. These locations were selected because high residuals of the $2D$ divergence were observed at these respective locations, in figure 5.10. In order to check if the derivative operations were responsible for the non-negligible amount of divergence residuals observed, the coherent velocity fields were smoothed by a Savitzky-Golay filter for $2D$ data and the derivative operations applied to the smoothed fields. Figures 5.11a and 5.11b shows that the smoothing operation does not considerably alter the velocity fields, and helps reduce the amplified noise level that resulted from the divergence operations in the original non-smoothed field. In the very near wake at $x^* \approx 0.5$, the divergence residual has dropped significantly by the smoothing operation, indicating the flow is dominantly $2D$ at this location. This observation can also be inferred from figure 5.11c, from which

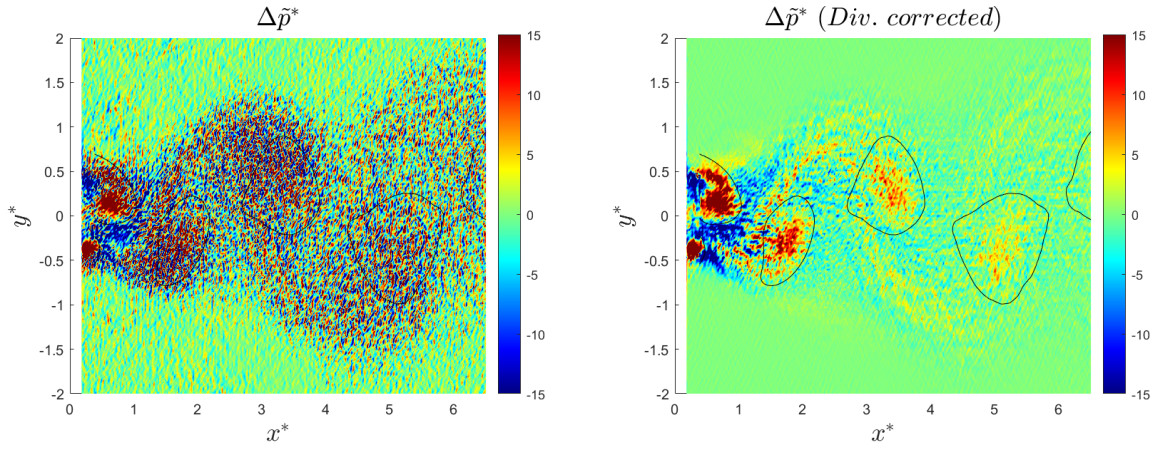

Figure 5.12: Comparison of the source term estimated using the original coherent velocity fields (a) and the divergence corrected coherent velocity fields (b).

it is clear that the residuals resulted from the noise level present.

On moving downstream, close to the location at which the vortex is fully formed prior to shedding, the smoothing operation has reduced the noisy peaks resulting from the divergence operation. However, the residuals remain high close to the center of the vortex. This can also be seen in figure 5.11c at $x^* \approx 0.8$, where close to the center of the wake, the flow is essentially $2D$, while moving towards the vortex center, there is a slight imbalance of $\partial_{x^*}\tilde{u}^*$ and $\partial_{y^*}\tilde{v}^*$ resulting in a residual as high as 0.3 after smoothing.

Figure 5.12 shows the source term of the coherent pressure Poisson equation without and with the divergence correction applied. The contours representing the boundary of the vortices detected using the $\Gamma(2)$ criterion are overlaid on top of the source term map. It is known that the Laplacian of the pressure shows positive values within the region of lower pressure and is related to the positive values of Q, where Q is the second invariant of the symmetric velocity gradient tensor. The positive value of Q indicates the dominant role of the vorticity compared to that of the local straining motion and is used to detect rotational vortices (see [47]). The Laplacian of the coherent pressure, which is also called the source term here, computed without any corrections applied on the coherent velocity field, does not accurately capture the low pressure region within the vortices in the near as well as the far wake. Moreover, the source term seems to be corrupted by an intense high frequency type noise. Even though the inversion of the Poisson operator acts as a filter, the noise still propagates to the estimated coherent pressure field. Figure 5.12b shows the source term of the coherent pressure computed using the divergence corrected coherent velocity fields. It shows that the divergence correction significantly reduces the noise level in the source term. The source term is now able to clearly distinguish the vortex regions even farther downstream, even though the field looks noisy with smeared out peaks close to the vortex center, capturing the essential physics, compared to figure 5.12a.

Figure 5.13 shows the pressure field induced by the coherent structures. The figure 5.1b shows that the two modes obtained by the POD technique is not perfectly periodic in nature because the points in the (a_1, a_2) plane does not follow a circular path and there

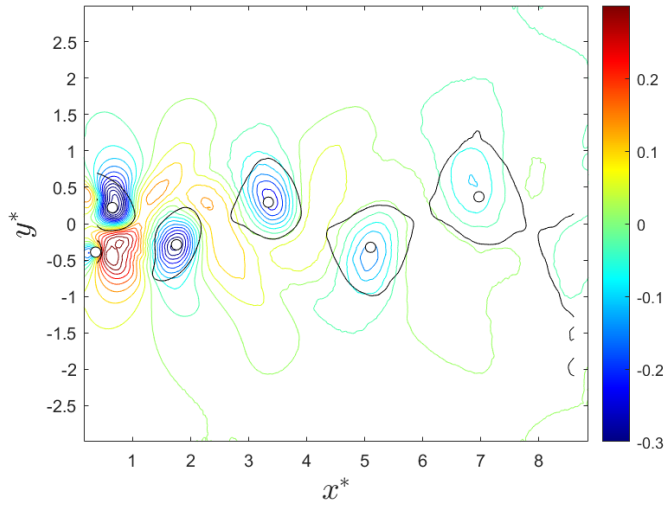

(a) .

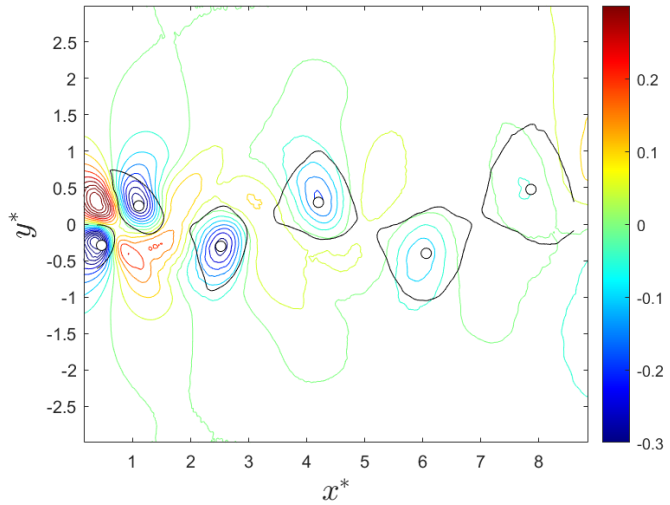

(b) .

Figure 5.13: Pressure coefficient due to the coherent structures at phase 1 and phase 4. The contours with continuous black line denotes the boundary of the vortices identified using $\Gamma(2)$ criterion and the white solid circles denote its centre. The black discontinuous line close to the body represents the *rri*.

exists a considerable amount of scatter. However, the periodicity is enforced by the POD method of coherent structure extraction. The estimated pressure $\tilde{p}^*$, also being periodic in nature, using a waveform representation then consists of a real part and a complex part. Therefore, it is sufficient to obtain the real and complex part of the waveform to describe it completely. Here, pressure coefficient $\tilde{c_p}$ of the phases ϕ_1 (the real part) and phase ϕ_4, $\frac{\pi}{2}$ radians apart from ϕ_1 forming its complex part (see figure 5.1b), are shown in figures 5.13a and 5.13b respectively.

As expected, pressure decreases at the center of the vortices. As the vortices are advected downstream, the pressure minima is also advected along. In figure 5.13b, there is an abnormal pressure rise in the upper region of the wake and pressure dip in the lower region. This is thought to be not physical and arising from the noise from the source as

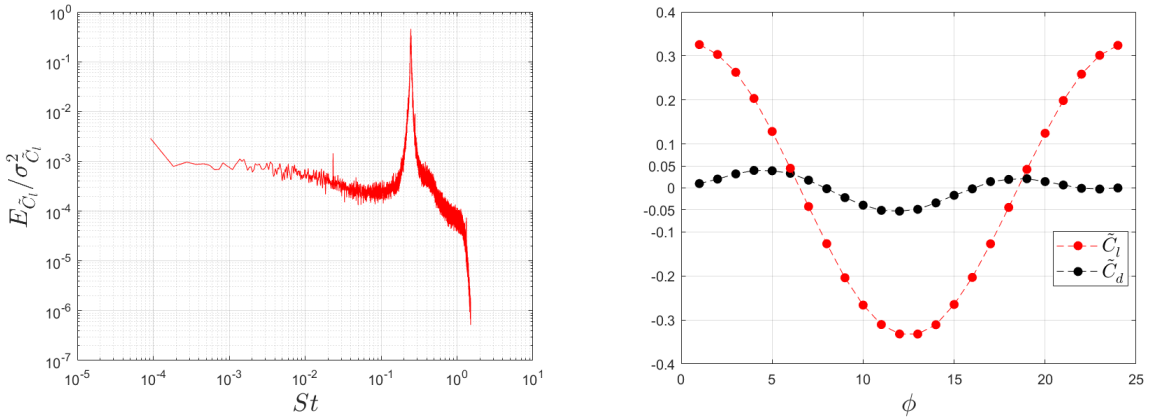

(a) (b)

Figure 5.14: The spectrum of the fluctuating lift coefficient as a function of the Strouhal number $St = fh/U_\infty$ (a), and the phase averaged lift and drag coefficients, phase averaged based on the band pass filtered fluctuating lift signal centered on the peak at $St \approx 0.24$ (b).

well as boundary terms of the coherent pressure Poisson equation.

5.3.2 Fluctuating lift and drag

Figure 5.14 shows the phase-averaged coherent lift and drag coefficient. Note that twice the number of phases, used for POD based averaging of velocity fields, has been used here in order to better represent the fluctuating $\tilde{C}_d$. The fluctuating lift and drag coefficient write,

$$C'_l = \int_\Gamma C'_p n_y \, \mathrm{d}\Gamma, \quad \text{and} \quad C'_d = \int_\Gamma C'_p n_x \, \mathrm{d}\Gamma, \tag{5.21}$$

where Γ, represents the surface of the body and C'_p the fluctuating pressure coefficients respectively which is estimated using the fluctuating pressure measurements obtained from the pressure sensors installed around the body. The spectrum of the fluctuating lift estimate, as a function of the Strouhal number, is shown in figure 5.14a, where a clear dominant peak at a Strouhal number $St \approx 0.24$, representing a periodic wake structure is seen. The fluctuating lift signal is then phase shifted using the Hilbert transform in order to determine the phase, and the fluctuating lift and drag estimate is then averaged based on the identified phase to obtain the phase averaged lift $\tilde{C}_l$ and drag $\tilde{C}_d$ coefficient shown in figure 5.14b. The periodic lift coefficient $\tilde{C}_l$, due to the periodic wake structure, varies in between ± 0.315. The phase averaged drag coefficient $\tilde{C}_d$ also displays a periodic variation, but with its period approximately half that of the phase averaged lift coefficient $\tilde{C}_l$.

Phase-averaged lift and drag may also be computed using the phase averaged integral momentum budgets. Note that the pressure signal is phase averaged using the time series of the fluctuating lift signal, whereas in order to perform the integral phase averaged momentum budgets we use the flow fields phase averaged using the POD method.

Figure 5.15 shows the coherent lift computed using the integral budget of the vertical

coherent momentum transport equation, integrated over a series of simple rectangular control volumes (CV), with the CV height h^*_{CV} kept constant and its size varied by displacing the outlet boundary in the streamwise direction, similar to the case in figure 3.11. Considering the CV in figure 3.8, the integral of the transport equation for the vertical momentum writes

$$\begin{aligned}\tilde{C}_l = -\frac{2}{U_\infty^2 h}\Bigg\{ &\int_S \left(\frac{\partial \tilde{v}}{\partial t}\right) \mathrm{d}S + \int_{CD} \left(2V\tilde{v} + \tilde{v}^2 + \langle v''^2\rangle - \overline{\tilde{v}^2} - \overline{\langle v''^2\rangle} + \frac{\tilde{p}}{\rho}\right) \mathrm{d}x \\ &- \int_{AB} \left(2V\tilde{v} + \tilde{v}^2 + \langle v''^2\rangle - \overline{\tilde{v}^2} - \overline{\langle v''^2\rangle} + \frac{\tilde{p}}{\rho}\right) \mathrm{d}x \\ &+ \int_{BC} \left(V\tilde{u} + \tilde{v}U + \tilde{u}\tilde{v} + \langle u''v''\rangle - \overline{\tilde{u}\tilde{v}} - \overline{\langle u''v''\rangle}\right) \mathrm{d}y \Bigg\},\end{aligned} \tag{5.22}$$

where the temporal derivative term is integrated over the surface of the control volume and S represents the surface area of the control volume. While estimating the coherent lift, the constant appearing from the solution of the coherent pressure estimate gets cancelled out due to the difference of the pressure terms on the lateral sides of the CV in equation (5.22). The only missing contribution from the lateral sides due to the missing upstream data is expected to be from the coherent pressure fluctuations. The $\tilde{C}_l$ estimated by using the finite difference approximated temporal derivative and the subsequent coherent pressure computed, reveals a very noise estimate in figure 5.15a. Close to the body, the $\tilde{C}_l$ for all the phases are centered around zero, whereas as one moves downstream the estimate worsens. The red dashed lines represent the minimum and maximum values of $\tilde{C}_l$ computed from the pressure signals, phase averaged based on the fluctuating lift estimate. The residual resulting from the integral momentum budget over the selected control volumes, shown in figure 5.15b, is seen to be very large, with the values in the range $\pm 30\%$. Comparing the figures 5.15a and 5.15b, the noisy shape of the lift estimate results from the large residuals in the integral momentum balance. This shows that the finite difference approximation of the temporal derivative and the coherent pressure estimated using this temporal derivative term on the boundaries does not provide a satisfactory balance of the integral momentum budget. The sources of the error in the estimate are numerous in figure 5.15a. It may arise from the approximation of the temporal derivative of velocity, estimated coherent pressure, inherent noise in the data or because of the two-dimensional approximations.

Once the temporal derivative is estimated using the Poisson equation for the temporal derivative of stream function, which is then used to recompute the coherent pressure, the coherent lift estimation improves significantly (see figure 5.16a). Close to the body as well as farther downstream, the noisy fluctuating lift estimate observed in figure 5.15a is corrected and the coherent lift estimate for each phase roughly settles to roughly a constant value, except for the wavy behaviour. Figure 5.16b shows the residual arising from the integral momentum budget of the phase averaged transverse momentum equation over the selected control volumes. The wavy behaviour in figure 5.16a is found to result from the residual in the transverse phase averaged integral momentum balance. Comparing figures 5.15b and 5.16b, it is seen that the residuals arising from the integral momentum budget has improved significantly. The value of the residuals was within the range $\pm 30\%$ using

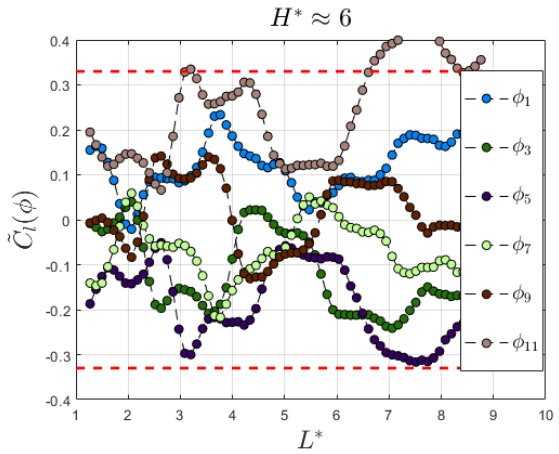

(a) Lift force coefficient due to the coherent structures, non corrected version.

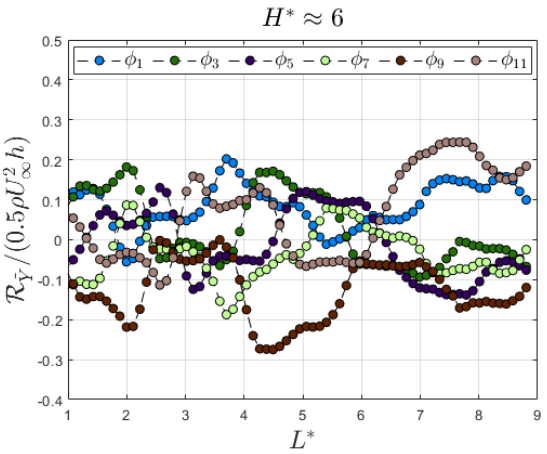

(b) Residual arising from the phase averaged integral transverse momentum balance.

Figure 5.15: Coherent lift computed using the integral budget of vertical momentum transport over a series of rectangular control volumes, (a) estimated using the finite difference approximation of the temporal derivative and the coherent pressure, computed using this first estimate of $\frac{\partial \tilde{v}}{\partial t}$, and (b) Residual arising from the phase averaged integral transverse momentum balance, along the rectangular CV. The red dashed line in (a) represents the maximum and the minimum values of the lift coefficients as obtained from the pressure sensors. The height of the rectangular control volumes chosen are kept constant at $H^* = 6$ with only the outlet displaced in the streamwise direction and $\tilde{C}_l$ computed for each CV.

the non corrected temporal derivative and the coherent pressure estimate, whereas once those are corrected, the residual in the budget drops down significantly to remain within the values $\pm 4\%$. Therefore, the velocity temporal derivative estimated using equation (5.14) and (5.15) is seen to improve the momentum budget and it further limits the errors propagated to the coherent pressure through the boundaries, as the temporal derivative appears on the boundary condition for solving the coherent pressure Poisson equation.

The $\tilde{C}_d$ due to the coherent structures can be estimated by performing the integral budget of the phase-averaged version of the streamwise momentum equation (5.23) that reads:

$$\begin{aligned}\tilde{C}_d = -\frac{2}{U_\infty^2 h}\Bigg\{ &\int_S \left(\frac{\partial \tilde{u}}{\partial t}\right) \mathrm{d}S + \int_{CD} \left(U\tilde{v} + V\tilde{u} + \tilde{u}\tilde{v} + \langle u''v''\rangle - \overline{\tilde{u}\tilde{v}} - \overline{\langle u''v''\rangle}\right) \mathrm{d}x \\ &- \int_{AB} \left(U\tilde{v} + V\tilde{u} + \tilde{u}\tilde{v} + \langle u''v''\rangle - \overline{\tilde{u}\tilde{v}} - \overline{\langle u''v''\rangle}\right) \mathrm{d}x \\ &+ \int_{BC} \left(2U\tilde{u} + \tilde{u}^2 + \langle u''^2\rangle - \overline{\tilde{u}^2} - \overline{\langle u''^2\rangle} + \frac{\tilde{p}}{\rho}\right) \mathrm{d}y \Bigg\}. \end{aligned} \tag{5.23}$$

Note that the pressure in equation (5.23) may be shifted due to the constant that arises from the integration of the Poisson equation using Neumann-type boundary condition.

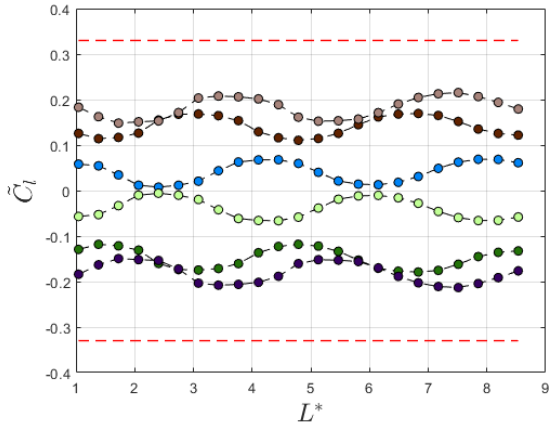

(a) Lift force coefficient due to the coherent structures, corrected version.

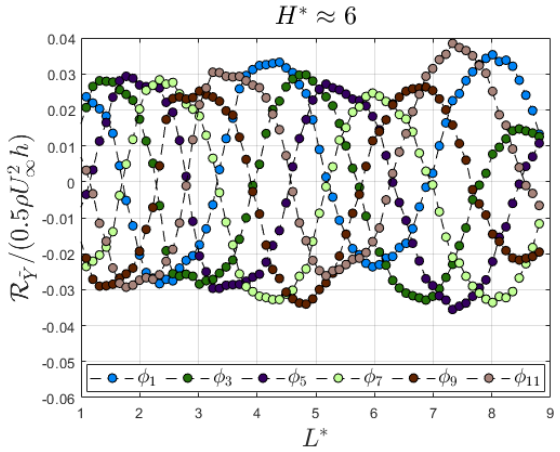

(b) Lift force coefficient due to the coherent structures, corrected version.

Figure 5.16: Coherent lift computed using the integral budget of vertical momentum transport over a series of rectangular control volumes, (a) estimated using the temporal derivative, estimated by solving the Poisson equation for $\frac{\partial \psi}{\partial t}$, and the coherent pressure, computed using this corrected temporal derivative $\frac{\partial \tilde{v}}{\partial t}$ and (b) Residual arising from the phase averaged integral transverse momentum balance, along the rectangular CV using the corrected temporal derivative and the coherent pressure estimate. The red dashed line represents the maximum and the minimum values of the lift coefficients as obtained from the pressure sensors. The height of the rectangular control volumes chosen are kept constant at $H^* = 6$ with only the outlet displaced in the streamwise direction and $\tilde{C}_l$ computed for each CV.

Figure 5.17a shows the $\tilde{C}_d$ using the equation (5.23), using a series of simple rectangular control volumes of height H^* and the streamwise outlet location at L^*. At the lower H^*, where the lateral sides of the CV are closer to the body, the $\tilde{C}_d$ estimate displays a wavy behaviour along the position of the L^*. As the CV height is increased, for example from $H^* \approx 2$ to 3, this behaviour decreases. At high enough H^*, the wavy behaviour is seen to disappear completely. From the coherent pressure field shown in figure 5.13a, the peaks and dips in the $\tilde{C}_d$ estimate is seen to correspond to the streamwise center or the space in between of the shed vortices. The figure 5.17b shows the residual $\mathcal{R}_{\tilde{X}}$, in performing the integral momentum budget over the closed control volume defined by the height H^* and lateral side length L^*. It is seen that the residual also displays a wavy behaviour similar to that seen in the $\tilde{C}_d$ estimate in figure 5.17a. Th amplitude of the wavy behaviour also corresponds to that seen in the $\tilde{C}_d$ budget and hence if the residual is subtracted from the $\tilde{C}_d$, we may suppress this behaviour to obtain a constant $\tilde{C}_d$ over the L^* considered. As the CV height is increased, this wavy behaviour decreases. Note that nevertheless, the normalised residual remains within 4%.

Considering the average of the $\tilde{C}_d$ represented as $\langle \tilde{C}_d \rangle$ over the entire L^* for each choice of H^*, the $\langle \tilde{C}_d \rangle$ is seen to increase, which could be caused by the coherent pressure estimate corrupted by the constant arising out of integrating pressure Poisson's equation using Neumann-type boundary condition.

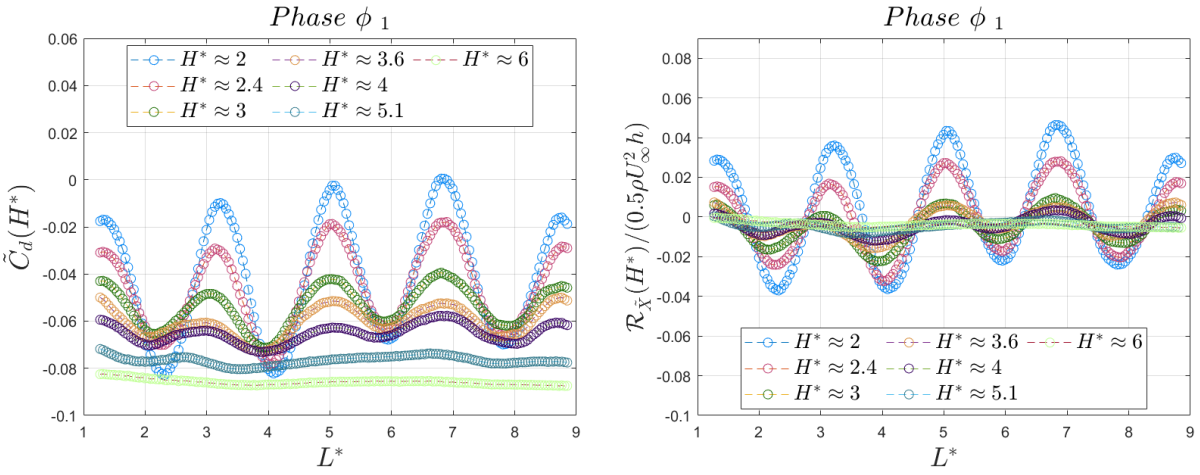

(a) (b)

Figure 5.17: The drag coefficient due to the coherent structures estimated using the phase averaged streamwise integral momentum budget (5.23) using a series of rectangular control volumes of height H^* and length L^* (a), and the residual of the integral momentum budget carried out along those rectangular control volumes (b). The budget is performed using the corrected temporal derivative and the coherent pressure estimated using these corrected temporal derivatives.

The variation of $\langle \tilde{C}_d \rangle$ with various choices of H^* is shown in the figure 5.18a. A linear trend, $\langle \tilde{C}_d \rangle = mH^* + k$ where m is the slope, is observed. This means that the constant in the coherent pressure estimate increases the $\langle \tilde{C}_d \rangle$ with increasing H^* due to the integration over a larger height H^*. In order to make the $\tilde{C}_d$ estimate CV independent, the slope of the linear trend, m, seen in figure 5.18a is subtracted from the phase averaged streamwise integral momentum budget equation (5.23), i.e., $\tilde{C}_{d,cor.} = \tilde{C}_d - \int_{BC} m \, dy^*$, and the corrected $\tilde{C}_{d,cor.}$ estimate is seen to be CV independent as shown in figure 5.18b. Similarly, the $\tilde{C}_d$ estimate is made CV size independent and its estimate for the largest CV size possible for the current data-set, is shown in figure 5.19a. The maximum and minimum limits of the $\tilde{C}_d$ estimated using the pressure signal data, shown in figure 5.14b, is shown by red dashed line. The estimated $\tilde{C}_d$ is seen to be within the limits of the reference $\tilde{C}_d$ obtained from measurements. Further, the $\tilde{C}_d$ is seen to be not a constant along the L^*, which is due to the residual arising from the integral momentum budget along the control volume. The residual of the integral phase averaged streamwise equation of momentum, is shown in figure 5.19b for all 12 phases and is found to be within $\pm 2\%$.

The coherent pressure estimation may further be corrected using the adjoint method proposed in section 3.1.2. However, this requires the pressure signal to be in phase with the PIV velocity fields. Moreover, unlike the pressure signal, the PIV velocity fields are not phase averaged using a time resolved reference signal, but relies on the POD technique which enforces periodicity using the first two spatially energetic modes. The result is that the time information is lost. As such, a matching coherent pressure signal for a coherent pressure field at a specific phase may not be feasible and hence the adjoint method was not applied to correct the coherent pressure field. Note that other methods such as dynamic mode decomposition [153], spectral POD [179], or least-squares-estimation POD [177] could circumvent this issue.

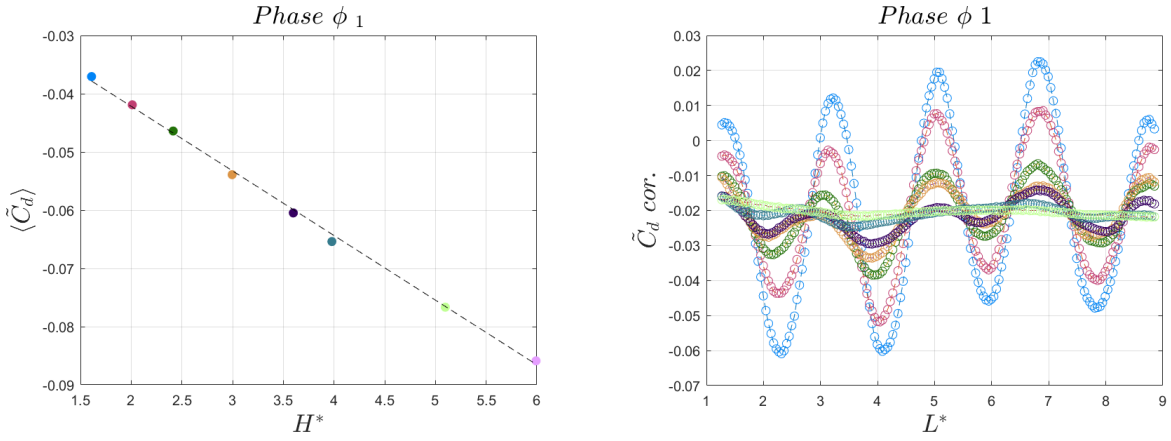

(a) (b)

Figure 5.18: Variation of the average $\tilde{C}_d$ over the outlet location L^* for a single selected H^*, denoted by $\langle \tilde{C}_d \rangle$, as a function of various choices of control volume height H^* (a), where the black dashed line represents the linear trend $\langle \tilde{C}_d \rangle = mH^* + k$, and (b) the corrected $\tilde{C}_d$ estimate, $\tilde{C}_{d,cor.} = \tilde{C}_d - \int_{BC} m \, dy^*$, which is independent of the size of the control volume.

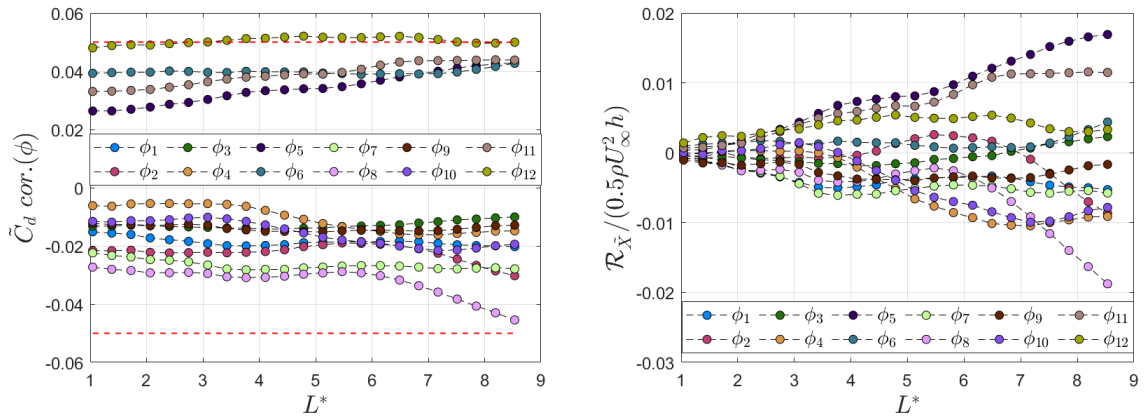

(a) (b)

Figure 5.19: The corrected $\tilde{C}_d$, $\langle \tilde{C}_d \rangle$, estimated using a control volume of height H^* with varying CV outlet L^* shown for all the 12 phases (a), where the red dashed line represents the limit of the maximum and minimum $\tilde{C}_d$ estimated using the phase averaged pressure signals, and (b) the residuals resulting from the phase averaged integral streamwise momentum budget performed over the rectangular control volumes.

5.4 Transport of coherent Reynolds normal stresses

The primary motive of estimating the coherent pressure is to analyse the balance of Reynolds stresses, at-least partially, in order to identify the dominant mechanisms that drive the dynamics.

5.4.1 Streamwise coherent stress transport

The transport equation for the first component of the coherent Reynolds stress tensor from its general form of equation (5.7) writes

$$\underbrace{U\frac{\partial\overline{\tilde{u}^2}}{\partial x}+V\frac{\partial\overline{\tilde{u}^2}}{\partial y}}_{\tilde{\mathcal{A}}_{11}}=\underbrace{-2\left\{\overline{\tilde{u}^2}\frac{\partial U}{\partial x}+\overline{\tilde{u}\tilde{v}}\frac{\partial U}{\partial y}\right\}}_{\tilde{\mathcal{P}}_{11}}\overbrace{-\frac{2}{\rho}\frac{\partial}{\partial x}\left(\overline{\tilde{p}\tilde{u}}\right)}^{\tilde{\mathcal{D}}^{\tilde{p}}_{11}}+\underbrace{\frac{2}{\rho}\overline{\tilde{p}\frac{\partial\tilde{u}}{\partial x}}}_{\widetilde{\mathcal{PS}}_{11}}\underbrace{-\left\{\frac{\partial}{\partial x}\left(\overline{\tilde{u}^3}\right)+\frac{\partial}{\partial y}\left(\overline{\tilde{u}^2\tilde{v}}\right)\right\}}_{\tilde{\mathcal{D}}_{11}}$$
$$\underbrace{-2\left\{\frac{\partial}{\partial x}\left(\overline{\langle u''^2\rangle\tilde{u}}\right)+\frac{\partial}{\partial y}\left(\overline{\langle u''v''\rangle\tilde{u}}\right)+\frac{\partial}{\partial z}\left(\overline{\langle u''w''\rangle\tilde{u}}\right)\right\}}_{\mathcal{D}''_{11}}$$
$$\underbrace{\left(-2\left\{\overline{\langle u''^2\rangle}\frac{\partial\tilde{u}}{\partial x}+\overline{\langle u''v''\rangle}\frac{\partial\tilde{u}}{\partial y}+\right\}\right)}_{\mathcal{P}''_{11}}-\cancelto{0}{\tilde{\varepsilon}_{11}}+\cancelto{0}{\mathcal{D}_\nu}. \tag{5.24}$$

The interpretation of the equation (5.24) is given in section 5.2.1. In $\mathcal{P}''_{11}$ and $\tilde{\mathcal{D}}_{11}$, since the coherent structures are assumed to be predominantly two dimensional, the third component which involves the out of plane gradient vanishes and hence not shown in equation (5.24). Therefore, the only remaining component inaccessible from planar PIV measurements is the third component of the diffusion term $\mathcal{D}''_{11}=\partial/\partial z(\overline{\langle u''w''\rangle\tilde{u}})$. which will be small only if the residuals $\mathcal{R}_{11}$ are close to null.

Figure 5.20a shows the balance of the transport equation for Reynolds streamwise normal stress $\overline{\tilde{u}^2}$ performed at $l^*_r/4$. The naming corresponds to various terms described in the equation (5.24). Ideally, with the advection term carried over to the right-hand side of equation (5.24), the sum of all the terms should be zero. Approaching the wake transversely from the free stream, all the terms are zero until $y^*\approx 0.8$. In between $0.5\leq y^*\leq 0.6$, there is a gain in energy due to the production $\tilde{\mathcal{P}}_{11}$ and due to the pressure diffusion term $\tilde{\mathcal{D}}^{\tilde{p}}_{11}$, where the latter dominates, which in part is drained away by the pressure strain term $\widetilde{PS}_{11}$ and $-\tilde{\mathcal{A}}_{11}$. Note that all these terms peak near the center of the mean shear layer, as denoted by the local half wake-width and the height of the recirculating flow bubble. Within the wake width, the largest gain due to $\tilde{\mathcal{D}}^{\tilde{p}}_{11}\to 0$ as $y^*\to 0$ is balanced by the losses due to $\widetilde{PS}_{11}$ and $\tilde{\mathcal{P}}_{11}$. The remaining terms are small and their magnitudes are comparable to that of the residual term $\mathcal{R}_{11}$ and hence no conclusion may be reached for them.

Figure 5.20b shows the local balance of the transport of $\overline{\tilde{u}^2}^*$ at $0.5l^*_r$, which corresponds to the streamwise location where $\overline{\tilde{u}^2}^*$ has a maximum contribution to the base pressure drag, figure 5.7a. Approaching the wake along y^* from the free-stream, $-\tilde{\mathcal{A}}_{11}$ is exactly balanced by $\widetilde{PS}_{11}$ and $\tilde{\mathcal{D}}^{\tilde{p}}_{11}$, until $y^*\approx 0.5$. As $y^*\to 0$ from 0.5, the flow is highly inhomogeneous with all the terms playing a significant role. The residual $\mathcal{R}_{11}$ rises and has the same shape of $\tilde{\mathcal{D}}_{11}+\mathcal{D}''_{11}$. Its magnitude is similar to that of $\tilde{\mathcal{D}}_{11}+\mathcal{D}''_{11}$ and the combined magnitude of $\widetilde{PS}_{11}$ and $\mathcal{P}''_{11}$. The residual may arise from the uncertainty in the coherent pressure or from the missing out of plane term from $\mathcal{D}''_{11}$. Nevertheless, $\widetilde{PS}_{11}$ may remain an energy sink. Near the center of the mean shear layer, energy is gained by

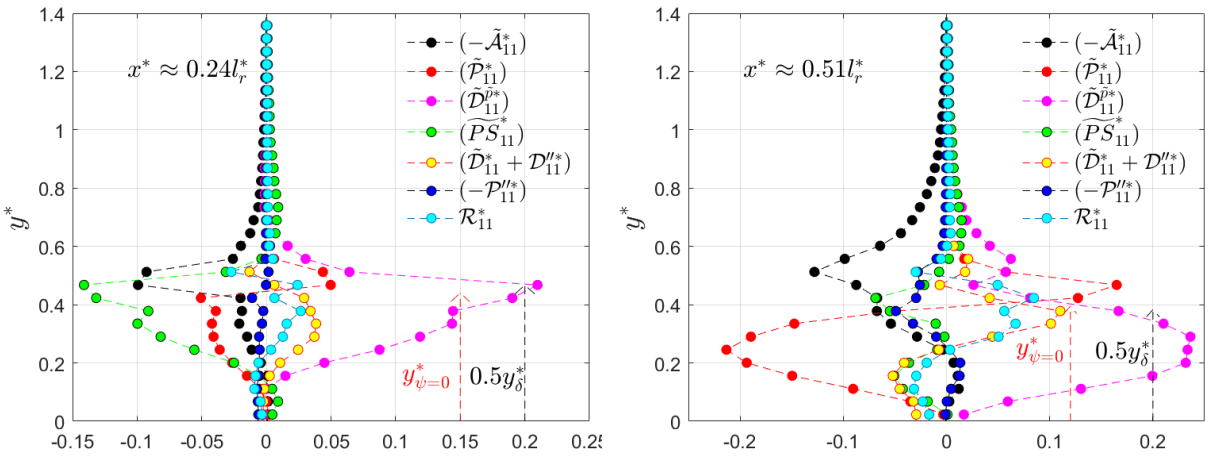

(a) (b)

Figure 5.20: Balance of equation for the transport of Reynolds streamwise normal stress $\widetilde{u^2}$ performed at $x^* \approx l_r^*/4$ and at $x^* \approx l_r^*/2$ for the flow at $Re_h \approx 2.8 \times 10^4$

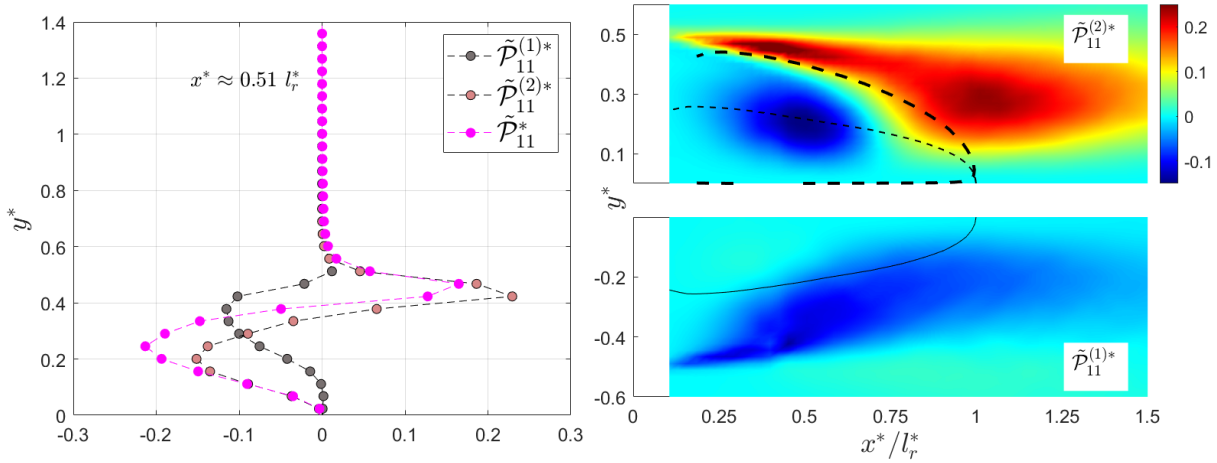

(a) (b)

Figure 5.21: Splitting the production term at $x^* \approx l_r^*/2$ (a) and the colormap showing the two constituent terms of the production $\tilde{\mathcal{P}}_{11}$ (b) for the flow at $Re_h \approx 2.8 \times 10^4$

$\tilde{\mathcal{P}}_{11}$, and it is not redistributed elsewhere but lost to $\widetilde{PS}_{11}$, $\mathcal{P}_{11}''$ and $-\tilde{\mathcal{A}}_{11}$. Approaching $y^* \to 0$, a large gain due to $\tilde{\mathcal{D}}_{11}^{\tilde{p}}$ is observed whose majority is lost to $\tilde{\mathcal{P}}_{11}$ within the recirculating flow bubble. A part of this gain is redistributed by $\tilde{\mathcal{D}}_{11} + \mathcal{D}_{11}''$ transversely, which is injected to incoherent structures through $\mathcal{P}_{11}''$ and across components through $\widetilde{PS}_{11}$. If $\mathcal{R}_{11}$ had resulted from the pressure term, then for $\mathcal{R}_{11}$ to be zero, either sink through $\widetilde{PS}_{11}$ increases or gain through $\tilde{\mathcal{D}}_{11}^{\tilde{p}}$ decreases. Then, even if $\mathcal{R}_{11}$ arises from the missing out of plane term, the conclusions reached is not much affected. Within the transverse centre of the recirculating flow bubble (see the schematic in figure 4.19), there seems to be a reverse flow of energy where relatively small amount of energy is gained by $\mathcal{P}_{11}''$.

.

The production term $\tilde{\mathcal{P}}_{11}$ in the local balance at $l_r^*/2$ acts as a source of energy near

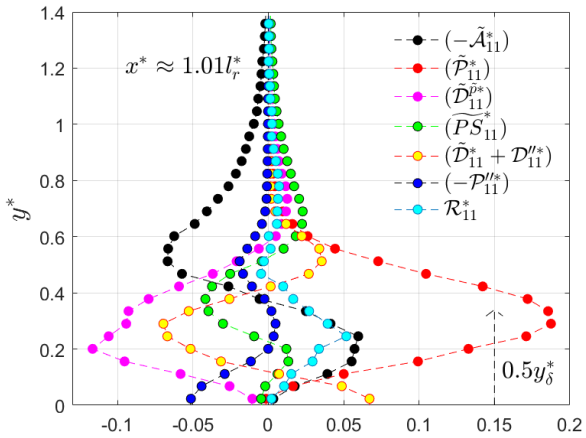

Figure 5.22: Balance of equation for the transport of Reynolds streamwise normal stress $\overline{\tilde{u}^2}$ at $x^* \approx l_r^*$ and for the flow at $Re_h \approx 2.8 \times 10^4$

the center of the shear layer whereas it acts as a sink near the wake centerline. Figures 5.21a and 5.21b show the production term split into its two components - normal $\tilde{\mathcal{P}}_{11}^{(1)}$ and shear component $\tilde{\mathcal{P}}_{11}^{(2)}$. They tend to oppose each other, specially within the mean growing shear layer. It is the shear component that dominates, due to the nonlinear interaction between the coherent Reynolds shear stress and the intense mean shear, peaking near the shear layer center. Within the recirculating flow bubble, they both tend to work together, resulting in a large energy sink shown in figure 5.21a. The shear component $\tilde{\mathcal{P}}_{11}^{(2)}$, as a source of energy, is intense within the shear layer especially near separation and l_r^*, the latter is associated with the length of vortex formation region. Within 3/4 of the recirculating region, the shear component acts as a sink, shown in figure 5.21b, peaking near the streamwise center of the bubble, primarily due to the momentum outflux represented by the positive Reynolds shear stress. The normal component $\tilde{\mathcal{P}}_{11}^{(1)}$, on the other hand, always acts as an energy sink. It is larger within the mean shear layer, specially near separation due to a higher spatial acceleration of the mean flow, and is weakened as the shear layer grows in space.

The coherent streamwise Reynolds normal stress peaks near the streamwise extent of the recirculating flow region (see figures 5.5a and 4.5), which also corresponds approximately to the peak of shear component of production $\tilde{\mathcal{P}}_{11}^{(2)}$ - the dominant energy source. The location balance at $x^* \approx l_r^*$ is therefore worth investigating, and is shown in figure 5.22.

Approaching the wake from the free-stream towards the wake centerline, $-\tilde{\mathcal{A}}_{11}$ spans a greater transverse distance compared to that at $l_r^*/2$ shown in figure 5.20b. It drives the spreading of the wake, driven by $\widetilde{\mathcal{PS}}_{11}$ and $\tilde{\mathcal{D}}_{11}^{\tilde{p}}$ where the former dominates until $y^* \approx 0.6$. As $y^* \to 0$ from 0.6, a large gain in energy is obtained through $\tilde{\mathcal{P}}_{11}$ peaking at the half wake-width and gradually declining to zero at the wake-centerline. The shear component $\tilde{\mathcal{P}}_{11}^{(2)}$, as shown in figure 5.21b, which is large here because of the interaction of coherent Reynolds shear stress, attaining its peak at $x^* \approx l_r^*$ (see figures 4.6a and 5.5b), with the diffused shear layer. Most of the gain is absorbed by $\tilde{\mathcal{D}}_{11}^{\tilde{p}}$. Similar to the balances performed upstream, the shape of the $\tilde{\mathcal{D}}_{11} + \mathcal{D}_{11}''$ curve shows that its function is to redistribute the energy transversely. This redistributed energy is further injected to the incoherent structures through $\mathcal{P}_{11}''$ at the wake centerline and at $y^* \approx 0.5$, the latter

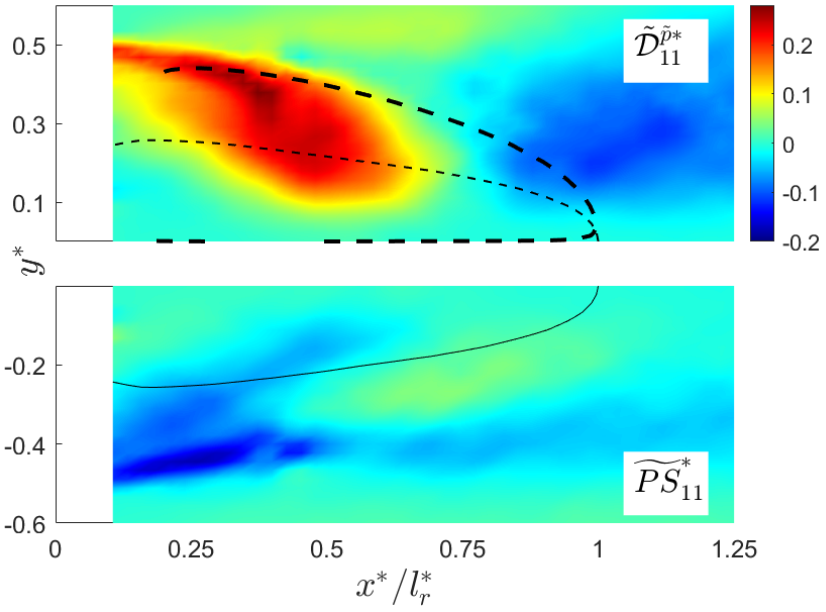

Figure 5.23: Colormap of the pressure diffusion $\tilde{\mathcal{D}}_{11}^{\tilde{p}}$ and the pressure strain $\widetilde{PS}_{11}$ fields for the flow at $Re_h \approx 2.8 \times 10^4$. The fields being symmetric, only one of the symmetric planes is shown.

location may correspond to the outer edge of the shear layer (see figure 5.21b or 4.9). This observation confirms the well known fact that the coherent structures drives the energy cascade [32, 75, 133, 174]. Further, it is known that the saddle points between the vortices play an important role in the production of turbulence [32]. The saddle points are not shown here, since our interest is in much simplified time averaged flow.

The colormap of the pressure diffusion $\tilde{\mathcal{D}}_{11}^{\tilde{p}}$ and the pressure strain term $\widetilde{PS}_{11}$ is shown in figure 5.23. The fields being symmetric, only one of the symmetric planes is shown. The pressure strain term $\widetilde{PS}_{11}$ is seen to be intense along the mean shear layer especially near the point of flow separation. It mostly acts as a sink of energy, which is supplied by the pressure diffusion term near separation, and is intense along the shear layer within a streamwise distance of $l_r^*/2$. This drained energy, as mentioned earlier, is redistributed among the normal components of the Reynolds stress. The pressure diffusion term $\tilde{\mathcal{D}}_{11}^{\tilde{p}}$ continues to act as s source of energy, compensating the energy sink created by the production term $\tilde{\mathcal{P}}_{11}$ within the recirculating flow region (see figure 5.20b), within a streamwise distance of $3/4l_r^*$, after which it switches to receive energy from the production term $\tilde{\mathcal{P}}_{11}$ as seen in figure 5.22.

The pressure diffusion term $\tilde{\mathcal{D}}^{\tilde{p}}$ is a transport term in divergence form which merely redistributes the energy extracted from the mean flow. This can be seen from the map 5.23, where it receives energy in the region close to l_r^* which is then redistributed in the region close to separation. This indicates that the energy associated with the transport of $\widetilde{u^2}$ is through the production term $\tilde{\mathcal{P}}_{11}$ from the mean flow, and the pressure diffusion term plays a major role in redistributing the energy or back-feeding this energy upstream. The energy fed upstream is then redistributed by the pressure strain term.

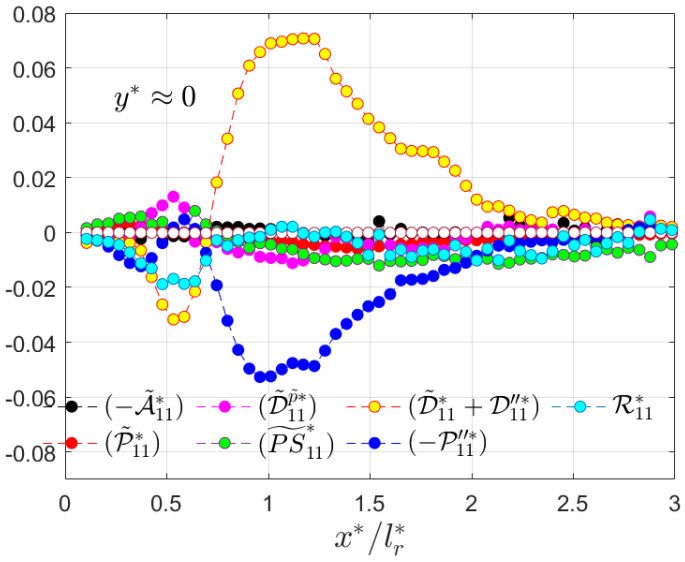

Figure 5.24: Local balance of equation for the transport of Reynolds streamwise normal stress $\overline{\tilde{u}^2}$ for the flow at $Re_h \approx 2.8 \times 10^4$, carried out along the wake centerline.

Figure 5.24 shows the balance in the transport equation for $\overline{\tilde{u}^2}$ along the wake centerline $y^* \approx 0$. The wake centerline is an interesting location for local balances analyses because of the similarity. However, all the terms except $\tilde{\mathcal{D}}_{11} + \mathcal{D}''_{11}$ and $\mathcal{P}''_{11}$ are of the same order of magnitude as the residuals. The balance is between the $\tilde{\mathcal{D}}_{11} + \mathcal{D}''_{11}$ and $\mathcal{P}''_{11}$, where the former injects energy to the incoherent structures through the latter with peaks at l^*_r. This trend is seen to continue until at least $x^* \approx 3/2 l^*_r$ after which the noise from the data takes over.

In order to obtain a global picture, an average integral contribution at a streamwise location is defined as,

$$I_t(x^*) = \frac{1}{L^*_y} \int_{y^*=0}^{L^*_y} t(x^*, y^*)\, dy^*, \tag{5.25}$$

where t denotes the term whose average contribution is taken. For example, the term $I_{-\tilde{\mathcal{A}}_{11}}$ represents the average integral contribution of the advection term. Similarly, the contribution from the remaining terms are averaged and its streamwise evolution is shown in figure 5.25. Note that the residual terms are close to zero indicating a satisfactory balance. The average of the incoherent production term $I_{-\mathcal{P}''_{11}}$ is very small and close to the magnitude of the averaged residuals. The diffusion term $I_{\tilde{\mathcal{D}}_{11}+\mathcal{D}''_{11}}$ remains negligibly small, indicating that this term is responsible only for the transverse redistribution of the energy, as observed in figure 5.20b or 5.22. The production term $I_{\tilde{\mathcal{P}}_{11}}$ remains small close to the body, whereas moving downstream it drains energy peaking at $l^*_r/2$ after which it switches at $x^* \approx 0.7 l^*_r$ to act as a source of energy. The main sink here is due to the presence of recirculating flow region, as seen in figure 5.21b. It continues to decay downstream after attaining a peak at l^*_r. The energy gained through the production term, in part feeds the advection term $I_{-\tilde{\mathcal{A}}_{11}}$. Since the residual is thought to arise from the inaccuracies in the coherent pressure affecting the pressure strain or pressure diffusion term, it can be said that a portion of the energy gained by the production term $I_{\tilde{\mathcal{P}}_{11}}$ is injected to the

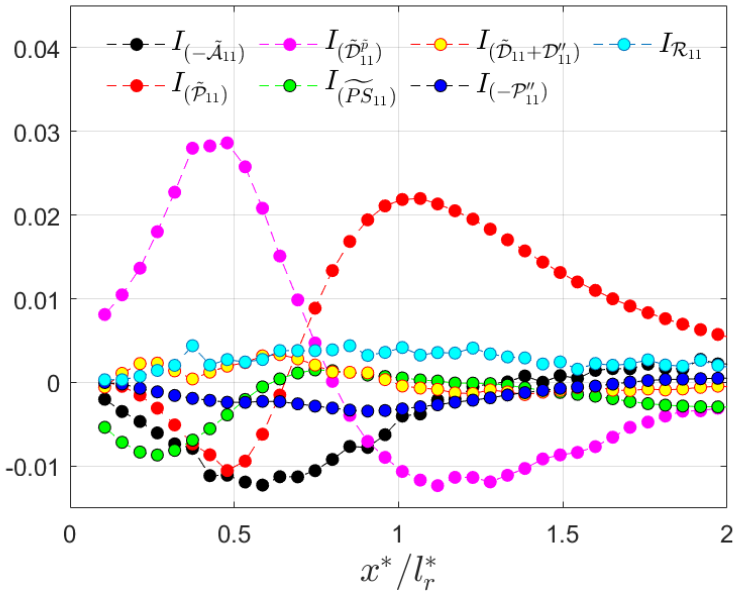

Figure 5.25: Transversely averaged balance of equation for the transport of Reynolds streamwise normal stress $\widetilde{u^2}$ for the flow at $Re_h \approx 2.8 \times 10^4$ along the streamwise direction normalized by the length of the recirculating flow region l_r^*.

incoherent stresses through the incoherent production term $I_{-\mathcal{P}''_{11}}$. The remaining energy is redistributed by the pressure diffusion term $I_{\tilde{\mathcal{D}}^{\tilde{p}}_{11}}$, feeding it upstream and forming a feedback loop. This redistributed energy is taken by the pressure strain term $I_{\widetilde{PS}_{11}}$ to be supplied to the other normal coherent Reynolds stress component.

5.4.2 Transverse coherent stress transport

The transport equation for the transverse normal component of the coherent Reynolds stress tensor from equation (5.7) reads,

$$\underbrace{U\frac{\partial\widetilde{\overline{v}^2}}{\partial x}+V\frac{\partial\widetilde{\overline{v}^2}}{\partial y}}_{\tilde{\mathcal{A}}_{22}}=\underbrace{-2\left\{\widetilde{\overline{u}\overline{v}}\frac{\partial V}{\partial x}+\widetilde{\overline{v}^2}\frac{\partial V}{\partial y}\right\}}_{\tilde{\mathcal{P}}_{22}}\overbrace{-\frac{2}{\rho}\frac{\partial}{\partial y}\left(\widetilde{\overline{p}\overline{v}}\right)}^{\tilde{\mathcal{D}}^{\tilde{p}}_{22}}+\underbrace{\frac{2}{\rho}\widetilde{\overline{p}\frac{\partial\overline{v}}{\partial y}}}_{\widetilde{\mathcal{PS}}_{22}}\underbrace{-\left\{\frac{\partial}{\partial x}\left(\widetilde{\overline{v}^2\overline{u}}\right)+\frac{\partial}{\partial y}\left(\widetilde{\overline{v}^3}\right)\right\}}_{\tilde{\mathcal{D}}_{22}}$$
$$\underbrace{-2\left\{\frac{\partial}{\partial x}\left(\widetilde{\langle u''v''\rangle\overline{v}}\right)+\frac{\partial}{\partial y}\left(\widetilde{\langle v''^2\rangle\overline{v}}\right)+\frac{\partial}{\partial z}\left(\widetilde{\langle v''w''\rangle\overline{w}}\right)\right\}}_{\mathcal{D}''_{22}}$$
$$\underbrace{-\left(-2\left\{\widetilde{\langle u''v''\rangle\frac{\partial\overline{v}}{\partial x}}+\widetilde{\langle v''^2\rangle\frac{\partial\overline{v}}{\partial y}}\right\}\right)}_{\mathcal{P}''_{22}}\cancelto{0}{-\tilde{\varepsilon}_{22}}+\cancelto{0}{\mathcal{D}_{\nu_{22}}}. \tag{5.26}$$

Similar to the case of coherent streamwise Reynolds stress transport in equation (5.24), the third component of $\mathcal{P}''_{22}$ and $\tilde{\mathcal{D}}_{22}$ vanishes due to bi-dimensionality and hence not

shown. Hence the only remaining component inaccessible from planar PIV measurements is the third component of the diffusion term $\mathcal{D}''_{22} = \partial/\partial z(\overline{\langle v''w''\rangle \tilde{w}})$ which will be small only if the residuals $\mathcal{R}_{22}$ are close to null.

The transport equation for the transverse coherent Reynolds stress $\overline{\tilde{v}^2}^*$ is carried out at three streamwise locations, $l_r^*/4$, $l_r^*/2$ and l_r^*, similar to the case of $\overline{\tilde{u}^2}^*$. The budget of the base pressure drag shows that initially, at $L^* \approx l_r^*/4$, the mean pressure due to $\overline{\tilde{v}^2}$ contributes approximately 25% to the budget, which increases monotonically to 30% at $l_r^*/2$ continuing to rise and finally peak at l_r^* contributing 40% to the base pressure drag budget. The first streamwise location, $l_r^*/4$, is chosen to analyse the Reynolds stress transport balance in order to understand the initial development of the transverse coherent Reynolds stress. The streamwise location $l_r^*/2$ shall serve to compare with the transport of streamwise coherent Reynolds stress $\overline{\tilde{u}^2}^*$, and the final location of l_r^* is chosen because $\overline{\tilde{v}^2}$, which is the major contributor to the mean pressure here, peaks close to this location.

Figure 5.26a shows the balance in the transport equation for the Reynolds normal stress $\overline{\tilde{v}^2}$ performed at $x^* \approx l_r^*/4$. Note that $\mathcal{R}_{22}$ remains negligible indicating that the third component of $\mathcal{D}''_{22}$ is essentially negligible.Comparing figures 5.20a and 5.26a, the energy drained through the pressure strain term $\widetilde{PS}_{11}$ from the former is injected as a source of energy in transporting $\overline{\tilde{v}^2}^*$ through $\widetilde{PS}_{22}$ in the latter. Here, the primary energy source is $\widetilde{PS}_{22}$ with its peak near the center of the mean shear layer. The gain is essentially balanced by $\tilde{\mathcal{D}}^{\tilde{p}}_{22}$, which primarily redistributes the transverse energy. Above the mean shear layer, the redistributed energy is mostly absorbed by $-\tilde{\mathcal{A}}_{22}$ and a small portion is given back to $\widetilde{PS}_{11}$. The energy absorbed by $-\tilde{\mathcal{A}}_{22}$ is sent to the incoherent stresses through $-\mathcal{P}''_{22}$ within the recirculation region. The remaining energy is diffused towards the centerline through $\tilde{\mathcal{D}}^{\tilde{p}}_{22}$ and lost to the sink by $\tilde{\mathcal{P}}_{22}$. The diffusion terms $\tilde{\mathcal{D}}_{22} + \mathcal{D}''_{22}$ have a negligible role to play here.

The local balance of transport budget for $\overline{\tilde{v}^2}$ at the streamwise location of $l_r^*/2$ is shown in figure 5.26b. Comparing figures 5.20b and 5.26b, the pressure strain terms, though small, inter exchange energy from streamwise to transverse coherent Reynolds normal stress within the wake width whereas it occurs in the opposite direction above the wake width. The residual R_{22} remains negligible. Unlike the case upstream (figure 5.26a), the energy is dominantly produced by $\tilde{\mathcal{P}}_{22}$, within the recirculating flow bubble. There is a complex network of redistribution processes through the ensemble of diffusion terms. Nevertheless, the dominant carrier of the energy produced by $\tilde{\mathcal{P}}_{22}$ is the pressure diffusion term $\tilde{\mathcal{D}}^{\tilde{p}}_{22}$, which distributes this energy to $-\tilde{\mathcal{A}}_{22}$. A small portion of this energy is injected to incoherent stresses through $\mathcal{P}''_{22}$ within the transverse center of recirculating flow. A reverse process may also be observed above the center but within the height of the bubble, where the incoherent structures feed energy, though small, to the coherent structures.

Figure 5.27a shows the production term $\tilde{\mathcal{P}}_{22}$ split into its components at $x^* \approx l_r^*/2$, along with the normal production $\tilde{\mathcal{P}}^{(1)}_{11}$ of the streamwise stress transport equation. Unlike the case of streamwise coherent normal stress, the shear and the normal components, $\tilde{\mathcal{P}}^{(1)}_{22}$ and $\tilde{\mathcal{P}}^{(2)}_{22}$ respectively, tends to work together as a sink. The latter, similar to $\mathcal{P}^{(2)}_{22}$ in figure 4.26b, has a global peak along the wake centerline near l_r^*, where the shear layers interact, and a sink within the first half of the recirculating flow bubble $x^* < 0.5l_r^*$ (see figure

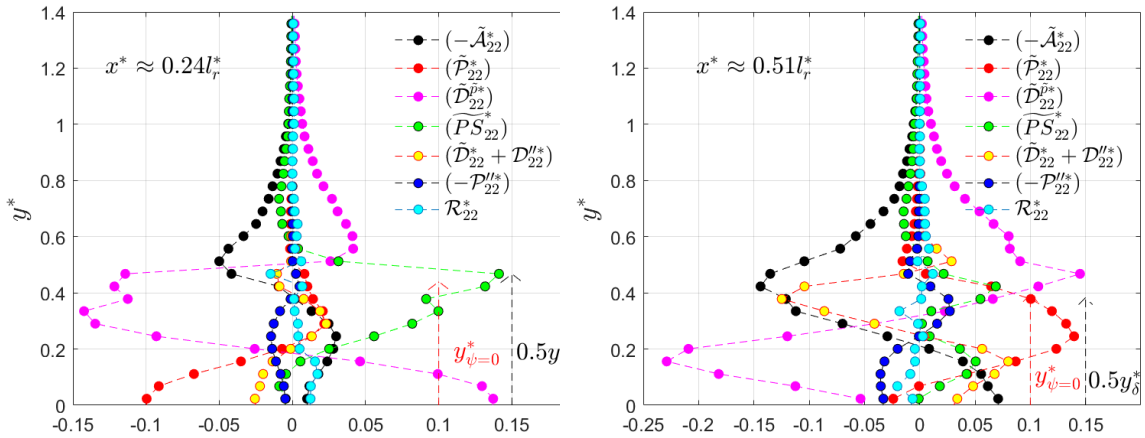

(a) (b)

Figure 5.26: Local balance of equation for the transport of Reynolds transverse coherent normal stress $\overline{\tilde{v}^2}$ for the flow at $Re_h \approx 2.8 \times 10^4$, carried out at $x^* \approx l_r^*/4$ (a) and $x^* \approx l_r^*/2$ (b) .

5.27b). This region is where the mass is entrained, by the lower side of the developing shear layer, resulting in a positive transverse gradient of the mean vertical velocity $\frac{\partial V^*}{\partial y^*}$ which while interacting with the momentum out-flux, represented by positive coherent Reynolds shear stress (figure 5.5b), results in a sink of $\tilde{\mathcal{P}}_{22}^{(2)}$. The former has similar features as that of $\mathcal{P}_{22}^{(1)}$ (see figure 4.26b), is significantly smaller than the normal component and has a global peak oriented along the *rri* (isoline $U = 0$). In figure 5.27a, it tends to oppose the normal production $\tilde{\mathcal{P}}_{22}^{(2)}$ near the shear layer center but soon switches role due to the presence of back flow. It is due to the dominating normal production $\tilde{\mathcal{P}}_{22}^{(2)}$, which peaks along the bubble periphery, that a major share of the energy is produced by $\mathcal{P}_{22}$.

Using the divergence-free mean flow, i.e. $\partial U^*/\partial x^* = -\partial V^*/\partial y^*$, the second term of the production may be written as

$$-2\overline{\tilde{v}^2}^* \frac{\partial V^*}{\partial y^*} = 2\overline{\tilde{v}^2}^* \frac{\partial U^*}{\partial x^*}.$$

Considering the normal production $\tilde{\mathcal{P}}_{11}^{(1)} = -2\overline{\tilde{u}^2}^* \frac{\partial U^*}{\partial x^*}$ which drains energy at $x^* \approx l_r^*/2$ while transporting $\overline{\tilde{u}^2}^*$, in figure 5.20b, comparing it with the normal production term $\tilde{\mathcal{P}}_{22}^{(2)} = 2\overline{\tilde{v}^2}^* \partial U^*/\partial x^*$, is roughly equal and opposite in magnitude (figure 5.27a). This implies that at the center of the recirculation region, the term $\tilde{\mathcal{P}}_{11}^{(1)}$ acts to redistribute the energy among the streamwise and the transverse coherent normal Reynolds stresses. Further, comparing the profiles of coherent Reynolds normal stress components in figures 5.5 and 5.5, both the normal stress components are not of similar nature and magnitude. This means that the behaviour of the normal production term seen in figure 5.27a is primarily due to the mean flow gradient within the recirculating bubble. Then, in comparison with $\mathcal{P}_{11}$ and $\mathcal{P}_{22}$ in figure 4.26a the energy produced by the interaction of incoherent stresses with the mean flow, for example: $\mathcal{P}_{11} - \tilde{\mathcal{P}}_{11}^{(1)}$, shall be of similar nature, i.e. an inter-component energy transfer through the normal production term.

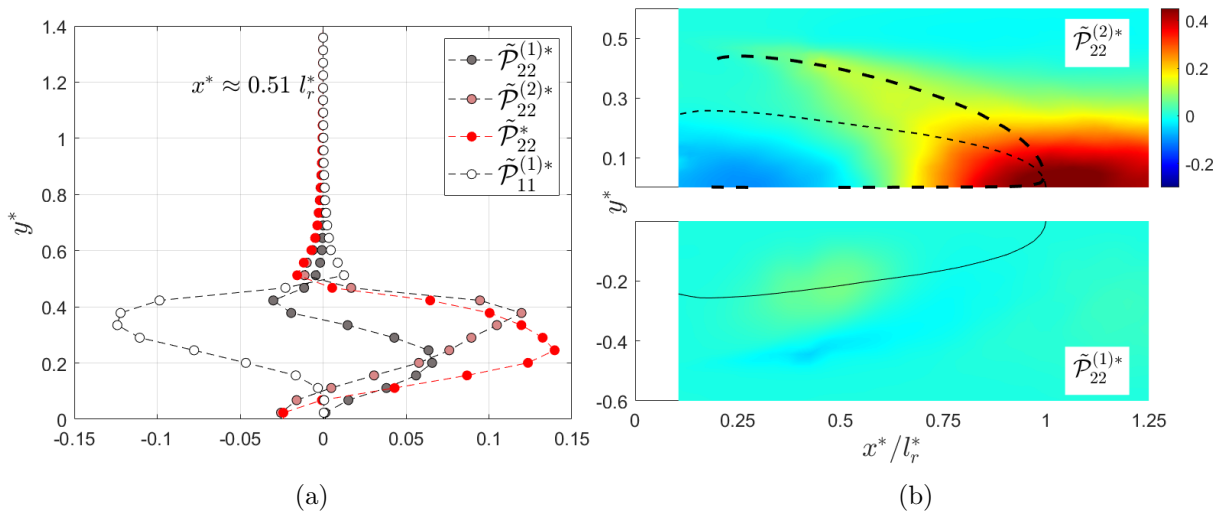

Figure 5.27: Splitting the production term $\tilde{\mathcal{P}}_{22}$ into its constituent parts (a) & (b) and comparison with the production term $\tilde{\mathcal{P}}_{11}^{(1)}$ at $x^* \approx l_r^*/2$ (a) for the flow at $Re_h \approx 2.8 \times 10^4$. The production terms $\tilde{\mathcal{P}}_{22}^{(1)}$ and $\tilde{\mathcal{P}}_{22}^{(2)}$ being symmetric, only one of the symmetric planes is shown. The thick and thin dashed lines represent the streamline $\psi = 0$ and the *rri* respectively.

Figure 5.28 shows the local balance of the transport equation for $\overline{\tilde{v}^2}^*$ at $x^* \approx l_r^*$. The residual $\mathcal{R}_{22}$ remains negligible throughout. Similar to the case at $0.5l_r^*$ a complex energy redistribution process may be seen. The dominant energy source is due to the normal production of $\tilde{\mathcal{P}}_{22}$, with a peak at $y^* = 0$. The produced energy is redistributed by $\tilde{\mathcal{D}}_{22}^{\tilde{p}}$ for the entrainment of $\overline{\tilde{v}^2}^*$ from the external flow, whereas $\tilde{\mathcal{D}}_{22} + \mathcal{D}_{22}''$ serves to transport $\overline{\tilde{v}^2}^*$ towards the wake-interior through $-\tilde{\mathcal{A}}_{22}$. Advection $-\tilde{\mathcal{A}}_{22} \to 0$ as $y^* \to 0$ implying that the $\overline{\tilde{v}^2}^*$ has reached its peak at the wake centerline. The intercomponent energy redistribution through $\widetilde{\mathcal{PS}}_{22}$ is week, while also taking place in both directions, i.e. supplying energy to $\overline{\tilde{u}^2}^*$ above the edge of the shear layer and in the reverse direction within the wake. A considerable amount of energy is also injected to the incoherent structures through $\mathcal{P}_{22}''$, which peaks close to the shear layer center, presumably by $\tilde{\mathcal{D}}_{22} + \mathcal{D}_{22}''$.

The map of the pressure diffusion and the pressure strain terms are shown in figure 5.29, where the pressure strain term $\widetilde{PS}_{22}$ is found to be equal and opposite to $\widetilde{PS}_{11}$, shown in figure 5.23, due to the two dimensional nature of the coherent structure. The map of the pressure diffusion term $\tilde{\mathcal{D}}_{22}^{\tilde{p}}$ shows that the sink through the pressure diffusion term is dominant near the end of the recirculating flow region at the center of the wake, which also corresponds roughly to the intense source of energy through the production term $\tilde{\mathcal{P}}_{22}^{(2)}$. In the region near the base of the body, corresponding to the sink of $\tilde{\mathcal{P}}_{22}^{(2)}$ at the first half of the recirculating flow region, the pressure diffusion term is seen to supply energy which is transported from elsewhere. The map indicates that the pressure diffusion term redistributes the energy that it primarily gains, from the production term $\tilde{\mathcal{P}}_{22}^{(2)}$ $x^* \approx l_r^*$ and also from the pressure strain term $\widetilde{PS}_{22}$ along the mean shear layer close to separation.

Finally, figure 5.30 shows the balance of the terms in the transport of $\overline{\tilde{v}^2}^*$ along the centerline.The residual $\mathcal{R}_{22}$ remains close to zero throughout. The dominant terms are

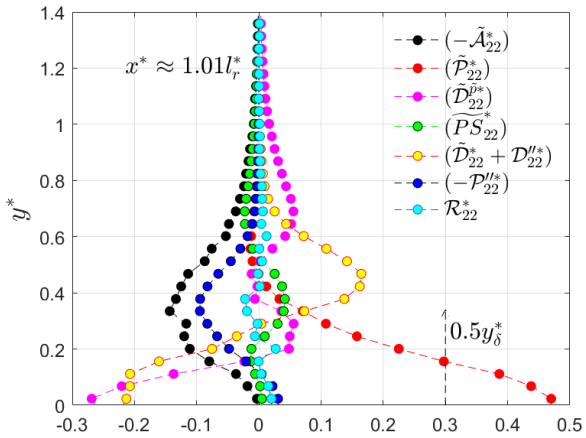

Figure 5.28: Local balance of the transport equation for the coherent transverse normal stress $\overline{\tilde{v}^2}^*$ performed at $x^* \approx l_r^*$ for the flow at $Re_h \approx 2.8 \times 10^4$.

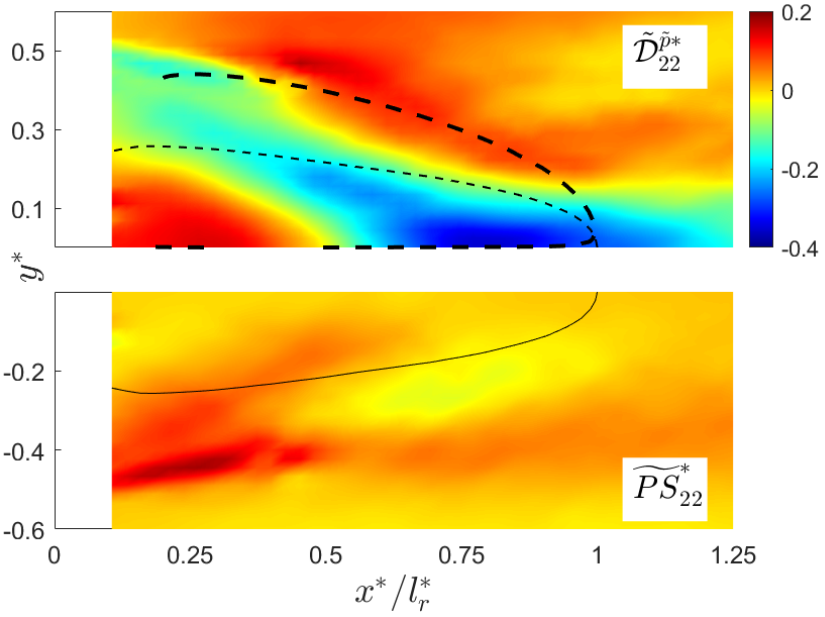

Figure 5.29: Pressure diffusion $\tilde{\mathcal{D}}_{22}^{\tilde{p}}$ field and the pressure strain $\widetilde{PS}_{22}$ field for the flow at $Re_h \approx 2.8 \times 10^4$. The fields being symmetric, only one of the symmetric planes is shown. The thick and thin dashed line represents the streamline $\psi = 0$ and rri respectively.

$\tilde{\mathcal{P}}_{22}$, $\tilde{\mathcal{D}}_{22}^{\tilde{p}}$ and $\tilde{\mathcal{D}}_{22} + \mathcal{D}_{22}''$. The advection $-\tilde{\mathcal{A}}_{22}$ is negligible on the centerline implying the local peaks of $\overline{\tilde{v}^2}^*$, except in a small region within the bubble where energy is lost to diffusion and incoherent structures. Near l_r^*, a reverse flow in energy, from incoherent to coherent, may be seen through $-\mathcal{P}_{22}''$. The energy produced by $\tilde{\mathcal{P}}_{22}$, with peak at l_r^*, is redistributed by the pressure diffusion term $\tilde{\mathcal{D}}_{22}^{\tilde{p}}$, peaking near $0.75 l_r^*$, which also feeds it back to the region close to the body base near $l_r^*/2$. The diffusion term $\tilde{\mathcal{D}}_{22} + \mathcal{D}_{22}''$ becomes active after $l_r^*/2$ and it redistributes the energy drained from the production term $\tilde{\mathcal{P}}_{22}$ within the near wake $l_r^*/2 \leq x^* \leq l_r^*$ as well as beyond l_r^*.

Similar to the case of Reynolds streamwise normal stress, an average balance of the

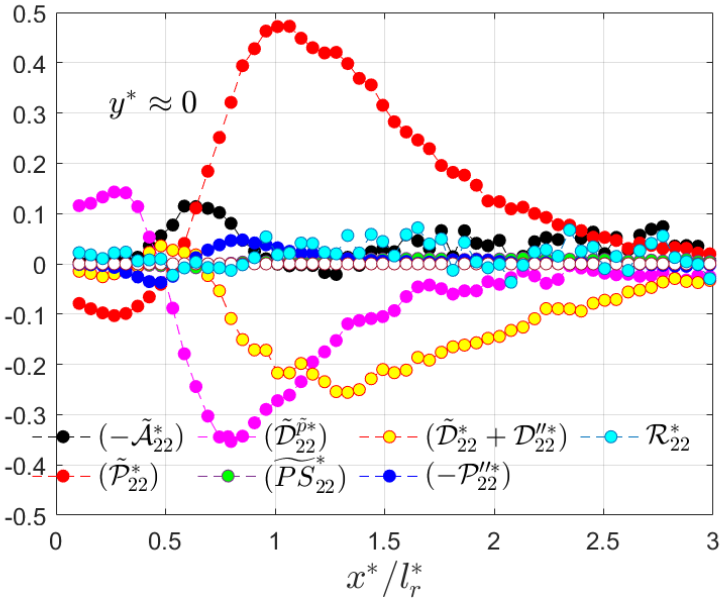

Figure 5.30: Local balance of the transport equation for the coherent transverse normal stress $\overline{\tilde{v}^2}^*$ performed along the wake centerline for the flow at $Re_h \approx 2.8 \times 10^4$.

transverse coherent normal Reynolds stresses can be performed by defining the average quantity as per equation (5.25). The resulting balance is shown in figure 5.31. The residuals $I_{\mathcal{R}_{22}}$ are negligibly small throughout. The diffusion terms including those of the coherent pressure remains negligible on averaging in the transverse direction. It was seen that the pressure diffusion term $\tilde{\mathcal{D}}^{\tilde{p}}_{22}$ is active in the region close to separation (see figure 5.26a) and towards the center of the recirculating flow region (see figure 5.26b) in redistributing the energy gained by the production as well as the pressure strain term. At the streamwise location of $l^*_r/2$, the sum of the diffusion terms $\tilde{\mathcal{D}}_{22} + \mathcal{D}''_2$ is active and at l^*_r it becomes dominant in redistributing the energy. The average of these terms in the transverse direction remaining close to zero indicates that they are involved only in the transverse redistribution of the energy. Close to the body base in figure 5.31, the pressure strain shows an average gain, which is the energy taken from the transport of coherent streamwise Reynolds normal stress (see figure 5.25).

There is a negligible, but non zero sink of energy through the production term within $0 \leq x^* \leq 0.3l^*_r$, due to the first half of the recirculating flow region. Moving further downstream, the production term acts as a source of energy which continues to rise monotonically to reach a peak near l^*_r, close to the point where the shear layers interact with one another. This gain in energy decays past $x^* \approx 1.2l^*_r$. The dominant gain in energy through the production term is mostly transported by the advection term $I_{-\tilde{\mathcal{A}}_{22}}$ resulting in a net rise in $\overline{\tilde{v}^2}^*$ peaking near l^*_r. The remaining energy is fed to the incoherent stresses through the production term $I_{-\mathcal{P}''_{22}}$, which is close to zero until $l^*_r/2$ after which, it rises to peak near l^*_r. This observation is in line with the well known conventions of turbulence, i.e. the energy is primarily produced at the larger scales and fed to the smaller ones. However, energy flow in the reverse direction has also been observed, though negligible, for example at $0.5l^*_r$. Beyond l^*_r, the incoherent stresses are constantly fed by the production term $I_{\tilde{\mathcal{P}}_{22}}$.

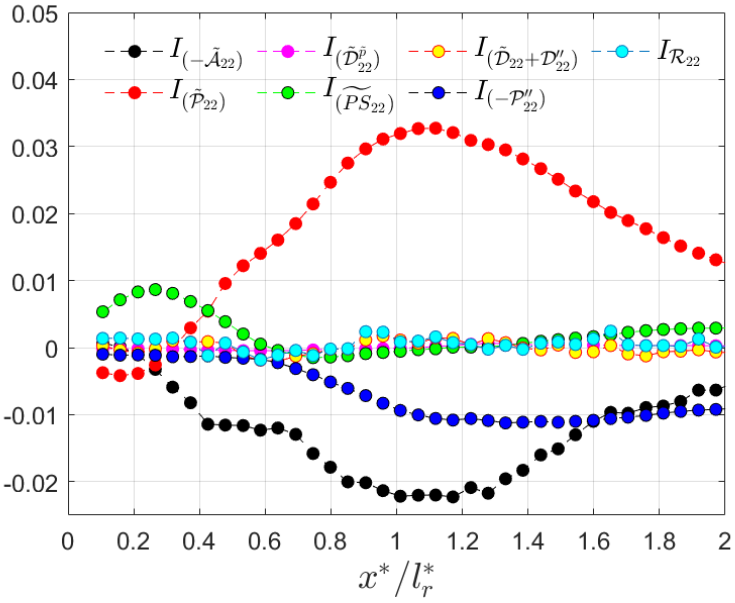

Figure 5.31: Transversely averaged balance of equation of the transport of Reynolds transverse normal coherent stress $\widetilde{v^2}$ for the flow at $Re_h \approx 2.8 \times 10^4$, along the streamwise direction scaled by l_r^*.

5.5 Conclusion

The decomposition of the flow revealed many qualitative features of the dominant vortex shedding generally observed in the wake of a bluff body [32, 29]. It permits to quantify the contribution due to various structures, and their interactions, to the drag. However, the *POD* method of flow decomposition computes uncorrelated modes and the coherent structures thus extracted which approximate the dominant vortex shedding but can be contaminated with other higher modes. The resulting decomposition of the Reynolds stress tensor does not contain information on those that arises from the interactions between the decomposed structures.

Decomposing the Reynolds stresses, the explicit contributions of the coherent and incoherent structures to the base pressure drag through coherent Reynolds shear and streamwise normal stresses were seen to be comparable. The incoherent stress contribution were primarily observed to result from the motions resembling the shear layer vortices generated immediately after separation.

The streamline $\psi = 0$ enclosing the recirculating flow region is characterized by a constant mean pressure in order to maintain force-equilibrium of the bubble. Exploiting the linear property of the Poisson equation for decomposition of mean pressure revealed that immediately after separation, the mean pressure is dominated by the mean flow deformations within the mean shear layer. As it continues to decay downstream, its contribution is compensated principally by the transverse Reynolds normal stress, which is dominated by the coherent structures. This shows the importance of the initial conditions of the separating shear layer, or the state of the boundary layer at separation, on the mean base pressure drag. Further, it also stresses on the importance of initial conditions on the developing coherent structures, which is a primary ingredient of the base pressure drag.

These observation are consistent with the literature (for example [148, 181, 120, 166]), where manipulating the boundary layer at separation or the properties of the separated shear layer led to drag reduction.

A novel method is introduced in order to estimate the coherent pressure through the coherent pressure Poisson equation, utilising only the triple decomposed flow fields and the proper orthogonal decomposition method to compute the spatial modes. This novel approach allows for estimating the temporal derivative of the coherent velocity fields by solving the Poisson equation for the temporal derivative of the streamfunction. The method significantly reduced the residuals arising out of the integral coherent momentum budget, both streamwise and transverse. The coherent drag and the lift coefficients estimated by performing the integral momentum budgets are seen to be within the range obtained by the coherent lift and drag estimated from the phase averaged fluctuating pressure signal. Since the method is used for the POD based modal decomposed flow, where temporal information is lost during the process but reconstructed using the method, the proposed method is a robust approach extendable to any modal decomposition such as by using OMD [12], image based flow decomposition methods [141], wavelet based methods [172, 53], conditional average using cross-correlation technique [84] or phase averaging using reference signal [128, 132, 83] providing a low-cost alternative to expensive time-resolved PIV.

The coherent pressure allows for the closure of the coherent Reynolds stress transport budget. It also allows for explaining the energy exchange mechanism between the mean flow and the coherent structures, and the manner in which it is redistributed to the components of normal stresses.

For coherent Reynolds streamwise normal stresses, the energy produced is primarily within the mean shear layer owing to the shear-production term. It is intense near separation. However, based on a local average, there exists a large sink of energy, formed by the total production term, immediately after separation due to the presence of the recirculation region. Based on the local average view, two important regions can be identified in the streamwise direction.

- Starting from the second region, near the end of the recirculating flow region $0.75l_r^* \leq x^* \leq 1.2l_r^*$, the coherent production term provides the dominant source of energy. The upper limit of this region is vaguely defined based on peaks observed in the dominant energy transport mechanisms, and may correspond to the extent of vortex formation region.

- Most of the energy is fed upstream the first region, which extends from the separation until $0.75l_r^*$. The pressure diffusion term drives a feedback loop, that feeds the pressure strain term and transfers energy to the other (transverse) normal coherent stress $\overline{\tilde{v}^2}^*$.

- A subregion is located in the vicinity of $l_r^*/2$, where the sink through the production term transfers the energy, redistributed by the pressure diffusion term, to the transverse normal coherent Reynolds stress $\overline{\tilde{v}^2}^*$.

In the balance of coherent transverse normal stress, the pressure diffusion is a dominant factor in the transverse energy redistribution process, both in the first and the second

regions. The diffusion due to coherent motion, is not active near separation but develops downstream. The primary source of energy, within the first region is due to the pressure strain, which connects the streamwise to the transverse coherent normal stress, where the energy produced within the shear layer is transported from the former to the latter. There is a gradual transition in the source of energy, while moving from the first to the second region, where now the normal production becomes the primary source of energy. Note that within the sub-region identified, the normal production from the coherent streamwise normal stress, transfers energy intercomponently. This transfer is primarily due to the nature of the mean flow gradient within the recirculating bubble and hence the property of the bubble. The dominant normal production for the transverse normal stress peaks near the end of the recirculating bubble, a major portion of which is taken up by the coherent and the remaining by the incoherent motion, where the shear layer interacts with each other. Finally, the dominant energy flow path is mean flow $\rightarrow$ coherent structures $\rightarrow$ incoherent structures, supported by many studies in the literature. However, local regions were identified where the energy transfer, though negligible, is from incoherent $\rightarrow$ coherent motions. This point is not investigated further.

To summarize, the shear layer forms an important feature of the bluff body wake where energy required to sustain the coherent motions are produced, either within the shear layer for streamwise normal stresses or near the region of their mutual interaction, the disruption or modification of which has been already reported to provide beneficial results of reduced drag such as the use of splitter plates [98, 16] or by control cylinders[166, 120, 175]. The recirculating bubble forms an important site for the inter-component/ spatial energy redistribution process through the normal production terms, diffusion terms and the pressure strain terms. Further, its interaction with the shear layer may form the main ingredient for energy production (for example: curvature effects [181, 28, 108]).

Chapter 6

Effects of perturbations on pressure drag and associated mechanisms

6.1 Reynolds number (Re) effects - Introduction

The increase in Re_h for the bluff body case under consideration witnesses certain changes in the flow properties, as mentioned in the Chapter 1 - Introduction. The objective of this part of the chapter is to identify the Re effects on the base pressure drag of the D-shaped bluff body under consideration, limited to within $Re \sim \mathcal{O}(10^4)$, and its associated mechanisms discussed in the previous chapters.

6.1.1 (Re) effects on the mean flow features

Starting with the boundary layer, it is well known that the laminar boundary layer evolves as $xRe_x^{-0.5}$ [152], where $Re_x = \frac{U_\infty x}{\nu}$ (In our case, $x = x_{sep}$, where x_{sep} is the streamwise location of the trailing edge of the bluff body at which the flow separates, is constant for all the flows). Since boundary layer measurements are not taken, the distance from the body surface $y^* = 0.5$ to the maximum value of the mean streamwise velocity profile at separation $U^*(x^*_{Sep}, y^*)$ is taken to be the distance that characterises the boundary layer thickness denoted by δ_{Sep}. The evolution of δ_{Sep} in figure 6.1b is linear with $Re_x^{-0.5}$ conforming to the prediction using the streamwise Reynolds number Re_x for the laminar boundary layer. A direct consequence is that the ensuing shear layer is enhanced in its strength as the mean shear increases. This change may have profound effects in the ensuing wake structure and shall be discussed in the following sections.

Another effect of Re_h is on the base pressure drag shown in figure 6.1a. It varies roughly in a linear fashion and the maximum variation with respect to the C_d at the lowest $Re_h \approx 2.8 \times 10^4$ is approximately 7%. A few other points require attention as well. The maximum velocity deficit U^*_s shows a linear increasing trend with Re_h in figure 4.2b, whereas the minimum streamwise velocity in the wake U^*_{min} remains roughly the same. The length-scales related to the growth of the mean shear layer, for eg: l^*_r or l^*_p in figure 4.3b, is also seen to increase with Re_h, however the maximum variation remains very small within approximately 1.5% with respect to the l^*_r of the lowest Re_h.

Comparison of the mean streamwise velocity at the similarity co-ordinate $x^*/l^*_r \approx 0.2$,

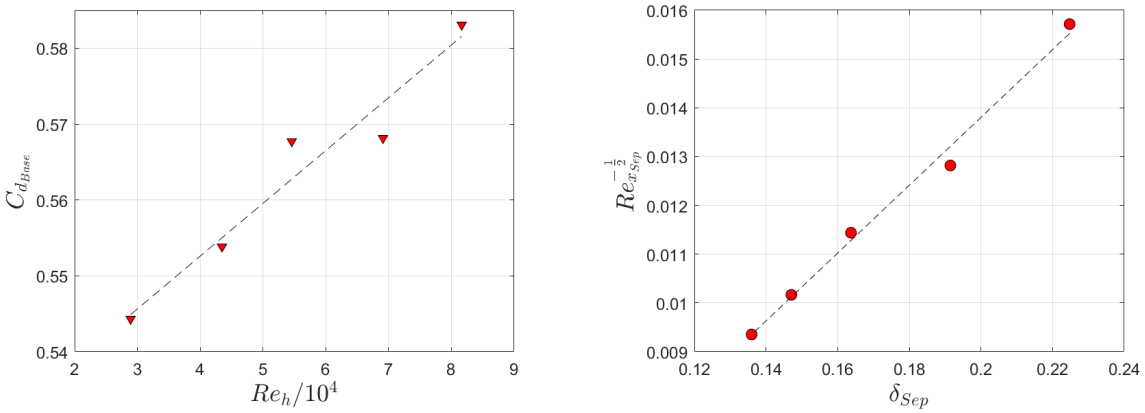

(a) (b)

Figure 6.1: The variation of $C_{d_{Base}}$ (a) and δ_{Sep} (b) along with the Re_h and $Re_{x_{Sep}}$ respectively for the baseline flow.

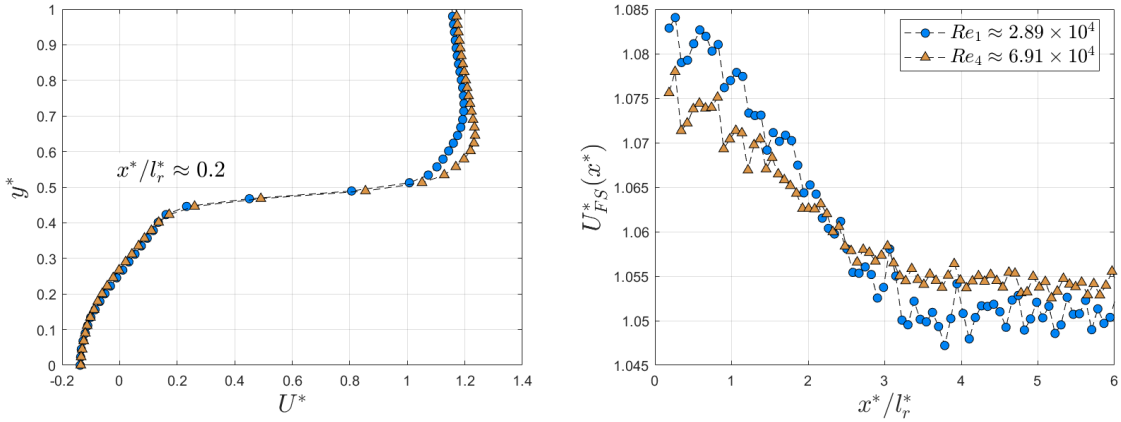

(a) (b)

Figure 6.2: Profile of mean streamwise velocity at $x^* \approx 0.2l_r^*$ (a) and the variation of the free stream velocity U^* (b) for the lowest and highest Re_h test cases.

near the point of separation, is shown in the figure 6.2a. The profiles of U^* is seen to evolve similarly along the vertical direction from the centerline until $y^* \approx 0.5$. Beyond $y^* \approx 0.5$, the mean velocity U^* shows a slight increase. The peak of U^*, which was at $y^* \approx 0.7$ for the lowest Re_h, has also decreased to $y^* \approx 0.6$, evidently due to the decrease in the inlet boundary layer thickness.

Figure 6.2b shows the variation of the free-stream velocity along the streamwise direction. It is high close to the separation, due to the blockage offered by the body, and decreases downstream due to the expansion of the flow. At the higher $Re_h \approx 6.91 \times 10^4$, U_{FS}^* remains roughly the same, indicating a negligible blockage effect due to the wind tunnel wall boundary layers. The profiles of the Reynolds shear stress for cases of two Re_h, scaled by the transverse length scale $y_{\delta_{min}}^*$, are shown in the figure 6.3a. The profiles are taken at the streamwise location of l_r^* since the Reynolds shear stress reaches its peak near it. The peaks of the $\overline{u'v'}^*$ are seen to scale with the square of the velocity deficit (shown in the inset of figure 6.3a). The coherent and the incoherent contributions to the Reynolds shear stress are comparable in magnitude, and both of them peak near the

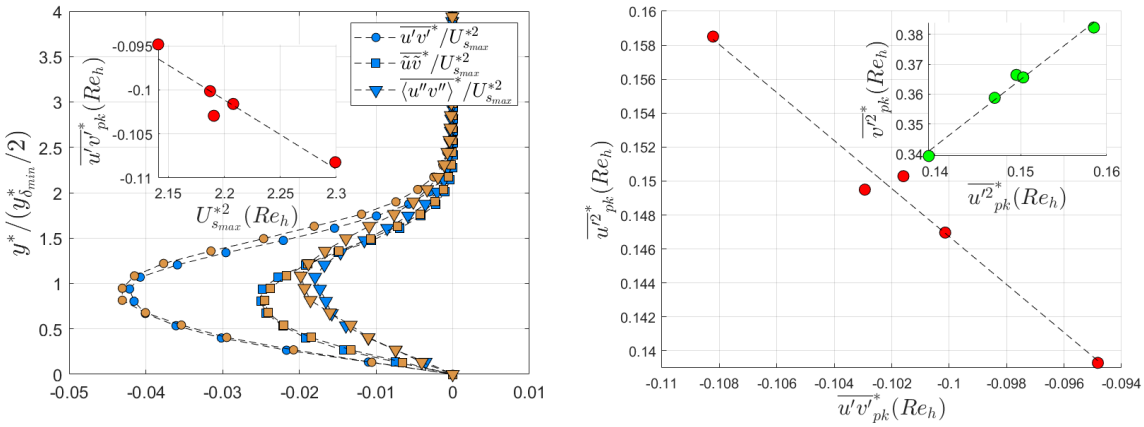

(a) (b)

Figure 6.3: Profile of the Reynolds shear stress at $x^* \approx l_r^*$ with the inset showing its peak evolving with the square of the velocity deficit (a) and the evolution of the Reynolds stress peak values (b) for all the Re_h test cases.

wake width $y^*_{\delta_{min}}/2$. The peaks of the Reynolds normal stresses, shown in figure 6.3b, also varies linearly with each other's peaks. This is to say that a velocity scale may be defined for the rms value of the fluctuations such that it is linearly related to the mean wake velocity deficit, i.e. $u \sim U_{s_{max}}$, and that the transverse variation of quantities scales with the characteristic scale of the wake width $y^*_{\delta_{min}}$.

6.1.2 (Re) effects on the mean base pressure drag

The integral mean momentum budget and the mean pressure decomposition showed that the Reynolds normal stresses, other than the mean flow, contributes significantly to the mean base pressure drag. Further, the mean pressure contributions due to $T^{P_M - P_{FS}}$ can be expected to increase with Re_h due to the effect of enhanced shear and the velocity deficit acting through the terms $T_m^{(1)}$ and $T_m^{(2)}$. This suggests that the mean base pressure drag is scaled by the square of the velocity deficit.

The scaled contributions to the mean base pressure drag is shown in figure 6.4. The superscript $\cdot^{\times}$ represents the scaling of the mean base pressure contributions, for example:

$$T^{P\times} = \frac{1}{U^{*2}_{s_{max}} h^{*CV}_{in}} t^P, \tag{6.1}$$

where division by the CV height is performed in order to for the terms to be devoid of the effect of integration height. All the contributions seems to scale as per (6.1). The total average contribution of the scaled mean pressure $T^{P\times}$ remains approximately at 0.42. Note that the Reynolds normal and shear stress contributions are not shown as it is clear that an increase in one results in a proportional change in the other since their peaks are proportional as per figure 6.3b. Changes may be noted in figure 6.4b, where the scaled coherent contributions to the drag decreases while the incoherent ones increases, which is to be expected since the increase in Reynolds number is known to enhance the three dimensional nature of the flow (see for example [206]).

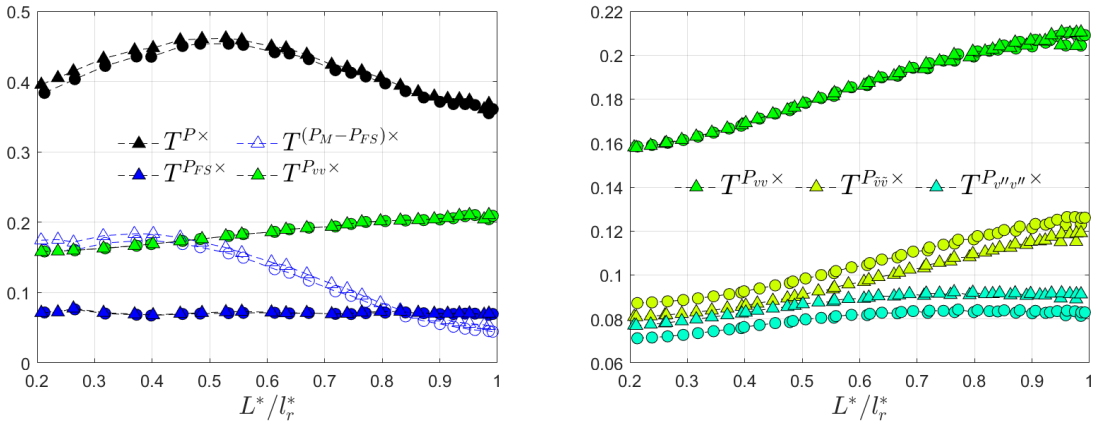

Figure 6.4: Decomposed and scaled mean pressure contributions to the mean base pressure drag for the flows at $Re_h \approx 2.89 \times 10^4$ & $Re_h \approx 6.91 \times 10^4$ (a) and the split and scaled contributions of the coherent and incoherent transverse normal stresses to the mean base pressure drag (b).

6.1.3 (Re) effects on the transport mechanism of coherent Reynolds stresses

The effects of the Reynolds number is particularly interesting here in order to understand the change in transport mechanisms of the Reynolds stresses. It is expected that the transport mechanism of the Reynolds stress resulting from the total fluctuations does not change drastically, since $\overline{u_i' u_j'}^*$ evolves with the mean velocity deficit squared and the transport terms, especially the dominant source of energy - production, are expected to scale with a certain combination of velocity deficit and the length-scales identified. Since, the residuals remain substantial, the physical mechanism is not discussed further.

The figure 6.4b shows the separation between the mean pressure due to coherent and incoherent stresses, i.e. to say that there is an increase in incoherent Reynolds stresses whereas the coherent ones remain more or less unchanged. The vertically integrated budget of the transport equation for the coherent normal Reynolds stresses are as shown in figure 6.5. Integration height is chosen as $L_y^* \approx 3y_{\delta_{min}}^*$ in order to extend to the external free-stream flow. The residuals arising from the budgets remains close to zero and are similar for both the cases of Re_h, shown in figures 6.5b and 6.5d. The streamwise evolution of the transport terms is scaled by the length of the recirculating flow region l_r^*. Also, as expected, the variation in Re_h doesn't bring about a drastic change in the physical mechanism of Reynolds stress transport. The spatial redistribution terms such as $I_{\tilde{\mathcal{D}}_{11}^{\tilde{p}}}$ and $I_{\tilde{\mathcal{D}}_{11}+\mathcal{D}_{11}''}$ remains more or less the same, except close to the body, the former decreases slightly which is reflected as a slight decrease in the energy drained by the pressure strain term $I_{\widetilde{PS}_{11}}$ (resulting in a slight reduction in the energy injected to transport $\overline{\tilde{v}^2}^*$ through $I_{\widetilde{PS}_{22}}$). The most noticeable change is in the increase in the energy extracted from the mean flow at l_r^* by the action of coherent stresses resisting mean flow deformation, which is then injected to the incoherent stresses through the production term $I_{-\mathcal{P}_{11}''}$.

In the case of transport of coherent transverse normal Reynolds stress $\overline{\tilde{v}^2}^*$, the effect

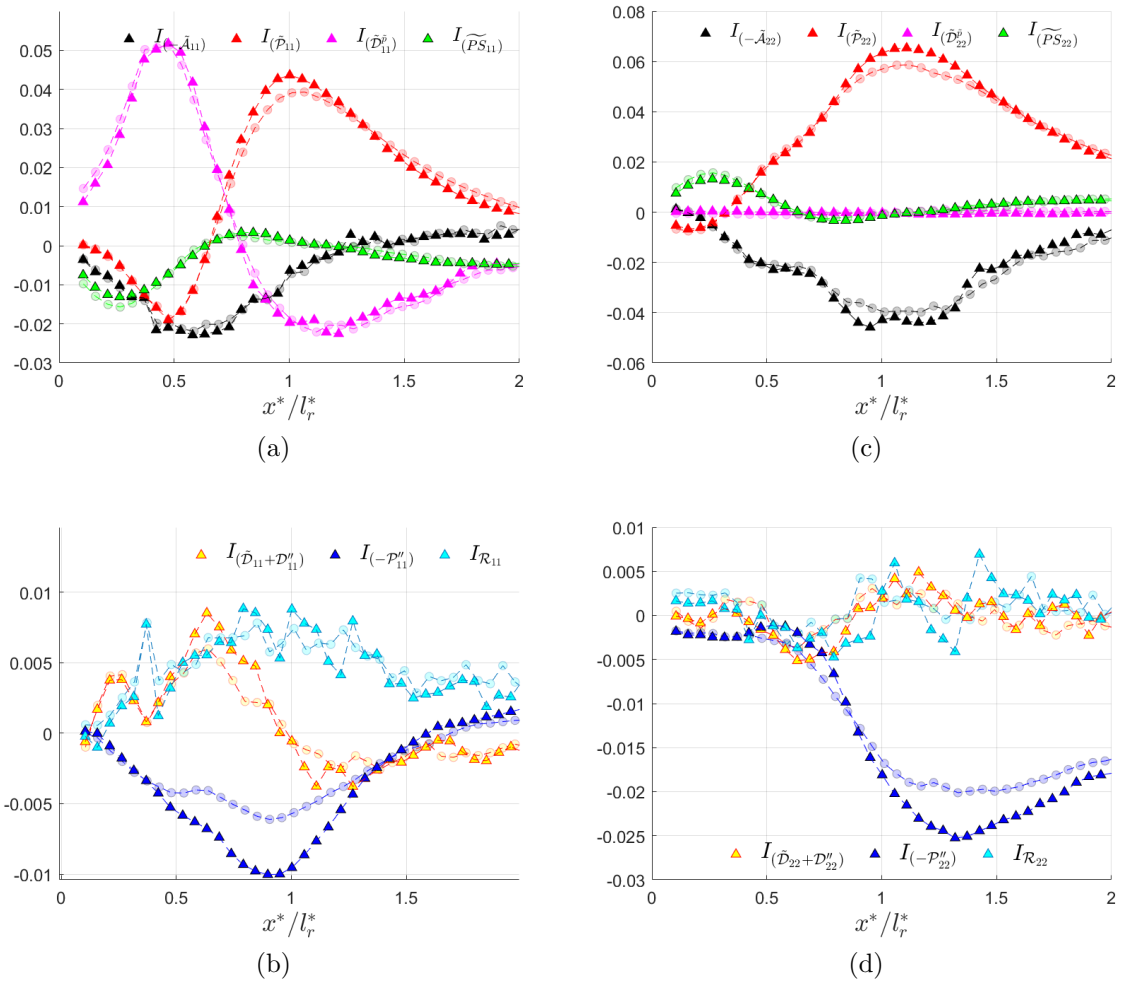

Figure 6.5: Comparison of the integrated transport terms involved in transporting coherent streamwise Reynolds normal stress $\overline{\tilde{u}^2}^*$ (a) & (b) and the coherent transverse Reynolds normal stress $\overline{\tilde{v}^2}^*$ (c) & (d) for $Re_h \approx 2.89 \times 10^4$ (solid circles) and $Re_h \approx 6.91 \times 10^4$ (solid triangles). Their streamwise evolution is scaled by the extent of the recirculating flow region l_r^*.

of Re_h on the energy redistribution mechanisms are not seen, because they are concerned with the transverse distribution of energy only. Similar to the case of the transport mechanisms of $\overline{\tilde{u}^2}^*$, the noticeable difference is visible in the energy extracted through the production term $I_{\tilde{\mathcal{P}}_{22}}$, which is then injected to the incoherent stresses through $I_{-\mathcal{P}''_{22}}$.

The impact of the wake inlet conditions on the base pressure drag has been documented in many studies. For example, [48] observed reduced base pressure drag while the boundary layer was thickened. They observed the weakening of the shed vortices with an increased boundary layer thickness and attributed these to the base pressure drag reduction observed. Another study by [148] had also observed decreased base pressure drag with an increased boundary layer thickness. All these studies point to the influence of the boundary layer in modifying the wake dynamics that influences the base pressure drag. Here, the increase in production terms is to be expected because of the wake inlet conditions. The thinner boundary layer enhances the shear layer strength, increasing the mean flow deformation and tending to increase the production. Going along the lines of [148],

the decreasing boundary layer thickness makes the time required , for the vorticity from one of the separating boundary layer in sufficient concentration, to initiate the shedding of the vortex of opposite sign, shorter thereby increasing the non dimensional shedding frequency. In the present study, the non-dimensional shedding frequency in terms of the Strouhal number, is found to increase with the Re_h. This implies that, as the vortices are enhanced in strength due to the wake-inlet conditions resulting in a higher non dimensional shedding frequency, the incoherent stresses increasingly resist the deformation of these large coherent structures resulting in a higher amount of energy being injected to the incoherent part through the production term $I_{-\mathcal{P}''_{22}}$. This is consistent with the view that the decreasing time scale of the large scale eddies enhancing the energy supplied to the smaller scales [174]. Therefore, the effect of Re_h on the Reynolds stresses is to increase the incoherent stresses, the energy for which is extracted from the mean flow by the coherent structures.

6.2 Effects of free-stream turbulence (FST) on the base pressure drag and associated mechanisms

6.2.1 Introduction

The effects of free-stream turbulence on the bluff body drag has been a complex subject of research, probably due to the large parametric space spanned by the length scales and the turbulence intensity level of the oncoming flow. Many studies in the past has shown that the mean drag coefficient is sensitive to the intensity and the scales of the turbulence [92, 19, 90, 111, 112, 82, 89]. Speaking about the scales, the most commonly used is the integral length-scale $\mathcal{L}_x$, where the subscript x refers to the longitudinal integral lengthscale, whose relative size with the body height has been observed to have a significant influence the the developing wake. For example, when the lengthscale of the incoming turbulence is small, (i.e when the ratio $\mathcal{L}_x/h \ll 1$), the incoming turbulent flow was found to primarily interact with the separating shear layer at the trailing edge of the body inducing vorticity fluctuations, enhancing mixing and forcing it to reattach or merge with the shear layer developing from the opposite side [90, 19, 82] . This led to the decrease of the length of the recirculating flow region, the shear layer curvature increased and as a consequence the drag was found to increase[90, 19]. With the scale of the incoming turbulent flow large, i.e $\mathcal{L}_x/h \gg 1$, the bluff-body wake is sensitive to the ambient turbulent flow as a quasi unsteady mean flow with slowly fluctuating velocities and without any significant interactions with the wake [19, 112]. The influence of the turbulent intensity, with the $\mathcal{L}_x/h \approx 2$ held constant [82], showed that the increasing turbulence intensity amplified the turbulent content of the shear layer, with the accelerated breakdown of shear layer vortices and earlier transition to turbulence thereby increasing entrainment and earlier merging of shear layers increasing its curvature. Another study [94] considering the effect of lengthscales, found minimal influence of integral length-scales on the mean drag coefficient. A recent study [89] with the integral lengthscale, $\mathcal{L}_x/h \approx 0.3$, observed the extension of the vortex formation region and a damping of the cross-stream mixing, in the presence of free-stream turbulence as high as 6.5%, with the corresponding reduction in drag. All these studies point to the complexities in understanding the influence of the free-stream turbulence on bluff body wakes.

In the present study, the bluff body experiences an inhomogeneous and high intensity incoming turbulent flow $T_u \approx 13\%$ with the integral length-scale not so large, $\mathcal{L}_x/h \approx 0.3$. The objective of this section is to understand the influence of the free-stream turbulence on the mean drag coefficient and the transport mechanisms of the coherent Reynolds stresses that dominantly contribute to the drag. The FST dampens the fluctuating lift coefficient, and reduces the mean drag coefficient (once the blockage effect is removed) together with an increase of the recirculating region. Using our mean pressure reconstruction technique, the mean vertical momentum budget is performed over the recirculating flow region interface in order to explain the mechanism for the recirculating flow region increase. The intimate relation between the diffusion lengthscale and the recirculating flow region lengthscale, as per [61], is also considered. Further, the novel coherent pressure reconstruction is used to close the time averaged coherent Reynolds normal stress budget in order to understand the influence of FST on the transport mechanism of the coherent Reynolds stresses.

6.2.2 Effects of perturbations on the mean flow characteristics

The boundary layer, as mentioned in section 4.1.1, is expected to be laminar at separation for the current case. The velocity profile for the two cases of the lowest Re_h, for baseline (without FST) and the perturbed (with FST) flow cases under study, are shown in figure 6.7a. An increase of the mean velocity U^* is observed in the free stream, compared to the baseline case. Approaching the wake center transversely from the free stream, U^* increases with FST and this increase occurs at a distance relatively lesser, compared to that of the baseline case, from the body-surface. The evolution of this distance, denoted as δ^*_{Sep} , which was chosen as a length scale characterising the boundary layer thickness in the absence of boundary layer measurements, is shown in the inset of figure 6.7a. Expecting a laminar boundary layer separation, the decrease of δ^*_{Sep} for the perturbed flow compared to the baseline cases, indicates the thinning of the boundary layer.The increase in the maximum U^* at δ^*_{Sep} indicates the increase of the velocity deficit. There seems to be a rise in the free-stream velocity U^*_{FS} in the case of perturbed flow, shown in figure 6.7b, approximately 5% to that of the baseline flow case. An increase in such magnitude may not be neglected, and may be a result of the increased blockage due to the wind-tunnel boundary layer, which might have transitioned to turbulent ones earlier than that of the baseline case and increased in thickness. As such, the increase in velocity deficit indicated by the increase in U^* at δ^*_{Sep} should be the result of this blockage.

The effects of blockage on the drag may be isolated. However, there could be other effects on the wake dynamics. For example, [162] noted a decrease in non dimensional shedding frequency of a square cylinder, with a 2.5% decrease in blockage at low Reynolds number $\mathcal{O}(10^2)$. An earlier study [198] reports an increase in shedding frequency and a distortion of the mean flow for the case of a cylinder at a higher Reynolds number $\mathcal{O}(10^4)$ for a blockage ratio in the range 0.06 to 0.16. The studies of [156] also reports an increase in shedding frequency, decreased size of the shed vortex and increased drag for the case of a square cylinder for blockage ratio varying in the range 0.15 and 0.3. In a recent study by [196], the range of blockage ratios on different bluff cylinders were reported, including the increase in shedding frequency, increase in drag, lengthening of the recirculating flow region etc, however the blockage ratios used were very high, from 0.25 up to 0.5. All

these studies point to the fact that increasing the blockage ratio has a clear effect on the mean flow properties as well as the wake dynamics. Figure 6.6a shows the variation in non-dimensional shedding frequency in terms of Strouhal number St_v, with the mean characteristic time-scale which indicates the time period of diffusion of the shear layers [61]. The mean velocity deficit scale, used to form the characteristic time scale, scales with the maximum mean streamwise velocity at the edge of the separated shear layer, which tends to increase with blockage. As expected, an almost perfect linear trend is seen. Following [61], It also indicates that the increase in non-dimensional shedding frequency could be due to the increased effective blockage, as evidenced in the literature.

The spectrum of lift coefficient in figure 6.6b, in the case of the baseline flow shows dominant peak of vortex shedding. Adjacent peaks are also seen, corresponding to various frequency cells in the spanwise direction which interact with each other in a nonlinear fashion [18]. The peak of the vortex shedding is strongly decreased with the addition of free-stream turbulence shown in the same figure. The energy is now distributed among various adjacent peaks and the spectrum around the dominant shedding frequency is broadened. The appearance of various modes with frequency centered around the dominant ones is the classic case of vortex dislocation in the wake, where the phase mismatch between the adjacent 'frequency cells 'causes twisted entanglement of adjacent vortices increasing their three-dimensional nature (see for example [18, 199, 121, 42]). With the addition of FST, these dislocations become even more pronounced leading to an increased three-dimensional wake.The time series of the fluctuating-lift signal for both the baseline and the FST perturbed flow fields, obtained from the pressure sensors, are shown in figure 6.6c. For the baseline case, the lift shows smooth periodic fluctuations with significant low frequency modulations indicating a quasi-periodic nature of the shed vortex shedding. Moving onto the perturbed case, these smooth periodic fluctuations seem to be disrupted by high-frequency events, while the low frequency modulations are still present. The disruptions witnessed from the fluctuating lift signal could possibly be due to significant three-dimensional motions generated by the FST interfering with the vortex shedding.

In our study, in the case of perturbed flow fields, the minimum increase in blockage is approximately 5% whereas the maximum goes up to 9% for the highest Re_h considered. For the observed increase in blockage ratio, the gap between the wall and the body is sufficiently large (see [135]), such that the modification of the wake flow by the increase in blockage may be considered negligible. In addition, it has to be the free-stream turbulence that directly influences the wake.

The base pressure drag is normally computed assuming a non varying free-stream pressure along the entire streamwise length of the body. The bluff body being very short in our case, i.e. $0.07H_s$, the growth of wind tunnel boundary layer within this distance is assumed negligible and as a consequence, the change in free-stream velocity U^*_{FS} within this distance is assumed negligible as well. While adding FST, assuming negligible effect due to the free-stream velocity, the decay in streamwise turbulence intensity on the free-stream pressure has to be accounted for. That is, according to the Bernoulli's equation,

$$P_\infty(x_l + l) - P_\infty(x_l) = \frac{1}{2}\rho\left(\overline{u'^2}(x_l) - \overline{u'^2}(x_l + l)\right), \tag{6.2}$$

where x_l and l denote the leading edge and the streamwise length of the body respectively and with $P_\infty(x_l) = 0$. The decay of turbulence intensity squared given by $\Delta\overline{u'^2}$ over this distance, in the present case, is approximately $0.02U^2_{in}$. The base pressure drag corrected

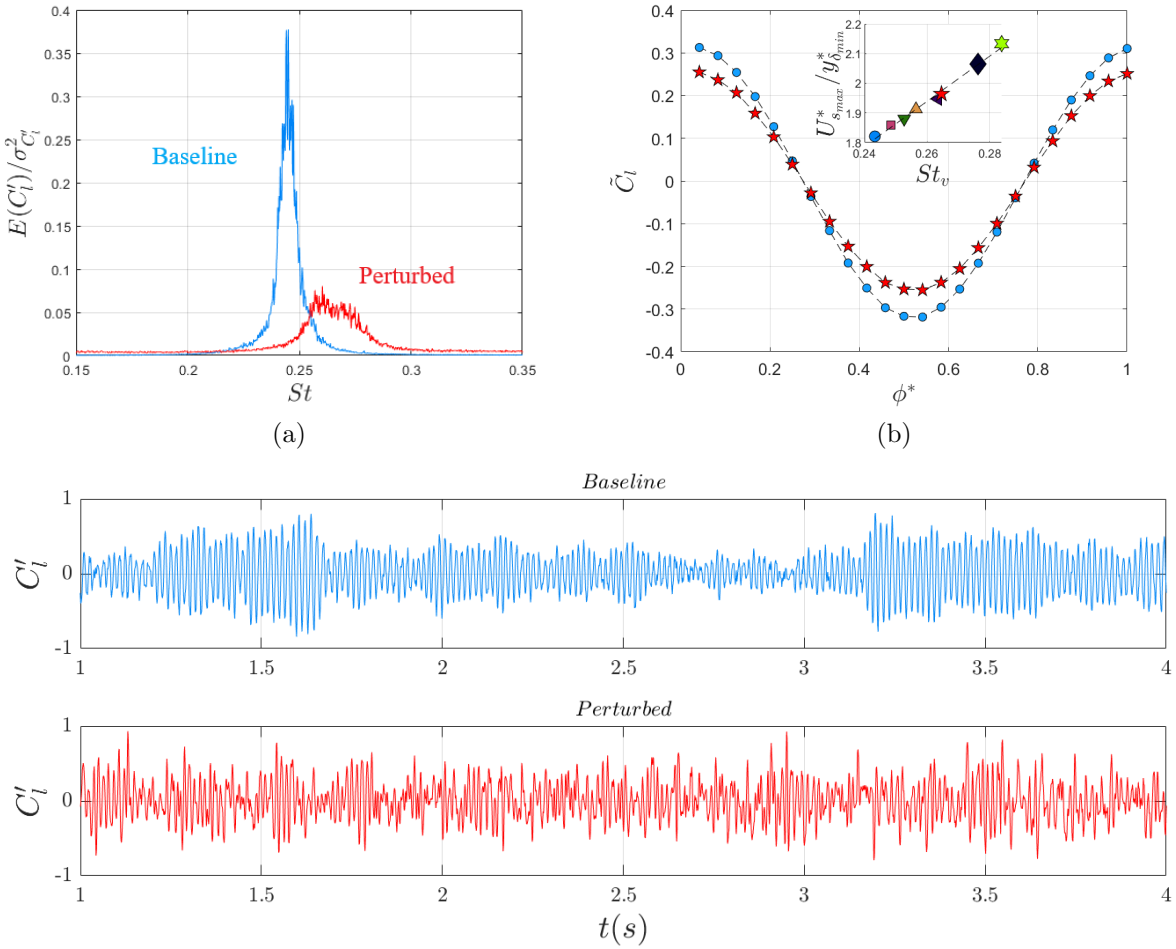

Figure 6.6: Spectrum of the fluctuating lift (a), Coherent lift extracted by the ensemble average of band-pass filtered signal (b), Variation of the dominant non dimensional shedding frequency with the mean diffusion time-scale (Inset of (b)) and the time series of the fluctuating lift signal compared for the baseline and the perturbed flow cases at $Re_h \approx 2.8 \times 10^4$ (c).

for this variation in free-stream pressure, according to equation (6.2), is shown in the inset of figure 6.7b. The base pressure drag is seen to increase with the addition of FST. However, this may just be an artifact due to the reduced free-stream pressure resulting from the increased blockage, witnessed in the evolution of free-stream velocity $U^*_{FS}(x^*)$ in figure 6.7b. The base pressure drag isolating the blockage and other contributions, accounting for the effects of the FST, shall be discussed in the following sections.

6.2.3 Effects of FST on the characteristic lengthscales

Changes in the length of the recirculating flow region

.

FST affects the wake in several ways; For example, a 15% increase in the length of the recirculating flow region is observed, indicating that the growth of shear layer is influenced by the FST. The mass locally transported by the mean flow $\rho\,(\mathbf{U}\cdot\hat{n})$ from the shear

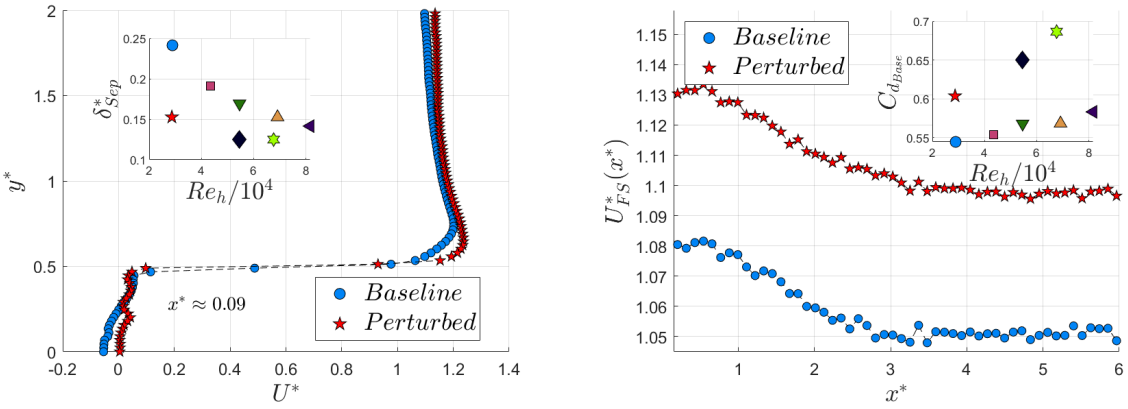

(a) (b)

Figure 6.7: The comparison of mean streamwise velocity U^* profiles at separation at $Re_h \approx 2.8 \times 10^4$ for the baseline and the perturbed flow fields (a), where the inset shows the variation of δ^*_{Sep} with Re_h, and the evolution of free-stream mean streamwise velocity U^*_{FS} for the baseline and perturbed flow cases (b), where the inset shows the variation of base pressure drag with Re_h with and without addition of FST.

layer, close to the end of the recirculating flow region, for the cases of baseline and the perturbed flow fields are shown in figure 6.8a. Comparing the baseline and the perturbed flow case, the center of the recirculating flow region where the mass flux crosses zero, is shifted in the streamwise direction with the presence of FST. Denoting the streamwise location of the center of the recirculating flow vortex as l^*_v, it varies linearly with l^*_r as shown in the inset of figure 6.8a. The difference between l^*_r and l^*_v seems to remain approximately at 0.44 for all the cases. Further, the peak of the mass influx does not seem to vary considerably for the cases of Re_h considered. The main difference seen is in the upstream, within $0.1l^*_r \leq x^* \leq 0.5l^*_r$, where the mass entrained by the shear layer decreases for the case of flow with the presence of FST.

The mechanism of the shear layer rolling up into vortices, following [61], consists of three principal steps where the fluid drawn across the wake by a growing vortex, on one side, is entrained partly by the growing shear layer and the growing vortex on the opposite side and a part of this fluid is drawn into the interior of the formation region. This means that the length of the mean shear layer, is influenced by the mechanism of the entrainment by the coherent shear layer that finally ends up as shed vortices.Figures 6.9a and 6.9b shows the coherent and incoherent Reynolds stress profiles close to the separation, at $x^* \approx 0.2$. Comparing the cases of baseline and perturbed flows, the Reynolds shear stress component, peaking at the wake-width, has been dampened with the addition of FST. This is also true in the interior of the wake where the positive peak of $\widetilde{\overline{u}}\widetilde{\overline{v}}$ is reduced by at least 30%. Decrease of $\widetilde{\overline{v}^2}$, within the wake interior, by at least 40% is also visible. Further, the damping of coherent Reynolds stress above the wake-width is also observed. Comparing the Reynolds incoherent stresses, note that the FST is included with the ensemble of incoherent motions. Reduction in the peak of incoherent stresses, comparing the baseline and perturbed flow fields, are also observed. In addition, from the profiles of incoherent transverse Reynolds normal stress $\overline{\langle v'' \rangle}^*$, beyond the wake width, it seems to be what looks like an erosion of incoherent momentum due to the presence of FST.

The evolution of Reynolds stress components, split into coherent and incoherent

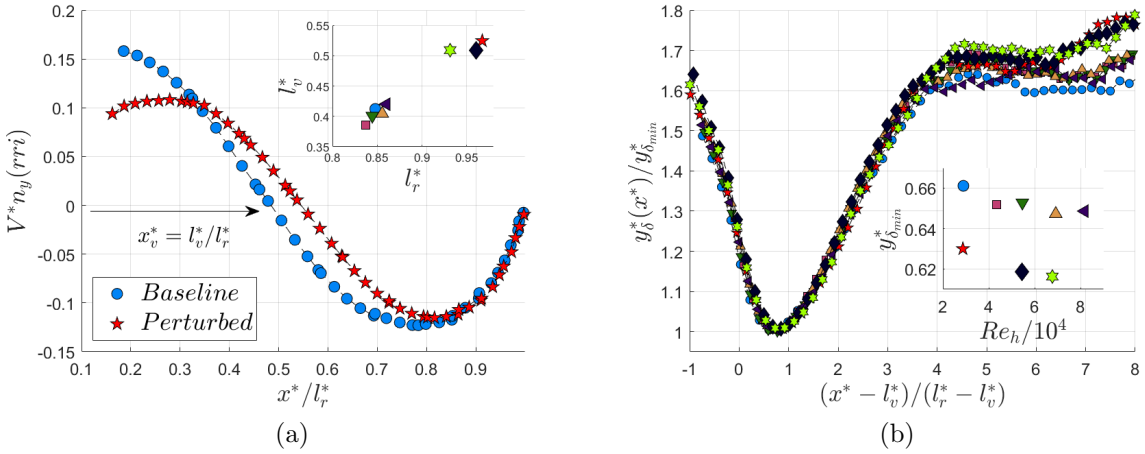

(a) (b)

Figure 6.8: The comparison of mass entrained by the mean flow along the mean rri, defined by the isoline $U = 0$, at $Re_h \approx 2.8 \times 10^4$ for the baseline and the perturbed flow fields (a), where the inset shows the variation of the length scale l_v^* with l_r^*, and the evolution of wake-width for the baseline and perturbed flow cases (b), where the inset shows the variation of the characteristic length scale $y_{\delta_{min}}$, which scales the transverse evolution of the flow, with Re_h with and without addition of FST.

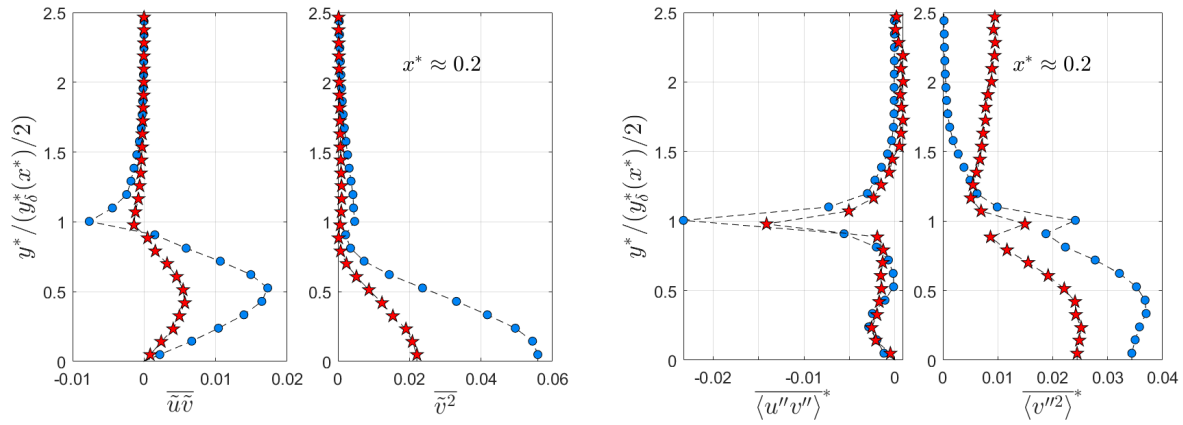

(a) (b)

Figure 6.9: Transverse evolution of the coherent (a) and Incoherent (b) Reynolds shear and transverse normal stresses for the baseline and perturbed flow cases at $Re_h \approx 2.8 \times 10^4$ at the streamwise location close to separation. The circles and the pentagrams represent the baseline and perturbed flow respectively.

stresses, along the rri, in the similarity coordinates, is shown in figure 6.10. The Reynolds shear stress along the first half of the bubble, i.e. upstream of l_v^*, is positive implying a momentum outflux from the recirculating flow region which is then taken up by the developing shear layer. This momentum outflux is dominantly due to the coherent structures, whereas the incoherent structures act to entrain momentum towards the interior of this region. This is qualitatively shown in figure 5.6. With a turbulent ambient condition, the incoherent shear stresses are expected to increase, since the entrained fluid includes the external flow and the superimposed background turbulence. The increased influx of momentum due to the incoherent structures and the decreased momentum outflux due to dampened coherent structures, reduces the overall fluctuating momentum outflux, in-

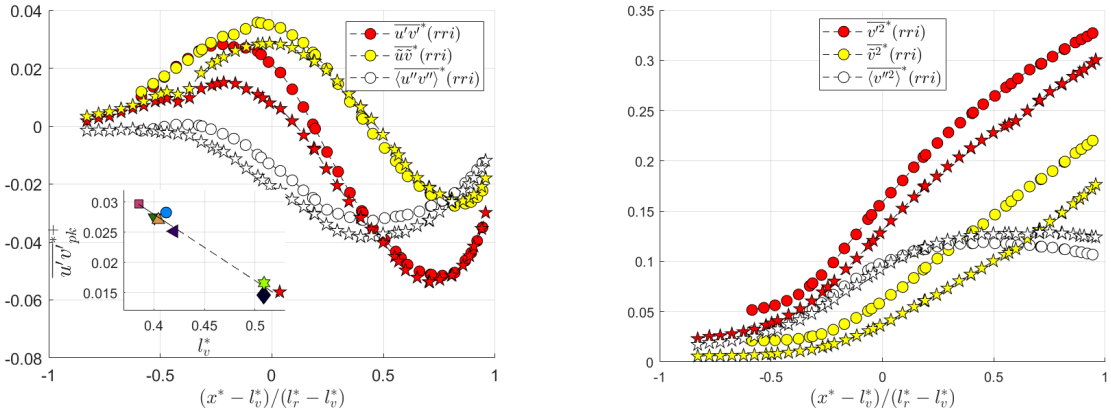

Figure 6.10: Evolution of Reynolds shear stress (a) and the Reynolds transverse normal stress (b) along the rri and split into coherent and incoherent contributions. The inset in (a) shows the variation of positive peak of Reynolds shear stress with l_v^*.

dicated by the reduction in the positive peak of $\overline{u'v'}^*$.

A simple integral-mass balance, $\int_{CV}(\mathbf{U}^* \cdot n)$ where the mass is unity due to normalisation, and transverse momentum balance,

$$\int_{CV}\left(U^*V^*n_x + V^{*2}n_y\right) = -\int_{CV}\left(P^*n_y + \overline{u'v'}^*n_x + \overline{v'^2}^*n_y\right), \tag{6.3}$$

neglecting the viscous terms and performed along the control volume enclosing the recirculating flow region, with its lateral bounds defined by the rri, may be carried out.

The resulting balance is shown in figure 6.11a, from which the transport of vertical mean momentum close to the body results from the balance of Reynolds shear as well as the transverse normal stress. The shear stress tends to increase the vertical mean momentum transport, while the transverse normal Reynolds stress tends to decrease it. The role of the mean pressure term is negligible here. The mean vertical momentum rises with the increase in magnitude of Reynolds normal and shear stresses. In the similarity streamwise coordinate, at the streamwise location of 0, the Reynolds shear stress starts to decrease to negative values reaching a peak at l_r^*. The pressure term also switches sign, starts to increase, to reach a peak value by the end of the bubble and is balanced by the transverse Reynolds normal stress. The residual is close to zero throughout the balance. The mean vertical momentum continues to increase and reaches a peak by the end of the recirculating flow region. It seems to be balanced by the Reynolds shear stress only. This may also be understood from the local vertical momentum balance, where it was seen that in the vicinity of the bubble, $\partial P^*/\partial y^* \approx \partial\overline{v'^2}^*/\partial y^*$. The streamwise gradient of the Reynolds shear stress is responsible for the local advection of the vertical momentum.

For FST, the reduction in the Reynolds shear stress and the transverse normal stress, close to the body (shown in figure 6.10), is then expected to reduce the vertical mean momentum entrained. The vertical momentum entrained along the rri interface in its first half, (i.e. $x^* \leq l_v^*$, given by $\int_\Gamma V^{*2}n_y d\Gamma$), is expected to scale with the mass entrained

(given by $\int_\Gamma V^* n_y d\Gamma$). This is shown in figure 6.11b, where the mass entrainment is seen to be proportional to the vertical momentum entrained. The scaling of mean vertical momentum in the second half of the recirculating flow region is also expected to vary proportionally to the mass entrained by the mean recirculating flow.

The Reynolds shear stress resulting from the total fluctuations, in the second half of the recirculating flow region, i.e. $x^* \geq l_v^*$, from figure 6.10a remains unchanged for the baseline and the perturbed flow cases. This means that the vertical momentum and the mass transported by the mean flow remains unchanged too. Moving over to the first half, the Reynolds shear stress and the transverse normal stress decreases for the perturbed flow. The coherent Reynolds shear stress arises out of the transport of the coherent momentum due to the coherent fluctuations. Then the observations shows that the coherent mixing, close to the body is dampened with the presence of FST. This acts to reduce the vertical momentum and also the mass transported by the mean flow. However, since the mass entrained into the recirculating flow region remains more or less unchanged, the same amount of mass has to exit through the first half of the recirculating flow region, which in turn leads to a downstream shift of recirculating flow region manifesting itself as an increase in l_v^*. For this reason, l_v^* is seen to vary proportionally with the mass entrained by the shear layer from the recirculating flow region, shown in the inset of figure 6.11b.

Similar reductions in the Reynolds shear stress, with the increase of the formation region was observed by [171], where they experimented with porous cylinders and observed increase in formation region with increasing porosity. Also, in the studies of [120], where a control cylinder was inserted in the near wake to modify the near wake properties, the increase of the recirculating flow region was associated with a damping of the Reynolds stresses within the near wake region. The study of [175], highlights that the reduction of drag was associated with a increase in the recirculating flow region, where they also observed reduction in the energy level of the streamwise velocity fluctuations. All these studies indicates that the length-scale l_r^* is strongly linked to the amplitude of the Reynolds stresses in the near wake. Following [61], it may be said that owing to the reduced strength of the shear layer, there is a reduced pull of fluid, from one of the shear layers towards the interior of the formation region or towards the first half of the recirculating flow region, and hence the vortices are shed further downstream compared to the baseline flow cases. This is thought to be the reason that causes an increase in l_r^*. Further, this means that manipulating the intensity of the Reynolds shear stress may be an effective way to change the properties of the mean shear layer by influencing its entrainment capacity. In addition, the decrease in Reynolds normal stress component in the near wake may also influence the base pressure drag, since it is the major contributor to the mean pressure.

The evolution of the wake width in the similarity coordinate and normalised by its characteristic lengthscale $y^*_{\delta_{min}}$ is shown in figure 6.8b. It collapses for all cases flow fields. The characteristic lengthscale $y^*_{\delta_{min}}$ is seen to decrease with the addition of FST , shown in the inset of figure 6.8b, and it further decreases with Re_h similar to the case of baseline flow fields. The deformation of the vortices in the presence of FST and with minimal blockage effects, has been reported in [89], where the shed vortices are seen to be elliptically deformed. Similarly, in the current study, since $y^*_{\delta_{min}}/2$ is the transverse location where the Reynolds shear stress peaks, its decrease is associated with a distorted vortex which is formed farther away from the body. The decrease in

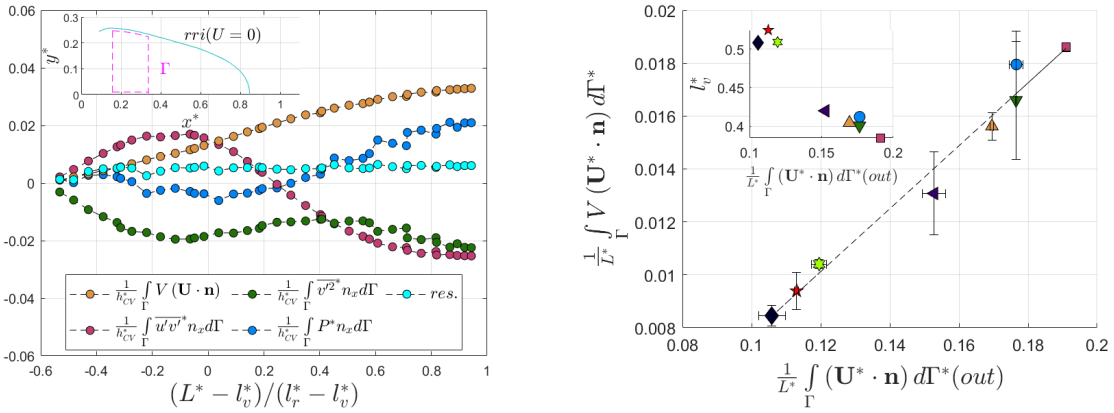

(a) (b)

Figure 6.11: Balance of the vertical mean momentum budget carried out on a CV defined by the rri (shown in the inset) (a) and the variation of mean momentum and mass transported by the mean flow, with the inset showing the variation of l_v^* with the mass entrained by the shear layer.

$y^*_{\delta_{min}}$ facilitates the interaction between the shear layers and according to [145], it leads to an increase in the non-dimensional shedding frequency which is consistent with the observations in this study (figure 6.6a). Further, this lengthscale is a diffusion lengthscale and is inversely related to the formation length [61]. A decrease in the former would imply a decreased time for the vorticity to be carried across the wake to initiate shedding, tending to increase the shedding frequency. The formation length associated with the extent of the recirculating flow region, in the present study, increases with the addition of FST while the characteristic wake-width lengthscale decreases, which follows the argument of [61] implying that both lengthscales $y^*_{\delta_{min}}$ and l_r^* are equivalent, i.e. $y^*_{\delta_{min}} \sim {}^1/_{l_r^*}$, consistent with other studies as well (see for example [89]) .

6.2.4 Effects of FST on the Reynolds stresses and the base pressure drag

The addition of perturbations to the flow was primarily to understand its influence on the mechanism driving the drag. The primary contributor to the base-pressure drag was understood to be due to the Reynolds transverse normal stresses which tends to increase the base pressure drag by driving the mean pressure. The damping of the Reynolds stresses by the influence of FST, as visible from figure 6.9, is then expected to lower its contribution to the mean pressure and hence reduce the mean base pressure drag. The amplitude of Reynolds stresses within the first half of the recirculating flow region being directly correlated to the lengthscale l_v^*, then if the peak $\overline{v'^2}^*$, attained near the end of the recirculating flow region, scales with the amplitude of $\overline{v'^2}^*$ in the first half of the recirculating flow region, then the lengthscale l_v^* could become directly correlated to the drag as reported in many studies in the past (see for example [99, 120]). However, this is not the case here.

The centerline evolution of the coherent and incoherent components of $\overline{v'^2}^*$ is shown in figure 6.12. The coherent stress $\overline{\tilde{v}^2}^*$ grows slowly in the first half of the recirculating flow region , i.e. $x^* \leq l_v^*$, when the coherent structures are in their initial stages of formation.

In the second half, the growth rate is exponential after which it reaches a peak near the end of the recirculating flow region and decays downstream. The location where it reaches a peak has been known as the formation length and corresponds to the streamwise location where the external free-stream flow is carried across the wake by the action of the growing vortices [25]. It is seen to be proportional to the extent of the recirculating flow region. In case of incoherent stress, there is an initial period of slow growth, until -0.5 in the similarity coordinates, after which there is an exponential growth and peaks within the second half of the recirculating flow region, i.e. $l_v^* < x^* < l_r^*$ due to the entrainment by the shear layer vortices, as seen in figure 5.6.

With the addition of FST, the vortex shedding is disrupted, as observed in figures 6.6c and 6.6b, damping the fluctuating coherent lift. The damping of $\overline{\tilde{v}^2}^*$ as well as the coherent Reynolds shear stress in the first half of the recirculating flow region is seen to be a determining factor in the lengthscale l_v^*.Comparing the lowest case of $Re_h \approx 2.89 \times 10^4$ for both the baseline and perturbed flow cases, there seems to be a difference between the peak of $\overline{\tilde{v}^2}^*$ at $x^* \approx 1.2 l_r^*$ and at the trailing edge, i.e. the difference approximates to 0.2 and 0.23 for the baseline and perturbed flow fields respectively. It is even higher at the highest Re_h for the case of perturbed flows. It is even significantly different in case of incoherent transverse Reynolds stresses, shown in the inset of figure 6.12. This indicates that the peak of $\overline{v'^2}^*$ at $x^* \approx 1.2 l_r^*$ may not be used to scale its evolution in the first half of the recirculating flow region and indicates a change in the physical mechanism within the initial region and the proceeding region.

As the non dimensional shedding frequency increases with Re_h for the case with FST (figure 6.6a), the longitudinal separation between the vortices decrease. The decrease in wake-width which facilitates shear-layer interactions, also brings the vortices closer. Combined with the decreased longitudinal spacing they increase their tendency to mutually entrain fluid.This may be thought as the reason for the increase in coherent stresses with Re_h for the perturbed flow fields. In case of incoherent stresses, the peaks align well in the similarity coordinates. With the addition of FST, the incoherent shear layer vortices are dampened during its initial development, as seen in section 6.2.3, and towards $x^* \approx l_v^*$, where the incoherent shear-layer vortices entrain the external free-stream fluid. Turbulent fluid is entrained by the shear layer vortices and hence, it leads to a rise in peak of incoherent Reynolds stress.

From the integral momentum budget, the highest contributor to the base pressure drag comes from the mean pressure near $x^* \approx 0.5 l_r^*$, the base pressure drag is expected to scale with the mean pressure at that location. Figure 6.13 shows the evolution of the pressure deficit, defined in equation (4.9), in similarity coordinates. Since, the velocity deficit is influenced by the increase in average streamwise velocity due to the blockage effect, a correction is applied to remove the excess momentum as,

$$(U^{*2}_{s_{max}})_{cor} = U^{*2}_{s} - \left(U^{*2}_{0,\infty} - \left(U^{*2}_{0,\infty} \right)_{ref} \right), \tag{6.4}$$

where $\left(U^{*2}_{0,\infty} \right)_{ref}$ refers to the free-stream velocity of the reference flow field, without perturbation, at the lowest $Re_h \approx 2.89 \times 10^4$. The deficit pressure P_d^* evolution along the wake centerline, seems to scale with the effective momentum deficit, where $U^*_{s_{max}} \sim U^*_{max} - U^*_{min}$ comprises the effect of shear layer through U^*_{max} at the outer edge of the shear layer at

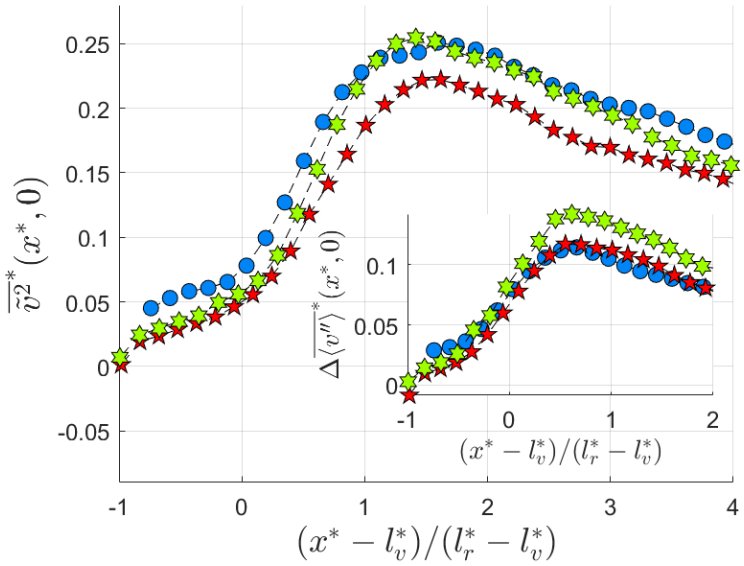

Figure 6.12: The evolution of transverse normal component of Reynolds stress at $Re_h \approx 2.89 \times 10^4$ for the baseline (circle) and perturbed flow (pentagram) and at $Re_h \approx 6.8 \times 10^4$ for the perturbed flow (hexagram).

separation and the recirculating flow region through U^*_{min} at the center of the recirculating flow bubble. The collapse of curves are almost perfect until the end of recirculating flow region after which a slight departure is noted. The inset on the top left shows the variation of mean pressure deficit P^*_d with Re_h, showing the reduction of base pressure drag (without considering blockage), especially at the lowest case of Re_h among the perturbed flows.

Performing the integral momentum budget along the CV defined by the streamline $\psi = 0$ reveals that the contributions to the mean base-pressure drag have changed within various terms. However, it is sufficient to understand the changes in contributions to the mean pressure through its different terms. Figure 6.14a shows the mean pressure decomposed into its constituent parts. Note that the pressure contribution to Reynolds shear stress and streamwise normal stress are not shown because they were negligible. The different terms are normalized by the spatially averaged base pressure, of the lowest Re_h case in the baseline flow, multiplied by the inlet height of the CV. From figure 6.14a, an increase in blockage of $\approx 5\%$ is seen. This translates into an increase in free-stream pressure coefficient of 10%. When compared with the base-pressure drag of approximately 0.54 at $Re_h \approx 2.89 \times 10^4$ this has to translate to approximately 20% relative increase in the blockage for the perturbed flow case compared with the baseline flow at the same Re_h.

Comparing the contribution of the mean pressure due to the mean flow deformation $T^{(P_M - P_{FS})}$, it seems slightly higher in the first half of the recirculating flow region, i.e. $x^* < l^*_v$. Expecting a thin boundary with the decrease in δ^*_{Sep} and with the rise in the average streamwise velocity due to an increased blockage, the mean flow deformation is expected to increase. However, towards the end of the recirculation region, there is a relative decrease in $T^{(P_M - P_{FS})}$ for the case of the perturbed flow compared to the baseline flow.The pressure due to the transverse normal Reynolds stress is relatively lower compared to the baseline flow, close to the trailing edge of the body, which was observed to

be the influence of the FST on the vortex shedding. Pressure increases to reach a peak at l_r^*. Note that the rate of increase is relatively higher compared to the baseline flow. The difference in $T^{P_{vv}}$ at l_r^* and the trailing edge, is seen to be proportional to the relative decrease of $T^{(P_M - P_{FS})}$ observed while nearing the end of the recirculating flow region. Splitting $T^{P_{vv}}$ into coherent and incoherent contribution in figure 6.14b shows that the incoherent contributions, though relative smaller compared to that of the baseline flow, at the trailing edge, becomes similar in amplitude beyond the first half of the recirculating flow region. The major change is in the coherent contribution which remains comparable to that of the incoherent contribution but rises towards the end of the recirculating flow region. The difference in $T^{P_{vv}}$ between the end of the recirculating flow region and the trailing edge observed in figure 6.14a is primarily due to the rise in contribution from the coherent structures. The observations indicate that the rise in coherent contribution to the mean pressure is intimately linked to the initial condition, i.e. at the trailing edge, where the $T^{(P_M - P_{FS})}$ remains at 0.5 and its deterioration close to l_r^* is then compensated by a rise in the coherent contribution. Comparing the evolution of $\overline{\tilde{v}^2}^*$ in figure 6.12 and the coherent contributions to the mean pressure in figure 6.14b, it may be said that the influence of free-stream turbulence is principally felt in the trailing edge, whereas nearing the end of the recirculating flow region, there is an influence of the relatively increased blockage, for the case of perturbed flow.

Since, the base pressure drag reduction observed for the lowest Re_h case is primarily due to the observed reduction of coherent transverse normal Reynolds stress, it would be interesting to understand the influence of FST on the transport mechanism of the coherent transverse Reynolds normal stress. However, the transport of transverse and streamwise normal stresses are linked as it was seen that there exists inter-component transfer of energy, extracted from the growing shear layer, due to redistribution by the coherent pressure diffusion and strain terms. This necessitates the investigation of the influence of FST on the transport mechanisms of both the coherent normal stresses.

6.2.5 Influence of FST on the transport mechanism of coherent normal Reynolds stresses

The transport mechanism in the case of perturbed flow fields for the streamwise coherent Reynolds normal stress is compared with that of the baseline flow field at $Re_h \approx 2.89 \times 10^4$, in figures 6.15a and 6.15b. The residuals resulting from the balance remains almost at the same level for both the cases. The peak of all the terms are seen to align well. For example, the gain in energy due to the production term $I_{(\tilde{\mathcal{P}}_{11})}$ and the sink due to the pressure diffusion term $I_{\mathcal{D}_{11}^{\tilde{p}}}$ peaks at l_r^* where the mean-shear layer from both sides of the bluff body merges together. The sink due to the production term peaks at l_v^* and the incoherent production term and the advection term peaks in between $l_v^* \leq x^* \leq l_r^*$. Finally the inter-component transfer due to the pressure strain term is active in the first half of the recirculating flow region (i.e. $x^* < l_v^*$).

Similar to the baseline flow, the transverse integration of diffusion terms are negligible for the perturbed flows since they act to redistribute the energy vertically. With the addition of FST, the production term does not seem to change much. A significant amount of this energy is redistributed upstream the recirculating flow region by the pressure diffusion term, whose peak at l_r^* does not seem to vary. The change is seen in the advection term as

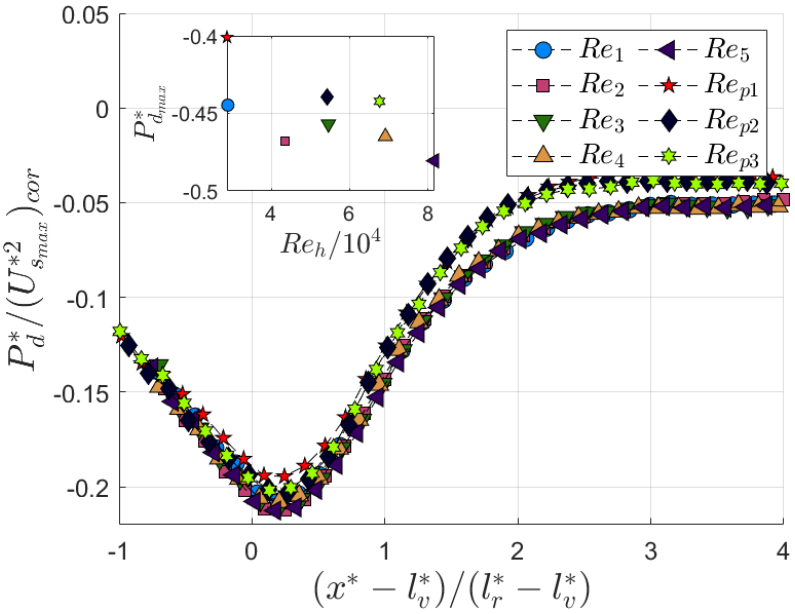

Figure 6.13: The evolution of the pressure deficit ΔP^*, scaled by the corrected mean deficit momentum. The inset on the top left shows the variation of the mean pressure deficit with Re_h.

well as the incoherent production term, meaning that the net increase of $\overline{\tilde{u}^2}^*$ has reduced slightly, and the remaining energy input by the production term is injected into the incoherent structures through the incoherent production term $I_{(-\mathcal{P}'')}$. At l_v^*, the diffusion by coherent pressure is dampened in presence of FST due to a higher extraction of energy by the incoherent structures. Since lesser amount of energy is available to be redistributed by the pressure diffusion term, the subsequent drain in energy through the production term and the pressure strain term is also reduced. This is also the case upstream of l_v^*, where less energy is made available to the pressure strain term to be transferred between normal stress components. Since at l_v^*, a major portion of the drain through production term $I_{\tilde{\mathcal{P}}_{11}}$ is injected to transport the transverse normal coherent Reynolds stress $\overline{\tilde{v}^2}^*$, a decrease in its magnitude is also expected to influence the transport of $\overline{\tilde{v}^2}^*$.

Figures 6.15c and 6.15d shows the comparison of the transport mechanism of coherent transverse Reynolds normal stress $\overline{\tilde{v}^2}^*$ of the perturbed flow-field with that of the baseline flow at $Re_h \approx 2.89 \times 10^4$. Similar to the case of streamwise coherent Reynolds normal stress $\overline{\tilde{u}^2}^*$, the length-scales originating from the recirculating flow region scales the evolution of transport mechanism of $\overline{\tilde{v}^2}^*$, with the coherent production $I_{\tilde{\mathcal{P}}_{22}}$ and the advection term $I_{-\tilde{\mathcal{A}}_{22}}$ reaching their respective peaks close to l_r^*. The residuals, for both the cases investigated, remains close to zero throughout the balance. Near the trailing edge of the body, where the flow separates, the energy input by the pressure strain term is decreased, due to the influence of FST on transport mechanisms of $\overline{\tilde{u}^2}^*$ (figures 6.15a and 6.15b), reflected in the decreased advection of $\overline{\tilde{v}^2}^*$. Close to l_v^*, the incoherent production has increased, turning from a sink to a source. Moving closer to l_r^*, the coherent production shows a relative decrease for the perturbed flow and consequently results in a decreased advection of $\overline{\tilde{v}^2}^*$. This is also true beyond l_r^*, where it is the coherent production that drives the advection and also feeds the incoherent structures through the incoherent production

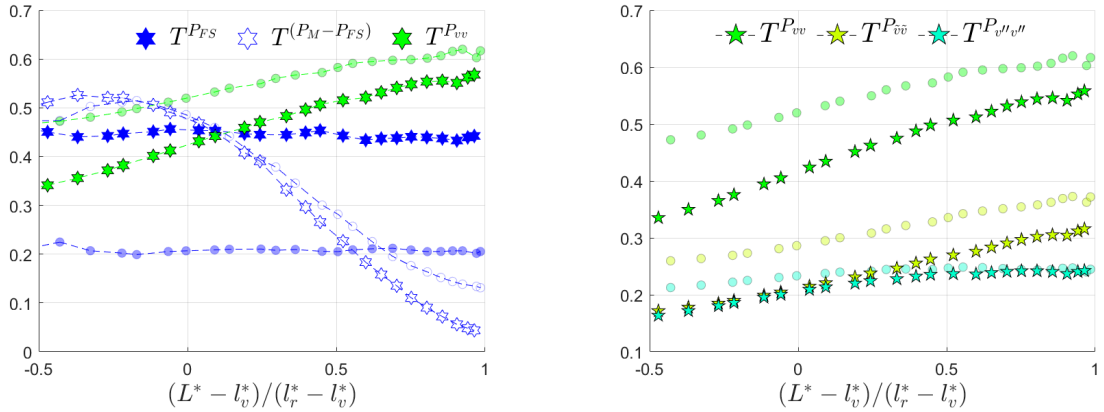

Figure 6.14: The evolution of decomposed components of the mean pressure integral contributions to the base pressure drag, normalised by the spatially averaged base pressure at lowest $Re_h \approx 2.89 \times 10^4$ of the baseline flow (a), and the decomposed contribution of transverse Reynolds normal stress from that of the coherent and incoherent structures (b) at $Re_h \approx 2.89 \times 10^4$ for the baseline (circles) and the perturbed (pentagram) flow cases.

term. Close to l_r^*, a slight increase in advection is seen, however this relative increase is approximately of the same magnitude of the residual.

Note that the transverse averaged view gives a global picture on the local evolution of the transport mechanism. A cumulative integral of the curves then shall be equivalent to the integral budget performed over a control volume. Then, the advection term remaining similar in amplitude for both the perturbed and the baseline cases in figure 6.15c, while the amplitude of $\overline{\tilde{v}^2}^*$ decreases for the former in figure 6.12, implies increased local entrainment presumably due to the increase in blockage. On a global view, the effect of FST is to damp the redistribution of energy through the pressure diffusion and strain terms, influencing the transport of coherent Reynolds normal stresses. However, the integral picture is incomplete as it hides the transverse redistribution mechanisms. A local balance is therefore necessary.

Three streamwise locations are selected for the local balance of transport equation. The end of the recirculating flow region $x^* \approx l_r^*$ is selected to investigate the balance of transport equation for $\overline{\tilde{u}^2}^*$ since it corresponds to the peak of coherent production $\tilde{\mathcal{P}}_{11}$, whose integral contribution does not vary with perturbation but changes are are noticed in the incoherent production. Similarly, the streamwise location close to the trailing edge of the body ($x^* \approx 0.16$) is selected to investigate the balance of transport equation for $\overline{\tilde{v}^2}^*$ since the integral input of energy, through the pressure strain term, is seen to be damped with FST.

Figure 6.16 shows the energy balance of the transport mechanism for $\overline{\tilde{u}^2}^*$ carried out at $x^* \approx l_r^*$. The peaks of the terms are seen to align well when scaled with the local wake width. Comparing the cases, the input of energy through production shows an increase. The dominant term being the shear production , since the coherent shear stress does not vary much for the perturbed flow and the mean shear is expected to increase with the thin separating boundary layer, the increase in $\tilde{\mathcal{P}}_{11}$ for the perturbed flow is to be expected. Local advection $-\mathcal{A}_{11}$ is not altered. Reduction in amplitudes of the

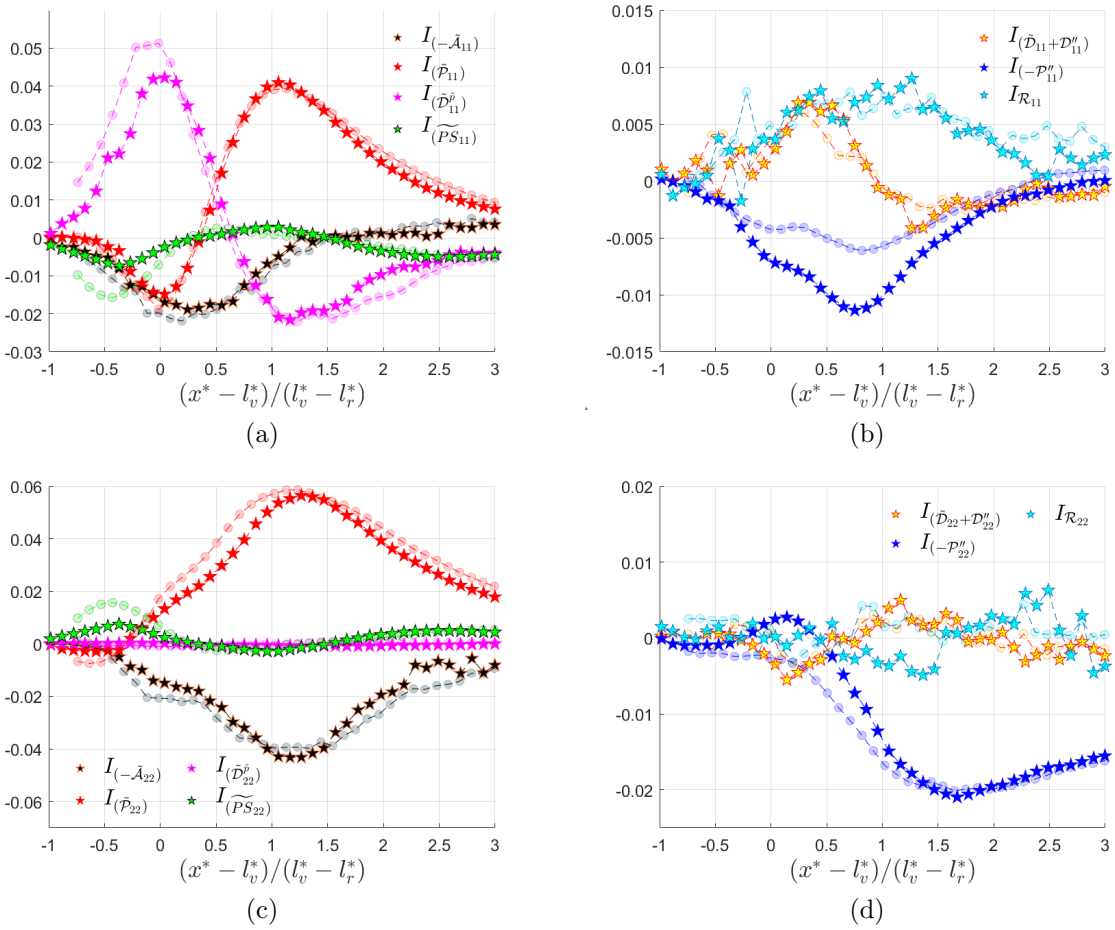

Figure 6.15: Comparison of Integral contributions to the transport of coherent streamwise (a) & (b), and transverse (c) & (d) Reynolds normal stresses, for the baseline flow (circles) and the perturbed flow-field (pentagram) at $Re_h \approx 2.89 \times 10^4$. The integration is carried out from $y^* \approx 0$ to $y^* \approx k y^*_{\delta_{min}}$, where k is a constant multiplier and is simply chosen such that the integral extends to the free-stream and lies within the PIV domain.

energy redistribution mechanism is also noted. The pressure strain term shows a relative decrease in amplitude, implying a reduction in the energy transferred to $\overline{\tilde{v}^2}$. Further, the diffusion terms $(\tilde{\mathcal{D}}_{11} + \mathcal{D}''_{11})$ shows an increase to redistribute the net increase in energy input to the incoherent structures through the incoherent production term $-\mathcal{P}''_{11}$ close to the wake centerline. A portion of the energy gained by the advection term $-\mathcal{A}_{11}$ above the wake width is lost in the wake interior. The extraction of this energy by the incoherent production is relatively higher, showing a relative increase close to the edge of the wake. Further, the reduction in the pressure strain term above the wake width is balanced by an increase in the incoherent production term.

Splitting the diffusion terms $(\tilde{\mathcal{D}}_{11} + \mathcal{D}''_{11})$ into its constituent components, in the inset of figure 6.16b, the diffusion of coherent Reynolds stresses by the coherent fluctuations $\tilde{\mathcal{D}}_{11}$ are opposed by the diffusion of incoherent Reynolds stresses by the coherent fluctuations $\mathcal{D}''_{11}$, with the latter dominating the former in the exterior and the interior of the wake. The dominant diffusion is due to the latter $\mathcal{D}''_{11}$. With the addition of FST, the diffusion term $\tilde{\mathcal{D}}_{11}$ does not vary, however an increase in the diffusion of incoherent Reynolds stresses are noted. With the ambient free-stream turbulence, the incoherent structures present in the

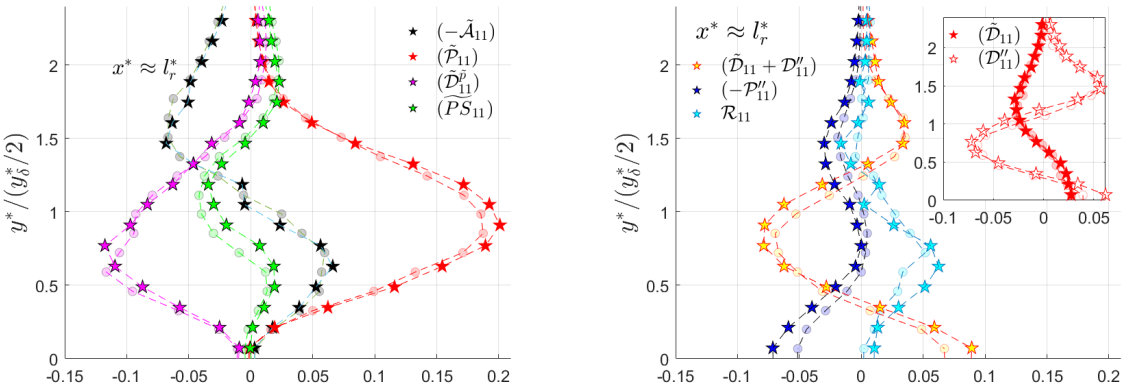

Figure 6.16: Comparison of Local contributions to the transport of coherent streamwise Reynolds normal stresses (a) & (b) at the streamwise location $x^* \approx l_r^*$, for the baseline flow (circles) and the perturbed flow-field (pentagram) at $Re_h \approx 2.89 \times 10^4$. The transverse distance is normalised by the local width of the upper symmetric plane of the wake $(y_\delta^*/2)$.

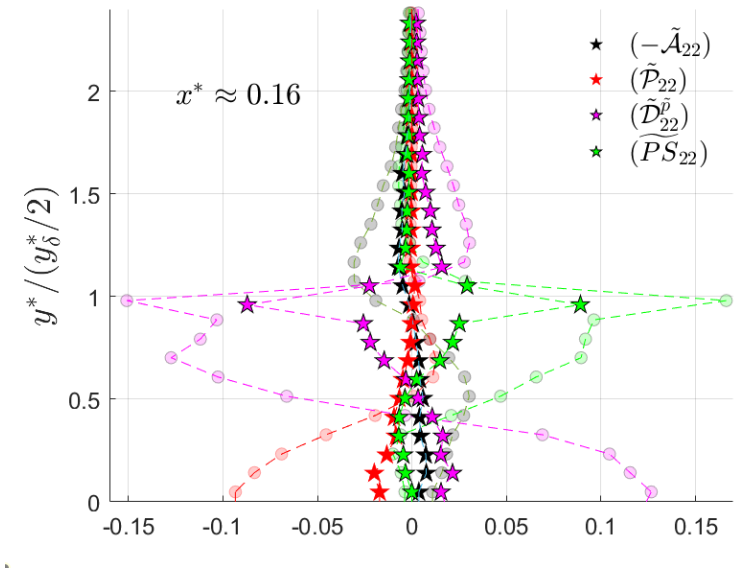

Figure 6.17: Comparison of the local contributions to the transport of coherent transverse Reynolds normal stress at the streamwise location $x^* \approx 0.16$ close to the trailing edge of the body, for the baseline flow (circles) and the perturbed flow-field (pentagram) at $Re_h \approx 2.89 \times 10^4$. Only the dominant terms are shown and the remaining are of the order $\mathcal{O}(\mathcal{R}_{22})$. The transverse distance is normalized by the local width of the upper symmetric plane of the wake $(y_\delta^*/2)$.

ambient fluid causes an increase in the incoherent Reynolds stresses due to the momentum flux between the free-stream turbulence and the bluff body wake. The relative increase in coherent production causes these incoherent stresses to be diffused towards the wake interior by the action of coherent structures.

The transport mechanism of $\overline{\tilde{v}^2}^*$ at the streamwise location close to the flow separation is shown in figure 6.17. Note that certain terms such as incoherent production and the diffusion terms are not shown as they are negligible and of the same order of mag-

nitude as the residual term. Comparing the baseline and the perturbed flow cases, the pressure strain shows a significant decrease at the wake edge. Since, the available energy input through the pressure strain term is less, the energy redistributed by the pressure diffusion term is also very less, with a significantly decreased peak at the wake-edge, and consequently the net rate of increase/decrease of $\overline{\tilde{v}^2}^*$ through the advection term $-\tilde{\mathcal{A}}_{22}$ is negligible. Further, the energy given off to the production term by the coherent pressure diffusion term has also been significantly decreased.

Whence, the effect of FST on the transport mechanism of coherent Reynolds stresses damps the energy redistribution through the coherent pressure diffusion and the pressure strain terms. It increases the energy fed to the incoherent structures, thus disrupting the net increase in coherent energy gain through the advection term.

6.3 Summary

This chapter focused on investigating the influence of the free-stream turbulence on the mean and the POD-phase-averaged wake. The fluctuating signal of the lift coefficient showed clear signs of interference due to FST. The peak of the lift coefficient in the frequency spectrum dropped and broadened, hinting to signs of pronounced vortex dislocations causing increased wake three-dimensionality, while the non dimensional shedding frequency increased. The frequency continued to increase with Re_h in the presence of FST. The non-negligible increase in blockage complicates the problem, since it is difficult to isolate its effect on the wake dynamics and comment on the influence of FST. The lowest Re_h test case showed a minimal increase in blockage and since the open area between the body and the presumed thick wind tunnel boundary layer is large, the influence of blockage can be assumed minimal.

The length of the recirculating flow region was found to increase in the presence of FST, which was also observed in the studies of [89] where the integral lengthscale of the incoming turbulence is similar to that of the current study. Local profiles show weak Reynolds stresses existing at separation. The integral mean vertical momentum budget showed a weakened mean momentum detrainment caused by the balance of a weakened Reynolds shear and transverse normal stresses in comparison with the baseline flow case. The flow decomposition showed that the weak Reynolds stress effect is due to the weak coherent structures at separation which reduced the strength of the shear layer thereby reducing its entrainment capacity. The reduction in coherent Reynolds transverse normal stress, being the dominant driving factor of the mean pressure, is expected to decrease the mean base-pressure drag. But, the incoherent transverse Reynolds normal stress, which peaks close to the end of the recirculating flow region, increases due to the entrainment of turbulent fluid. At the lowest Re_h test case, the peak of the incoherent transverse Reynolds normal stress is similar to that of the baseline flow, which combined with a reduced coherent Reynolds stress leads to the reduction of mean base-pressure drag. However, with an increase in Re_h in the presence of FST, the coherent transverse Reynolds normal stress continues to increase, probably due to the induced velocity associated with an increased shedding frequency. The decomposition of the integral mean pressure contribution, in comparison with the centerline evolution of the coherent transverse Reynolds stress showed that while the turbulent flow acts to weaken the coherent stresses at the trailing edge post separation, the effect of the blockage causes it to rise by

the end of the formation region, strengthening the coherent structures. The entrainment of the turbulent external fluid is enhanced in the presence of stronger coherent structures and hence the incoherent stresses also increase with Re_h in the presence of FST, thus contributing to the mean pressure and hence the mean base pressure drag increases as well. The drag reduction observed is approximately 10% at the lowest Re_h test case with FST, due to the decreased cross-stream mixing.

An investigation into the transport mechanism of coherent Reynolds stresses revealed that the influence of the FST is primarily felt in the first half of the recirculating flow region $x^* < l_v^*$. The transverse integral budget revealed that, the energy produced in the mean shear layer while transporting coherent streamwise Reynolds normal stress, essentially through shear production, is increasingly injected to the incoherent structures through the incoherent production term. As such, the energy redistribution mechanism by the coherent pressure diffusion and the inter-component energy transfer through the coherent pressure strain is interrupted, resulting in a decreased energy transferred to transport the coherent transverse Reynolds stress. A further investigation of the local balance of coherent streamwise Reynolds normal stress revealed an increase in the coherent diffusion of the Reynolds incoherent stresses which redistributed the produced energy to be injected to the incoherent stresses. The observations suggest that the redistribution through the coherent pressure is an important mechanism that contribute to the overall increase/decrease of the coherent Reynolds stresses, and that the influence of the incoming turbulent field with an integral lengthscale comparable to that of the body size, was to disrupt this energy transfer mechanism thus damping the coherent Reynolds stresses and consequently tending to decrease the mean base pressure drag.

Chapter 7

Concluding remarks and brief outlook

The wake of a two-dimensional bluff body at $Re \sim \mathcal{O}(10^4)$ is investigated, primarily using the measurements obtained by 2D planar PIV technique. The objective is to identify the physical mechanisms in the wake that drive the drag. The D-shaped body is designed in order to minimize the influence of leading edge separation on the wake.

The strategy is to analyze the physical equations governing momentum and energy transports. A method for combining sparse sensors and PIV-based measurements for an accurate estimation of the mean pressure field, required for the closure of mean momentum transport equation, is discussed in Chapter 3. Qualitative features of the estimated pressure field were discussed in Chapter 4. The dominant contribution to the mean drag is from the mean pressure, identified through an integral momentum budget over the recirculation region. Exploiting the linearity of the Poisson operator, the mean pressure is found to be driven by the mean flow deformation immediately after separation whereas the transverse component of the Reynolds normal stress becomes the main contributor once the shear layer has grown sufficiently. The mean momentum budget, both local and integral, further reveals that it is the Reynolds normal stress components that play a key role in the mean drag, acting as a source/sink of mean pressure/drag whilst the Reynolds shear stress re-distribute the momentum. The primary source of energy for these normal components are found to be localized within the growing mean shear layer and near the region where they mutually interact and merge. However, the description of transport mechanism is incomplete due to unresolved terms such as pressure terms and dissipation.

The closure of the transport of the Reynolds stresses is addressed in Chapter 5 where the flow is decomposed into coherent and incoherent motions using the POD based approach, both of whose contributions to the sink of base pressure are comparable whilst the former dominates in driving the mean pressure. A novel method of pressure reconstruction for the coherent structure is introduced, extendable to any kind of modal decomposed flows. The availability of coherent pressure permits the estimation of coherent fluctuating lift and drag through the budgets of coherent fluctuating momentum, whose values are in agreement with those measured by a set of pressure sensors. It further allows the estimation of coherent pressure diffusion and strain terms which forms important physical mechanisms, amongst others, while considering the energy exchange process between the mean flow and the coherent fluctuations. One of the advantage of the method is that

even at high Reynolds number one may analyse the modal energy budgets without the requirement of expensive numerical simulations. One may further improve the method by simply using a time resolved reference signal to accurately extract the coherent structure of choice without relying on POD technique, the latter which mixes up the energy content of various higher order physically significant modes. The method can further be extended for the study of multi-scale flows where the interaction between multiple coherent structures are of interest.

The energy exchange between the mean and the coherent structure, similar to the total normal Reynolds stress components, is localized within the mean shear layer, immediately after separation and near the region of their mutual interaction. The role of coherent pressure diffusion and pressure strain terms are to redistribute the extracted energy spatially, feeding the incoherent structures in the process, as well as between the normal coherent stress components. The existence of the well-known energy cascade is also seen where the large scale coherent structures are mostly responsible for feeding the energy to the incoherent structures. Increasing the Reynolds number Re the turbulence kinetic energy was found to increase thereby resulting in an increased drag due to the incoherent structures.

The drag was found to decrease with the addition of free-stream turbulence, with an integral length-scale $\mathcal{L}_x/h < 1$ (h refers to the body-height), in Chapter 6. The spectrum of fluctuating lift signal shows signs of pronounced vortex dislocations which is known to increase the three-dimensional nature of the wake. This leads to a weakening of coherent structures. The integral transverse mean momentum budget over the recirculation region shows that the integral mean momentum and mass flux evolves proportionally, the weakening of the former due to weakened coherent structures leads to lengthening of the recirculation region. The decrease in drag is not in proportion to this weakening because of the blockage of the wind tunnel, identified by decomposing mean pressure and showing the importance of mean wake-inlet condition on the drag. The transport equation of coherent Reynolds stresses showed that the FST interacts with the shear layer immediately after separation tampering with the energy redistribution mechanism leading to a decrease in the coherent normal stress components near separation. This decrease however is not sustained downstream due to the blockage, visible through the local increase of advection. The observations further suggest that the identified mechanism of coherent Reynolds stress transport is robust to perturbations.

In brief, it is very well known that the mean drag of the bluff body wake is determined by properties of the incoming boundary layer, the separated shear layer, their mutual interaction and the recirculating flow region. The perturbation of any of these features reflects as changes in the other and consequently in the mean force components as well. The current study adds to the existing knowledge, by the comprehension of momentum exchange process within the very near wake that leads to drag. Further, the coherent structures are identified as the key contributors to the drag and the novel tools presented allows the identification of the energy-exchange mechanism between the coherent structures and the mean flow. The mechanism is interrupted by the FST interacting with the separated shear layer consequently tending to reduce the mean drag, whilst the influence of the blockage tends to oppose it.

One of the evident drawbacks of the study is the relatively simple nature of the flow and the method by which flow is decomposed to coherent / incoherent structures, the latter which greatly simplifies the problem while also obscuring the physics. The latter may however be overcome by carefully planning the experiments. The study was limited to time-averaged properties only, owing to time-schedule constraints, which further simplified the problem. One may deepen the analysis by considering a quasi-unsteady energy exchange mechanism, in particular since the quasi-temporal term acts as a inter-phase momentum/energy exchange term, and in case of transverse coherent momentum it has been observed as a dominant term responsible for the coherent lift. This may also be of interest in various other applications of bluff body such as those centered around the phenomenon of vortex induced vibrations.

Considering the number of inherent degrees of freedom in the bluff body wake, the current study takes a small step while making a solid contribution in the comprehension of the problem, although several questions remain unanswered. One may easily extend the present similar analysis to a more complex situation in case of 2D bluff body-wakes, for example by manipulating the wake inlet conditions, introduction of multiple scales, or by decreasing the ground proximity in order to gain insights into the changes in dominant mechanism of drag. The mechanism presented can further motivate the development of simple and low-cost scaling laws for the prediction of mean flow properties in a control-applied scenario, or for the improvements in reduced order modelling approaches, for example: by the empirical Galerkin models, which forms a key ingredient nowadays for an efficient, active closed-loop flow control in order to reduce drag. Finally, a successful extension of the present tools and analysis to a 3D complex wake such as those of "Ahmed Body", representative of the wake features of a real vehicle, would be of a significant value in the development of efficient and practical drag control devices.

Appendix A

Appendix

A.1 Appendix

A.1.1 Pressure Estimation - Methodology

To describe the methodology, consider a 2-dimensional flow field with data distributed on qx × py Cartesian grid, i.e. the data forms an py × qx matrix , where x and y denotes the streamwise and transverse directions respectively. We rewrite equations (3) and (4) conveniently as:

$$\nabla P \cdot n = g\big(\overline{U}, \overline{u_i u_j}\big) \;\; on \;\; \Gamma \tag{A.1}$$

$$\Delta P = f\big(\overline{U}, \overline{u_i u_j}\big) \;\; in \;\; \Omega \tag{A.2}$$

where Γ and Ω represents the computational boundary and domain respectively, and n is the unit normal to the boundary.

The Laplace operator of the Poisson pressure equation can be approximated by a discretizing matrix as:

$$\Delta \approx D_{2D} = \left[\frac{1}{h_x^2} K_x \otimes I_y + I_x \otimes \frac{1}{h_y^2} K_y\right] \tag{A.3}$$

where $\otimes$ represents the kronecker delta product of matrices and $I_x \in \mathbb{R}^{q \times q}$ and $I_y \in \mathbb{R}^{p \times p}$ represents Identity matrices. The letter h with subscripts x and y represents the grid spacing in the streamwise and transverse directions respectively.

Here, $K_x \in \mathbb{R}^{q \times q}$ and $K_y \in \mathbb{R}^{p \times p}$ denotes the finite order discretizing matrix in x and y directions respectively. For example, K_x forms a matrix:

$$K_x = \begin{bmatrix} 2 & -5 & 4 & -1 & & \\ 1 & -2 & 1 & & & \\ & 1 & -2 & 1 & & \\ & & & \ddots & & \\ & & & 1 & -2 & 1 \\ & & -1 & 4 & -5 & 2 \end{bmatrix} \tag{A.4}$$

Where a second order four point forward and backward finite difference scheme is employed at the boundary and a second order central difference scheme is employed at the internal

grid nodes. A similar matrix is formed for K_y. To implicitly insert the Neumann boundary conditions to the discretization matrix, it is approximated by a using a second order one-sided difference scheme and inserted it into the respective discretization matrix. For example, considering 1 single dimension and the boundary with normal in the streamwise direction, we have:

$$\nabla P \cdot n_{x=0} \approx \frac{1}{h_x}\Big(-\frac{3}{2}P_0 + 2P_1 - \frac{1}{2}P_2\Big) = g_0 \tag{A.5}$$

and

$$\nabla P \cdot n_{x=q\Delta x} \approx \frac{1}{h_x}\Big(\frac{1}{2}P_{q\Delta x-2} - 2P_{q\Delta x-1} + \frac{3}{2}P_{q\Delta x}\Big) = g_{q\Delta x} \tag{A.6}$$

These boundary approximations (A.5) and (A.6) are inserted into the interior of the discretization matrix. Considering the 1 dimensional case on the first interior grid node after the boundary grid node, we have:

$$\Delta P_{x=1} \approx \frac{1}{h_x^2}\Big(P_0 - 2P_1 + P_2\Big) = f_1 \tag{A.7}$$

Eliminating the boundary value of P_0 in (A.7) using (A.5):

$$\Delta P_{x=1} \approx \frac{1}{h_x^2}\Big((\frac{4}{3} - 2)P_1 + (-\frac{1}{3} + 1)P_2\Big) = f_1 + \frac{2}{3}\frac{g_0}{h_x} \tag{A.8}$$

In a similar manner, the boundary conditions in the 2 dimensions are approximated and implicitly inserted into interior of the respective discretization matrix.New discretization matrices D_x and D_y are formed from the original K_x and K_y respectively, taking in only the interior of the original with the implicitly implemented boundary conditions, such that $D_x \in \mathbb{R}^{(q-2)\times(q-2)}$ and $D_y \in \mathbb{R}^{(p-2)\times(p-2)}$. The RHS matrix of the Poisson pressure equation is formed implementing the boundary values implicitly as in (A.8) and is represented by F. The modified discretized form of Laplace operator can be written as:

$$\Delta \approx B_{2D} = \Big[\frac{1}{h_x^2}D_x \otimes I_{Dy} + I_{Dx} \otimes \frac{1}{h_y^2}D_y\Big] \tag{A.9}$$

where I_{Dx} and I_{Dy} are identity matrices with the same dimensions as that of discretization matrices D_x and D_y respectively. Now, the Poisson pressure equation (A.2) can be finally expressed in discretized form as:

$$\Delta P \approx B_{2D} vec(P) = vec(F) \tag{A.10}$$

where *vec* denotes a column vector matrix.

The x and y discretization matrices D_x and D_y can be decomposed in the Eigen-domain as $D_x = S_x\Lambda_x S_x$ and $D_y = S_y\Lambda_y S_y$, where S represents the Eigen-vector matrix and Λ represents the Eigen-value matrix of the respective Discretizing matrix. Using the properties of inverse matrix and Kronecker delta products, we find the Eigen-vector and Eigen-values of B_{2D} matrix of (A.9) as:

$$B_{2D} = \big(S_x \otimes S_y\big)\Big(\frac{1}{h_x^2}\Lambda_x \otimes I_{Dy} + I_{Dx} \otimes \frac{1}{h_y^2}\Lambda_y\Big)\big(S_x^{-1} \otimes S_y^{-1}\big) \tag{A.11}$$

From (A.10) and (A.11), the numerical approximation of pressure poisson equation is given by:

$$(S_x \otimes S_y)\left(\frac{1}{h_x^2}\Lambda_x \otimes I_{Dy} + I_{Dx} \otimes \frac{1}{h_y^2}\Lambda_y\right)(S_x^{-1} \otimes S_y^{-1})vec(P) = vec(F) \tag{A.12}$$

Equation (A.12) can be inverted and simplified using matrix inversion and Kronecker delta product properties:

$$(S_x^{-1} \otimes S_y^{-1})vec(P) = \left(\frac{1}{h_x^2}\Lambda_x \otimes I_{Dy} + I_{Dx} \otimes \frac{1}{h_y^2}\Lambda_y\right)^{-1} vec(S_y^{-1}FS_x^{-1}) \tag{A.13}$$

The $pq \times pq$ matrix with the eigen values can be reshaped to form a $p \times q$ Λ matrix for computational efficiency.

$$Eigen\ \ value\ \ matrix : \Lambda(i,j) = \frac{\Lambda_{y,i}}{h_y^2} + \frac{\Lambda_{x,j}}{h_x^2}$$

The inverse of the eigen basis matrices on the LHS of equation (A.13) can be inverted to finally yield the solution as:

$$vec(P) = vec(S_y(S_y^{-1}FS_x^{-1} \cdot /\Lambda)S_x) \tag{A.14}$$

Equation (A.14) can be implemented equivalently as:

$$P = S_y(S_y^{-1}FS_x^{-1} \cdot /\Lambda)S_x \tag{A.15}$$

A.1.2 Pressure Estimation - Validation

Synthetic velocity and pressure field data a time-decaying vortex is generated using the Lamb-Oseen vortex model. As the model provides analytic expressions for velocity and pressure, it is an ideal candidate to be used as a reference for comparing the solver accuracy. The model expresses the velocity components of the vortex in cylindrical co-ordinates (r, θ, z) representing radial, tangential and axial directions respectively, with the only nnon-zero component in tangential direction given as :

$$V_\theta(r,t) = \frac{\sigma}{2\pi r}\left(1 - exp\left[\frac{-r^2}{4\nu t}\right]\right) \tag{A.16}$$

and

$$V_r = 0 \qquad V_z = 0$$

The analytic expression of pressure field is given by:

$$\frac{\partial p}{\partial \theta} = \rho\frac{v^2}{r} \tag{A.17}$$

where σ, ν, t and ρ represents the circulation of the vortex core, kinematic viscosity of the fluid, time and the fluid density respectively. The tangential velocity field represented by (A.16) is simply projected into a 2 dimensional Cartesian grid (x,y) to yield V_x and V_y

velocity components in x and y respectively.The pressure field to be used as a reference, is obtained on integrating equation (A.17) as:

$$p = \rho\frac{\sigma^2}{4\pi^2}\left\{Ei\left(\frac{r^2}{2\nu t}\right)\frac{1}{4\nu t} - \frac{1}{2r^2} - Ei\left(\frac{r^2}{4\nu t}\right)\frac{1}{4\nu t} - \frac{\exp\{(-r^2/2\nu t)\}}{2r^2} + \frac{\exp\{(-r^2/4\nu t)\}}{r^2}\right\} \tag{A.18}$$

Three instantaneous velocity fields sufficiently close in time were generated, such that a good estimate of the velocity time derivative is obtained.

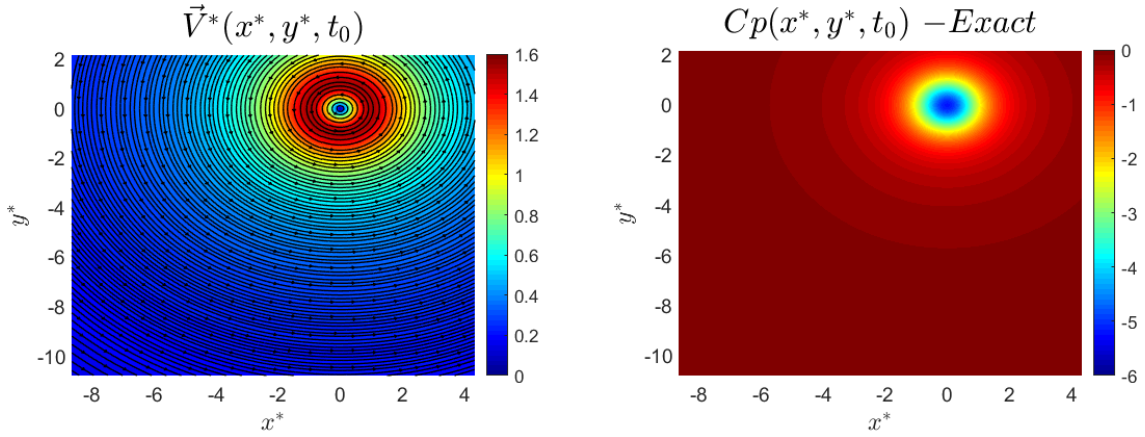

(a) Velocity field.

(b) Estimated C_p field.

Figure A.1: Synthetic data generated by Lamb Oseen vortex model.

Figure A.1a and A.1b shows the synthetic instantaneous velocity and pressure field at initial time t_0 generated using the Lamb-Oseen model (A.16) and (A.18) respectively. The superscript * represents normalized variable. Here, the x and y co-ordinates are normalized with the vortex core radius and the velocity field is normalized with the circulation per unit span. The pressure coefficient C_p is defined as:

$$C_p = \frac{p}{\frac{1}{2}\rho U^2}$$

where, U is the absolute maximum value of the velocity component in x direction. The synthetic pressure field is referred to as *exact* C_p *field* hereinafter.

The instantaneous pressure field is estimated with the Poisson pressure equation and Neumann boundary condition by using the synthetic velocity fields.

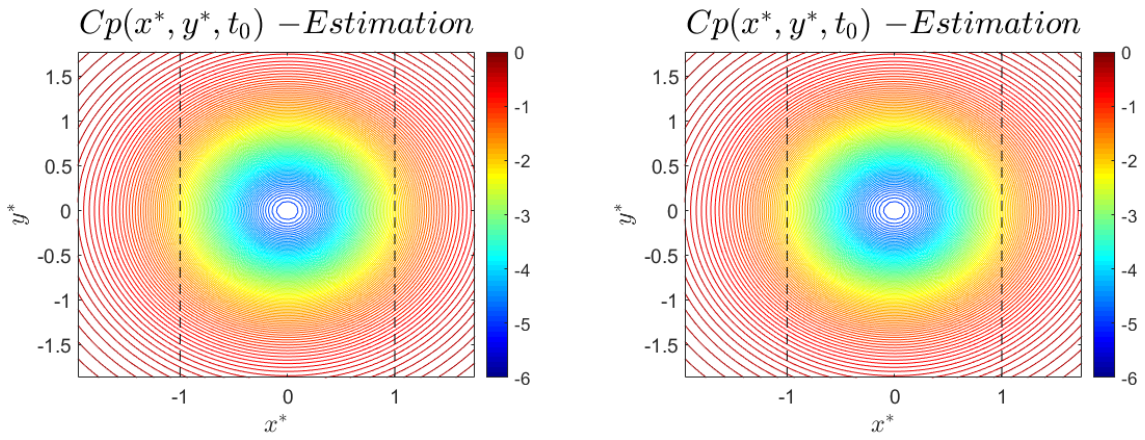

(a) Exact C_p field.

(b) Estimated C_p field.

Figure A.2: C_p field zoomed in on the vortex core region. (a) represents the exact Lamb-Oseen C_p field and (b) represents the C_p field estimated from the Lamb-Oseen velocity fields.

The Fig. A.2a and A.2b above zooms in on the vortex core region. The coordinate axes of the contour plot is normalized by the vortex core radius and the dashed black line denotes the streamwise extent of the vortex core. On a closer look at the *Estimated* C_p field, there exists a slight dissimilarity, to the *Exact* C_p field where the contours inside the vortex core ,represented by yellow colour, are shifted relatively. The difference is clear in Fig. A.3a where the *Estimated* C_p represented by black solid circles is offset with respect to the *Exact* C_p.

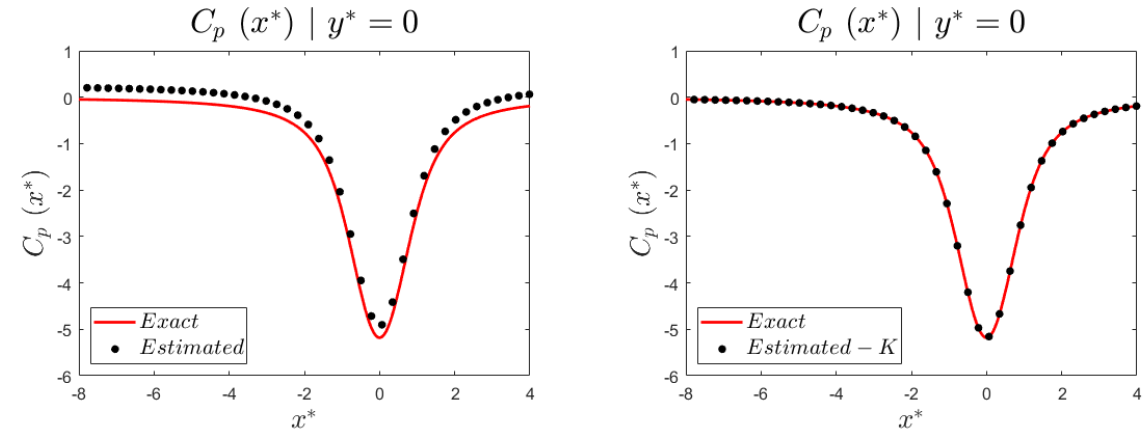

(a) Exact C_p field.

(b) Estimated C_p field.

Figure A.3: A global view of the evolution of the pressure coefficient C_p along the vortex centerline. (a) Identifies the shift between the exact and the estimated pressure field and (b) represents the estimated pressure field coinciding with the exact one on removal of the constant K.

On verifying the compatibility condition, the difference is less than 0.2 percent, which is the consequence of numerical scheme used and thus represents the solver inaccuracies. Verification of the compatibility condition implies that the pressure estimated is offset to

the exact pressure by a constant K, as shown in A.3b. The results prove to be consistent with the theory in 3.1.1. Also, The maximum error level defined by:

$$\| \epsilon \|_\infty := max(| \epsilon_1 |, | \epsilon_2 |, ..., | \epsilon_n |)$$

where ϵ denotes the difference between the exact and estimated value, is found to be less than 0.2 percent.

Further, the numerical scheme used is tested for its convergence using a simple analytic function and comparing the numerical solution with the exact analytic solution.

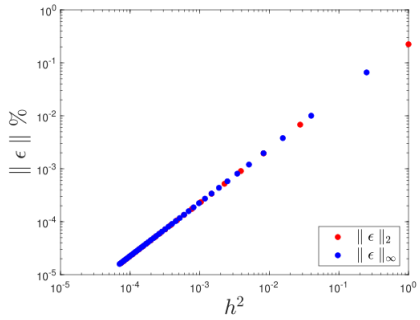

Figure A.4: Convergence test of Numerical scheme

Figure A.4 above shows that the error level denoted in percentage decreases log linearly with the square of the grid spacing indicating the convergence of the numerical scheme. Therefore from the above tests, it is concluded that the pressure solver gives consistent and accurate results.

A.1.3 Comparison of pressure between simulation and experiment.

A difference is observed in the pressure coefficient C_p computed from the experimental data and the synthetic pressure field output by the $k-\omega$ SST turbulent solver (figure 3.2). The evolution of C_p shown in figure 3.9 prior to the application of pressure correction strategies. Note that the flow develops differently along the body's surface prior to separation, for the simulation and the experiment. In the experiment, boundary layers are laminar whereas in the simulation, the $k-\omega$ SST model implicitly assumes turbulent boundary layers. The result is a shorter mean recirculation region for the synthetic data ($l_r^* \approx 0.62$) relative to the experiment ($l_r^* \approx 0.92$).
This behaviour observed in the simulation data is to be expected in real experiments with turbulent boundary layers since the increase of growth rate of the separated shear layers induced by the turbulent boundary layer leads to a shorter reattachment length, indicated by the length of the mean recirculation region l_r (see for instance [1, 165]). This is also related to the dip in the minimum base pressure observed in the wake [202]. In order to compare C_p for both the simulation and the experiment, we compute the reduced pressure coefficient defined by Chapman *et al.* [34] as

$$\tilde{C_p} = \frac{C_p - C_{p,m}}{1 - C_{p,m}}, \tag{A.19}$$

where $C_{p,m}$ refers to the minimum value of pressure observed on the wake centerline. Figure A.5 shows the evolution of reduced pressure coefficient $C_{p,m}$ along the wake centerline with the streamwise distance normalized by the mean recirculation region length

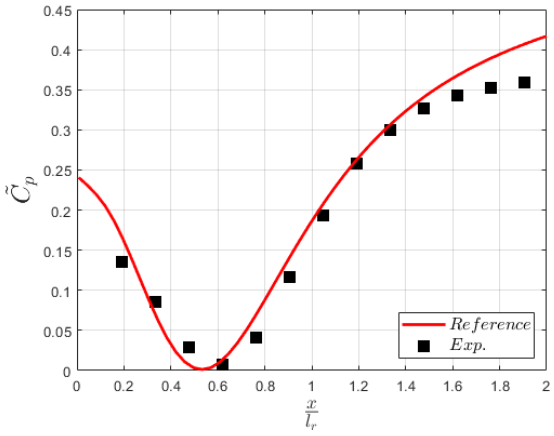

Figure A.5: The evolution of reduced pressure coefficient $\tilde{C_{p,m}}$ along the wake centerline. The streamwise distance x is normalized with the mean recirculation region length l_r. 'Reference' represents the pressure directly obtained from the turbulent solver and 'Exp.' refers to the pressure from the experimental data obtained after the application of pressure correction scheme.

(l_r). It is observed that both cases agree well until $x/l_r \approx 1.5$, after which a mismatch is observed. The mismatch observed in the regular C_p (3.31) between the synthetic data and the experimental data is expected to be induced by the difference in the development of the upstream boundary layer. An interested reader may refer to earlier works [202, 1] in this regard.

Bibliography

[1] E. Adams and J. Johnston. Effects of the separating shear layer on the reattachment flow structure part 1: Pressure and turbulence quantities. *Experiments in Fluids*, 6(6):400–408, 1988.

[2] S. R. Ahmed, G. Ramm, and G. Faltin. Some salient features of the time-averaged ground vehicle wake. *SAE Transactions*, pages 473–503, 1984.

[3] E. Anderson and A. Szewczyk. Effects of a splitter plate on the near wake of a circular cylinder in 2 and 3-dimensional flow configurations. *Experiments in Fluids*, 23(2):161–174, 1997.

[4] R. Antonia and S. Rajagopalan. Determination of drag of a circular cylinder. *AIAA journal*, 28(10):1833–1834, 1990.

[5] C. Apelt and G. West. The effects of wake splitter plates on bluff-body flow in the range $10^4 < \mathrm{R} < 5 \times 10^4$. part 2. *Journal of Fluid Mechanics*, 71(1):145–160, 1975.

[6] C. Apelt, G. West, and A. A. Szewczyk. The effects of wake splitter plates on the flow past a circular cylinder in the range $10^4 < \mathrm{R} < 5 \times 10^4$. *Journal of Fluid Mechanics*, 61(1):187–198, 1973.

[7] P. Ashill. Flow control: Passive, active, and reactive flow management m. gad-el-hak cambridge university press, the edinburgh building, cambridge cb2 2ru, uk. 2000. 421pp. illustrated.£ 60. isbn 0-521-77006-8. *The Aeronautical Journal*, 105(1045):150–150, 2001.

[8] T. Avadiar, M. Thompson, J. Sheridan, and D. Burton. Characterisation of the wake of the drivaer estate vehicle. *Journal of Wind Engineering and Industrial Aerodynamics*, 177:242–259, 2018.

[9] G. Bagheri, S. E. Hosseini, and M. A. Wahid. Effects of bluff body shape on the flame stability in premixed micro-combustion of hydrogen–air mixture. *Applied Thermal Engineering*, 67(1-2):266–272, 2014.

[10] H. Bai and M. M. Alam. Dependence of square cylinder wake on reynolds number. *Physics of Fluids*, 30(1):015102, 2018.

[11] P. Baj, P. J. Bruce, and O. R. Buxton. The triple decomposition of a fluctuating velocity field in a multiscale flow. *Physics of Fluids*, 27(7):075104, 2015.

[12] P. Baj and O. R. Buxton. Interscale energy transfer in the merger of wakes of a multiscale array of rectangular cylinders. *Physical Review Fluids*, 2(11):114607, 2017.

[13] S. Balachandar, R. Mittal, and F. Najjar. Properties of the mean recirculation region in the wakes of two-dimensional bluff bodies. *Journal of Fluid Mechanics*, 351:167–199, 1997.

[14] R. J. Bastiaans. *Cross-correlation PIV; theory, implementation and accuracy*. Eindhoven University of Technology, Faculty of Mechanical Engineering, 2000.

[15] T. Baur. PIV with high temporal resolution for the determination of local pressure reductions from coherent turbulence phenomena. In *Proc. 3rd Int. Workshop on PIV-Santa Barbara*, pages 101–106, 1999.

[16] P. Bearman. Investigation of the flow behind a two-dimensional model with a blunt trailing edge and fitted with splitter plates. *Journal of fluid mechanics*, 21(2):241–255, 1965.

[17] P. Bearman. Bluff body flows applicable to vehicle aerodynamics. 1980.

[18] P. Bearman. Near wake flows behind two-and three-dimensional bluff bodies. *Journal of Wind Engineering and Industrial Aerodynamics*, 69:33–54, 1997.

[19] P. Bearman and T. Morel. Effect of free stream turbulence on the flow around bluff bodies. *Progress in aerospace sciences*, 20(2-3):97–123, 1983.

[20] P. W. Bearman and J. C. Owen. Reduction of bluff-body drag and suppression of vortex shedding by the introduction of wavy separation lines. *Journal of Fluids and Structures*, 12(1):123–130, 1998.

[21] J. H. Bell and R. D. Mehta. Development of a two-stream mixing layer from tripped and untripped boundary layers. *AIAA journal*, 28(12):2034–2042, 1990.

[22] T. Berk, T. Medjnoun, and B. Ganapathisubramani. Entrainment effects in periodic forcing of the flow over a backward-facing step. *Physical Review Fluids*, 2(7):074605, 2017.

[23] R. B. Bird, W. E. Stewart, and E. N. Lightfoot. Transport phenomena, revised 2nd edition, 2006.

[24] M. S. Bloor. The transition to turbulence in the wake of a circular cylinder. *Journal of Fluid Mechanics*, 19(2):290–304, 1964.

[25] M. S. Bloor and J. Gerrard. Measurements on turbulent vortices in a cylinder wake. *Proceedings of the Royal Society of London. Series A. Mathematical and Physical Sciences*, 294(1438):319–342, 1966.

[26] D. G. Bohl and M. M. Koochesfahani. Mtv measurements of the vortical field in the wake of an airfoil oscillating at high reduced frequency. *Journal of Fluid Mechanics*, 620:63–88, 2009.

[27] M. Brachet. Direct simulation of three-dimensional turbulence in the Taylor–Green vortex. *Fluid dynamics research*, 8(1-4):1, 1991.

[28] P. Bradshaw. Effects of streamline curvature on turbulent flow. Technical report, ADVISORY GROUP FOR AEROSPACE RESEARCH AND DEVELOPMENT PARIS (FRANCE), 1973.

[29] M. Braza, R. Perrin, and Y. Hoarau. Turbulence properties in the cylinder wake at high reynolds numbers. *Journal of fluids and Structures*, 22(6-7):757–771, 2006.

[30] H. H. Bruun. Hot-wire anemometry: principles and signal analysis, 1996.

[31] J. Calvert. Experiments on the low-speed flow past cones. *Journal of Fluid Mechanics*, 27(2):273–289, 1967.

[32] B. Cantwell and D. Coles. An experimental study of entrainment and transport in the turbulent near wake of a circular cylinder. *Journal of fluid mechanics*, 136:321–374, 1983.

[33] I. Castro, M. Dianat, and A. Haque. Shear layers bounding separated regions. In *Turbulent shear flows 6*, pages 299–312. Springer, 1989.

[34] D. R. Chapman, D. M. Kuehn, and H. K. Larson. Investigation of separated flows in supersonic and subsonic streams with emphasis on the effect of transition. 1958.

[35] J. J. Charonko, C. V. King, B. L. Smith, and P. P. Vlachos. Assessment of pressure field calculations from particle image velocimetry measurements. *Meas. Sci. and Tech.*, 21(10):105401, 2010.

[36] S. Childress. *An introduction to theoretical fluid mechanics*, volume 19. American Mathematical Soc., 2009.

[37] H. Choi, W.-P. Jeon, and J. Kim. Control of flow over a bluff body. *Annu. Rev. Fluid Mech.*, 40:113–139, 2008.

[38] K. Cooper. Bluff-body aerodynamics as applied to vehicles. *Journal of Wind Engineering and Industrial Aerodynamics*, 49(1-3):1–21, 1993.

[39] J. O. Dabiri, S. Bose, B. J. Gemmell, S. P. Colin, and J. H. Costello. An algorithm to estimate unsteady and quasi-steady pressure fields from velocity field measurements. *Journal of Experimental Biology*, 217(3):331–336, 2014.

[40] L. Dalla Longa, A. Morgans, and J. Dahan. Reducing the pressure drag of a d-shaped bluff body using linear feedback control. *Theoretical and Computational Fluid Dynamics*, 31(5):567–577, 2017.

[41] J. Dandois, E. Garnier, and P. Sagaut. Numerical simulation of active separation control by a synthetic jet. *Journal of Fluid Mechanics*, 574:25–58, 2007.

[42] R. M. Darekar and S. J. Sherwin. Flow past a square-section cylinder with a wavy stagnation face. *Journal of Fluid Mechanics*, 426:263–295, 2001.

[43] L. David, T. Jardin, and A. Farcy. On the non-intrusive evaluation of fluid forces with the momentum equation approach. *Meas. Sci. and Tech.*, 20(9):095401, 2009.

[44] R. de Kat and B. Ganapathisubramani. Pressure from particle image velocimetry for convective flows: a Taylor's hypothesis approach. *Meas. Sci. and Tech.*, 24(2):024002, 2012.

[45] R. De Kat and B. Van Oudheusden. Instantaneous planar pressure determination from PIV in turbulent flow. *Exp. fluids*, 52(5):1089–1106, 2012.

[46] J. Derakhshandeh and M. M. Alam. A review of bluff body wakes. *Ocean Engineering*, 182:475–488, 2019.

[47] Y. Dubief and F. Delcayre. On coherent-vortex identification in turbulence. *Journal of turbulence*, 1(1):011, 2000.

[48] V. Durgesh, J. W. Naughton, and S. A. Whitmore. Experimental investigation of base-drag reduction via boundary-layer modification. *AIAA journal*, 51(2):416–425, 2013.

[49] A. Elshaer, G. Bitsuamlak, and A. El Damatty. Enhancing wind performance of tall buildings using corner aerodynamic optimization. *Engineering Structures*, 136:133–148, 2017.

[50] G. Elsinga and I. Marusic. Evolution and lifetimes of flow topology in a turbulent boundary layer. *Physics of Fluids*, 22(1):015102, 2010.

[51] A. Etebari and P. P. Vlachos. Improvements on the accuracy of derivative estimation from DPIV velocity measurements. *Exp. fluids*, 39(6):1040–1050, 2005.

[52] M. Felli, M. Falchi, and F. Pereira. Investigation of the flow field around a propeller rudder configuration: on-surface pressure measurements and velocity pressure phase-locked correlations. In *Proceedings of the Second International Symposium on Marine Propulsors smp*, volume 11, 2011.

[53] L.-H. Feng and L.-K. Ran. Wavelet multi-scale analysis of the circular cylinder wake under synthetic jets control. *International Journal of Heat and Fluid Flow*, 69:73–82, 2018.

[54] R. G. Flay. Bluff body aerodynamics. In *Advanced Structural Wind Engineering*, pages 59–84. Springer, 2013.

[55] A. Fluent. ANSYS Fluent theory guide 15.0. *Inc, Canonsburg, PA*, 2013.

[56] J.-M. Foucaut and M. Stanislas. Some considerations on the accuracy and frequency response of some derivative filters applied to particle image velocimetry vector fields. *Meas. Sci. and Tech.*, 13(7):1058, 2002.

[57] J. H. Fransson and S. Shahinfar. On the effect of free-stream turbulence on boundary-layer transition. *Journal of Fluid Mechanics*, 899, 2020.

[58] N. Gautier and J. Aider. Real-time planar flow velocity measurements using an optical flow algorithm implemented on gpu. *Journal of Visualization*, 18(2):277–286, 2015.

[59] W. K. George. Lectures in turbulence for the 21st century. *Chalmers University of Technology*, 2013.

[60] W. K. George, P. D. Beuther, and A. Shabbir. Polynomial calibrations for hot wires in thermally varying flows. *Experimental Thermal and Fluid Science*, 2(2):230–235, 1989.

[61] J. H. Gerrard. The mechanics of the formation region of vortices behind bluff bodies. *Journal of Fluid Mechanics*, 25(2):401–413, 1966.

[62] S. Ghaemi, D. Ragni, and F. Scarano. PIV-based pressure fluctuations in the turbulent boundary layer. *Exp. fluids*, 53(6):1823–1840, 2012.

[63] K. Gkoumas, F. Petrini, and F. Bontempi. Piezoelectric vibration energy harvesting from airflow in hvac (heating ventilation and air conditioning) systems. *Procedia engineering*, 199:3444–3449, 2017.

[64] L. Graftieaux, M. Michard, and N. Grosjean. Combining piv, pod and vortex identification algorithms for the study of unsteady turbulent swirling flows. *Measurement Science and technology*, 12(9):1422, 2001.

[65] M. Grandemange, M. Gohlke, and O. Cadot. Turbulent wake past a three-dimensional blunt body. part 1. global modes and bi-stability. *Journal of Fluid Mechanics*, 722:51–84, 2013.

[66] R. Gurka, A. Liberzon, D. Hefetz, D. Rubinstein, and U. Shavit. Computation of pressure distribution using PIV velocity data. In *Workshop on particle image velocimetry*, volume 2, 1999.

[67] C. He, Y. Liu, and L. Gan. A data assimilation model for turbulent flows using continuous adjoint formulation. *Physics of Fluids*, 30(10):105108, 2018.

[68] C. He, Y. Liu, and L. Gan. Instantaneous pressure determination from unsteady velocity fields using adjoint-based sequential data assimilation. *Physics of Fluids*, 32(3):035101, 2020.

[69] J. Heller, D. Henrion, and T. Pajdla. Stable radial distortion calibration by polynomial matrix inequalities programming. In *Asian Conference on Computer Vision*, pages 307–321. Springer, 2014.

[70] J. Howell, A. Sheppard, and A. Blakemore. Aerodynamic drag reduction for a simple bluff body using base bleed. *SAE transactions*, pages 1085–1091, 2003.

[71] H. Huang, H. Fiedler, and J. Wang. Limitation and improvement of piv. *Experiments in fluids*, 15(4):263–273, 1993.

[72] W. Hucho and G. Sovran. Aerodynamics of road vehicles. *Annual review of fluid mechanics*, 25(1):485–537, 1993.

[73] F. Huhn, D. Schanz, S. Gesemann, and A. Schröder. FFT integration of instantaneous 3d pressure gradient fields measured by lagrangian particle tracking in turbulent flows. *Exp. fluids*, 57(9):151, 2016.

[74] J. Hunt and A. Savill. Guidelines and criteria for the use of turbulence models in complex flows. *Prediction of turbulent flows*, pages 291–343, 2005.

[75] A. F. Hussain. Coherent structures and turbulence. *Journal of Fluid Mechanics*, 173:303–356, 1986.

[76] A. F. Hussain and M. Hayakawa. Eduction of large-scale organized structures in a turbulent plane wake. *Journal of Fluid Mechanics*, 180:193–229, 1987.

[77] J. Isaza, R. Salazar, and Z. Warhaft. On grid-generated turbulence in the near-and far field regions. *Journal of Fluid Mechanics*, 753:402, 2014.

[78] M. J. Janocha and M. C. Ong. Vortex-induced vibrations of piggyback pipelines near the horizontal plane wall in the upper transition regime. *Marine Structures*, 75:102872, 2021.

[79] Y. J. Jeon, G. Gomit, T. Earl, L. Chatellier, and L. David. Sequential least-square reconstruction of instantaneous pressure field around a body from TR-PIV. *Exp. fluids*, 59(2):27, 2018.

[80] E. Jogensen Finn. How to measuer turbulence with hotwire anemometers. *Dantec Dynamics*, 2002.

[81] P. Jonáš, O. Mazur, and V. Uruba. On the receptivity of the by-pass transition to the length scale of the outer stream turbulence. *European Journal of Mechanics-B/Fluids*, 19(5):707–722, 2000.

[82] I. Khabbouchi, H. Fellouah, M. Ferchichi, and M. S. Guellouz. Effects of free-stream turbulence and reynolds number on the separated shear layer from a circular cylinder. *Journal of Wind Engineering and Industrial Aerodynamics*, 135:46–56, 2014.

[83] K. Kim, M. Lee, S. Yoon, J. Boo, and H. Chun. Phase averaged velocity field in the near wake of a square cylinder obtained by a piv method. *Journal of visualization*, 5(1):29–36, 2002.

[84] E. Konstantinidis, S. Balabani, and M. Yianneskis. Conditional averaging of piv plane wake data using a cross-correlation approach. *Experiments in Fluids*, 39(1):38–47, 2005.

[85] V. Koschatzky, P. Moore, J. Westerweel, F. Scarano, and B. Boersma. High speed PIV applied to aerodynamic noise investigation. *Exp. fluids*, 50(4):863–876, 2011.

[86] A. Kourta, H. Boisson, P. Chassaing, and H. H. Minh. Nonlinear interaction and the transition to turbulence in the wake of a circular cylinder. *Journal of Fluid Mechanics*, 181:141–161, 1987.

[87] A. Kremheller. The aerodynamics development of the new nissan qashqai. Technical report, SAE Technical Paper, 2014.

[88] D. Kurtulus, F. Scarano, and L. David. Unsteady aerodynamic forces estimation on a square cylinder by TR-PIV. *Exp. fluids*, 42(2):185–196, 2007.

[89] D. Lander, C. Letchford, M. Amitay, and G. Kopp. Influence of the bluff body shear layers on the wake of a square prism in a turbulent flow. *Physical Review Fluids*, 1(4):044406, 2016.

[90] A. Laneville et al. An explanation of some effects of turbulence on bluff bodies. 1977.

[91] J. LAU and A. ROSHKO. Some observations on transition and reattachment of a free shear layer in incompressible flow(conditions determining if reattachment is laminar or turbulent in supersonic flow reattachment region for various geometrical configurations, noting chapman-korst criterion). 1965.

[92] B. Lee. Some effects of turbulence scale on the mean forces on a bluff body. *Journal of Wind Engineering and Industrial Aerodynamics*, 1:361–370, 1975.

[93] M. Lemke and J. Sesterhenn. Adjoint based pressure determination from PIV-data validation with synthetic PIV measurements. *Euro. J. Mech.-B/Fluids*, 58:29–38, 2016.

[94] Y. Li, C. Chung, and F. Fang. Effect of turbulent uniform flow past a two-dimensional square cylinder. *Journal of Applied Fluid Mechanics*, 11(5):1185–1192, 2018.

[95] X. Liu and J. Katz. Instantaneous pressure and material acceleration measurements using a four-exposure PIV system. *Exp. fluids*, 41(2):227, 2006.

[96] X. Liu and J. Katz. Cavitation phenomena occurring due to interaction of shear layer vortices with the trailing corner of a two-dimensional open cavity. *Physics of fluids*, 20(4):041702, 2008.

[97] X. Liu and J. R. Moreto. Error propagation from the piv-based pressure gradient to the integrated pressure by the omni-directional integration method. *Meas. Sci. Tech.*, 2020.

[98] V. Mansingh and P. Oosthuizen. Effects of splitter plates on the wake flow behind a bluff body. *AIAA journal*, 28(5):778–783, 1990.

[99] A. Mariotti, G. Buresti, and M. V. Salvetti. Connection between base drag, separating boundary layer characteristics and wake mean recirculation length of an axisymmetric blunt-based body. *Journal of Fluids and Structures*, 55:191–203, 2015.

[100] J. Marklund and L. Lofdahl. Influence of a diffuser to the wake flow of a passenger car. In *Fluids Engineering Division Summer Meeting*, volume 44755, pages 53–62. American Society of Mechanical Engineers, 2012.

[101] A. Mashhadi, A. Sohankar, and M. M. Alam. Flow over rectangular cylinder: Effects of cylinder aspect ratio and reynolds number. *International Journal of Mechanical Sciences*, 195:106264, 2021.

[102] J. McClure and S. Yarusevych. Optimization of planar PIV-based pressure estimates in laminar and turbulent wakes. *Exp. fluids*, 58(5):62, 2017.

[103] J. McClure and S. Yarusevych. Planar momentum balance in three-dimensional flows: applications to load estimation. *Experiments in Fluids*, 60(3):41, 2019.

[104] P. Meunier and T. Leweke. Analysis and treatment of errors due to high velocity gradients in particle image velocimetry. *Exp. fluids*, 35(5):408–421, 2003.

[105] S. Mittal and A. Raghuvanshi. Control of vortex shedding behind circular cylinder for flows at low reynolds numbers. *International journal for numerical methods in fluids*, 35(4):421–447, 2001.

[106] M. A. Mooneghi and R. Kargarmoakhar. Aerodynamic mitigation and shape optimization of buildings. *Journal of building engineering*, 6:225–235, 2016.

[107] D. Moore, C. Letchford, and M. Amitay. Energetic scales in a bluff body shear layer. *Journal of Fluid Mechanics*, 875:543–575, 2019.

[108] R. D. Moser and P. Moin. The effects of curvature in wall-bounded turbulent flows. *Journal of Fluid Mechanics*, 175:479–510, 1987.

[109] P. M. Nadge and R. Govardhan. High reynolds number flow over a backward-facing step: structure of the mean separation bubble. *Experiments in fluids*, 55(1):1–22, 2014.

[110] Y. Naka, M. Stanislas, J.-M. Foucaut, S. Coudert, J.-P. Laval, and S. Obi. Space–time pressure–velocity correlations in a turbulent boundary layer. *J. Fluid Mech.*, 771:624–675, 2015.

[111] Y. Nakamura and Y. Ohya. The effects of turbulence on the mean flow past two-dimensional rectangular cylinders. *Journal of Fluid Mechanics*, 149:255–273, 1984.

[112] Y. Nakamura and S. Ozono. The effects of turbulence on a separated and reattaching flow. *Journal of Fluid Mechanics*, 178:477–490, 1987.

[113] J. Nedić, B. Ganapathisubramani, and J. C. Vassilicos. Drag and near wake characteristics of flat plates normal to the flow with fractal edge geometries. *Fluid Dynamics Research*, 45(6):061406, 2013.

[114] J. Nedić, O. Supponen, B. Ganapathisubramani, and J. C. Vassilicos. Geometrical influence on vortex shedding in turbulent axisymmetric wakes. *Physics of Fluids*, 27(3):035103, 2015.

[115] H. Nicholson and J. P. Field. Some experimental techniques for the investigation of the mechanism of flame stabilization in the wakes of bluff bodies. In *Symposium on combustion and flame, and explosion phenomena*, volume 3, pages 44–68. Elsevier, 1948.

[116] M. Noor, A. P. Wandel, and T. Yusaf. Analysis of recirculation zone and ignition position of non-premixed bluff-body for biogas mild combustion. *International Journal of Automotive and Mechanical Engineering*, 8(1):1176–1186, 2013.

[117] Z. Pan, J. Whitehead, S. Thomson, and T. Truscott. Error propagation dynamics of PIV-based pressure field calculations: How well does the pressure poisson solver perform inherently? *Meas. Sci. and Tech.*, 27(8):084012, 2016.

[118] Z. Pan, J. P. Whitehead, G. Richards, T. T. Truscott, and B. L. Smith. Error propagation dynamics of PIV-based pressure field calculation (3): What is the minimum resolvable pressure in a reconstructed field? *arXiv preprint arXiv:1807.03958*, 2018.

[119] D. D. Papailiou and P. S. Lykoudis. Turbulent vortex streets and the entrainment mechanism of the turbulent wake. *Journal of Fluid Mechanics*, 62(1):11–31, 1974.

[120] V. Parezanovic and O. Cadot. Experimental sensitivity analysis of the global properties of a 2d turbulent wake. *J. Fluid Mech*, 693:115, 2012.

[121] H. Park, D. Lee, W.-P. Jeon, S. Hahn, J. Kim, J. Kim, J. Choi, and H. Choi. Drag reduction in flow over a two-dimensional bluff body with a blunt trailing edge using a new passive device. *Journal of Fluid Mechanics*, 563:389–414, 2006.

[122] P.-Y. Passaggia, V. K. Chalamalla, M. W. Hurley, A. Scotti, and E. Santilli. Estimating pressure and internal-wave flux from laboratory experiments in focusing internal waves. *Experiments in Fluids*, 61(11):1–29, 2020.

[123] P.-Y. Passaggia, T. Leweke, and U. Ehrenstein. Transverse instability and low-frequency flapping in incompressible separated boundary layer flows: an experimental study. *J. Fluid Mech.*, 703:363–373, 2012.

[124] P.-Y. Passaggia, N. Mazellier, and A. Kourta. On the effect of free-stream turbulence on the aerodynamics of a simplified road vehicle. *J. Fluid Mech.*, page In revision, 2020.

[125] M. Pastoor, L. Henning, B. R. Noack, R. King, and G. Tadmor. Feedback shear layer control for bluff body drag reduction. *Journal of fluid mechanics*, 608:161–196, 2008.

[126] G. Paterakis, K. Souflas, A. Naxakis, and P. Koutmos. A study of recirculating flow fields downstream of a diverse range of axisymmetric bluff body geometries suitable for flame stabilization. *Aerospace*, 8(11):339, 2021.

[127] R. Perrin, M. Braza, E. Cid, S. Cazin, P. Chassaing, C. Mockett, T. Reimann, and F. Thiele. Coherent and turbulent process analysis in the flow past a circular cylinder at high reynolds number. *Journal of fluids and structures*, 24(8):1313–1325, 2008.

[128] R. Perrin, M. Braza, E. Cid, S. Cazin, F. Moradei, A. Barthet, A. Sevrain, and Y. Hoarau. Near-wake turbulence properties in the high reynolds incompressible flow around a circular cylinder by 2c and 3c piv. In *Engineering Turbulence Modelling and Experiments 6*, pages 441–450. Elsevier, 2005.

[129] A. Perry, M. Chong, and T. Lim. The vortex-shedding process behind two-dimensional bluff bodies. *Journal of Fluid Mechanics*, 116:77–90, 1982.

[130] R. Peyret. *Spectral methods for incompressible viscous flow*, volume 148. Springer Science & Business Media, 2013.

[131] S. B. Pope. Turbulent flows, 2001.

[132] F. A. Portela, G. Papadakis, and J. Vassilicos. Turbulence dissipation and the role of coherent structures in the near wake of a square prism. *Physical Review Fluids*, 3(12):124609, 2018.

[133] F. A. Portela, G. Papadakis, and J. Vassilicos. The role of coherent structures and inhomogeneity in near-field interscale turbulent energy transfers. *Journal of Fluid Mechanics*, 896, 2020.

[134] A. Prasad and C. H. Williamson. The instability of the shear layer separating from a bluff body. *Journal of fluid mechanics*, 333:375–402, 1997.

[135] S. PRICE, D. SUMNER, J. SMITH, K. LEONG, and M. PAÏDOUSSIS. Flow visualization around a circular cylinder near to a plane wall. *Journal of Fluids and Structures*, 16(2):175–191, 2002.

[136] A. Pumir. A numerical study of pressure fluctuations in three-dimensional, incompressible, homogeneous, isotropic turbulence. *Physics of Fluids*, 6(6):2071–2083, 1994.

[137] M. Raffel, C. E. Willert, F. Scarano, C. J. Kähler, S. T. Wereley, and J. Kompenhans. *Particle image velocimetry: a practical guide*. Springer, 2018.

[138] D. Ragni, A. Ashok, B. Van Oudheusden, and F. Scarano. Surface pressure and aerodynamic loads determination of a transonic airfoil based on particle image velocimetry. *Meas. Sci. and Tech.*, 20(7):074005, 2009.

[139] S. Rajagopalan and R. Antonia. Flow around a circular cylinder—structure of the near wake shear layer. *Experiments in fluids*, 38(4):393–402, 2005.

[140] B. Ran and J. Katz. Pressure fluctuations and their effect on cavitation inception within water jets. *J. Fluid Mech.*, 262:223–263, 1994.

[141] J. Ren, X. Mao, and S. Fu. Image-based flow decomposition using empirical wavelet transform. *Journal of Fluid Mechanics*, 906, 2021.

[142] W. Reynolds and A. Hussain. The mechanics of an organized wave in turbulent shear flow. part 3. theoretical models and comparisons with experiments. *Journal of Fluid Mechanics*, 54(2):263–288, 1972.

[143] D. Riabouchinsky. On steady fluid motions with free surfaces. *Proceedings of the London Mathematical Society*, 2(1):206–215, 1921.

[144] A. Roshko. On the development of turbulent wakes from vortex streets. 1953.

[145] A. Roshko. On the drag and shedding frequency of two-dimensional bluff bodies. 1954.

[146] A. Roshko. On the wake and drag of bluff bodies. *Journal of the aeronautical sciences*, 22(2):124–132, 1955.

[147] A. Roshko. Perspectives on bluff body aerodynamics. *Journal of Wind Engineering and Industrial Aerodynamics*, 49(1-3):79–100, 1993.

[148] A. Rowe, A. Fry, and F. Motallebi. Influence of boundary-layer thickness on base pressure and vortex shedding frequency. *AIAA journal*, 39(4):754–756, 2001.

[149] A. K. Saha, K. Muralidhar, and G. Biswas. Vortex structures and kinetic energy budget in two-dimensional flow past a square cylinder. *Computers & fluids*, 29(6):669–694, 2000.

[150] H. Sakamoto, K. Tan, and H. Haniu. An optimum suppression of fluid forces by controlling a shear layer separated from a square prism. 1991.

[151] W. S. Saric, H. L. Reed, and E. J. Kerschen. Boundary-layer receptivity to freestream disturbances. *Annual review of fluid mechanics*, 34(1):291–319, 2002.

[152] H. Schlichting. *Boundary layer theory*, volume 960. Springer, 1960.

[153] P. J. Schmid. Dynamic mode decomposition of numerical and experimental data. *J. Fluid Mech.*, 656:5–28, 2010.

[154] P. J. Schmid and D. S. Henningson. *Stability and transition in shear flows*, volume 142. Springer Science & Business Media, 2000.

[155] T. Shaqarin, P. Oswald, B. Noack, and R. Semaan. Drag reduction of a d-shaped bluff-body using linear parameter varying control. *Physics of Fluids*, 33(7):077108, 2021.

[156] E. M. Sharify, H. Saito, H. HARASAWA, S. Takahashi, and N. Arai. Experimental and numerical study of blockage effects on flow characteristics around a square-section cylinder. *Journal of the Japanese Society for Experimental Mechanics*, 13(Special_Issue):s7–s12, 2013.

[157] A. Sharma and V. Eswaran. Heat and fluid flow across a square cylinder in the two-dimensional laminar flow regime. *Numerical Heat Transfer, Part A: Applications*, 45(3):247–269, 2004.

[158] K. Sharma and S. Dutta. Flow control over a square cylinder using attached rigid and flexible splitter plate at intermediate flow regime. *Physics of Fluids*, 32(1):014104, 2020.

[159] C. Sieverding and H. Heinemann. The influence of boundary layer state on vortex shedding from flat plates and turbine cascades. 1990.

[160] A. Sjunnesson, C. Nelsson, and E. Max. Lda measurements of velocities and turbulence in a bluff body stabilized flame. 1991.

[161] A. J. Smits, B. J. McKeon, and I. Marusic. High–reynolds number wall turbulence. *Annual Review of Fluid Mechanics*, 43:353–375, 2011.

[162] A. Sohankar, C. Norberg, and L. Davidson. Low-reynolds-number flow around a square cylinder at incidence: study of blockage, onset of vortex shedding and outlet boundary condition. *International journal for numerical methods in fluids*, 26(1):39–56, 1998.

[163] C. Solomon and T. Breckon. *Fundamentals of Digital Image Processing: A practical approach with examples in Matlab*. John Wiley & Sons, 2011.

[164] G. R. Spedding and A. Hedenström. PIV-based investigations of animal flight. In *Animal Locomotion*, pages 187–201. Springer, 2010.

[165] F. Stella, N. Mazellier, and A. Kourta. Scaling of separated shear layers: an investigation of mass entrainment. *Journal of Fluid Mechanics*, 826:851–887, 2017.

[166] P. J. Strykowski and K. R. Sreenivasan. On the formation and suppression of vortex 'shedding'at low reynolds numbers. *Journal of Fluid Mechanics*, 218:71–107, 1990.

[167] P. Sturm. Some lecture notes on geometric computer vision. University Lecture, 2013.

[168] G. Sui, X. Shan, H. Tian, L. Wang, and T. Xie. Study on different underwater energy harvester arrays based on flow-induced vibration. *Mechanical Systems and Signal Processing*, 167:108546, 2022.

[169] R. Sullerey, A. Gupta, and C. Moorthy. Similarity in the turbulent near wake of bluff bodies. *AIAA journal*, 13(11):1425–1429, 1975.

[170] B. M. Sumer et al. *Hydrodynamics around cylindrical strucures*, volume 26. World scientific, 2006.

[171] C. Sun, A. M. Azmi, T. Zhou, H. Zhu, and Z. Zang. Experimental study on wake flow structures of screen cylinders using piv. *International Journal of Heat and Fluid Flow*, 85:108643, 2020.

[172] X. Sun, C. Yu, A. Rinoshika, L. Li, and Y. Zheng. Phase averaging on square cylinder wake based on wavelet analysis. In *2018 International Conference on Wavelet Analysis and Pattern Recognition (ICWAPR)*, pages 168–174. IEEE, 2018.

[173] M. Tanner. A method for reducing the base drag of wings with blunt trailing edge. *Aeronautical Quarterly*, 23(1):15–23, 1972.

[174] H. Tennekes and J. Lumley. First course in turbulence. *First Course in Turbulence*, 1972.

[175] B. Thiria, O. Cadot, and J.-F. Beaudoin. Passive drag control of a blunt trailing edge cylinder. *Journal of fluids and structures*, 25(5):766–776, 2009.

[176] B. H. Timmins, B. W. Wilson, B. L. Smith, and P. P. Vlachos. A method for automatic estimation of instantaneous local uncertainty in particle image velocimetry measurements. *Exp. fluids*, 53(4):1133–1147, 2012.

[177] C. E. Tinney, F. Coiffet, J. Delville, A. M. Hall, P. Jordan, and M. N. Glauser. On spectral linear stochastic estimation. *Exp. Fluids*, 41(5):763–775, 2006.

[178] N. Tombazis and P. Bearman. A study of three-dimensional aspects of vortex shedding from a bluff body with a mild geometric disturbance. *Journal of Fluid Mechanics*, 330:85–112, 1997.

[179] A. Towne, O. T. Schmidt, and T. Colonius. Spectral proper orthogonal decomposition and its relationship to dynamic mode decomposition and resolvent analysis. *J. Fluid Mech.*, 847:821–867, 2018.

[180] L. N. Trefethen. *Spectral methods in MATLAB*, volume 10. Siam, 2000.

[181] R. Trip and J. H. Fransson. Bluff body boundary-layer modification and its effect on the near-wake topology. *Physics of Fluids*, 29(9):095105, 2017.

[182] F. Tröltzsch. *Optimal control of partial differential equations: theory, methods, and applications*, volume 112. American Mathematical Soc., 2010.

[183] T. Tronchin, L. David, and A. Farcy. Loads and pressure evaluation of the flow around a flapping wing from instantaneous 3D velocity measurements. *Exp. fluids*, 56(1):7, 2015.

[184] C. Tropea, A. L. Yarin, J. F. Foss, et al. *Springer handbook of experimental fluid mechanics*, volume 1. Springer, 2007.

[185] D. Tsahalis. The effect of seabottom proximity of the vortex-induced vibrations and fatigue life of offshore pipelines. 1983.

[186] M. Unal, J.-C. Lin, and D. Rockwell. Force prediction by PIV imaging: a momentum-based approach. *Journal of fluids and structures*, 11(8):965–971, 1997.

[187] P. Valente and J. C. Vassilicos. The decay of homogeneous turbulence generated by multi-scale grids. In *Seventh International Symposium on Turbulence and Shear Flow Phenomena*. Begel House Inc., 2011.

[188] J. Van der Kindere, A. Laskari, B. Ganapathisubramani, and R. De Kat. Pressure from 2d snapshot PIV. *Exp. fluids*, 60(2):32, 2019.

[189] B. Van Oudheusden. Principles and application of velocimetry-based planar pressure imaging in compressible flows with shocks. *Exp. fluids*, 45(4):657–674, 2008.

[190] B. Van Oudheusden. PIV-based pressure measurement. *Meas. Sci. and Tech.*, 24(3):032001, 2013.

[191] B. Van Oudheusden, F. Scarano, and E. Casimiri. Non-intrusive load characterization of an airfoil using piv. *Experiments in Fluids*, 40(6):988–992, 2006.

[192] B. Van Oudheusden, F. Scarano, N. Van Hinsberg, and D. Watt. Phase-resolved characterization of vortex shedding in the near wake of a square-section cylinder at incidence. *Experiments in Fluids*, 39(1):86–98, 2005.

[193] J. J. C. Villanueva and L. F. F. da Silva. Study of the turbulent velocity field in the near wake of a bluff body. *Flow, Turbulence and Combustion*, 97(3):715–728, 2016.

[194] C. Y. Wang, Q. Gao, R. J. Wei, T. Li, and J. J. Wang. Spectral decomposition-based fast pressure integration algorithm. *Exp. fluids*, 58(7):84, 2017.

[195] Q.-Y. Wang, S.-J. Xu, L. Gan, W.-G. Zhang, and Y. Zhou. Scaling of the time-mean characteristics in the polygonal cylinder near-wake. *Experiments in Fluids*, 60(12):1–15, 2019.

[196] X. Wang, J. Chen, B. Zhou, Y. Li, and Q. Xiang. Experimental investigation of flow past a confined bluff body: Effects of body shape, blockage ratio and reynolds number. *Ocean Engineering*, 220:108412, 2021.

[197] T. Wei and C. R. Smith. Secondary vortices in the wake of circular cylinders. *Journal of Fluid Mechanics*, 169:513–533, 1986.

[198] G. S. West and C. J. Apelt. The effects of tunnel blockage and aspect ratio on the mean flow past a circular cylinder with reynolds numbers between 104 and 105. *Journal of Fluid Mechanics*, 114:361–377, 1982.

[199] C. H. Williamson. Oblique and parallel modes of vortex shedding in the wake of a circular cylinder at low reynolds numbers. *Journal of Fluid Mechanics*, 206:579–627, 1989.

[200] C. H. Williamson. Vortex dynamics in the cylinder wake. *Annual review of fluid mechanics*, 28(1):477–539, 1996.

[201] B. M. Wilson and B. L. Smith. Uncertainty on PIV mean and fluctuating velocity due to bias and random errors. *Meas. Sci. and Tech.*, 24(3):035302, 2013.

[202] T. Y.-T. Wu. Cavity and wake flows. *Annual Review of Fluid Mechanics*, 4(1):243–284, 1972.

[203] J. Xie. Aerodynamic optimization of super-tall buildings and its effectiveness assessment. *Journal of Wind Engineering and Industrial Aerodynamics*, 130:88–98, 2014.

[204] W. Xu, S. Zhang, Y. Ma, and B. Liu. Fluid forces acting on three and four long side-by-side flexible cylinders undergoing flow-induced vibration (fiv). *Marine Structures*, 75:102877, 2021.

[205] K. Yang, T. Qiu, J. Wang, and L. Tang. Magnet-induced monostable nonlinearity for improving the viv-galloping-coupled wind energy harvesting using combined cross-sectioned bluff body. *Smart Materials and Structures*, 29(7):07LT01, 2020.

[206] M. W. Yiu. *Turbulent structures in the wake of circular cylinders*. Hong Kong Polytechnic University (Hong Kong), 2005.

[207] Q. Zhang, Y. Liu, and S. Wang. The identification of coherent structures using proper orthogonal decomposition and dynamic mode decomposition. *Journal of Fluids and Structures*, 49:53–72, 2014.

[208] T. Zhou, S. M. Razali, Y. Zhou, L. Chua, and L. Cheng. Dependence of the wake on inclination of a stationary cylinder. *Experiments in fluids*, 46(6):1125–1138, 2009.

Roshan SHANMUGHAN

Contribution to the analysis of turbulent wakes of bluff bodies: Impact on the aerodynamic drag.

Abstract: Flow separation is a phenomenon at the origin of aerodynamic performance-losses such as drag increase for a vehicle. This work focuses on understanding the physical mechanism driving the drag of a simplified vehicle – a 2D bluff body, by the balance of mean momentum and Reynolds stress equations in its wake. A tool for accurate estimation of mean pressure field is developed which allows the closure of the mean momentum equation. The method utilizes the concept of optimal control to correct the mean pressure, estimated from PIV-based velocity fields, using sparse reliable pressure measurements. The budget of mean momentum, along a control volume in the near wake, reveals the role and contribution of mean pressure and the Reynolds stress components to the mean drag. The normal components of the Reynolds stress tensor act as a dominant source, through the mean pressure, and a sink for the mean drag. On the other hand, the Reynolds shear stress component redistributes the momentum spatially. The mechanisms driving the normal Reynolds stresses are addressed partially by decomposing the fluctuations into coherent and incoherent contributions. A novel method of coherent pressure reconstruction is presented, allowing for the closure of the coherent Reynolds-stress transport equation. The balance shows that the coherent pressure diffusion and strain terms play key roles in redistributing the energy spatially as well as between the normal stress components. The perturbation of this mechanism leads to the decrease of coherent normal Reynolds stresses, and consequently, a drag reduction. The study also highlights the regions playing key roles in the interplay between the mean flow and the coherent structures.
Keywords: Drag reduction, momentum transport, coherent structures, Reynolds-stress transport, pressure reconstruction.

Contribution à l'analyse du sillage turbulent d'un corps épais : Impact sur la traînée aérodynamique.

Résumé: Le décollement massif est un phénomène à l'origine de la perte de performance aérodynamique comme l'augmentation de la traînée pour un véhicule. Ce travail contribue à la compréhension des mécanismes qui contrôlent la traînée d'un véhicule simplifié, un corps épais bidimensionnel. Les équations de transport de quantité de mouvement moyen et des contraintes de Reynolds dans le sillage sont analysées à partir de la vélocimétrie obtenue par imagerie de particules. Un outil d'estimation précise du champ de pression moyen est développé, permettant la clôture du bilan de quantité de mouvement moyenne. La méthode utilise le concept de contrôle optimal pour corriger la pression, estimée à partir de la PIV, et utilisant des mesures de pression fiables et éparses. Le bilan révèle le processus d'échange de quantité de mouvement dans le sillage proche. Les composantes normales du tenseur des contraintes Reynolds jouent un rôle de source et de puits pour la traînée, tandis que la composante de cisaillement redistribue la quantité de mouvement. Les mécanismes de transport des composantes normales des contraintes de Reynolds sont abordés partiellement en décomposant les fluctuations en structures cohérentes et incohérentes. Une nouvelle méthode d'estimation de la pression des structures cohérentes est introduite. Les équations de transport des contraintes de Reynolds associées aux structures cohérent révèlent que les termes associés à la pression cohérente jouent un rôle important dans la redistribution de l'énergie. La perturbation de ce mécanisme entraîne la diminution des contraintes de Reynolds et, par conséquent, la réduction de la traînée. L'étude met également en évidence les régions qui jouent un rôle clé dans l'interaction entre l'écoulement moyen et les structures cohérentes.
Mots clés: Réduction de traînée, transport de quantité de mouvement, structures cohérentes, transport des contraintes de Reynolds, reconstruction du champ de pression.

Laboratoire PRISME,
8 **rue Léonard de Vinci,**
45072 **Orléans Cedex 2.**